Nusrat Sajid

Chemical patterning and nano-mechanical measurements for understanding and controlling nerve growth

PhD

September 2014

Chemical patterning and nano-mechanical measurements for understanding and controlling nerve growth

Nusrat Sajid

A thesis submitted for the degree of doctor of philosophy

Department of Physics and Astronomy

The University of Sheffield

September 2014

Declaration

The work described in this thesis was undertaken at the University of Sheffield between Dec 2009 and April 2014 under the supervision of Dr. Jamie Hobbs. Unless stated, it is work of the author and has not been submitted in whole or in part for any other degree at this or any other institute.

Nusrat Sajid

This thesis is dedicated to my mother

for her countless and unforgotten love

Abstract

Nerve injury repair is a complex challenge in tissue engineering. Complete and correct nerve regeneration is difficult to obtain due to loss of motor and sensory functions. Injured nerve has a significant ability to re-grow but their repair tends to fail due to neurite outgrowth complexity which involves the interaction through surface receptors with the extracellular inhomogeneous environment for the detection of guidance cues towards the appropriate location. Chemical and mechanical interaction plays a potential role in neurite outgrowth guidance that can be provided by a chemically modified pattern surface. Various photo patterning techniques have been employed to study the growth cone extension along with neurite (axon and dendrite) extension on patterned surfaces and an AFM has been used for cell mechanics measurements under physiological conditions.

In the present work, two maskless far-field photolithography setups have been developed. These setups with a spatial light modulator and without the spatial light modulator, have been used for the fabrication of patterned structure on BPRS-100 resist as proof of principal. Next, the masksless setup without a spatial light modulator has been used for patterning structures on NPPOC protected aminosiloxane monolayers and reactive patterned SAM surfaces which were further chemically functionalized with a PMPC brush. The grafting density of PMPC brushes were measured by analysis of the brush thickness data at different patterning speed and different polymerization time in the dry state and under water. Maskless photolithography with a spatial light modulator also fabricated patterned structures on NPPOC protected SAM using UV light.

AFM has been employed to investigate the topography of primary Schwann cells, RN-22 cells and NG-108-15 neuronal cells. Mechanical properties of primary Schwann cells neuronal cells and growth cones were measured with two different probes. However, sharp tips were used to measure the nano-mechanic of long and thin neurites. Cell topographic information have been obtained with the set-point and contact-point maps and it has been shown that the contact-point is an effective and meaningful way to clearly resolve the cell edge protrusions. Stiffness maps present the inherent stiffness of different regions of cells in neurites and growth cones.

Acknowledgements

I would like to express my greatest gratitude to my supervisor, Professor Jamie Hobbs for guidance, support and expertise throughout the completion of this study. I greatly acknowledge Professor John W. Haycock for his continuous support, guidance and knowledge throughout the cell biology project and greatly appreciate Juliet bell for technical assistance, guidance and encouragement for cell culture of the NG-108-15 neuronal cells, RN-22 Schwann cells and primary Schwann cells. I would also like to thank Miss Claire Johnson and Mr. Mark Wagner for technical support in the laboratory.

I greatly acknowledge to Professor Prof. Graham J. Leggett and his group members Alexander Johnson and Abdullah M Alswieleh for continuous support for samples preparation and polymer brush growth on patterned surface.

Sincere gratitude also goes to Dr. Ehtsham U Haq for all his help, support and advice from the very beginning for my P.hD project of mask-less photolithography setup. I would also like to thank to Dr. Osama El- Zubir and Dr. Nic Mullin for valuable discussion and constructive suggestions for maskless experimental setup.

I am also grateful to Prof. David Lidzey for his support for clean room for sample preparation that potentially contribute a lot during my maskless photolithography setup development.

I would like to acknowledge COMSATS institute information and technology, Islamabad, Pakistan for P.hD funds and ESPR for my project funding here at the University of Sheffield. I greatly thanks to Jake Albon about cell mechanics discussion, Ross Carter for MFP software help, Paul Chapman for answering my many questions about polymer brush data and Dr. Rebecca for proof-reading of my thesis chapters. I would also like to thank all group members of SPM family for their support during my study. I would like to express my special thanks to my husband, my family and friends for their continuous encouragement and support to accomplish this goal.

List of Abbreviations

2D	Two dimensions
3D	Three dimensions
AC	Dynamic mode
AFM	Atomic force microscope
AFS	Atomic force spectroscopy
AM-AFM	Amplitude modulation atomic force microscope
APTES	Aminopropyl triethoxysilane
ATRP	Atom transfer radical polymerization
CNS	Central nervous system
CW	Continuous wave
DMD	Digital micro mirror
DMT	Derjaguin-Müller-Toporov
DPN	Dip pen nanolithography
DNA	Deoxyribonucleic acid
DMEM	Dulbecco's ‘modified Eagle’s medium
DRG	Dorsal root ganglia
EBL	Electron beam lithography
ECM	Extracellular matrix
EGF	Epidermal growth factor
FCS	Fetal calf serum
FFM	Friction force microscopy
FIBL	Focus ion beams lithography frequency modulation

FM-AFM	Frequency modulation atomic force microscope
IC	Integrated circuit
IMS	Industrial methylated spirits
InVOLS	Inverse optical lever sensitivity of the cantilever
IPL	Isopropanol
JKR	Johnson-Kendall Roberts
kPa	Kilo pascal
MOPL	Mask-less optical projection lithography
MEMs	Micro electro-mechanical systems
MFP	Molecular force plot
NA	Numerical aperture
OTS	Octadecyltrichlorosilane
PBS	Phosphate-buffered saline
PDMS	Poly (dimethylesiloxane) polydimethylsiloxane
PFA	Para-formaldehyde
PLL	Poly-L-lysine
PMPC	Poly 2-methacryloyloxy ethyl phosphorylcholine
PMMA	Polymethyl methacrylate
PNS	Peripheral nervous system
RAIRS	Reflection-absorption infrared spectroscopy
ROMP	Ring opening metathesis polymerization
SAMs	Self-assembled monolayers
SEM	Scanning electron microscopy

SET-LRP	Single-electron transfer living radical polymerization
SLM	Spatial light modulator
SNOM	Scanning near-field optical microscopy
NMP	Nitroxide mediated polymerization
TFAA	Trifluoroacetic anhydride
TPA	Two photon absorption
TPP	Two photon lithography
USA	The unites state of America
UV	Ultra Violet
µCP	Micro-contact printing
XPS	X-ray photoelectron spectroscopy
ZPAPL	Zone-plate-array photolithography

Contents

Chapter 1 - Introduction

1.1 Overview

Damage to the peripheral nervous system is common and its repair and regeneration is a big challenge in nerve tissue engineering. Although nerve function recovery occurs in many mild injuries often outcomes are disappointing following severe trauma. Various nerve repair and regeneration strategies have been employed to provide correct orientation to regenerating nerve cells either in the form of nerve guidance channels or supporting cells or both. To fabricate nerve guidance conduits on the micron to nanoscale, various techniques such as photolithography, micromachining, electro-spinning and micro-contact-printing have been employed. Advancement in technology has contributed to fabrication processes, nanoscale science and engineering. Different mask based lithography systems combined with different fabrication processes e.g., deposition and etching are used to create micro- and nanoscale structures. Maskless far-field photolithography is a cost effective technique to replicate a pattern rapidly with high throughput and can contribute significantly by opening new routes for micron to nanoscale fabrication. These micro- and nanoscale patterned structures can be further utilized in various applications such as biology, chemistry and nanomedicine.

Atomic force microscope (AFM) is a versatile and widespread tool for topographical and mechanical investigation on a wide variety of samples including, semiconductors, polymers, living cells and materials. In cell biology, AFM is considered as one of the promising and effective techniques for the investigation of micro-and nano-mechanical properties of cells, small filaments and neurites. Various micro mechanical techniques are available but AFM is the only tool that provides nano-mechanical properties on various types of samples.

One of the main themes of this report is to build a maskless photolithography experimental setup for the fabrication of micron to sub-micron structures on different substrate. A detailed description of two different masksless photolithographic experimental setups is given and further these setups are used to define patterns on resist and self-assembled monolayers. The second main aim of this report is to use the atomic force microscope to identify the true topography of neuronal cells and two different Schwann cells as well as to measure nano-mechanical properties of the neuronal cells and the primary Schwann cells. The long term aim of the project, beyond the scope of the current thesis, is to use maskless photolithographic patterning to control the surface chemistry of complex 3-dimensional structures designed to guide nerve regeneration, the chemical modification providing cues to direct growth that re-

enforce the topographic guidance provided by the structures. By coupling this with the AFM imaging methods developed in this thesis, it is hoped that improved understanding of the mechanisms behind nerve cell guidance can be gained in the future, helping to improve future methods of nerve regeneration. It is hoped that the maskless photolithography experimental setup developed can be used for the fabrication of 2D and 3D micron length scale patterns that can be utilized in cell biology to control and regulate cell growth as well as in chemistry to study the stimuli-response of different polymer brushes of varying thickness on micro-patterns.

1.2 Thesis outline

The thesis outline is as follows. Chapter 1 gives a brief introduction to the photolithography technique used in far-field and near field patterning and different working modes of atomic force microscope that have been used to investigate cell topography and mechanics. Other techniques for the investigation of cell mechanical properties are also described.
Chapter 2 describes the maskless photolithography experimental setups development based upon a spatial light modulator and without a spatial light modulator. The experimental setups performance was evaluated on the commercially available resist material due to fast and easy handling.

Chapter 3 describes two maskless photolithography techniques that are used for the fabrication of patterned structures on NPPOC protected aminosiloxane monolayers through UV (351 nm) irradiation. Further, poly(2-(methacryloyloxy)ethyl phosphorylcholine) (PMPC) was grown on a UV deprotected surface and polymer thickness was characterized with AFM in dry state and water.

Chapter 4 describes the AFM imaging of three different types of cells including live primary Schwann cells, live and fixed RN-22 Schwann cells and the fixed NG-108-15 in tapping mode to investigate the cells topography and its growth pathways.

Chapter 5 describes the investigation of mechanical properties of peripheral nervous system with AFM. In this study, colloidal and sharp probes were used to measure the mechanical properties of primary Schwann cells, the neuronal cells and growth cones and sharp probes were used to describe the properties of neurites.

Chapter 6 presents the conclusions based on the experimental work conducted by author in this thesis. This chapter also presents future work, first, maskless photolithography setups can

be used to create 2D and 3D patterned to monitor the growth pathway of different cells. Second, polymer brush thickness investigation under different liquid at different conditions.

1.3 Micro- and nanolithography techniques

1.3.1 Photolithography

Photolithography is used to define a pattern on a substrate by exposing a light sensitive resist to visible or UV light. After development various structures can be formed on the substrate. Photolithography is used extensively in the semiconductor and IC industry during the production of microchips and MEMs [1–7]. Fig. 1.1 schematic representation shows the main steps of photolithography.

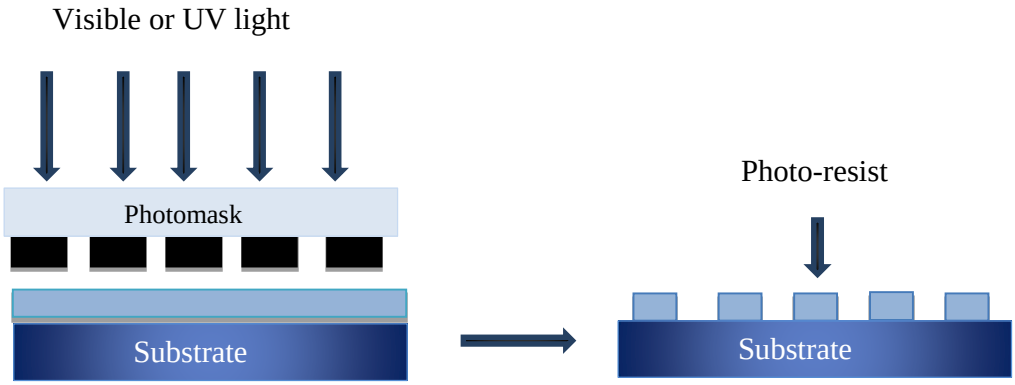

Fig. 1.1. Schematic representation shows the main steps of photolithography. (a) Exposure, where a photo-resist coated substrate is exposed to UV light through a mask (b) Development, where the exposed photo-resist is removed and the patterned surface is formed.

Optical lithography can be divided into two types, mask-based and maskless lithography. In mask-based lithography a photo-mask on the resist coated substrate is irradiated to form features in the shape of the holes in the photo-mask after development. There are three types of mask based photolithography: contact printing, proximity printing and projection printing [7,8]. These are schematically illustrated in Fig. 1.2. In contact and proximity lithography the photo-mask is directly in contact with the photo-resist. Contact and proximity lithography are used to fabricate patterns in the micrometre range.

In contrast, projection lithography is mainly used in the semiconductor industry for device fabrication. In optical projection lithography a pattern is created on the mask four times larger than the desired features to be patterned onto the silicon. Homogeneous laser beam is passed through the photo-mask and the mask image is projected onto a silicon wafer using complex reduction lenses.

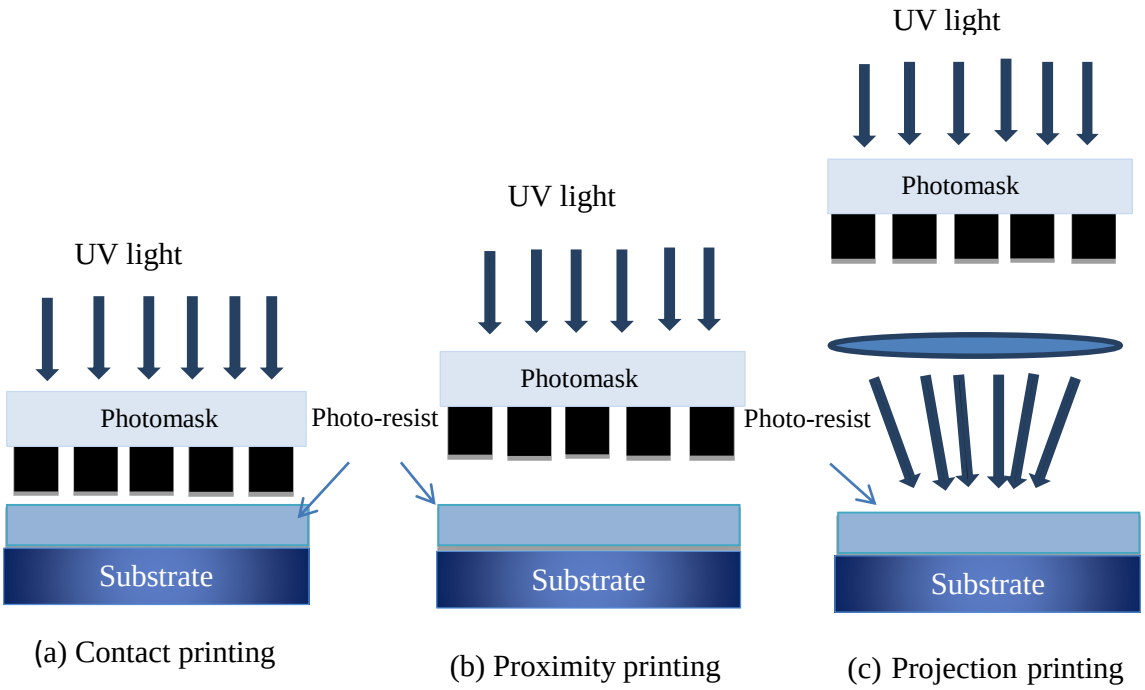

(a) Contact printing (b) Proximity printing (c) Projection printing

Fig. 1.2. Schematic illustration of three types of photolithography (a) contact printing (b) proximity printing and (c) projection printing [7].

Currently an advanced two step lithography system, called a scanner and stepper, is used to image the photo-mask pattern many times onto the same Si wafer. In the scanning part, a small area of a photo-mask is irradiated in a continuous scanning motion until the whole pattern has been transferred onto one part of the silicon wafer. In the stepping part, the silicon wafer is moved to the next area and scanning is repeated. The operative wavelength for advanced lithography is 193 nm, throughput is 60 or more silicon wafers per hour, and the minimum feature size is around 25 nm [3,9].

In photolithography the resolution of the optical exposure system is very important because it defines the limit of feature size. One of the major factors that limit the resolution is the numerical aperture (NA) of the physical objective lens and wavelength of light used. The numerical aperture (NA) of lens is defined as

$$NA = n \sin \alpha \qquad (1.1)$$

Where n is the refractive index of the air or fluid in which lens is immersed and α is half the angular aperture. NA defines the ability of the lens to collect the diffracted light. The resolution of an optical system is defined as

$$R = k \lambda/NA \qquad (1.2)$$

where, R is resolution, λ is the wavelength of light and k has a value ≥ 0.25 [10].

The resolution of an optical lithography system can be improved by using a shorter wavelength and an objective lens with higher NA. Other techniques to improve resolution include photo-mask modification, optical proximity correction, off-axis illumination, phase-shift mask and optical proximity effect correction [10–12].

In conventional photolithography the diffraction limit is another constraint on the fabrication of very small features. Extreme ultraviolet and X-ray radiation is used to fabricate nanoscale features and this is both complicated and difficult to use. Recently, with a transition from 193 nm to 157 nm wavelengths, projection lithography required new resist material, photo-mask and compatible optics. There are three major issues for projection lithography at 157 nm, firstly the lens material needs to be crystalline calcium fluoride to avoid intrinsic birefringence, secondly optical elements to be coated with thin dielectric material for anti-reflective purpose and thirdly, the working area must be in an atmosphere of high purity nitrogen. Due to trace contaminants in the N_2 gas, scattered 157 nm radiation decompose organic material more effectively and then liberate volatile contaminants which may form photoinduce deposits on the surface of optics. The problems associated at 157 nm are more complicated and difficult to resolve than those faced in the transition to 193 nm and many strategies have been employed to deal with the challenges related to its practical implementation [13]. If lithography at 157 nm becomes possible then it would enable the projection lithography to provide timely solution for semiconductor devices shrinkage and can help to sustain vigor of the semiconductor industry at least half decade [13].

1.3.2 Far-field photolithography (mask based) on self-assembled monolayers

Self-assembled monolayers (SAMs) are atomically organized and uniform layers of photosensitive molecules with a thickness of 2-5 nm and are used as a resist because of their well-understood chemistry. Exposing the SAM to UV light through a mask in the presence of air leads to the formation of a micro-pattern. Fig. 1.3 shows the schematic procedures of UV photo patterning in the far-field region where the sample-light source distance is larger than the wavelength of light used. Micro patterning has been reported on different monolayers

such as carboxylic acid terminated SAM, methyl terminated SAM and amine terminated SAM [14–17]. Extensive work has been done on micro-pattering of SAMs of alkanethiols on gold and silver. Exposure of alkanethiols on gold to UV light in air leads to the conversion of alkanethiols into alkylsulfonates. These are soluble in water and when the sample is subsequently rinsed with water the alkylsulfonates dissolve and leave the required unexposed part of the pattern [18]. A similar method has been used to fabricate patterned SAMs on silver. The photo-oxidation mechanism of alkanethiols on silver is different from that of alkanethiols on gold. In this case, the oxidation of the exposed area converts the strongly adsorbed thiolates into weak alkylsulfonates. Immersing the sample into a second thiol solution replaced the weakly bonded sulfonate and formed a clear and well defined pattern of two chemically distinct molecules [19,20]. Similarly, micro scale structures have also been formed of SAMs of phosphonic acids on aluminium oxide [17].

The irradiation of SAMs through the mask results in a reactive surface that can be used for further chemical reactions, such as functionalization and adhesion. The photo-reactive mechanism of SAMs depends on the wavelength, the nature of the functional groups, and the environment. An application of photo-patterning is the combination of photolithography with the attachment of bio-molecules and polymers. One recently reported example are micro and nano-patterns of NPPOC protected aminosiloxane monolayers on oxide surface [21]. Samples of NPPOC protected monolayers were exposed at 325 nm through the mask in the presence of air. This resulted in the formation of a free amine group on the surface of the exposed areas which were further functionalized with trifluoroacetic anhydride (TFAA) and polymer nanoparticles for higher contrast [21].

SAM preparation is relatively simple, the layers have high density, are thermodynamically stable and produce relatively defect-free structures [22]. They are potentially useful in biology where patterned structures can be functionalized with different proteins. On the other hand, SAMs have limited choice of substrates and are easily contaminated. Other potential areas of application include electrochemistry, protein binding and DNA assembly [23].

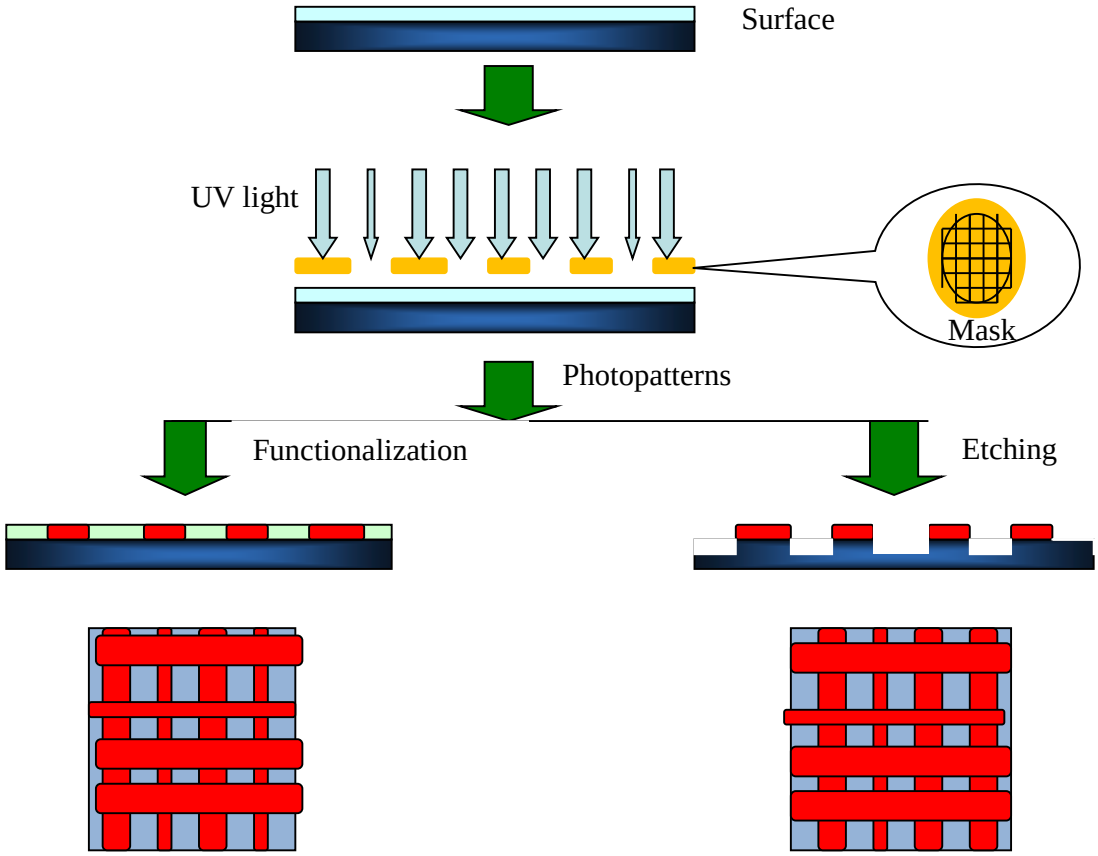

Fig. 1.3. Schematic illustration of UV photo patterning in the far-field photolithography

1.3.3 Maskless far-field photolithography

Maskless photolithography is based on the conventional lithography except that the photo-mask is replaced with a focused spot or an addressable array of light-modulating elements. There are various forms of maskless lithography techniques, such as focused ion beam lithography (FIBL) [24] and scanning electron beam lithography [25], spatial light modulator for maskless optical projection lithography [26], zone-plate-array photo lithography [3,27] and two photon lithography [28].

A spatial light modulator is one example that is used instead of a photo mask in maskless lithography. There are various types of spatial light modulators, such as tilting mirrors, pistons, amplitude modulation, combined phase and amplitude modulation. All the spatial light modulators have different operating principles but their common function is to create an image on the wafer via controlled diffraction limited spots or interference patterns. Maskless optical projection lithography (MOPL) is one of the potential tools with a programmable reflective spatial light modulator (SLM) which is a replacement for photo masks. In MPOL

the spatial light modulator consist of arrays of micron sized electrostatically driven mirrors, a high-power pulsed laser source (~ 1 kilo hertz) and has a large number of pixels, typically over ten million. An image contrast is formed by interference of light with a wavelength 193 nm of excimer laser through phase modulation. The phase is controlled by actuation, either by tilting the mirrors or piston-motion mirrors. There are two main drawbacks in MOPL, the high power laser can limit the switching speed of the spatial light modulator, and the demagnification of the micron-sized pixel through the reflective optics is another burden [26].

Zone-plate-array photolithography (ZPAPL) is used for parallel writing and consists of focused light spots which are created by a spatial light modulator after passing through high numerical aperture diffractive lenses [3,27-28]. The light on each spot is supplied by a continuous wave (CW) laser at a wavelength of 400 nm and is controlled by one pixel of the spatial light modulator. The silicon wafer is coated with a resist material and scanned under these modulated focused spots. In ZPAPL the periodic pattern resolution corresponds to k_1= 0.287 and the line width obtained is 135 nm. For non-periodic patterns, the k_1 value increases to 0.29 and the minimum reported feature size is 140 nm. This maskless photolithography technique is a cost effective and a potentially useful method for parallel writing [3].

Two-photon lithography (TPP) is a masksless technique for the fabrication of micron to sub-100 nm 3D structures. Sapphire lasers, which have an ultra-short pulse width of less than 100 fs, are used as a beam source for TPP nanofabrication. The laser beam is tightly focused through the high numerical aperture onto the photo-polymerizable resin, resulting in the photosensitization of the resin via a two photon absorption (TPA) in the chromophores. Complex structures can be created by moving the laser spot with a piezoelectric stage [29-30].

TPP is a powerful tool for well-controlled 3D fabrication for various applications. However, TPP also has some drawbacks; firstly, it has a low throughput and is unsuitable for mass production as compared to conventional processes in the micro-electronics industry [30]. Secondly, TPP has a lower resolution compared to e-beam lithography. TPP opens a new route for small-scale production that can be used for research purposes including 3D scaffold for cell biology, micro-optic components, photonic crystals, and highly complex 3D micro structures [30].

Maskless lithography is cost effective and a rapid way for micron to sub-100 nm resolution fabrication in the laboratory. Various masksless lithography techniques are used to fabricate

micro-fluidic devices, 2D and 3D patterned channels, complex 2D and 3D micro, photonic crystals and other nano structures that can be used in physics, chemistry, engineering and cell biology. However, small throughput is the biggest challenge in maskless lithography.

1.3.4 Electron beam lithography (EBL)

Electron beam lithography (EBL) has the capability to offer high resolution features down to 2 nm [31]. It has been an attraction for the semiconductor industry owing to its short wavelength, primarily to create a mask that is then used for photolithography or soft lithography. A wide variety of commercial equipment is available for electron beam lithography. Fig. 1.4 shows schematic illustration of electron beam lithography (EBL). In direct writing EBL the lift-off process is commonly used, which involves transferring the pattern onto the resist-coated substrate with a beam of electrons. The exposed resist is developed and a metal (e.g. gold) is evaporated onto the substrate and the lithographed mask is subsequently removed, leaving the patterned metal on the substrate [32]. There are two main types of resists, positive and negative, both of which are high molecular weight polymers [32,33]. Fig. 1.5 shows a schematic representation of electron beam lithography on positive and negative resist.

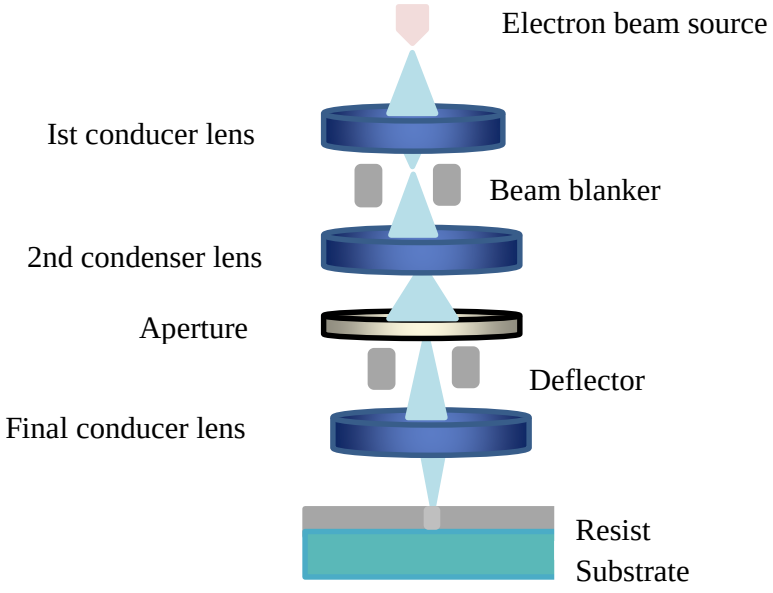

Fig. 1.4. Schematic representation of electron beam lithography where the electron beam is focused on a resist film to fabricate a pattern being exposed.

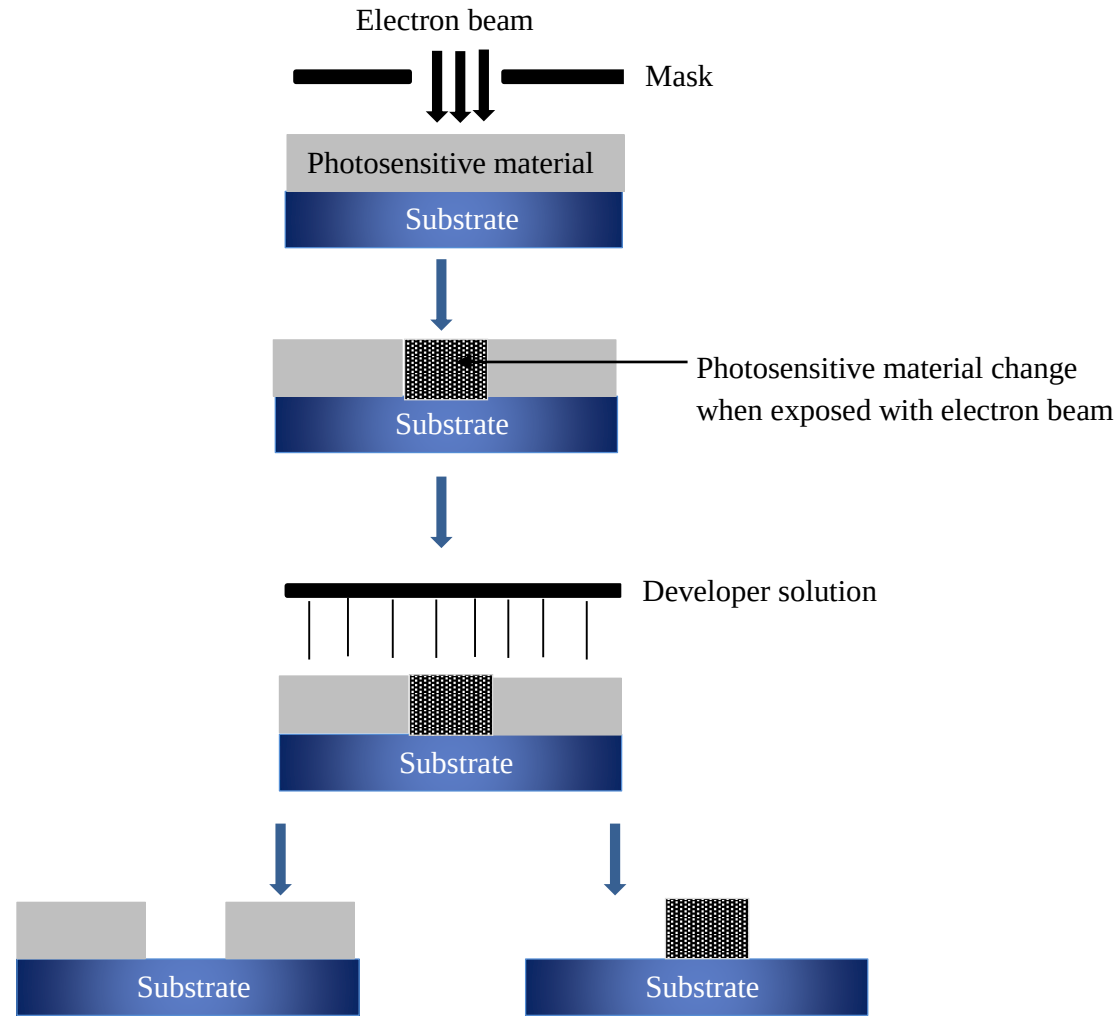

Fig. 1.5. Schematic representation of electron beam lithography on positive and negative resist.

Nanoscale patterned surface have been fabricated by combining electron beam lithography with gas-phase silanation, which provides features down to 20 - 25 nm [33]. In this technique, top-down and bottom-up approaches have been used to define the chemically nano-patterned substrate. First, electron beam lithography is used to create nanoholes in the polymer mask which has been spun cast over the substrate. Subsequently, high quality chemically functional monolayers are formed by gas-phase silanisation. This method was successfully demonstrated by Pallandre et al. who showed the importance of the choice of resist as this could affect the silanisation conditions. Electron resist films such as poly(methyl methacrylate) (PMMA) [33]

and polydimethylsiloxane (PDMS) are found to be physically and chemically stable under the high vacuum silanisation conditions [33].

Electron beam lithography is widely used for fabrication of nanoscale structure and devices and mask fabrication for nanoscale physics but it also has some limitation in many applications due to its extremely low throughput, something that makes mass production difficult. Furthermore, developing a practical source of electron beams is a problem that limits the use of this technique in the manufacturing process.

1.4 Near-field photolithography

Optical lithography has been a mainstay of the semiconductor industry for the fabrication of nanoscale structures. Typically lens-based optical systems have been used with improved nanoscale resolution being obtained by reducing the wavelength. Reduction of the wavelength, development of compatible optical systems and resist materials is a great challenge that only increases the pressure to develop new lithographic techniques with better resolution than those commercially available today. Another way to enhance resolution without lowering the wavelength is near-field lithography [34,35]. When light propagates through an aperture near field light is created in an extremely localized area at a sample distance much smaller than the wavelength of light. Fig. 1.6 shows a schematic representation of near field lithography. In the localized area, evanescent waves are generated whose electric field fluctuation is not subjected to diffraction

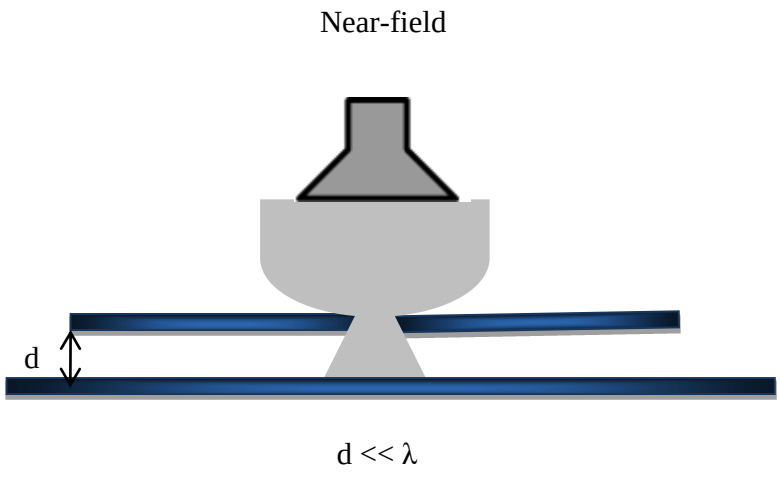

Fig. 1.6. Schematic representation of near field lithography wherein the sample is placed close enough to a nanoscopic aperture such that light is not subjected to normal diffraction limit.

In 1928, Irish scientist E.H. Synge introduced the idea that the diffraction limit can be overcome using near-field light and image resolution can be achieved significantly higher than allowed by the Rayleigh criterion limit [36]. Synge's idea was to form a sub-wavelength sized light source, a nanoscopic aperture on a screen, and to translate the screen over the sample by keeping the distance constant between the sample and the aperture. With such a system, optical resolution of the aperture size can be achieved. Later on this technique was applied to photolithography, such as contact printing and projection printing, wherein a mask is placed at a distance of a few nanometres above the resist, resulting in high spatial resolution. Both the approaches have some practical limitations, for example it is extremely difficult to maintain the screen-sample distance constant, and a small dust particle between the sample, mask or screen can create a gap causing diffraction effects and thus significantly reducing the resolution.

In 1984, 56 years after the invention of near-field lithography, the groups of D.W. Pohl and A. Lewis realized this idea would allow optical imaging with the resolution of $\lambda/20$. The technique they developed is called scanning near-field optical microscopy (SNOM) [34,37,38]. Betzig et al first used SNOM for photolithography [39] and early SNOM lithography studies reported that thick layers of resist gave poor resolution due to diffusion or thermal agitation on such small length scales underneath the aperture. Various strategies were employed to control the far-field excitations, such as aluminium coated fibres, uncoated fibres, and amorphous GeSbTe films, but it was found that resolution was only improved by using SAMs of a few nanometre thick [34,40,41].

Near-field light is an advanced lithographic technique that allows resolution beyond the diffraction limit but there are enormous practical limitations to its implementation, such as the new infrastructure tools, processing technology, development and research cost. Furthermore, SNOM cannot be used for 3D fabrication.

1.4.1 Dip-pen nanolithography

In dip-pen nanolithography (DPN) an AFM tip is inked with molecules to be deposited onto a substrate. A schematic representation of DPN is shown in Fig. 1.7. Stable nanostructures are formed by using suitable molecules which attach to the substrate via chemisorption or electrostatic interactions [42–45]. The feature sizes of structures can be written as small as 10 nm by transferring tiny collections of molecules (e.g. DNA or proteins) from the tip to the surface through a water meniscus.

DPN allows several different kinds of molecules to be attached in parallel on the substrate without having any risk of cross-contamination. However, one of the problems of this technique is that the approach completely depends on relative humidity and substrate wetting properties. Thus, silane-based inks can rarely be used because of its incompatibility with water meniscus and polymerization during ink deposition for this reason the majority of DPN studies are limited to thiol molecules as the ink [45].

The patterning of bio-molecules and proteins in micro and nanoarrays by DPN has been extensively studied. Recently studies have focused on using DPN to pattern SAMs followed by their derivatization to form DNA arrays and other biomolecules to be used for the detection and analysis of biomolecule entities. The properties of molecules which include size, shape such as shape, size, electrical conductivity and hydrophilicity can be monitored in situ with an AFM [41].

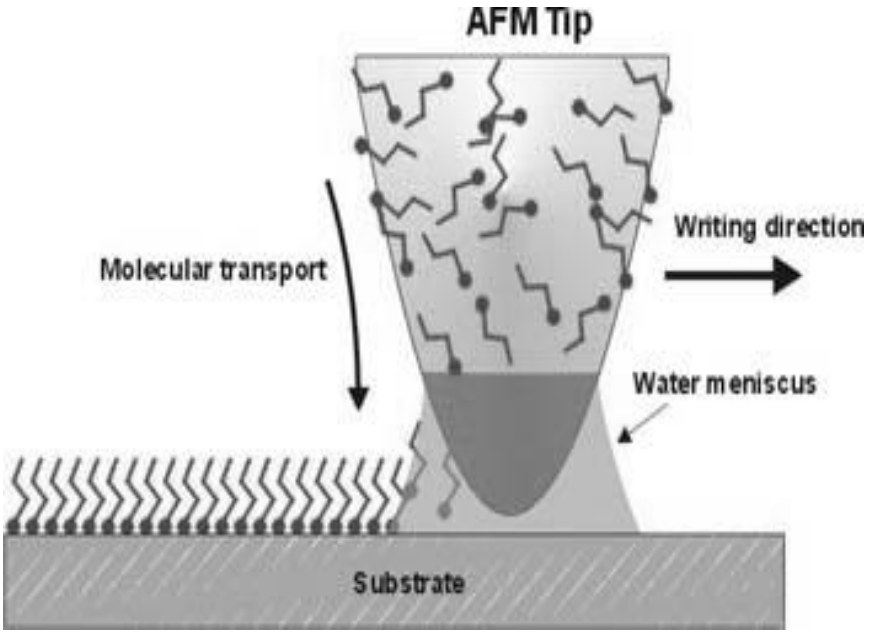

Fig. 1.7. Schematic illustration of dip-pen lithography. Transport of molecules to the surface occurs via the water meniscus. Figure was used by permission [45]. Copyright (1999) Science.

This makes it possible to attach specific molecules in a specific orientationto the desired patterns. On the other hand, it was discovered that with unmodified silicon nitride cantilevers it was difficult to control DNA patterns of different sizes and shapes. Mirkin and co-workers solved this through surface modification of the silicon nitride AFM cantilever with 3-aminopropyltrimethoxysilane which gave a better adhesion of the DNA to the tip [42]. In

conclusion, a good combination of an ink, substrate and relative humidity is necessary to utilize DPN to the maximum extent of its potential [42].

1.4.2 Soft lithography

Microcontact printing (μCP) is a common soft lithographic technique, and was introduced by Whitesides and co-workers [46]. The process of stamp fabrication and micro contact printing are shown schematically in Fig. 1.8. The resolution achieved depends on the conformal contact between the surface and the stamp. Microcontact printing is widely used because it only requires inexpensive materials and offers a rapid and useful mean of patterning monolayers on the micron scale. In μCP a polydimethylsiloxane (PDMS) stamp is inked with a thiol solution and placed on a gold substrate. Regions which are not coated with stamp

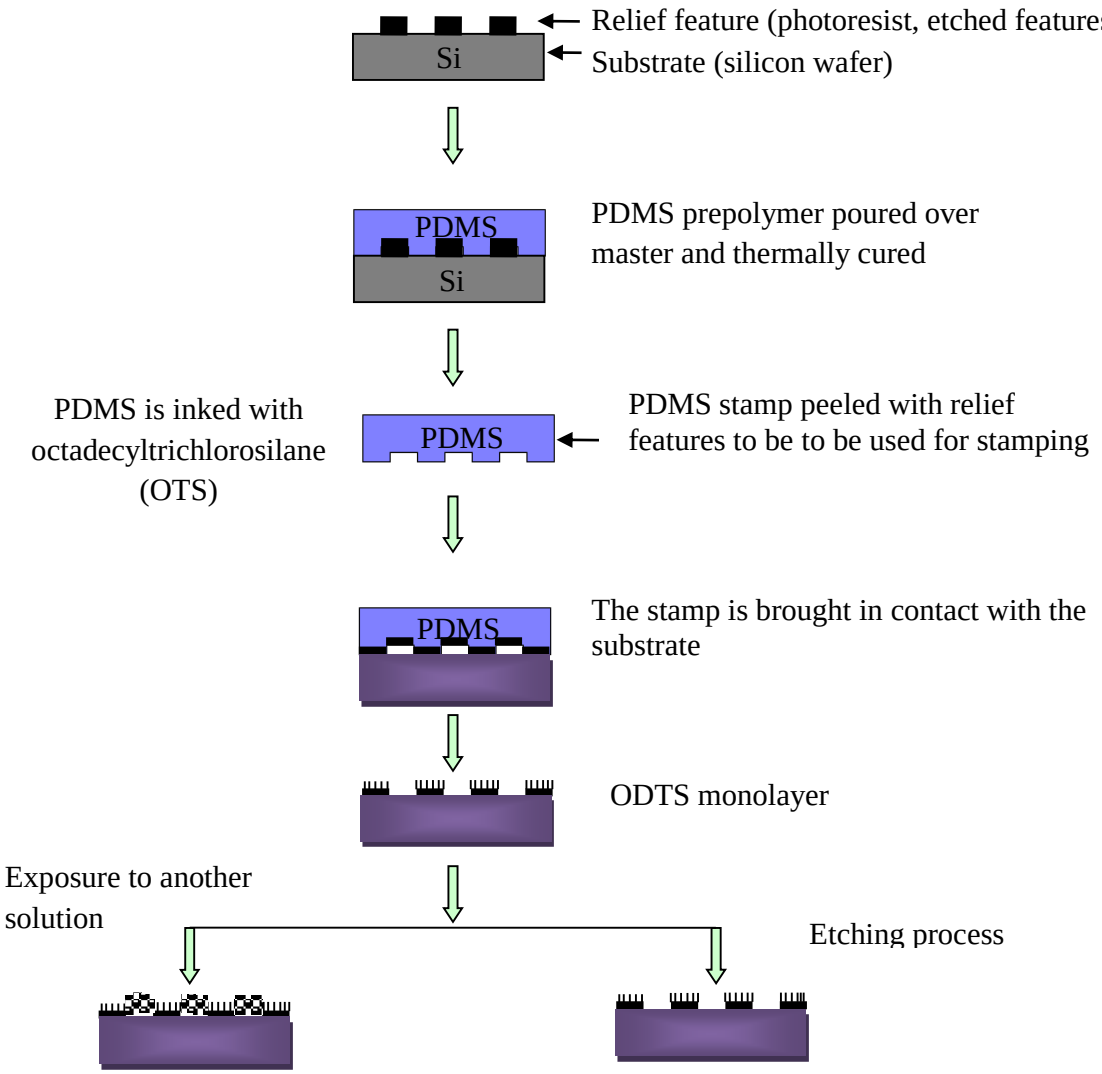

Fig. 1.8. Schematic illustration of the fabrication of a PDMS stamp and the procedure for microcontact printing of octadecyltrichlorosilane (OTS) on silicon.

molecules can be further functionalized with the second thiol in a solution-phase deposition [47–49]. Micro patterning of alkanethiols on gold surfaces with a features size down to 1 μm was initially developed by Whitesides et al. [46] and even today various research groups used the same method due to the highly ordered monolayers of Au-thiol SAMs it creates [47,50]. The technique can also be used for silane SAMs, but then the stamp is inked under N_2 atmosphere in order to minimize the amount of polymerization of the silane before contacting the surfaces [51]. Some of the advantages of this technique are the formation of structured and stably patterned SAMs in solvent-free environment [46,52,53].

Microcontact printing (μCP) typically utilizes a stamp made of PDMS. PDMS is extensively chosen due to its homogenous, optically transparent, elastic and isotropic characteristics. Moreover, the non-degradability of PDMS makes it reusable for over 100s of times over a period of several months. Despite this extensive use of PDMS, there are a few discussions about issues. Graham et al. have explored silicon contamination during stamping and suggested an exhaustive pre-cleaning process to be used on the stamp, and the use of high ink concentration [54]. The cleaning procedure involved three steps: the extraction of the stamp in hexane, followed by drying and sonication. Moreover, it required the elimination of low molecular weight PDMS from the stamp to prevent them being transferred to the thiol during the stamping procedure [54].

Nuzzo and co-workers performed detailed studies of self-assembled films of octadecyltrichlorosilane (OTS) formed by contact printing. A number of factors that influence the OTS film patterning were studied, e.g. adsorption time, substrates and concentration. The surfaces were characterized with X-ray photoelectron spectroscopy (XPS), reflection-absorption infrared spectroscopy (RAIRS), ellipsometry, scanning electron microscopy (SEM) and atomic force microscopy (AFM) [50]. It was found that the quality and fidelity of the OTS films directly depended upon the stamp contact time. With a very short contact time (~ 10s) or long stamp contact time (~ 60s) adverse effect were observed, either by introducing unacceptable defects or reducing the lateral dimensions of features. Highly stable and densely packed monolayers were formed after 30s of contact printing time [52].

1.4.3 Nanoimprint lithography

Nanoimprint lithography is a nonconventional lithographic method proposed by Stephen et al. [55] which has the ability to produce features down to 25 nm over large areas at low cost and with high throughput. In nanoimprint lithography a hard mold with nanoscale relief features on its surface is pressed into a thin resist material cast on a substrate. During this

step, the resist material is heated above its glass transition temperature and changes into a viscous liquid that deforms into the mold shape. This creates a pattern in the resist material, followed by the removal of the mold. Thereafter the thin residual layer of resist in the compressed area is removed through an etching process to get the contrast pattern over the entire resist [55,56]. A schematic representation of nanoimprint lithography is shown in the Fig. 1.9.

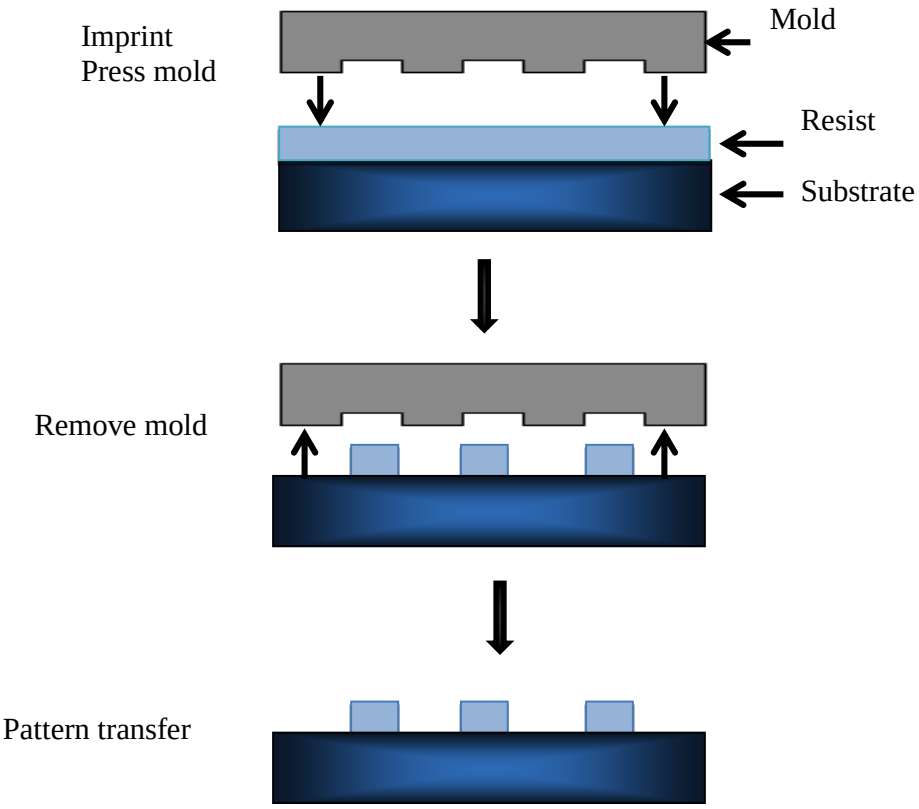

Fig. 1.9. Schematic illustration of the nanoimprint lithographic procedure.

Nanoimprint lithography has been used successfully to fabricate nanoscale photodetectors, silicon quantum dots and quantum wires. Unlike conventional lithography, in nanoimprint lithography resolution is not limited by diffracted waves, back scattering or interference [55,56].

1.5 Self-assembled monolayers

The term self-assembly is used to describe the formation of ordered monolayers or multilayers of amphiphilic materials by physical adsorption or chemisorption. The monolayers are commonly used as model templates in the study of surface modification for micro patterning. Different substrates have been reported for the formation of self-assembled monolayer. In recent years, the majority dealt with thiols on metal surfaces such as gold [14,15], silver

[57,58] and silanes on hydroxylated surfaces [16,59–61]. Self-assembled monolayers (SAMs) are formed on a particular substrate when the substrate is placed in a solution of precursor molecules or in the gas phase. As schematically illustrated in Fig. 1.10, SAMs are a system of three basic components; an active head group, a tail group and alkyl chain which links the two. A strong specific interaction of the head group with the solid substrate results in the chemisorption of molecules onto the surface. The formation of stable monolayers involves an exothermic reaction between the head group and the substrate and as a result every available binding site on the surface is likely to be occupied. The tail group may be virtually any organic functional group and is positioned at the monolayers-air interface. In SAM formation, adsorbates contain a long alkyl chain or an aromatic ring in order that strong interchange interactions between chemisorbed molecules cause ordering of molecules within the film. SAMs are more stable mechanically, thermodynamically and chemically in contrast to monolayers formed through the Langmuir Blodgett technique [62,63].

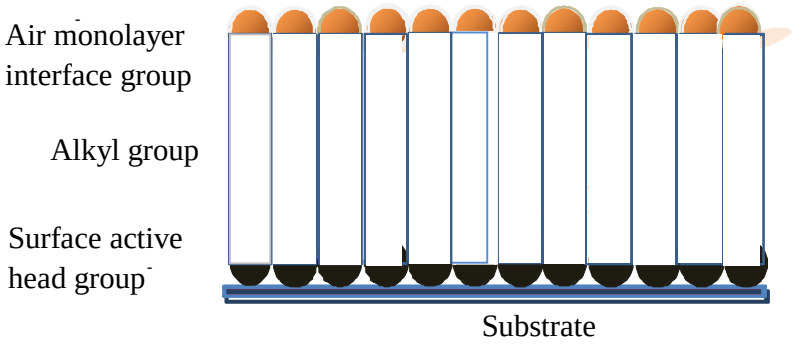

Fig. 1.10. Schematic diagram illustrates the main components of self-assembled monolayers

1. 6 Polymer brush synthesis techniques

Polymer brush synthesis has become a fascinating field for physicists and chemists due to its importance in applied research. Polymer brushes refer to polymer chain assemblies which are attached to a solid substrate either through covalent bonding or physical adsorption. Chemical attachment is typically preferred in many studies to avoid adhesion problems. Polymer attachment to a solid surface through chemical bonding can be accomplished by two methods, either by “grafting to “or “grafting from” as shown in Fig. 1.11 and 1.12, respectively.

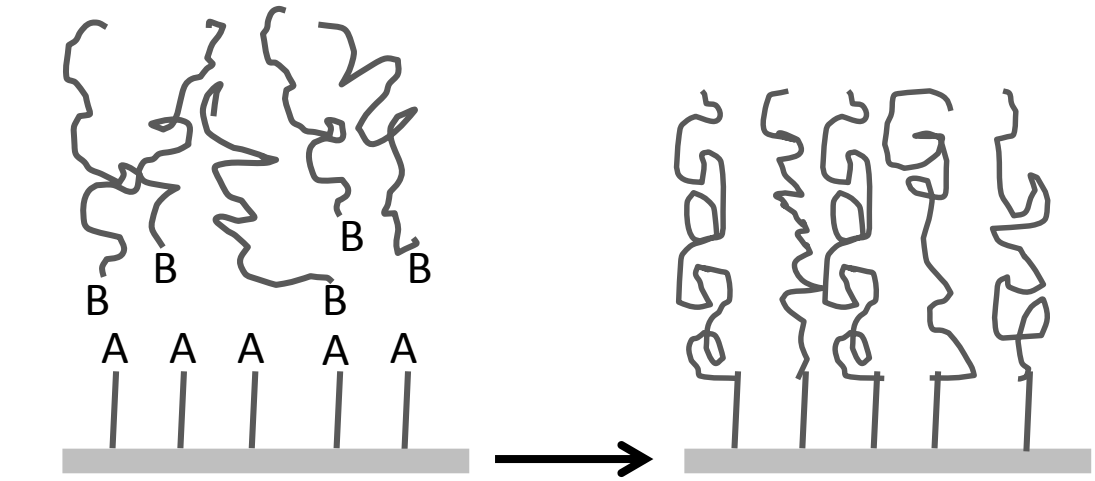

Fig. 1.11. Schematic representation of the “grafting to” a polymer chain process

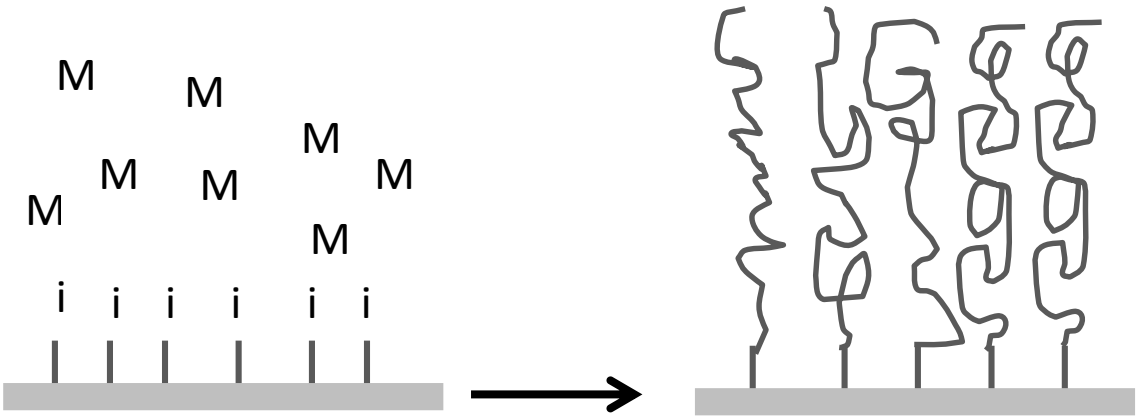

Fig. 1.12. Schematic representation of the “grafting from” a polymer chain process

In the “grafting to” technique end functionalized polymer chains react with the surface group and polymer chains will be grafted to the substrate surface. Grafting is usually performed through polymer solution or melting. The “grafting to” technique usually produces low density polymer brushes as the attachment of polymer chain may be hindered by the presence of already attached chain The primary advantages of this technique are easy polymer brush synthesis and simple characterization of polymer brush properties [64,65].

The “grafting from” technique (also called surface initiated polymerization) is a straight forward way of polymer brush synthesis. This technique involves chain polymerization from an initiated functionalized surface [64,65]. The “grafting from” technique introduces a reliable and controllable method for the formation of high density polymer brushes and can be applied to a number of available polymerization methods such as atom transfer radical

polymerization (ATRP), single-electron transfer living radical polymerization (SET-LRP), ring opening metathesis polymerization (ROMP) and nitroxide mediated polymerization (NMP) [66–68].

1.7 Atomic force microscopy

AFM was proposed by Binning and Rohrer in 1986 and has been used to obtain topographic information, mechanical properties, electrical conductance and magnetism. It has been employed on a wide variety of samples including, semiconductors, polymers, biology and materials to obtain nanometre imaging resolution. Atomic force spectroscopy has also been used as a powerful, widespread and analytical tool to measure inter and intra molecular forces of various materials and mechanical properties of biological and synthetic systems. The basic operation of an AFM is shown in Fig. 1.13.

The AFM cantilever with a sharp pyramid tip at one end scans over the sample surface. To form the image, the tip is brought into contact with the sample surface and force acting between the tip and the sample results in a measurable cantilever deformation. The cantilever bends downward or upwards, due to attractive or repulsive interactions. The force acting on the tip depends upon the operating mode and the imaging conditions used. AFM is divided into two operating modes. Static-mode (DC) where the probe does not oscillate during imaging and the dynamic mode (AC) where the probe oscillates near to its resonance frequency. Dynamic mode (AC) can either be frequency modulation AFM (FM-AFM) or amplitude modulation AFM (AM-AFM).

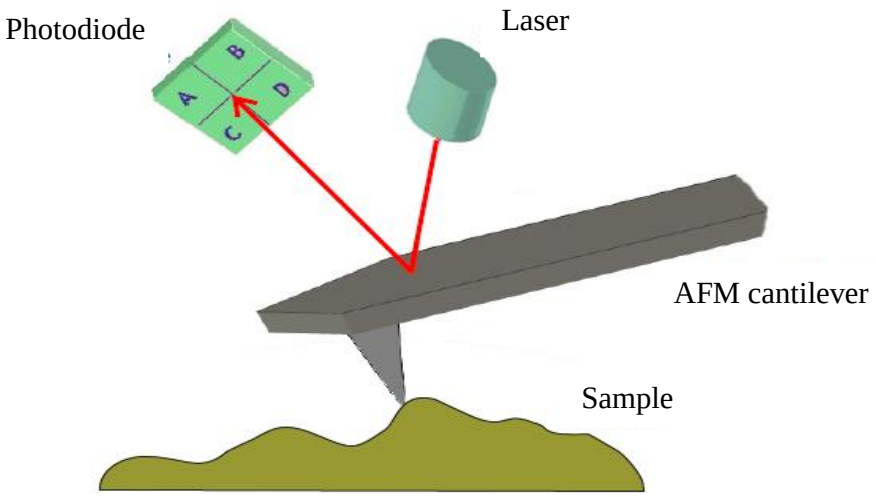

Fig. 1.13 Schematic diagram of the basic components of an AFM.

Amplitude modulation AFM (AM-AFM) is usually referred to as semi-contact or intermittent contact or tapping mode and frequency modulation AFM (FM-AFM) is sometimes referred to as non-contact mode. Other dynamic modes such as phase modulation (PM-AFM) have also been developed. DC mode is also referred to as contact mode and frictional force microscopy is an alternative form of contact mode.

1.7.1 Contact mode

In this mode, images are acquired when the tip is in close repulsive contact with the sample surface. This usually operates in constant height mode or constant force mode depending on which feedback is used. In constant height mode, the spatial variation of the deflection of the cantilever is used to produce the topographic image of the sample surface at constant piezo scanner height. Constant height modes are more often used to acquire atomic scale images of flat surfaces. In constant force mode, deflection of the cantilever is kept constant by extending and retracting the piezo scanner. The topographic image is generated from the piezo scanner motion. In this method, a feedback loop adjusts the sample height by changing the applied voltage to the piezo scanner. This is the standard mode used in conventional AFM to acquire high resolution images at atomic and molecular level [69]. Since AFM measures the interaction force and generates an image, the force is measured by calculating the deflection of the lever

$$F = k\,x$$

F is a force given by Hooke's Law, k spring constant of the cantilever, and x is the cantilever deflection.

Additionally, when imaging in air, most surfaces are covered by a layer of adsorbed water and other contaminants, whose surface tension pulls the tip downwards. The changes between the tip and sample due to electrostatic interactions can give rise additionally to long-range forces and complicate imaging. Thus, a significant force must be applied to overcome the surface contamination effects or capillary forces. Consequently, contact AFM imaging in air is not appropriate for soft samples (e.g. polymeric materials and most biological systems) [70]. Different research groups have used contact mode imaging in liquid to control these effects which reduces the tip-sample interaction [71,72]. Contact mode is very attractive due to high scan speed and can provide high resolution images at atomic and molecular level such as crystal surfaces like mica, salt crystal, organic layers and polymer crystals.

1.7.2 Amplitude modulation atomic force microscope (AM-AFM)

AM-AFM was first proposed by Zhong et al. in 1993 [73]. In AM-AFM, a stiff cantilever with a sharp tip oscillates close to its resonance frequency and oscillation amplitude with its maximum value damps to a lower value when it encounters a structural change on the surface. The changing amplitude of the probe is used as a feedback [74].

Oscillating amplitude is the key parameter in AM-AFM. A change in oscillation amplitude directly depends upon attractive and the repulsive tip-sample interactions [73]. Many studies reported the step like transition in the amplitude curve (i.e., oscillation amplitude as a function of the average tip-sample separation) on polystyrene, mica samples and GaAs [75]. These transitions correspond to coexistence of two stable oscillation states. The coexistence of the low and high amplitude state directly depends upon the sample properties such as elasticity, adhesion and operating parameter like the free oscillation amplitude [75,76]. On the other hand drastic variation in morphology was observed at low and high amplitude. Jagged topography was reported at the high amplitude in contrast to the small amplitude that reported clearly a visible and a clear morphology of the antibodies imaged [75].

AM-AFM offers another powerful method called phase contrast imaging. The cantilever oscillation phase lag relative to the drive signal of the cantilever oscillation provides the measure of energy dissipation during the tip-sample interaction. Phase lag sensitivity reflects the variation in the mechanical properties of the sample. The feedback loop is applied to obtain the surface topography. The phase contrast is observed while the topographic image is being recorded so that both the topography and the material properties can be acquired simultaneously [77].

Hansma et al. were first use AM-AFM in liquid. They imaged plasmid DNA on a mica surface under liquid with contact and AM-mode with the same cantilever. AM-AFM experiments in liquid are hard to perform because the dynamics of the cantilever in the liquid are far more complex than in air. AM-mode under the liquid also significantly reduces the disruptive influence of the lateral forces and typically gives less deformation on soft biological samples [78,79]. AM-AFM is a robust method for imaging biological samples due to biological materials delicacy and has also provided the platform to address important questions in various areas of the cell biology such as cell signaling and adhesion, the cell morphology and division, and embryonic and tissue development [80].

1.7.3 Frequency modulation atomic force microscopy (FM-AFM)

Martin et al (1987) introduced the idea of FM-AFM and Albrecht et al first use the FM-AFM to measure the interaction force between the probe and the surface [81,82]. In this mode, the probe vibrates at its resonance frequency and the small change in the cantilever frequency occurs as a result of the tip-sample interaction. This frequency shift is used for feedback and hence to generate the surface topography [74,83].

FM-AFM is a very powerful tool for the precise determination of the tip-sample interaction. It provides material properties including adhesive interactions, elastic constant and the tip geometry by fitting standard mesoscopic models [75,83]. Quantitative force measurements wit FM-mode revealed the unbinding force of a single molecule interaction including the receptor–ligand interaction and the polymer un-folding [83]. Atomic defects on a crystal surface can more easily be achieved in FM-AFM mode in contrast to contact mode where the tip sample force gradient is monitored to contact the tip position rather than the tip-sample force [69]. Generally, semiconductor surfaces require a non-contact mode in order to reduce surface contamination and damage. Wang et al. [84] reported nanometre structure writing on Si (100) surfaces by non-contact operation. In this technique, the tip was positioned far away from the silicon surface to measure the long-range Van der Waals attractive forces between the tip and the sample.

1.7.4 Friction force microscopy

Friction force microscopy (FFM) is an alternative form of contact mode operation. In contact mode, a laser beam deflection is detected by photo detector in vertical direction to acquire the surface topography. Meanwhile, in FFM the cantilever deflection is measured in the horizontal direction. The tip scan across the surface causes a frictional interaction between the tip and the sample while moving under constant force. FFM has been used extensively to analyze the surface chemical composition and molecular organization of materials in the nanoscale regime [85].

The frictional force can be used to distinguish chemically heterogeneous surfaces. Fig. 1.14 illustrates a chemically patterned surface functionalized with polar and non-polar adsorbates. Frisbee et al. studied the tip-surface interaction to explore the intermolecular forces of different functional groups [86]. The polar tip interacts strongly with polar regions giving rise to high energy dissipation and high frictional force, thus resulting in bright contrast in polar regions in contrast to non-polar areas. Friction images of the surface can be obtained which

is potentially useful for monolayer patterned surface, as a strong frictional interaction occurs that leads to bright contrast [85].

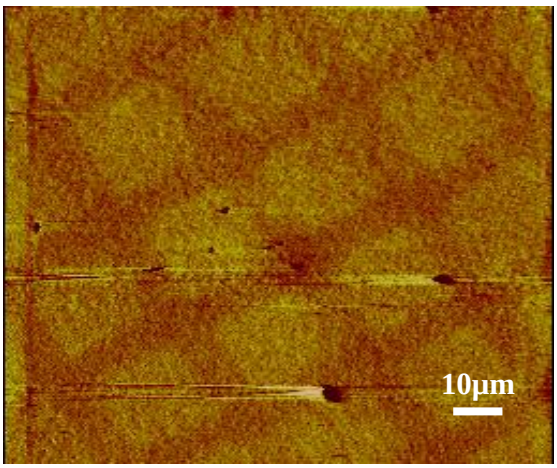

Fig. 1.14. FFM image of NPPOC protected monolayers.

Quantification of the surface friction can be achieved from a friction loop, in which lateral deflection is measured with the photo detector. The friction data is obtained by subtracting the retrace data from the trace data from a single line [87,88]. According to Amontons' Law, the friction force is directly proportional to the applied load normal to the surface,

$$F = \mu L$$

µ is the friction coefficient and obtained from the gradient of the line. F and L are the friction and applied load respectively. This equation is based on a macroscopic friction interaction that involves contacts with multiple asperities on the sliding surfaces [85]. For a nanoscale single asperity, the friction can vary with applied load. Johnson-Kendall Roberts (JKR) or the Derjaguin-Müller-Toporov (DMT) models have been proposed for a single asperity by assuming the frictional force is proportional to contact area between the asperity and the surface and the friction force would vary nonlinearly with load [85]. There is abundant evidence for monolayers that reported a linear relationship between the friction and the load [89–91]. Recently, a negative coefficient of the friction was reported in the low-load region due to adhesion between the tip and graphite surfaces, with friction increasing as the load decreases during the retraction [92].

1.7.5 AFM force spectroscopy

In an AFM force spectroscopy experiment, the cantilever moves down towards the sample surface until it makes a contact with it and then retracts. An interaction between the tip and

the sample of interest is measured. Fig. 1.15 (a) is a schematic diagram that shows the cantilever movement towards the sample during the approach and retraction in the force spectroscopy experiment and Fig. 1.15 (b) shows a schematic representation of the approach and retraction curves between the tip and sample in air.

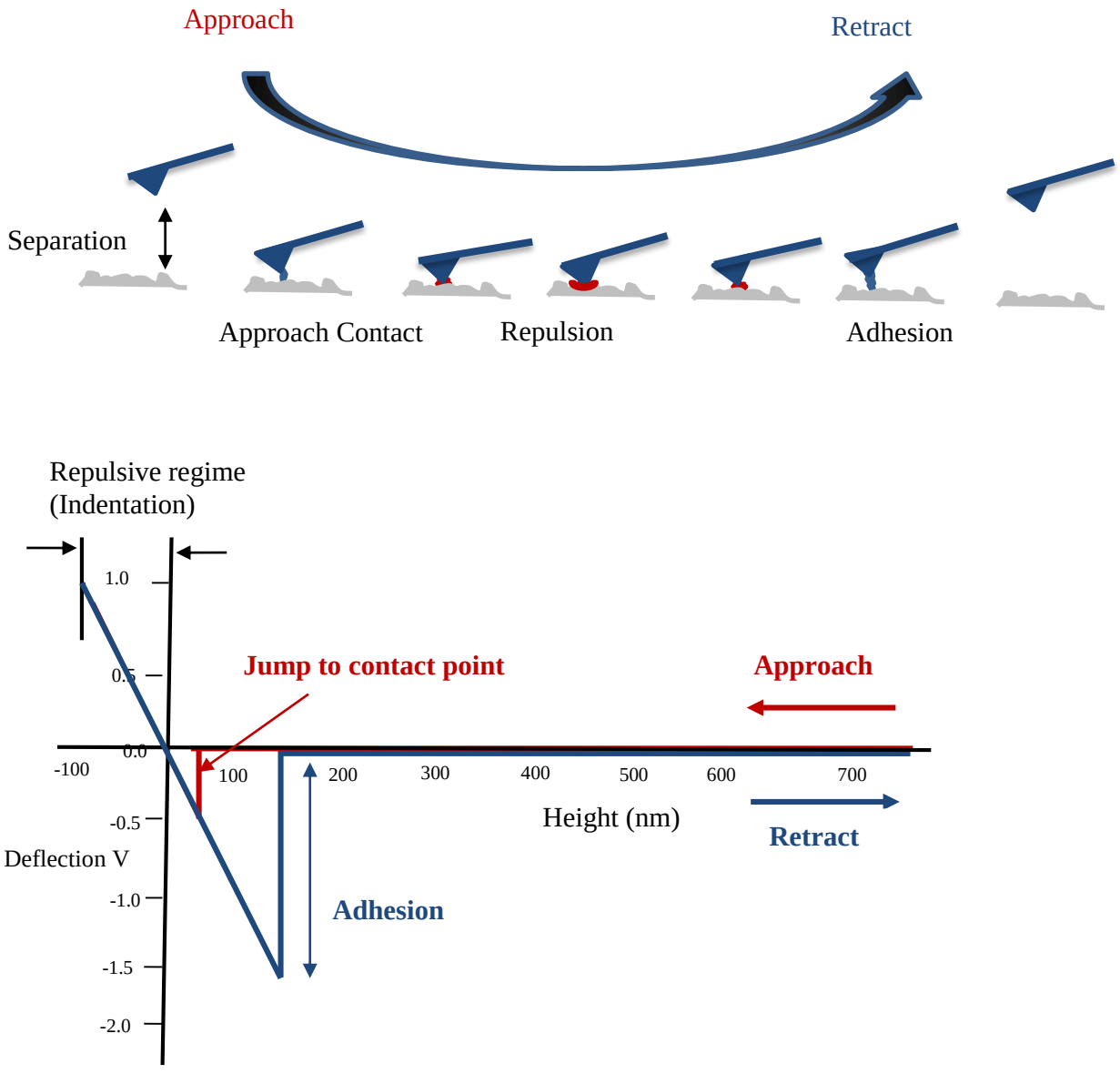

Fig. 1.15 (a). Schematic illustration of the tip movement during approach and retraction. (b) Force-distance curves showing the approach and retraction curve.

As the cantilever comes closer to the surface, the cantilever experiences small forces where the deflection of the cantilever cannot be measured, and the cantilever is considered to remain in its undisturbed position. At the tip-sample distance, the attractive forces (Van der Waals forces and capillary forces) overcome the spring constant of the cantilever and the tip jumps into the sample surface. Once the tip makes contact with the sample surface, it remains in

contact till the deflection of the cantilever reaches the defined trigger value and the cantilever retracts from the surface. Sometimes the tip remains in contact with the surface because of adhesion. This adhesion usually arises in air due to capillary forces between the tip and the sample. Force indentation experiments can be used to determine the mechanical properties of the surface. The elastic modulus determination is done by fitting the force-indentation curves to the Hertz model [93]. Further detail on this model is given in chapter 5.

Force-volume mapping is a technique where force curves and the cell topography are acquired simultaneously at a number of points on the sample surface. Usually data points are recorded in a square matrix, e.g., 50 x 50, 150 x 150 or 512 x 512 pixels. First the force curve array is collected over the surface and then subsequently assembled into the force volume [94]. Further force curves can be used to reconstruct the contact-point map and the stiffness map describing the real topography and the elasticity variation throughout the cell surface respectively. Force-volume map resolution depends upon how many points are recorded [94–96].

In AFM force spectroscopy, mechanical properties of biological systems and materials can be obtained with high spatial resolution. AFM measured interaction forces between nanometre-sized objects and is used to create spatially-resolved force-volume maps of the sample surface or to describe the material properties of the sample including adhesion, stiffness and specific ligand–receptor bond-breaking force [94]. Force-volume maps provide detail of biological structures and are becoming a significant tool for the characterization of essential biological systems [94,96]. Force-volume maps allow the user to measure the topographical and mechanical properties of the biological samples simultaneously under the physiological conditions. In the field of cancer, mechanical properties of the cancer cells acquired through force-volume maps provide important information for a better understanding of metastasis and differentiation [97,98]. Force spectroscopy can be used to identify the ligand-receptor interaction over the cell surface and fluorescent markers are helpful to identify the ligand-receptor affinity for force curve measurements. AFM provides the mechanical properties of different cellular behaviour including cell division, extension, and ageing [98,99].

1.8 Atomic force microscope (AFM) and the peripheral nervous system

The function of the peripheral nervous system requires connection between neuronal cells and Schwann cells. The neuronal cell is the most complex and intricate cell in the body and its complexity makes it difficult to resolve its detailed structure, either in terms of the growth

cone or neurite outgrowth. AFM is a powerful tool for the investigation of cell topography and mechanics. The neural cells, neurite outgrowth and primary Schwann cell topography and mechanical information are important to understand nerve regeneration process after injury. A brief description of the nervous system, the neurons and growth cones, Schwann cells and various elasticity measurement methods are given below.

1.9 The nervous system

The nervous system consists of two main parts, the central nervous system (CNS) and the peripheral nervous system (PNS). The CNS consists of a brain and a spinal cord. In the peripheral nervous system, the nervous tissue is composed of neurons and glial cells (also containing Schwann cells). Glial cells have indirect contact with neurons and also surround neurons for protection. Glial cells are also known as supporting cells for the nervous system. The main functions of the glial cells are to provide nutrients and the oxygen to the neurons, to insulate them from the other neurons and to clean up the dead and unnecessary neurons [100,101].

1.9.1 Neurons

Neurons are the building block of the central nervous system. The number of neurons varies from species to species. It is estimated approximately 100 billion neurons are present in the human brain [102]. Neurons are specialized to carry information in the form of an electrical signal and transmit it to other cells through the synaptic bulb which are terminal point of the neurons.

Neurons consist of three main parts, the cell body or the soma, which contains the nucleus, an axon and dendrite extensions. Dendrites are thread or spike like structures extending out from the cell body several hundred microns and branching multiple times and increasing the surface area of the cell. A large number of dendrite extensions help to create connections with neighboring neurons to receive information in the form of chemical signals. The other extension that is different from dendrites is called the axon, which is larger than dendrites and can be as long as three feet. A long axon is usually enclosed by a myelin sheet containing a series of Schwann cells wrapped around the axon. Fig. 1.16 shows the schematic diagram of the neuron. These cells provide the protection from the surrounding environment and serve as an insulating sheet around ‘the electrical wire’. At the long end of the axon there is synaptic bulb which is also called terminal buttons. The main function of the axon is to pass on the information in the form of an electro-chemical signal. First, signals are collected by dendrites,

travel by the cell body and continued to move along the axon where it is transmitted to the next neurons [100,101]. The synaptic bulb at the end of the axon establishes the connection with the other neurons [103].

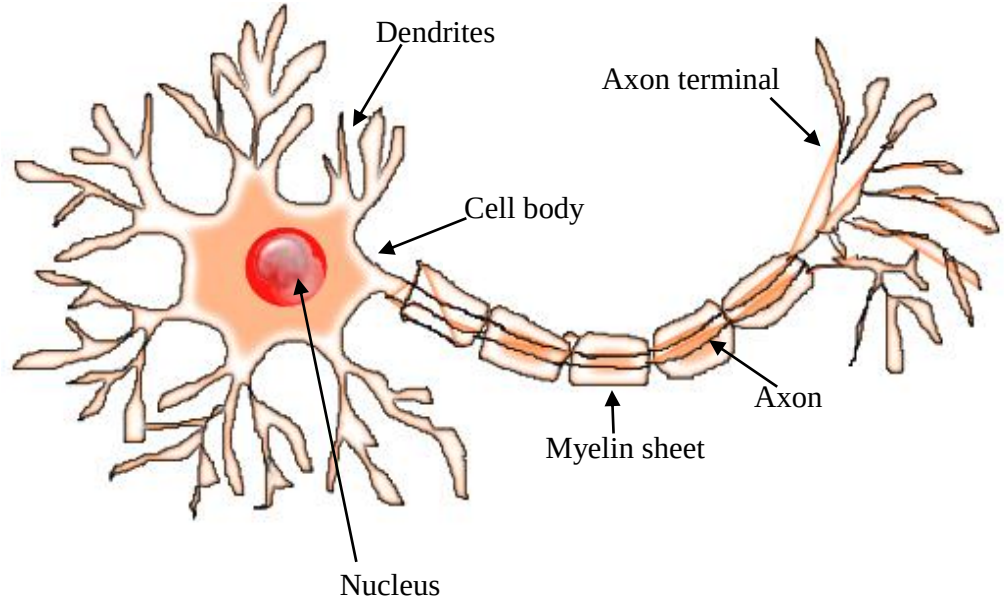

Fig. 1.16. Schematic illustration of the neuron showing detail of the cell body and neurites.

1.9 .2 Growth cone

The growth cone is a sensory, highly dynamic and motile structure at the leading edge of the developing axon that has established synaptic connection. The growth cone guides the axons towards its target location by providing the mechanical and chemical guidance cues that regulate the axon cytoskeleton structure and subsequently determine the path for the axon outgrowth [104]. The growth cone was originally discovered by Santiago et al. during the anatomical study of fixed embryo cell [44,105]. Keshishian studied the outgrowth of the live growth cone of the nerve cell [106].

Growth cones with conical or round morphology have two kinds of protrusions. Fine and thin finger like protrusion of growth cones are known as filopodia which contain bundles of actin filaments (F-actin) running parallel to each other. Filopodia are the most prominent structures in the growth cone which is several microns long. Other flat sheet extensions are named lamellipodia which contain a dense mesh work of actin filaments and exist between two filopodia [107,108].

The growth cone consisted of three main regions, the central domain (C), the transitional (T) and the peripheral (P) domain. The central (C) domain contains a stable, long microtubule-

based cytoskeleton which is located at the centre of the growth cone closer to the axon shaft. The C domain is thicker containing other organelles and vesicles of various sizes. The peripheral (P) domain is located at the outer edges of the growth cone and contains long actin filaments running parallel to each other that form the filopodia and a mesh network of branched actin filaments which form a lamellipodia. The transitional (T) region is located between the central domain (C) and the peripheral (P) domain [107]. Fig. 1.17 shows a fluorescence image of the NG-108-15 growth cone along with schematic representation of the neuron and the growth cone structural detail [109,110].

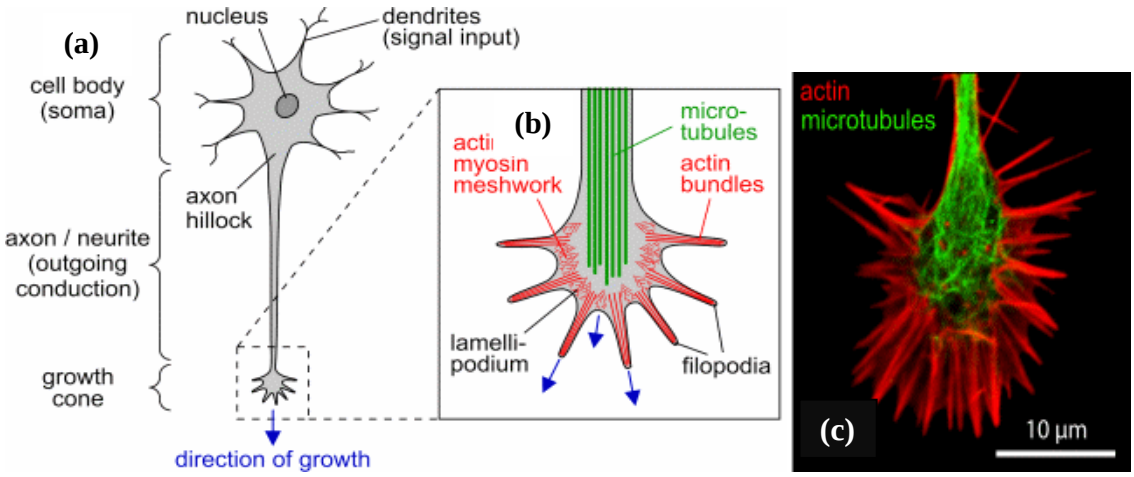

Fig. 1.17. (a) Schematic representation of the neuron with the growth cone, (b) marked dotted square area shows the growth cone, Fig. was used by permission [111]. Copyright S Pawlizak, (2009). (c) Fluorescence image of the NG-108-15 growth cone, an image was used by permission [112]. Copyright D Koch, (2007).

Primary hippocampal neurons, immature neurite outgrowth dynamics, and the axon specification have been extensively studied during development. Developing hippocampal neurons first extend a small veil like protrusion that develop into several immature neurites and then after a few days, one of the neurites ultimately elongates into a single axon while the remaining other neurites become the shorter dendrites [113–115]. Fig. 1.18 is a schematic representation of the neuron differentiation that undergoes different morphological changes, shows the neurite outgrowth and the growth cone formation that helps to explore the local environment for further extension, targeting and synaptogenesis [110,114].

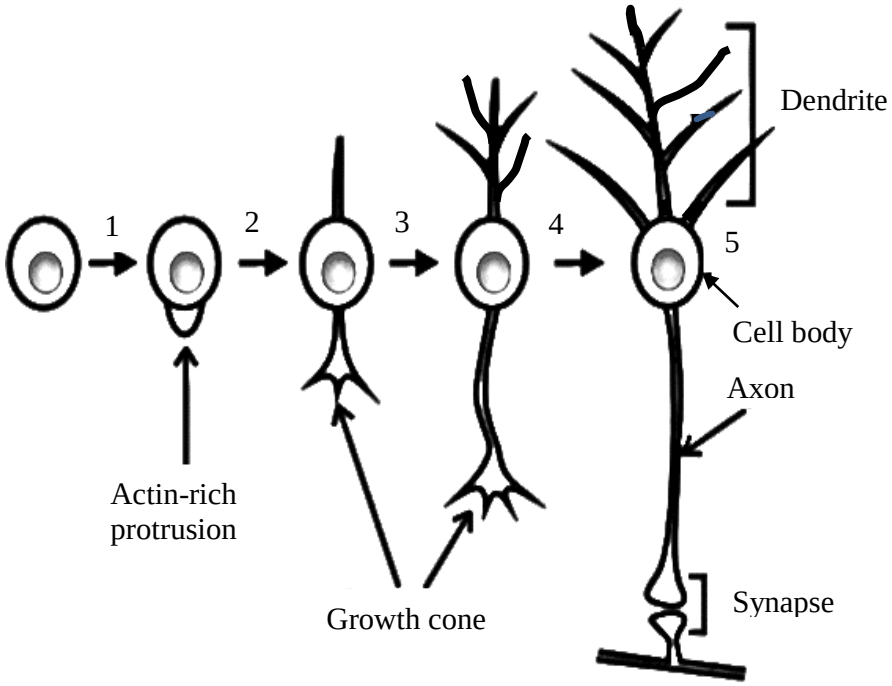

Fig. 1.18. Schematic diagram shows the morphological changes of the neuron. Stage (1) the neuronal cell body, stage (2) thin actin-rich peripheral protrusions around the cell body. Subsequently, stage (3 and 4) shows the neurite outgrowth path finding, and targeting which is driven by the motile and dynamic growth cone. At stage (5) the growth cone at the target location forms synaptic connection with the other synaptic cell [110].

Fig. 1.19 shows optical images of the NG-108-15 neuronal cells (author's data) that are in agreement with a defined schematic representation in Fig. 1.18. These images show the immature neurite extension, the growth cone formation and the single axon extension with the growth cone at its leading edge.

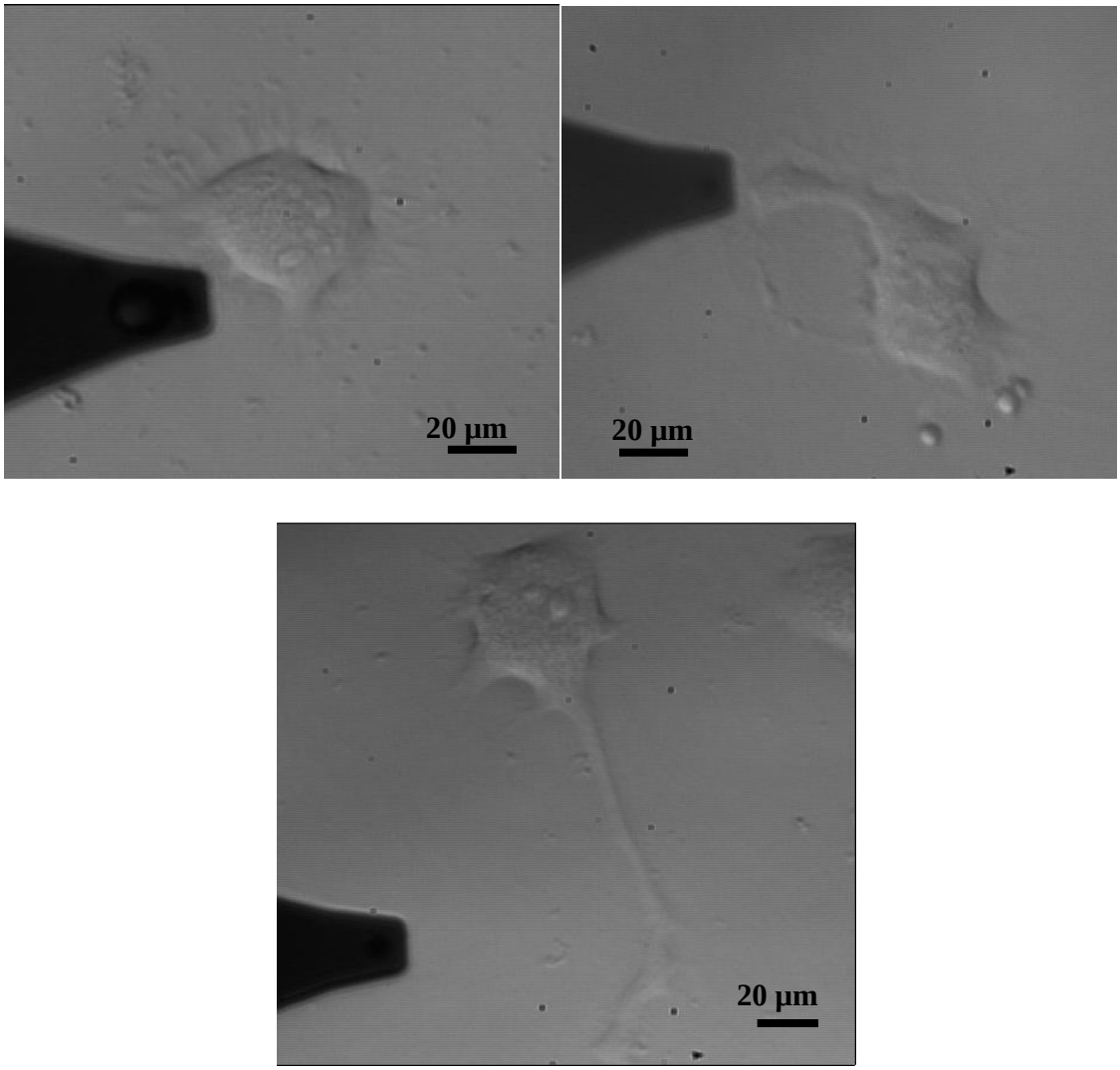

Fig. 1.19. Optical images of the NG-108-15 neuronal cells illustrates the different stages of the neuronal growth.

1.9.3 Schwann cells

Schwann cells are peripheral nervous system structures that usually wrap neural axons to form an insulating coating such as the myelin sheath. Schwann cells have the ability to regenerate the axon. The Schwann cell cytoskeleton is a dynamic structure which is responsible for defining the shape and organization of many components in their interior. The cytoskeleton is built on a network of three types of filaments such as microtubules, intermediate filaments and actin filaments. Intermediate filaments form a network all through the cytoplasm; surround the nucleus and extend towards the cell periphery. Microtubules are important for various cellular processes including cell division, intercellular structural organization and intracellular transport. Actin filaments are also found throughout the cytoskeleton and are concentrated just beneath the plasma membrane. Actin filaments are linked with each other

by actin binding proteins and form a network that helps to support the outer surface of the cell, called the cortex. It also provides mechanical strength to the cell [100]. Fig.1.20 shows an optical image of a primary Schwann cell.

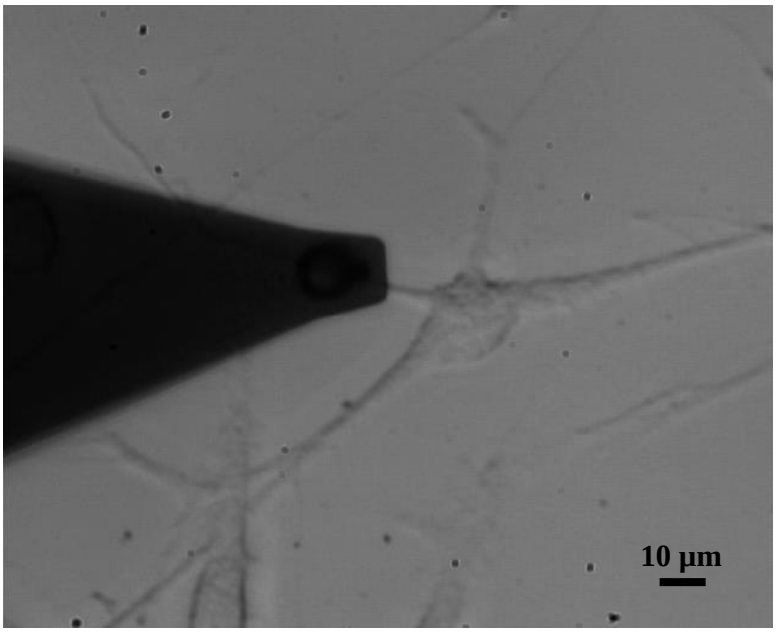

Fig. 1.20. Primary Schwann cell optical image captured before an experiment.

1.9.4 Nerve regeneration and outgrowth

Nerve regeneration after nerve injury and its controlling neurite outgrowth is one of the great problems in nerve tissue engineering. Functional recovery after injury involves various steps that delay the nerve regenerative process. In the peripheral and central nervous system, Wallerian degeneration (i.e., degeneration of the distal end of the axon occurs when the axon continuity from the neuronal cell body is interrupted) occurs after axon injury and the injured axon regeneration begins within the first 24 hours after nerve injury, where a single axon makes multiple axon sprouts. Initially, the regenerating axon unit contains only unmyelinated sheath (i.e., without white fatty material that forms insulating sheath) in contrast to the parent axon with myelinated sheath. Structural changes occur with time and the regenerating unit tries to establish contact with the extra perineurial environment. If the regenerating axon failed to make contact then a neuroma will be formed. In the leading edge of the axon sprout, the growth cone explores the local environment to make a physical contact for further growth processing. Subsequently, the Schwann cells proliferate and break down the myelin sheet and phagocytosis the myelin debris. This process takes almost 1-3 months for complete removal of myelin debris. The proliferated Schwann cells organize into columns and associate

themselves with the axon sprouts and endoneurial tubes provide the potential pathway for the axon sprout growth cone for successful growth [116–118].

Nerve regeneration is only possible when the injured axon sprout is intact and the neurite growth cone detects and responds to guidance cues in a local external environment by changing its direction through various stimuli. Schwann cells provide a supportive surrounding for neurite outgrowth and release neurotrophic factors, cell surface ligands, and also synthesize the extracellular matrix (ECM) [119–121]. Neurotrophic factors regulate the neuronal growth and its differentiation and serve to promote the neuronal survival. The directional orientation of Schwann cells on neurite outgrowth during the axonal regeneration has not only been observed in injured peripheral nerve tissue but also in oriented collagen gels and in oriented fibro-nectin mats [119,122,123].

1.9.5 Micro pattern and neurite outgrowth

Researchers have made extensive efforts to design various micro patterns for nerve guidance cues. They have investigated chemically modified patterned surfaces and how they influence the neuronal adhesion and the cell spreading in vitro. Micro-patterned surfaces have been considered as a potential tool for investigating and controlling neurite outgrowth for the past few decades. Various micro-patterning techniques have been employed to study the growth cone extension along with neurite (axon and dendrites) extension in vitro [124]. Neural adhesion and neurite outgrowth is observed on laminin modified micro patterned surfaces, the pattern created on the resist through mask-based photolithography [124]. An artificial neural network has successfully been studied on a micro pattern created through photolithography on the photo resist, before or after protein immobilization [125]. Hippocampal neurons from embryonic mice and out-growth neurites were studied on modified patterned geometries with a poly(l-lysine) coating and found a degree of cellular compliance to the pattern surface [126]. All well-defined approaches describe the role of directional growth for nerve repair but in fact the picture is more complicated because axon growth on a 3D extracellular matrix is different from that on two dimensional surfaces [127–129]. 3D surfaces provide a variety of cellular and extracellular factors which are important for a successful recovery from nerve injury. Various fabrication methods have been used for the fabrication of three dimensional guidance conduits and fibre structures [130,131]. Nerve guidance conduits have been created as porous rods or as hollow tubes. These conduits have been found to be good for nerve regeneration because the extracellular matrix helps to promote the cell-substrate adhesion and provide guidance towards the axon regeneration. A

variety of synthetic polymer materials such as poly(ethylene glycol) and poly(vinyl alcohol) have been used as the hydrogel for 3D cell culture [129]. Recently, 3D hydrogel micro-patterns were created using a digital micro mirror (DMD) for neural cell culture and studied the embryonic dorsal root ganglia (DRG) neurite outgrowth was studied [132].

1.10 Elasticity interrogation of living cells

Today researchers have established connection between the cellular function and its structural unit. The cell function and structural unit play an important role towards shape, motility, stability and DNA synthesis that contribute to its mechanical properties. The cytoplasm viscoelasticity is a crucial physical parameter for many cellular processes and the cell has the ability to recover its shape after complete removal of external force. AFM force spectroscopy allows the mechanical properties of a living cell to be probed. The elastic modulus can be determined from the recorded data upon the application of a constant stress on the area of the cell of interest. Relaxation modulus can be determined when stiffness of material reaches equilibrium. The elastic modulus and relaxation modulus of the cells following indentation can be successfully used as biomarkers for mechanical property characterization of many kinds of cell [133]. Cell mechanics have been studied in vitro. E.chen et.al investigated the stiffness change with respect to corresponding internal pressure of an isolated hair cell under hyper and hypotonic media [134,135].

N. Wang et al. investigated the contribution of intermediate filaments to cell mechanics and measured cells stiffness upon the application of stress. Significantly large stiffness was measured in the long cell spreading due to intermediate filaments at its edges [136,137]. The contribution of actin filaments to cell mechanics has been investigated by Haga et al. [138]. The already existing studies reported the cell nucleus stiffness with respect to the cytoskeleton structure and the nucleus was found to be three to ten times softer and also has the twice viscosity as that of the surrounding cytoskeleton structure [138]. Researchers have investigated the elasticity of the cancerous cell lines, ageing and wound healing [139–141].

1.10.1 Methods for elasticity measurement

Various methods have been employed for cell mechanics measurements including micro-pipette aspiration, magnetic bead microrheometry, optical tweezers and atomic force microscope (AFM). Brief introductions of these methods are given below.

1.10.2 Micropipette aspiration

In 1951, Mitchison and Swann introduced an instrument for the measurement of the cell surface mechanics which consisted of a glass micropipette connected to a small moveable water reservoir, the micropipette tip is brought up to the cell (eggs of various sea urchins) to measure by an optical microscope the degree of bulging of the cell surface by lowering the water reservoir [142]. This method was modified by Rand et al. in 1964 to measure the stress required for red blood cell membrane rupture [143]. This method can equally be applied to soft and stiff cells such as neutrophils [144] and outer hair cells for measurements of mechanical properties [145].

The micropipette aspiration technique has been used in a similar manner as employed by Mitchison et al. almost 60 years ago [142]. However, its use is limited due to advancement in the technology which offers more modern methods. In this method, the small glass micropipette with known diameter is filled with water connected to a moveable water reservoir. The micropipette is placed carefully to make a contact with the cell membrane through the use of an attached micromanipulator. A known negative hydrostatic pressure is exerted inside the reservoir volume by using a micrometre screw, the small cell membrane portion is sucked up into the glass micropipette lumen and movement of the cell edges can be monitored with the video screen [146,147]. Robert M. Hochmuth obtained ± 25 nm micropipette aspiration accuracy on living cells using the monochromatic light and also plotted the cell membrane deformation graph against the negative hydrostatic pressure to describe the cell membrane elasticity [146,147].

1.10.3 Optical tweezers

Optical tweezers were first reported by A. Ashkin in 1986. Micron-sized particles are accelerated and trapped inside the optical potential well by the force of laser radiation pressure [148]. Ashkin et al. observed the trapping and manipulation of a tobacco mosaic virus and an E. coli bacterium with optical tweezers [149]. Optical tweezers were used for the colloidal sphere traction by the creation of a computer generated intensity pattern over the sample area [150,151]. Later this technology was used to characterize the biological systems including the cytoskeleton probe, the cells motility and molecular motors for precise measurement of force and its local viscoelastic effects [152].

Optical tweezers have the ability to manipulate a single molecule with nanometre precision and also to measure the force with great accuracy on a single molecule that opens a new

pathway for biophysics related research [153]. Single molecule manipulation studies have allowed researchers to measure a single molecule force e.g., DNA with the optical trapping interferometer [154]. It is possible to monitor the movement of a single enzyme acting on a DNA molecule and observe the single molecular motors applying forces on biological molecules [153,155,156].

In biological applications, optical tweezers have used an infrared laser which reduces the specimen heating while manipulating and giving the high stiffness during the trapping without damaging the biological samples. Most biological samples are transparent to an infrared light wavelength that minimizes the absorption into the sample. Moreover, an ideal physiological condition cannot be maintained due to transfer of the small amount of heat to the sample surface [147,152].

1.10.4 Magnetic tweezers

The magnetic tweezers technique is often mentioned beside optical tweezers, as both the techniques involve manipulation of beads to impose force on different biological systems, bio-molecules or polymers of interest. In magnetic bead microrheometry, beads are normally coated with bio adhesive proteins including fibro-nectin and functionalized ligands and surface receptors e.g., epidermal growth factor (EGF). The diameter of beads used in this technique is usually around 5 μm and made up of ferromagnetic materials. Once the protein coated bead is bound to the cell surface then it can simply be twisted or displaced by applying a magnetic field. A twisting motion can be obtained by imposing the magnetic field which is known as ‘magnetic twisting cytometry’ and bead displacement is defined as ‘magnetic bead rheometry’.

Magnetic tweezers are a potential tool which has been used to study the viscoelastic response of the cells to externally applied force. Stepwise force is applied to bound magnetic beads to the cytoskeleton to record cell deformation [157]. Local viscoelastic properties of an apical (i.e., plasma membrane that faces the inner space of a tubular structure) membrane of human umbilical vein endothelial cells were studied by magnetic tweezers microrheometry [158]. A magnetic bead with a specific coating couples to different integrins that induce change in the intracellular signaling via a short force. Quantitative linear viscoelasticity and the local mechanical properties of the cell envelope was measured from the beads deflection [158]. The viscoelastic properties of the cell studied by using magnetic chains rotation containing 3-4 nano-particles upon the application of rotating magnetic field. As the bead rotates,

mechanical stress opposes the developed rotation within the cell, viscoelastic properties can be extracted from beads angular displacement measurements [159].

1.10.5 Cell mechanics using atomic force microscopy

AFM has the ability to provide force from nN range to pN with great accuracy. Conical and spherical tips can be used to acquire the cell mechanical data and the AFM tip can be modified in different ways. For large AFM tip sample contact area, spheres can be attached to the tip-less cantilevers or at the back of the tip on standard cantilevers. AFM colloidal probe provides the average cell mechanical properties in contrast to the sharp tip cell mechanical studies. AFM tips with attached spheres can also be modified chemically to carry out adhesion studies. Radmacher et al. [160] first investigated mechanical properties of the platelets that were on red blood cell fragments and the elastic modulus of platelets was found to be in the range of 1-50 kPa. Force indentation data was fitted with the Hertz model [160]. Various AFM studies have investigated the role of the cytoskeleton in cell mechanics in different cells types. Rotsch et al investigated the rat liver kupper cells mechanical properties using force-volume maps and the modulus map of the cell was reconstructed from the Hertz model fitted data. They also investigated the cell mechanics after drug i.e., cytochalasin D, treatment on the cell which disassembles the actin filaments and measured a seven times smaller elastic modulus within 40 minutes [161]. Dvorak et al. studied the muscle cell and bovine embryo skin cells during the mitosis phase and found the decrease in the stiffness due to cytoskeleton structure reorganization [162]. Karl et al. studied the role of microtubule filaments in XTH-2 cells, using a drug i.e., colcemid, on the cell to inhibit microtubule polymerization and an increase in the elastic modulus was observed. He observed the increase in stiffness due to a 2-3 fold increase in actin filaments that increases the tension in the cell [163]. Wu et al. investigated the elastic modulus of mouse fibroblast cells in the range of 4kPa. When force is applied to cells, deformation occurred as the result of slow cytoskeleton compression, this did not recover back after the removal of force. They also measured the elastic modulus when applying different drugs to cells and found an approximately 45% reductions in the elastic modulus upon application of cytochalasin D to the cell and 100% increase in the elastic modulus after application of cytochalasin D and colcemid [164]. Rotsch et al. studied the microtubule disruption in two different cell lines of fibroblast using colcemid and found similar elastic modulus on both fibroblast cell lines by using the same drug concentration. Researchers also investigated the cellular elasticity during actin filaments disruption and found less elasticity in contrast to cellular elasticity during the microtubule disruption [165].

Haga et al. found elastic variation within the cell through force-volume maps and found that the nucleus was much softer than the cell periphery and the elastic modulus was approximately 4 kPa which was 10 times smaller than the cell periphery [138]. To investigate the effect of applied force to the cytoskeleton using AFM, Han et al. studied the intra-cellular structural changes in rat cerebral endothelial cells. In this study, force curves were acquired in AC mode after applying nano-Newton (nN) force to the individual cytoskeleton bundles. Before acquiring the force curve data, the cell was imaged first in tapping mode and then force was applied to the cell. The cell was imaged again after the force curves and compared with the first image and rebuilding of the cytoskeleton networks was found after tapping the single point on cytoskeleton filaments bundles. They suggested that certain stress sensitivity points present on cytoskeleton filaments networks and elaborate change in the cell shape and structure can be obtained under the externally applied stress to the cell [166]. In this study, forces (36.2 nN and 71.5 nN) applied on cytoskeleton fibres were high in contrast to the other AFM studies and they did not clearly mention what cytoskeleton filaments are investigated. It can be suggested that structural change may have resulted of cytoskeleton filaments destruction and also because of the capture time difference between the first and second images. It is difficult to rule out the possibility that structural changes might have happened naturally. However, this study shows AFM potentially applied on the small area of interest and observed in real time [167].

In another study, Goldman et al. investigated the cytoskeleton role on cell mechanics on mouse embryonic carcinoma cells which had deficiency of the vinculin protein. Vinculin links the actin filaments to other proteins in the focal adhesion plaques and is also present in the cell-cell junction plaques in the epithelial cells. In force-volume maps, the vinculin deficient area was found to be softer than the wild type cells having vinculin [168]. In 1999, Lakka et al. studied the normal and cancerous cell lines to investigate the difference in mechanical properties. They used two normal human epithelial cell lines and three cancerous cell lines. The elastic modulus was found by fitting experimental data with the Hertz model and the normal cell elasticity was found to be approximately ten times higher than the cancerous cells, suggesting that the difference might occur due to a structural change in the cytoskeleton organization. This is an acceptable reason in the case of cancer which is associated with cytoskeleton alteration [169].

Berdyyeva et al. also investigated the variation in the elasticity of human epithelial cells with AFM and studied the aging effect on individual cells by comparing the elastic modulus of young and old cells. In this study, the author prepared colloidal probes to attach a 5 μm silica sphere to the cantilever end to increase the contact are to acquire the average measurements.

Force-volume mode data was analyzed with the Hertz model and the elastic modulus was measured two-to four-times higher in old cells in contrast to younger cells [170]. Age determination of blood stains is an unsolved problem in forensic case work. Strasser et al. used the AFM to examine blood stains for its age estimation. AFM has used to acquire force curve data over the fresh dried blood spot and the old blood spot sample and the elastic modulus was measured using the Hertz model. They observed a decrease in the elastic modulus with time. AFM can be a potential tool for the estimation of blood spot age [171]. The above studies provide a small insight into the versatility and the growing importance of AFM in the field of cell biology.

Chapter 2 - Maskless Photolithography Experimental Setup Detail

2.1 Introduction

This chapter describes the experimental setup developed for the fabrication of micron to sub–micron patterns using maskless far-field photolithography. Compared to mask-based photolithography setups these maskless techniques are not reliant on multiple layers of masks in order to fabricate different microstructures in the same patterned area. For this reason one of the main purposes of this project was to create the patterns without using a mask. The setup we have developed not only has the ability to fabricate two and three dimensional structures on a flat surface but also to fabricate the micro patterns on non-planer surfaces.

One of our maskless experimental setups used a spatial light modulator (SLM) consisting of programmed electrical addressable device with liquid crystal overlaid on microscale mirror pixels. Another maskless photolithography setup simply consisted of optical components; such setups can be used to create a pattern on any planar substrate. Different microstructures were created in a single area by controlling the writing speed with LabVIEW software. This type of maskless photolithography system can potentially be used for direct writing in a small and large area, offering a higher degree of flexibility, speed and fabrication cost compared to scanning near field optical lithography [172].

We describe here the details of our maskless far-field photolithography systems both with and without a spatial light modulator. These experimental setups were then characterized to investigate their ability to create micro patterns on photo resist. BPRS-100 resist material was chosen due to its easy handling and quick sample preparation for this experimental characterization.

2.2 Maskless setups with optical system

Two experimental maskless photolithography setups were built for patterning, one based upon the spatial light modulator and other without the spatial light modulator. A continuous argon-ion laser (351 nm, Innova I328, Coherent, Santa Clara, USA) with maximum power 200 mW was used in both setups. Here details of optical components that were used in both experimental setups are presented.

2.2.1 Periscope

The periscope is an instrument that has an ability to reflect an image that is not directly observed in the line of sight. The simplest form of periscope consisted of two mirrors

(PF05-03-F01, UV enhanced aluminum mirror 250 nm-450 nm, Thorlabs, UK) which were mounted on the adjustable height (P = 12, Ø1.5, Thorslabs UK) post at an angle of 45^{o} with their faces to each other. The laser beam from the source with a diameter of 1.2 mm hit the mirror at an angle of 45^{o} and reflected the laser beam at the same angle. The light then hit another mirror and then subsequently reflected off the mirror at an angle of 45^{o} towards the other optical component. The schematic representation of the periscope is shown in the Fig. 2.1.

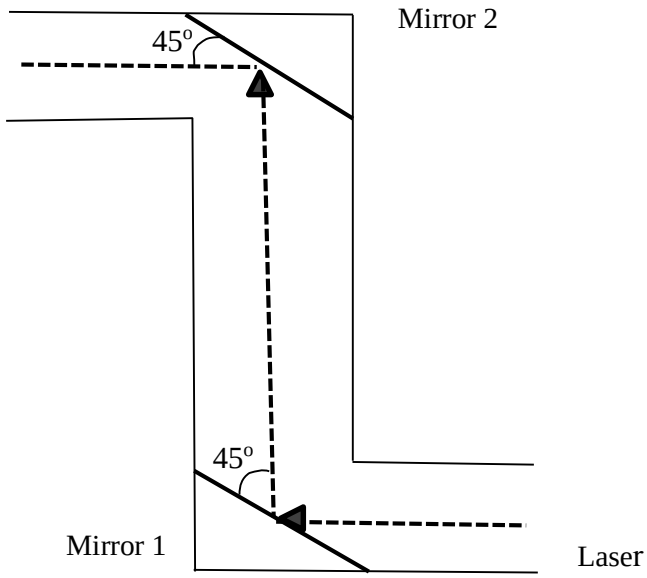

Fig. 2.1. Schematic representation of mirror periscope.

2.2 Spatial filter and beam expander

The spatial filter provides a potential way to eliminate arbitrary fluctuation from a laser intensity profile and improves the resolution especially required for holography and data processing. The laser beam usually acquires variation in the intensity profile from dust particles and also from scatter by defective optics.

The spatial filter consisted of an objective (LMU-39X-NUV, Thorslabs, UK) and a pinhole (P5S - Ø5 µm, Thorlabs, UK). The objective was assembled on a collimator adapter (AD1109F-SM05, Thorslabs, UK) that had an iris diaphragm (SM1D12SS-SM1, Ø0.9-Ø12 mm, Thorslabs, UK) and a pinhole (P5S-Ø5 µm, Thorlabs, UK) which was positioned on xyz kinematic mount (KC1-S, 30 mm-Cage for Ø1, Thorslabs, UK). Both objective and pinhole along with xyz kinematic mount were mounted on xy translation stage (2480, CVI Melles Griot, UK). A laser beam expander with a spatial filter is shown in Fig. 2.2.

An input beam with an initial diameter of 1.2 mm was focused by an objective at focal length of 4 mm where the pinhole aperture with the diameter of 5 µm was positioned that spatially filtered out the ring patterning, all random fluctuation in the intensity profile and scattered light. The spatial filter allows 99% of the beam intensity to pass and produces a collimated and clean Gaussian beam. The light beam was subsequently collimated by a collection objective (5x, 0.15A, LJ plan fluor, Nikon, UK) that had a focal length of 40 mm. The resulting laser beam had a 12 mm diameter, so the beam expander increased the beam diameter by a factor of 10x.

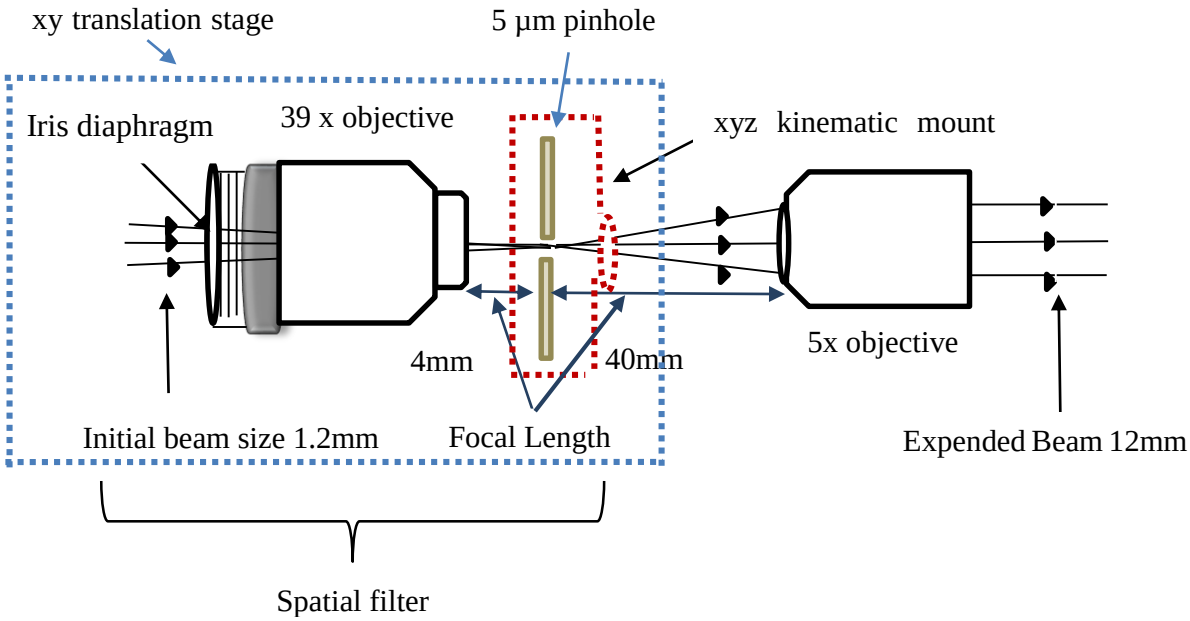

Fig. 2.2. Schematic representation of the laser beam expander with the spatial filter.

2.3 Experimental setup for maskless photolithography with a spatial light modulator

An argon-ion laser (351 nm, Innova I328, Coherent, Santa Clara, USA) was used to create diffraction limited spots for far-field maskless photolithography. The experimental setup is as shown in Fig. 2.3.

The argon-ion laser was horizontally polarized, then passed through a periscope which raised the beam vertically to the level of a polarizer (GT10-Glan-Taylor Polarizer, Thorlabs, UK) that turned the beam by 90°. Next, the light passed through another polarizer (GT10-Glan-Taylor Polarizer, Thorlabs, UK) that was used to obtain the plane-polarized light before sending it through a half-wave plate (WPH05M-355-Ø1/2, Thorlabs, UK). The main function of the half-wave plate was to control the polarization orientation of the light that was incident on the principal axis of spatial light modulator (351 nm, Boulder nonlinear system, Inc, USA).

After passing through the half-wave plate a mirror reflected by 90^{o} to allow it to pass through a spatial filter which collimated and expanded the beam from an initial diameter of 1.2 mm to 1.2 cm by the use of an objective (LMU-39X-NUV, Thorslabs, UK) with focal length 4 mm and a pinhole aperture (P5S-Ø5 µm, Thorlabs, UK) with diameter of 5 µm. The light was subsequently collimated by a collection objective (5x, 0.15A, LJ plan fluor, Nikon, UK) that had a focal length of 40 mm.

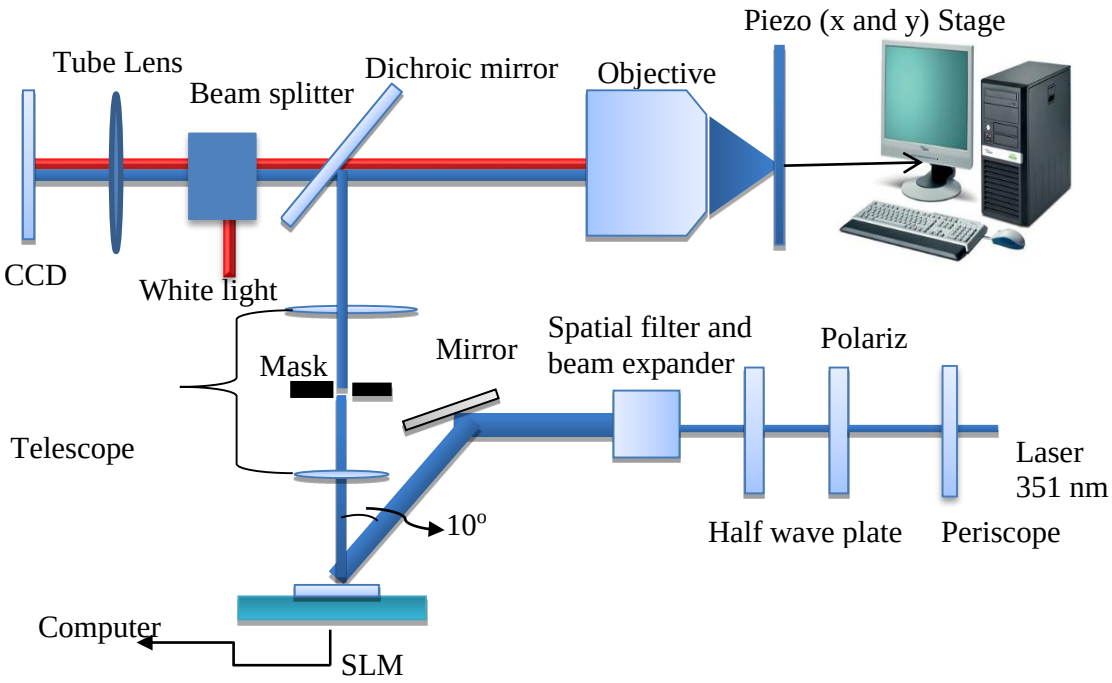

Fig. 2.3. The experimental setup used for SLM maskless patterning.

The clean Gaussian beam reached the SLM through a mirror. The angle between the incident and reflected light of the SLM was approximately 10^{o}. After the SLM, the laser beam covered 200 mm distance to a telescope lens (LB1199-N-BK7 Bi-Convex Lens, Ø, Thorlabs, UK) with focal length of 200 mm, followed by a second telescope lens (LB1889-N-BK7 Bi-Convex Lens, Ø2", Thorlabs, UK) with a focal length of 250 mm placed at a distance of 450 mm from the first. A dichroic mirror (BBSQ2-E02-2" x 2", Thorlabs, UK) was placed after the second lens to direct the beam at 90^{o} to the level of the optical port of an objective. The distance between the second telescopic lens and the objective was 250 mm. A telescope was used in this setup to scale down the SLM modulator image to the back size of objective aperture (20x/0.5, DIC plan fluor and 40x/0.60, ELWD Plan fluor, Nikon, UK). Further, the telescope also provided the parallel light to the infinity corrected objectives (20x or 40x).

To view the sample surface, a white light (PL-800, Dolan-Jenner Industries, USA) was passed through the beam splitter (BS013-50:50, Thorlabs, UK), dichroic mirror and then the objective that focused the light on the sample surface. The objective has the ability to collect the reflected white light and UV light from sample surface and subsequently focused on the image plane of CCD camera by using a tube lens (Stock No. 32-873, Edmund Optics Inc. UK) which had a focal length of 125 mm. A piezo sample stage (Agilis^{TM}, AG-LS25 (x and y), Newport, USA) was controlled with LabVIEW software to create the pattern.

Single and multiple diffraction limited spots were created by the SLM by using the 20x objective (NA = 0.50) as shown in Fig. 2.4 and 2.5. A single diffraction limited spot was used to create patterns and Image J software was used to obtain the Fourier transform, Gaussian distribution profile and the point spread function of the spot. Fig. 2.5 shows the multiple, single spot and its corresponding Fourier transform and point spread function.

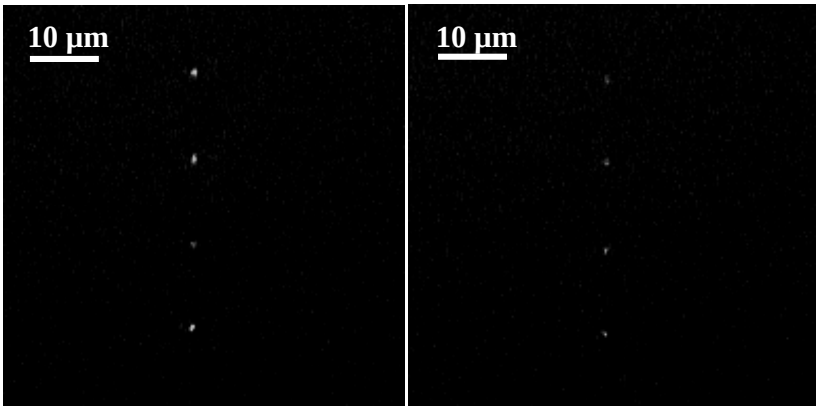

Fig. 2.4. Multiple diffraction limited spots which were created by the SLM.

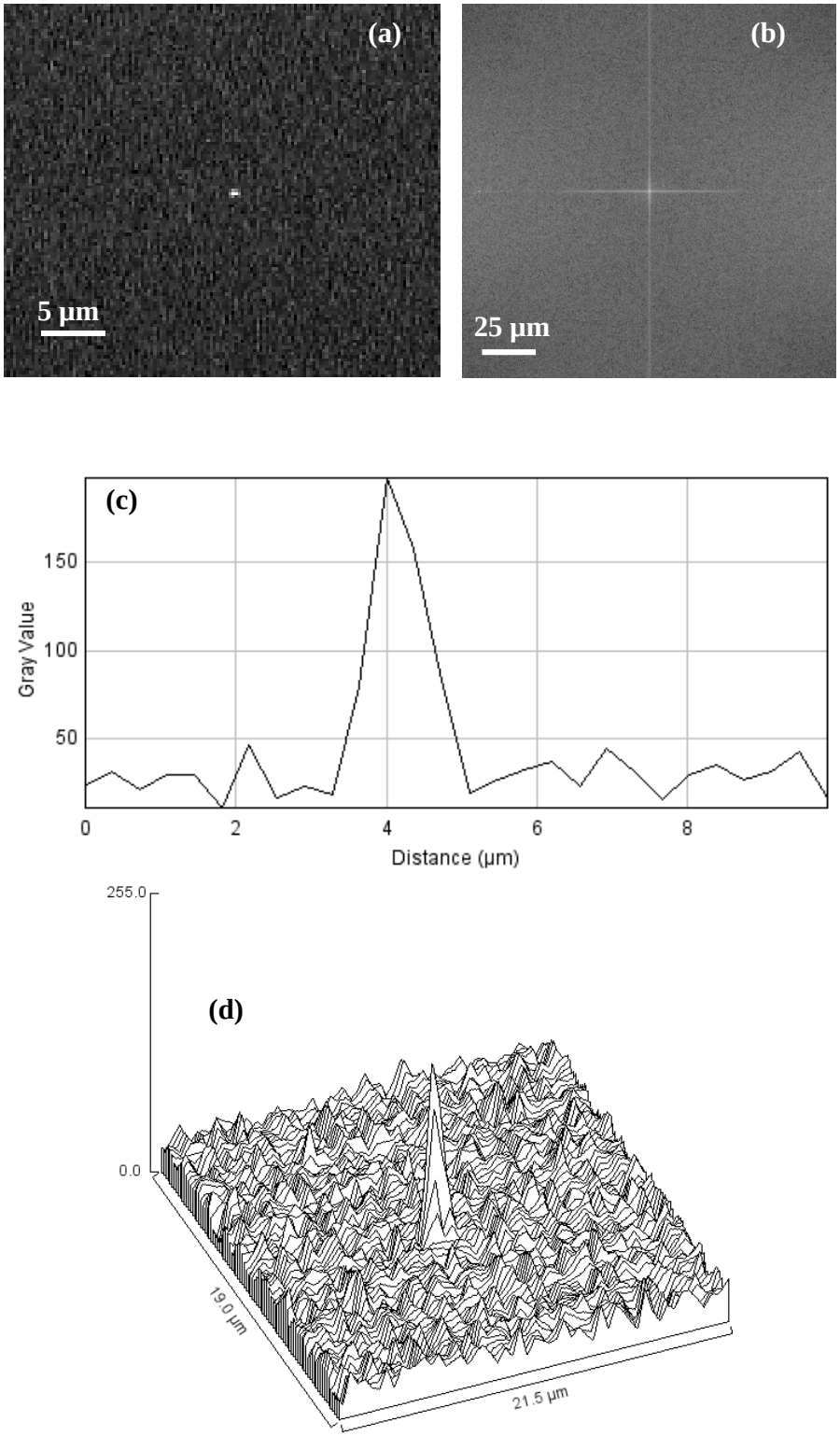

Fig. 2.5. Single spot with its corresponding Fourier transform Gaussian distribution profile and point spread function.

2.3.1 Spatial Light modulator (SLM)

A spatial light modulator (351 nm, Boulder nonlinear system, Inc, USA) is an electrically programmable device that modulates the wave front of incident light according to a fixed pixel pattern [173]. The XY phase flat series SLM transforms digital data into coherent optical information for a wide variety of instrumentation such as optical tweezers, beam steering, and diffractive optics. Phase based flat SLM produce phase variation in the incident beam by changing the refractive index of the liquid crystal.

A cross section illustration of a ferroelectric liquid crystal SLM is shown in Fig. 2.6. Coherent polarized light enters the device from the top cover glass, passes through a transparent electrode and falls on the ferroelectric liquid crystal layer overlaid on the pixel surface based on the silicon die circuitry.

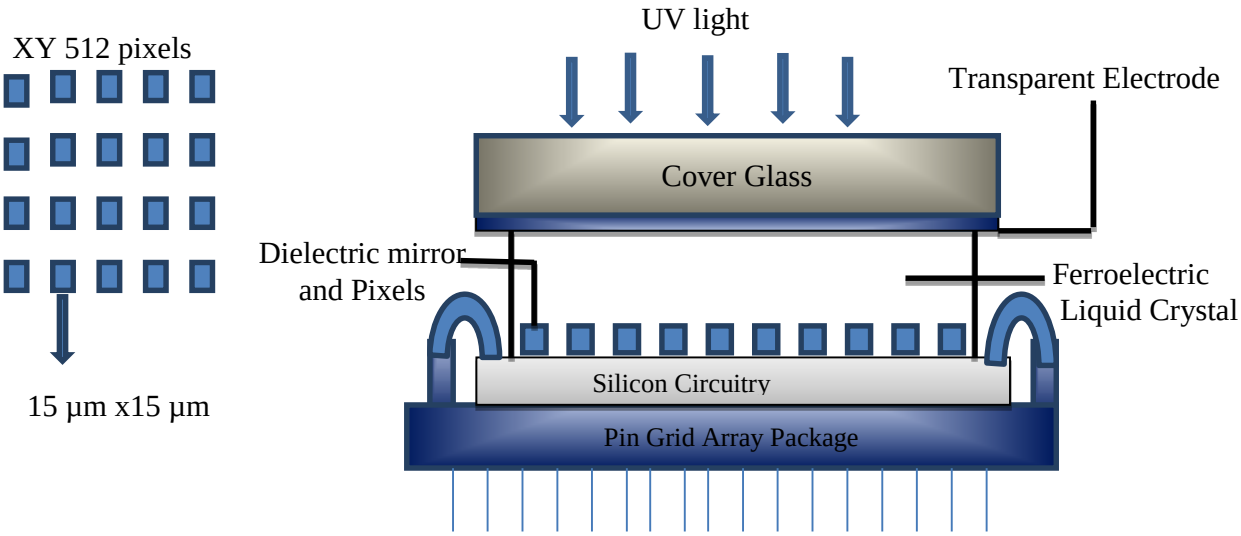

Fig. 2.6. A cross-section illustration of a SLM.

Drive signals pass through the pins on the base of the pin-grid array connected with the bond wires and silicon die circuitry. The transparent electrode is common to all pixels and the voltage applied to each pixel across to ferroelectric crystal is the difference between the transparent electrode voltage and that applied to the each dielectric mirror and pixel voltage. The voltage provided to each electrode (pixel) generates an electric field between the electrode and the transparent electrode on the cover glass. This electric field creates a change in the optical properties of ferroelectric liquid crystal by changing its orientation [173]. When the incident light passes through the liquid crystal at different applied voltage, then the output of the phase modulation reflected light beam directly depend upon the short and long axes molecular orientation which correspond to different refractive indices [174,175] as shown in Fig. 2.7. The refractive indices (n_e extraordinary and n_o ordinarily) difference generates a

phase delay [175] as the light wave propagates through the medium of the ferroelectric liquid crystal with the thickness d_m at a given wavelength and the phase of emerging modulated wave (φ_m) from the medium is

$$\varphi_m = 2\,\pi \quad \frac{d_m\,(n_e - n_o)}{\lambda} \qquad (2.1)$$

where λ is the wavelength of light.

The SLM pixels are controlled individually and the phase of the incident light can be controlled by applying a different voltage to each pixel. The SLM used in our setup was 512 x 512 pixels and can produce 512 phase levels (8-bit) and each pixel size was 15x15 µm.

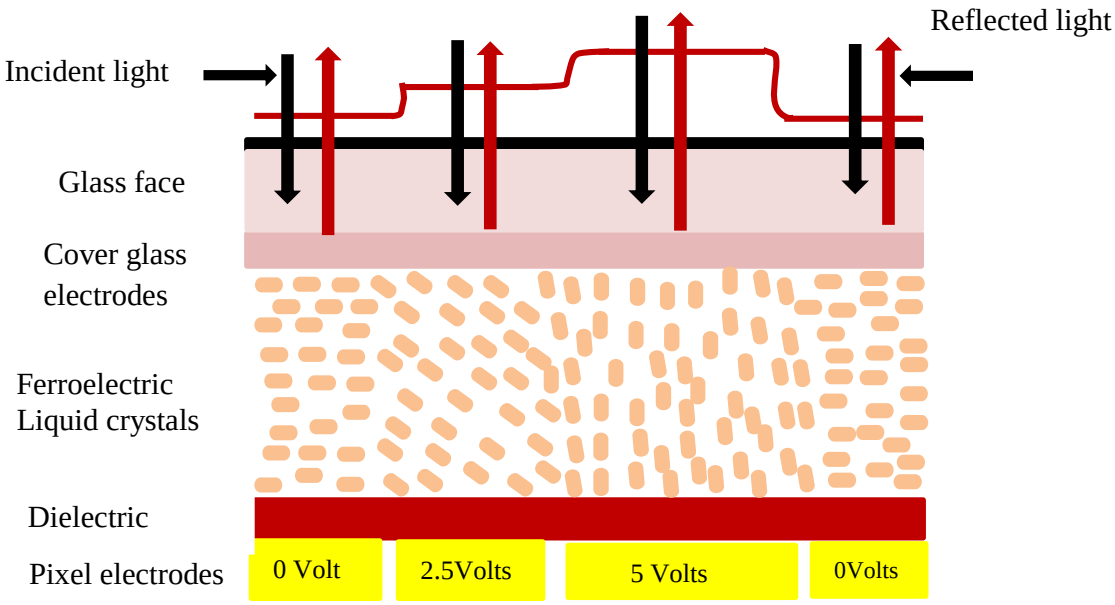

Fig. 2.7. Cross-section of the ferroelectric crystal based SLM. The refractive index of each liquid crystal overlaid on dielectric mirror is modified with applied voltage and different output phase modulated waves is obtained.

An incident laser beam is defined as complex field that falls on the SLM

$$v = a \exp(i\varphi) \qquad (2.2)$$

where 'a' is the amplitude and φ is phase of the wave. The SLM performs as a phase hologram that modifies the phase of the incident beam of light which is given by Eq. 2. The SLM transforms Eq. 2. 2 into $v = a \exp(i\varphi + \varphi_p)$ [174]. The Hotgui (holographic optical trapping graphical user interface) software [173] was used to generate the phase patterns and the modified beam was focused at the image plane of the lens. Considering fact of the Fourier transform property of lens, we can describe the Fourier transform relationship between the

complex field (v_j) in the focal point of lens, which is an image plane of the SLM and the complex field (v_k) at the focal point of lens in the image plane as shown in Fig. 2.8. The relationship between two complex fields is expressed as

$$v_j(x_j, y_j) = F\{v_k(x_k, y_k)\} \qquad (2.3)$$

If one of the complex fields is known then the other field can be measured by Fourier transform or inverse Fourier transform. The image plane created here is considered as a scale version of Fraunhofer diffraction pattern that can be produced by reflected beam by the SLM [174].

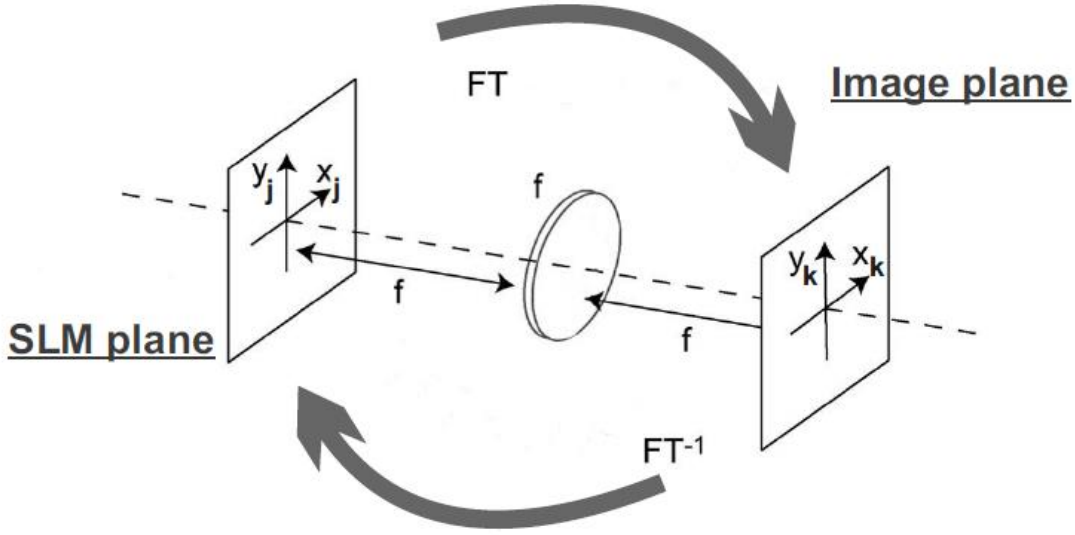

Fig. 2.8. Fourier relationship between the SLM plane (plane of hologram) and image plane of the lens. The image can easily move from one plane to other plane by Fourier transform (FT) and inverse Fourier transform (FT^{-1}).

2.4 Experimental setup for maskless photolithography without a spatial light modulator

The main aim of building this experimental setup was to create a line pattern using a diffraction limited spot as good as the theoretical limit of the instrument. For this purpose a new maskless photolithography setup without spatial light modulator was developed, based upon the laser beam with 1.2 mm diameter, two polarizers, a spatial filter, and an objective. The experimental setup is as shown in Fig. 2.9.

An argon ion laser (351 nm, Coherent Innova I328, Coherent, Santa Clara, USA) emitted a beam that was horizontally polarized (GT10-Glan-Taylor Polarizer, Thorlabs, UK), then

passed through a periscope which was used to adjust the vertical height of the laser beam to the optical axis of a polarizer that turned the polarization by 90°. Thereafter the light passed through a polarizer where the transmission axis was adjusted to reduce the beam intensity. The beam was then expanded and collimated from its initial diameter of 1.2 mm to 12 mm by a spatial filter consisting of an objective (LMU-39X-NUV, Thorslabs, UK) with 4 mm focal length and a pinhole (P5S-Ø5 µm, Thorlabs, UK) with diameter of 5 µm, and a collection objective (5x, 0.15A, LJ plan flour, Nikon, UK) with 40 mm focal length.

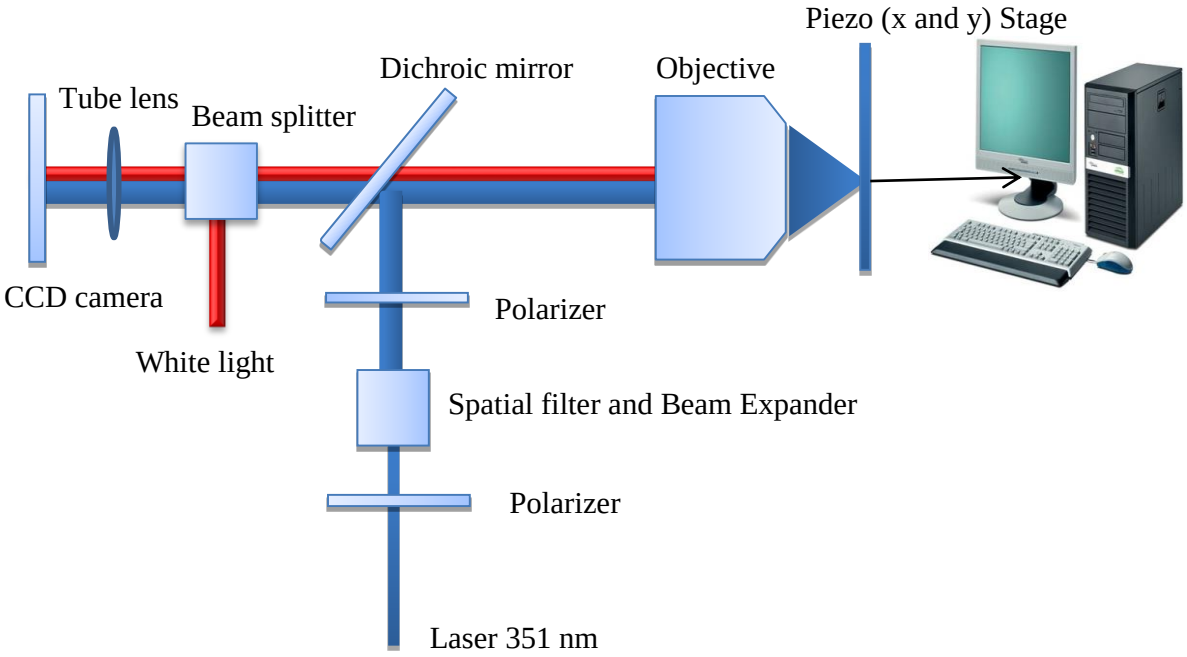

Fig. 2.9. Schematic illustration of the maskless photolithography setup without the SLM.

Collimated and clean planar Gaussian profile reached a second polarizer (GT10-Glan-Taylor Polarizer, Thorlabs, UK) that further reduced the intensity of the beam. Next, a neutral density filter (NENIR03A-Ø25 mm, Thorlabs, UK) was used to reduce the background scattered light and a dichroic mirror (BBSQ2-E02-2" x 2", Thorlabs, UK) which directed the laser at 90° to the level of the optical port of a 40x objective (NA = 0.60, ELWD Plan fluor, Nikon, UK)). The objective was used to focus the light on the selected area of the sample mounted on a piezo sample stage (Agilis™, AG-LS25 (x and y), Newport, USA) which was controlled with LabVIEW software to create the pattern. To view the sample surface and diffraction limited spot, a white light (PL-800, Dolan-Jenner Industries, USA) was focused by the objective on the sample surface after passing through the beam splitter (BS013-50:50, Thorlabs, UK) and dichroic mirror. The objective collected the reflected light and focused it on the image plane of CCD camera by a tube lens (Stock No. 32-873, Edmund Optics Inc. UK).

A clean and tightly focused optical spot depends on the numerical aperture used that defines the resolution limit. Using a high numerical aperture, a sharp, clean and focused Airy disc was used to create a lined pattern. Experimental diffraction limited spots created by the maskless setup without the SLM were analyzed with Image J software to obtain the line profile and point spread function of the spot. Fig. 2.10 shows the spot and the corresponding Gaussian profile and point spread function.

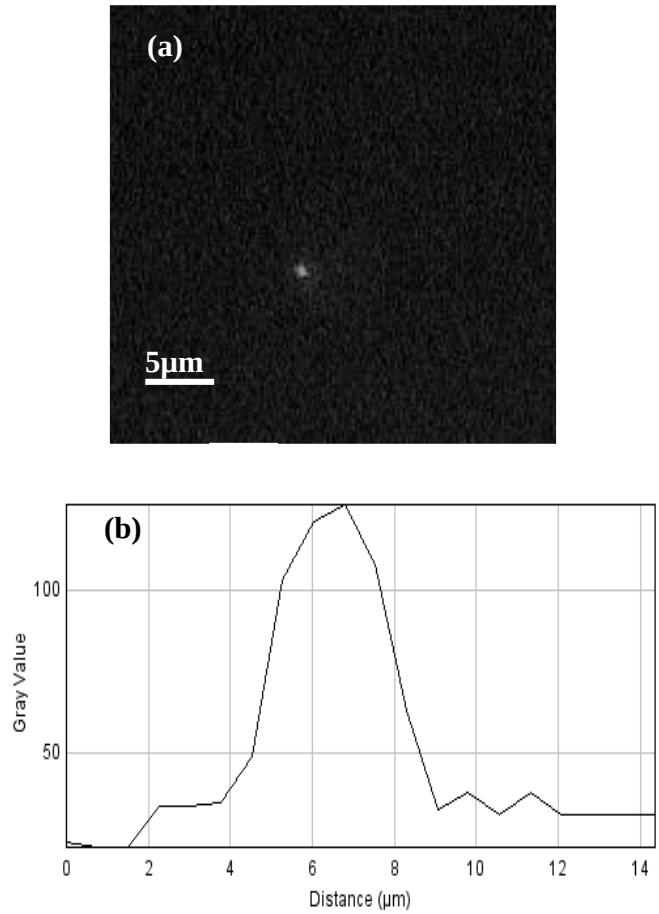

Fig. 2.10. A spot obtained with a 40x objective and its corresponding Gaussian distribution profile in (a and b).

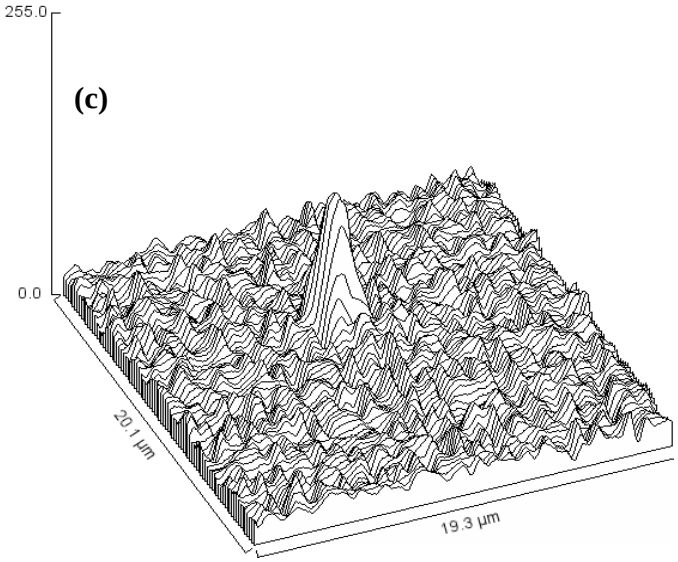

Fig. 2.11. The spot obtained with a 40x objective and its corresponding point spread function.

2.5 Sample preparation

Sample preparation was performed in three steps: First, a silicon substrate was washed with isopropanol (IPA) solution to remove any contamination in the form of particulates, organic or inorganic substances which might cause imperfections and poor adhesion of the resist. Secondly, the substrate was spin coated at 4000 rpm for 30 seconds with a small quantity of BPRS-100 photo-resist in liquid form applied with a pipette. Thirdly, the resist-coated substrate was placed on a hot plate at 100^{o} C to remove excessive solvent and to avoid the risk of unbaked resist film evaporating over time. After the baking process most of the solvent had evaporated and the resist film were stabilized at room temperature. BPRS-100 resist material was used in this study due to simple sample preparation.

2.6 Results

2.6.1 Results of maskless photolithography with a spatial light modulator on BPRS-100 resist

The diffraction limited spots created by the SLM [26,27,29,176] and a stationary focused spot was used to fabricate patterns on selective area of the sample which was mounted on the piezo motor and the speed of the piezo motor was controlled with LABVIEW software. Multiple diffraction limited spots can be used to create the multiple parallel patterns but as proof of principal this study exposed the resist to a single focused spot above the upper threshold that experiences a photochemical reaction. Line width data on different resist thickness was acquired with a 20x objective (NA = 0.30). The micro-pattern was created after immersion of

the exposed resist in a PLSI solution. The patterned features depend upon the spot size, resist characteristics, and the post processing that was performed. Atomic force microscopy was used to characterize the sample patterns. Fig. 2.12 (a-c) show topography images of micro patterns in resist with a thickness of 1.2 µm, created at a scan speed of 500 μms^{-1} at exposure powers of 35 µW, 50 µW and 65 µW, respectively. It was found that a different line width is created at different exposure times with the same laser power and that the line width could be reduced by increasing scan speed until the diffraction limit of the numerical aperture used occurs (Fig. 2.13).

Increasing the laser intensity above the resist threshold value produced a constant and smooth line and the line width increased with a further increase of power. Moreover, by increasing the intensity continuously at the same the exposure time a linear behaviour of the resist material was observed (Fig. 2.14).

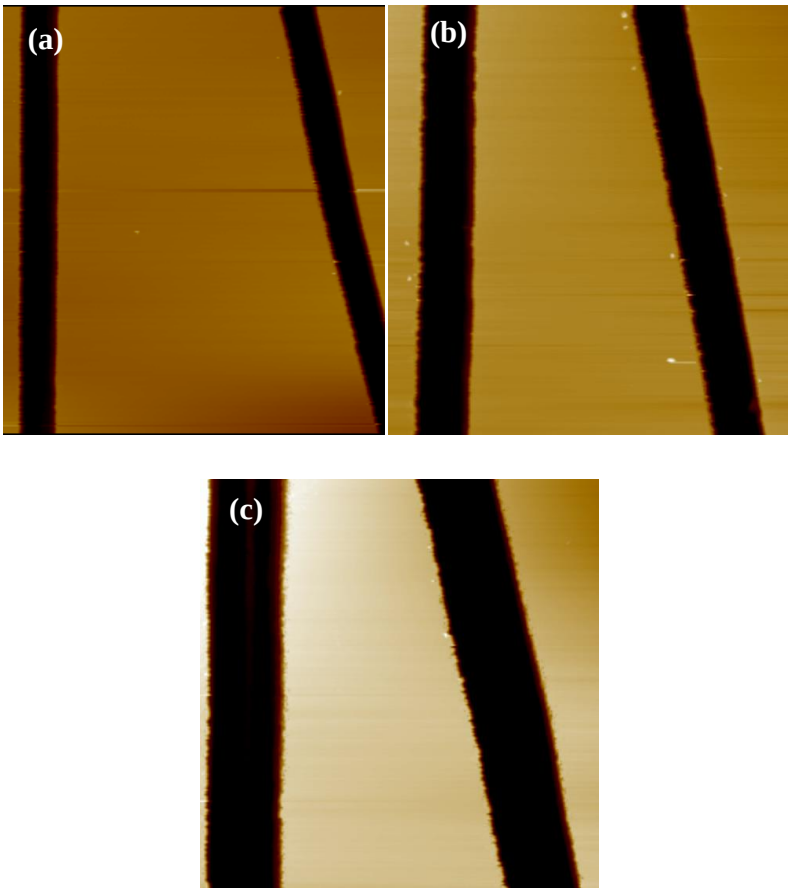

Fig. 2.12. AFM topography images of micro patterns in resist with a thickness of 1.2 µm, created at a scan speed of 500 µm s^{-1} but different exposure power. Line widths and exposure powers are (a) 2.9 µm and 35 µW (b) 3.99 µm and 50 µW (c) 5.67 µm and 65 µW. All images are 30 µm wide.

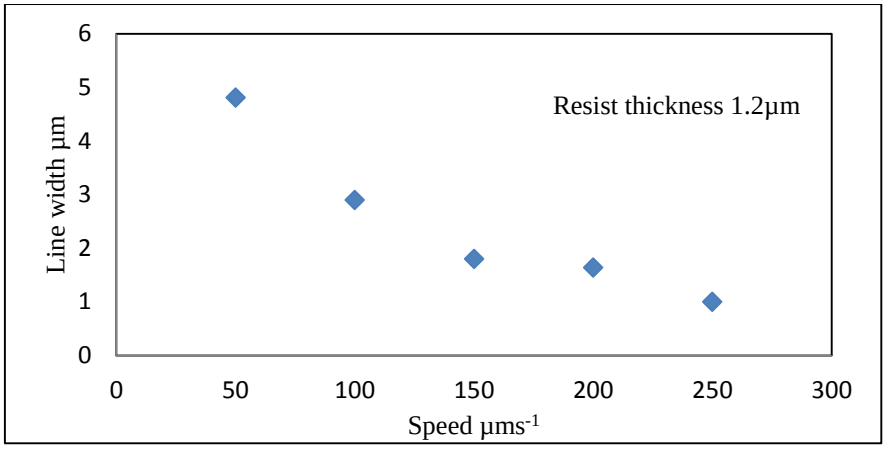

Fig. 2.13. The line width versus scan speed, showing a monotonic decrease with faster speeds.

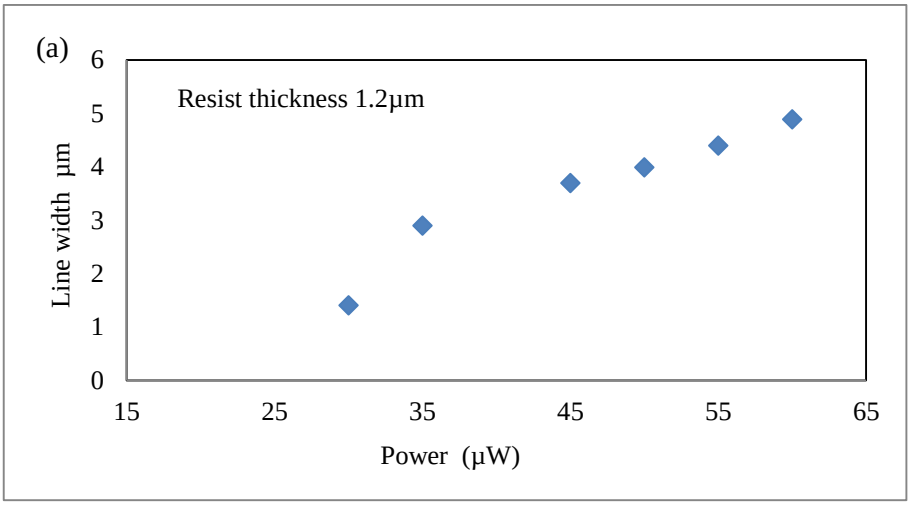

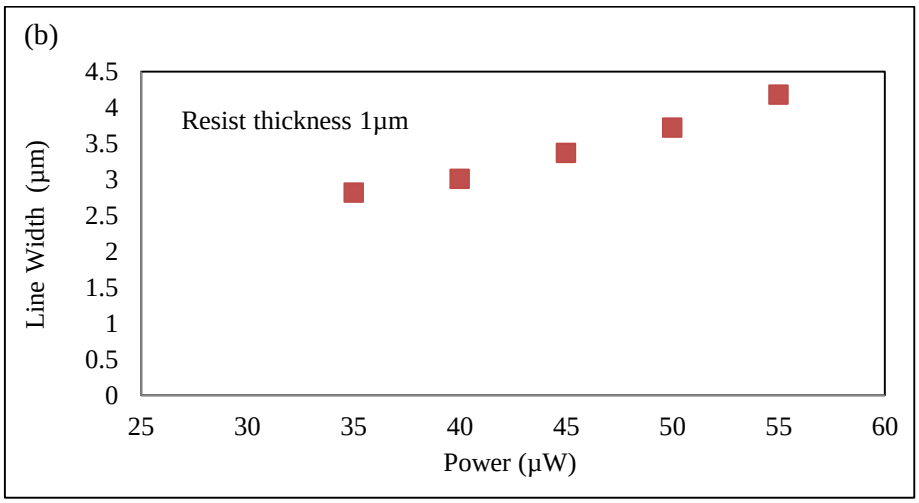

Fig. 2.14. Pattern line width obtained at different laser power (a and b).

Small scale features ware fabricated with a 40x objective (NA = 0.60) and spot size was also adjusted by placing the neutral density filter to remove scattered light around the spot. A line width of 512 ± 6 nm obtained at a speed of 5 $\mu ms^{-1}$and exposure power of 5 µW is presented in Fig. 2.15.

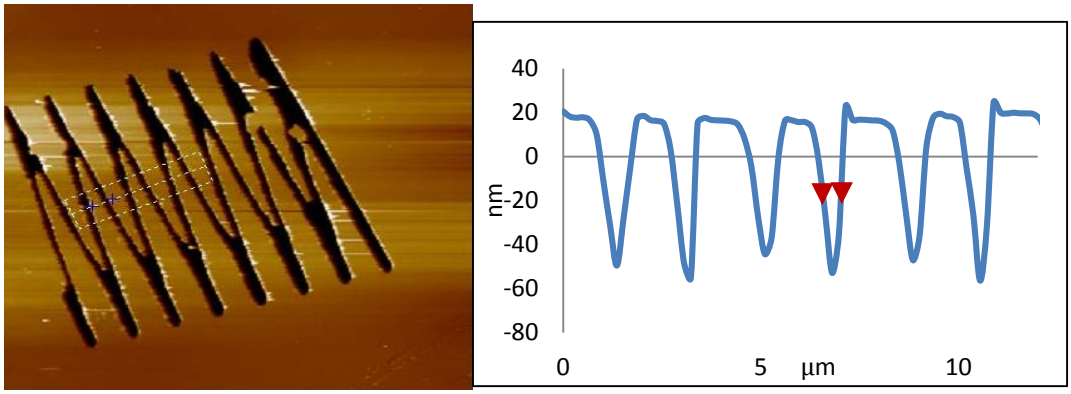

Fig. 2.15. A 40 µm x 40 µm AFM topography image and cross section profile of resist patterned at a speed of 5 μms^{-1} and an irradiation of 5 µW.

2.6.2 Results of maskless photolithography without a spatial light modulator on PBRS-100 resist

The diffraction limited spot was created by maskless setup without an SLM (section 2.4) and the diffraction limited spot was adjusted by using the neutral density filter to remove the excessive scattered light in the surrounding area of focused spot. The focused stationary spot was used to create patterns on BPRS-100 resist with a thickness of 1.2 µm by controlling the piezo motor speed with LABVIEW software. Line patterns were obtained at the power of 5 µWand speed of 5 μms^{-1} and 3 μms^{-1} (Fig. 2.16), resulting in the line width of 621 ± 6nm and 314 ± 8 nm respectively. Similarly pattern structures were obtained by maskless photolithography without SLM on NPPOC protected siloxane monolayers at different speed, of which a detailed discussion of experimental results will be given in the next chapter.

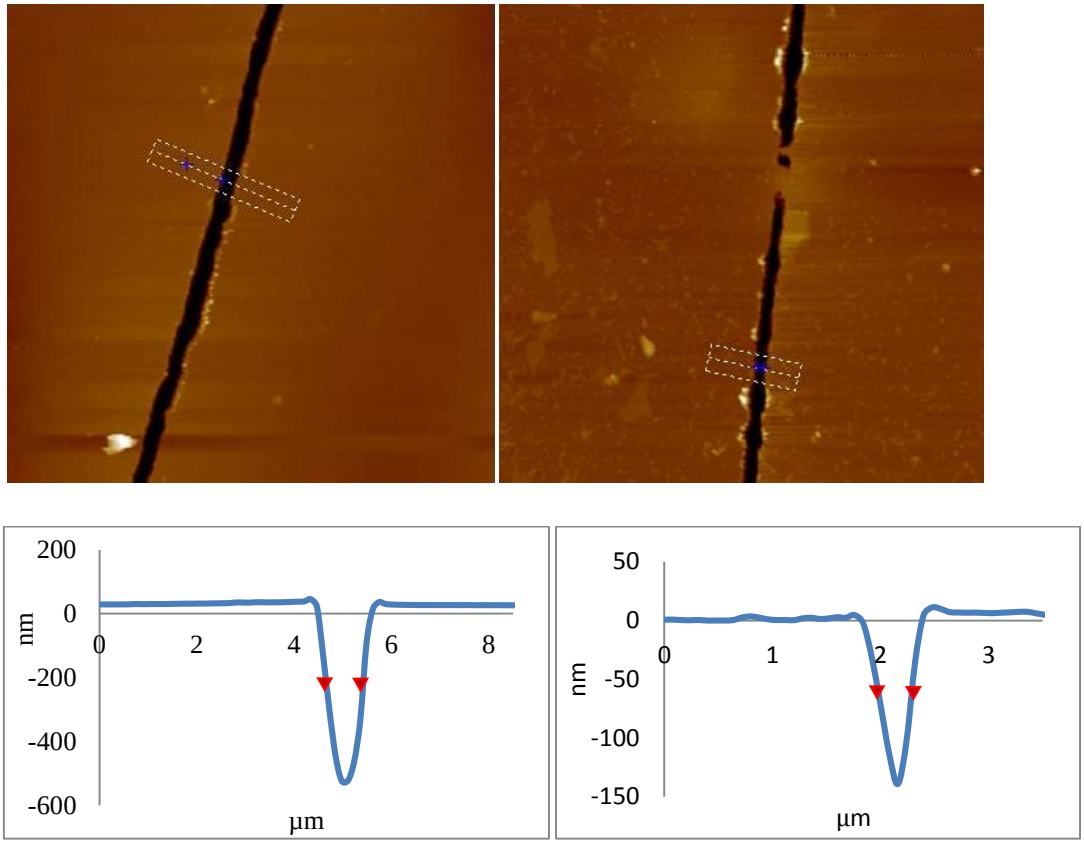

Fig. 2.16. AFM tapping mode height images acquired at the speed of 5µms^{-1}and 3µms^{-1} on BPRS-100 resist. Image width 30 µm and 20 µm respectively.

2.7 Conclusion

In this study, maskless far-field photolithography systems with and without a spatial light modulator were developed. These masksless photolithography setups have a capability to create micron and sub-micron structures with a large throughput. Such setups also have the ability to create both 2D and 3D patterns on planar surfaces by controlling the scanning stage in all three dimensions. To test our experimental setups, BPRS-100 resist-coated samples were used to check the resolution limit. Smaller line widths were obtained with the maskless setup based solely on optical components. These maskless experimental setups can potentially be used in many applications of cell biology and chemistry which use micro patterned structures.

Chapter 3 - Maskless Photo-lithography on 2-Nitrophenylpropyl-oxycarbonyl (NPPOC) Protected Aminosiloxane

3.1 Introduction

The objective of this chapter is to describe how the maskless photolithography experimental setup was used to fabricate patterned structures on 2-nitrophenylpropyloxycarbonyl (NPPOC) protected aminosiloxane through UV (351 nm) irradiation. Further, poly(2-(methacryloyloxy)ethyl phosphorylcholine) (PMPC) was grown on a UV deprotected surface and the polymer thickness characterized with AFM in both the dry state and in water.

The combination of photolithography and self-assembled monolayers (SAMs) is an area of extensive research. SAMs have attracted significant interest because of their potential use in a wide range of nano and micro patterning techniques. A wide variety of lithographic methods have been used, such as nanoimprint lithography, soft lithography, interference photolithography, scanning probe photolithography, electron beam lithography, anodic oxidation lithography, and atomic force microscopic nanolithography [7,46,177–181]

Self-assembled monolayers are atomically organized and uniform layers of molecules with a thickness of 2-5 nm. The conventional photolithography process can be followed on the SAM, using the SAM as the resist. Different SAM systems, such as alkylthiolates on gold, alkylsilanes on silicon dioxide and alkylphosphonic acids on oxide surfaces [47] have been employed using various lithography techniques. Whitesides and co-workers developed the micro contact printing technique which is widely used for the patterning of alkylthiolate SAMs [46]. In micro-contact printing a poly(dimethylesiloxane) (PDMS) stamp is inked with a thiol solution and placed on a gold substrate to transfer the thiol [46]. Another method whereby SAMs are patterned by UV exposure through a mask has been used for photo patterning of alkylthiolates, alkylsilanes on silicon dioxide, and alkylphosphonic acids on oxide surfaces [46,47].

Maskless photolithography is an interesting approach because it is a fast and simple method for fabricating patterns on SAMs. At the nanometre scale, dip-pen nanolithography, Inkjet printing, and scanning near-field photolithography have been used to fabricate nano-patterns [47,50,177,178,182,183] but there is limited data available for maskless far-field photopatterning on SAMs. A potential use of the maskless patterning of SAMs is the chemical patterning of features on curved or highly topographic surfaces, as the SAM ‘resist’ is surface specific and the laser focus is controllable in 3D.

Stimuli-responsive polymer brushes offer promising perspectives in a wide variety of applications, including sensors, micro-fluidic devices and drug delivery technology [184–186]. Patterned structures can be fabricated on SAMs by a variety of lithography techniques, and polymer brush growth on selective areas provides a platform for stimuli-responsive phenomena. Most research studies are focused on the fabrication of polymer brushes through 'grafting from' and 'grafting to' techniques [184,187–189]. 'Grafting to' involves the chemical reaction of preformed, functionalized polymers with a surface having functional groups [64]. However, this technique does not produce sufficiently dense polymer brushes as the chain attachment might be hindered by the existing attached polymer layer [64,189]. As a result of these limitations, the 'grafting from' technique is considered to be the best option for polymer brush synthesis.

In this chapter, two masksless photolithography setups are used for the fabrication of patterned structures on NPPOC protected aminosiloxane monolayers. First, a simple and robust maskless photolithography setup without a SLM produces patterned structures on NPPOC protected SAMs by exposure to UV on selective areas after degradation of NPPOC. Friction force microscopy (FFM) is used to reveal mask based and maskless photopatterns. In order to observe the variation in line width as a function of writing speed the reactive patterned SAM surface is further chemically functionalized with a PMPC brush with an initiator using atom radical polymerization. Tapping mode AFM images show the line width variation as well as polymer thickness variation as a function of speed and different exposure doses. It is also seen that different polymerization times describe the thickness of polymer brushes in both dry state and in water, and corresponding data show that grafting density varies at different speed. Finally, we present how maskless photolithography with a spatial light modulator can be used for the fabrication of patterned structures on NPPOC protected SAMs by UV light, and the characterization of the polymer brushes thickness.

3.2 Method and material

3.2.2 Experimental method for mask based micro-patterning on NPPOC protected aminosiloxane

An argon ion laser emerged as a small spot with diameter of 1.2 mm and passed through the polarizer and enlarged the beam diameter to a 12 mm by beam expander and then fell on the mirror at the position of 45^{o} to focus the beam at the sample surface. The SAMs were cleaned with ethanol and dried with nitrogen before being placed on a fixed stage directly underneath the mirror. Electron microscope grids with a square pattern1500 mesh (Agar, Cambridge,

UK) were used as a mask placed directly on the sample surface. A clean quartz bar was placed on the mask and sample to ensure the mask remained in position during the experiment.

3.2.1 Sample preparation

The silicon oxide slide was placed in a Schlenk tube fitted with subaseal septa and the air in the tube was evacuated by vacuum pumping and replaced with dry nitrogen. A 1 mM solution of NPPOC-silane was prepared in toluene into a 100 ml flask and transferred it into the Schlenk tube using a syringe and left for reaction. After the completion of reaction, the silicon oxide slide was washed with toluene, ethanol, then dried under the stream of nitrogen and placed in a vacuum oven for 45 min [190].

The height images of NPPOC-monolayer on silicon substrate before patterning were acquired by AFM in tapping mode, as shown in Fig. 3.1.

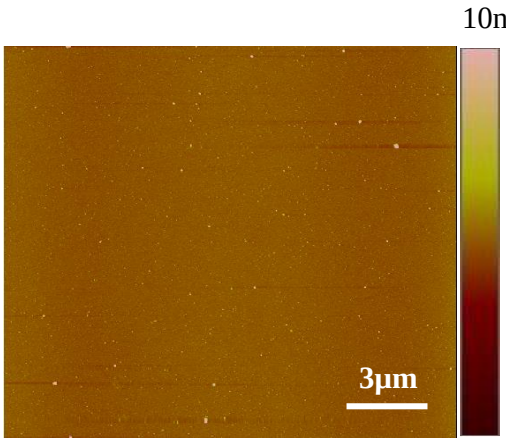

Fig. 3.1. Tapping mode height image of un-patterned NPPOC protected aminosiloxane. Height colour bar represents the height variation in image.

3.2.3 Experimental method for maskless photopatterning on NPPOC protected aminosiloxane monolayers

An argon-ion laser (351 nm, Coherent Innova I328, Santa Clara, USA) was used to create the diffraction limited spot for maskless photolithgraaphy. The detailed experimental description was given in the previous chapter. NPPOC protected aminosiloxane monolayers were irradiated with a diffraction limited spot on selected areas by controlling the speed of the piezo motor with LABVIEW software.

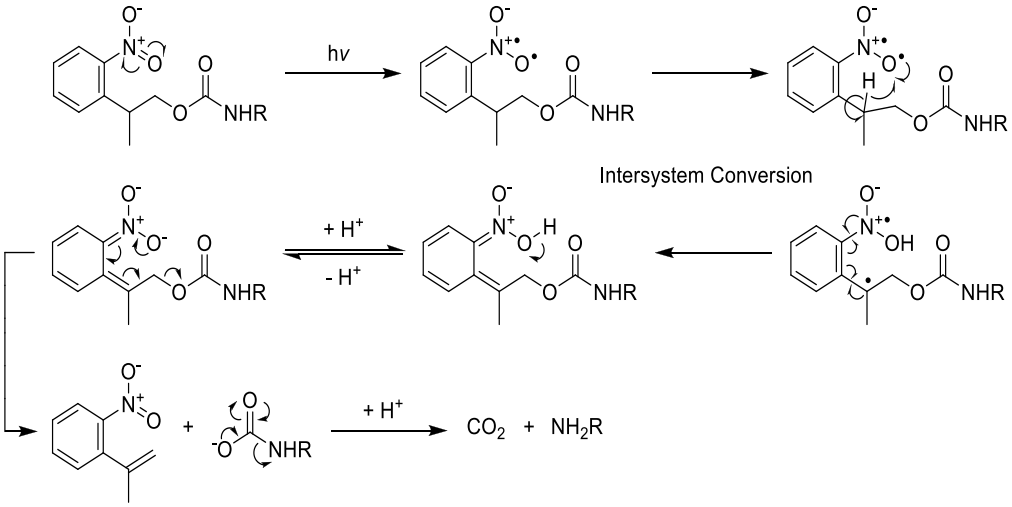

Scheme 3.2. The proposed mechanism of NPPOC de-protection by UV light, Scheme was used by permission [191]. Copyright (2009) American Chemical Society.

SAMs of NPPOC undergo a photochemical reaction to produce an amine reactive surface that was used for further reactions after the removal of a NPPOC group. The reaction mechanism is shown in scheme 3.2.

The anionic polyelectrolyte macro initiator was adsorbed on the NPPOC deprotected areas then initiator functionalized (3-aminopropyl) triethoxysilane (APTES) was used to grow brushes of poly(2-(methacryloyloxy)ethyl phosphorylcholine)) (PMPC) by atom transfer radical polymerization (ATRP). The line width with polymer brush was characterized by atomic force microscopy. The reaction mechanism is shown in scheme 3.3.

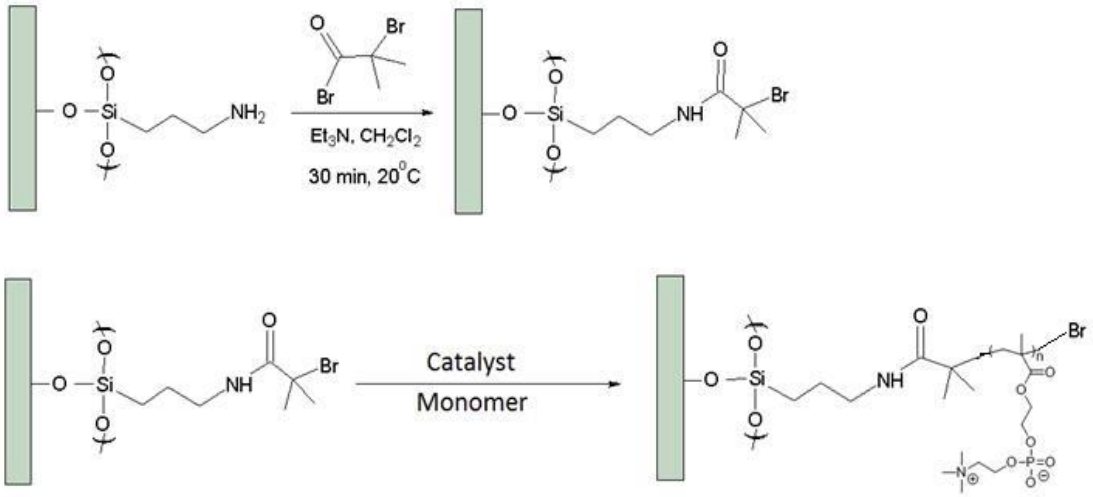

Scheme 3.3. Illustration of the reaction mechanism for PMPC brushes. The first step couples the initiator group with the NPPOC deprotected area, the second step initiates the surface that was used to grow a graft the PMPC brush [192].

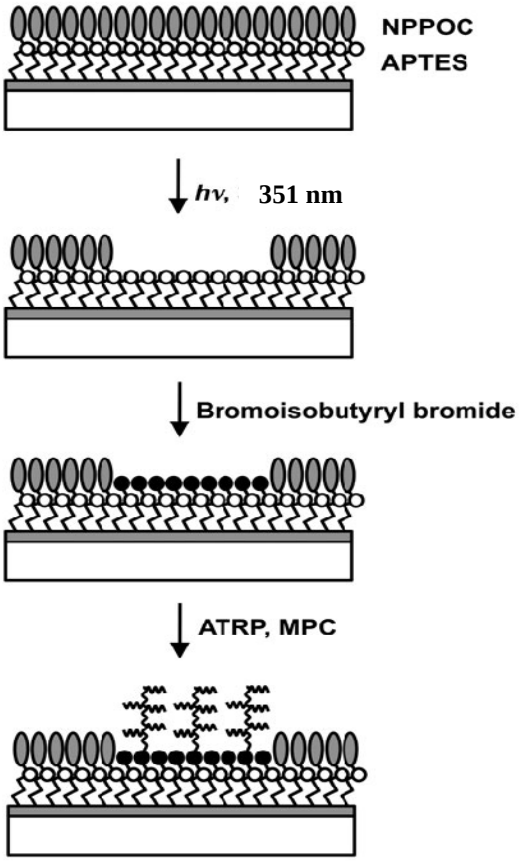

Fig. 3.4. Schematic diagram of fabricating a patterned polymer brush structure by maskless photolithography, figure was used by permission [193]. Copyright (2012) Nanotechnology.

In this study the PMPC brushes were grown on the deprotected areas in collaboration with the Leggett Group in the department of Chemistry at the University of Sheffield. Brush synthesis was carried out by Abdullah Alswieleh.

3.3 Results and Discussion

3.3.1 Mask-based micro patterning of NPPOC protected aminosiloxane monolayers

The sample was exposed to an argon ion laser through the mask as described in section 3.2.2. A laser power of 12 mW was focused on an area of 0.24 cm^2. Friction force microscopy (FFM) was used to distinguish the effect of exposure on surface composition, and to distinguish areas with different chemistries and hence different surface energies. Clear friction contrast was obtained with a 2.4 J cm^{-2} exposure, as seen in the Fig. 3.5. The square exposed areas resulted in brighter contrast than the masked areas, corresponding to amine groups and nitro groups respectively. The clarity of contrast depends upon the interaction of the polar silicon nitride AFM tip with the polar amino group and non-polar nitro group [190]. Higher contrast in the exposed area indicates a higher friction force and energy dissipation due to the interaction between the AFM tip and the amino group, in agreement with previous studies [190]. The low friction contrast was observed in masked areas where the polar AFM tip interacts weakly with non-polar nitro group, leading to low energy dissipation.

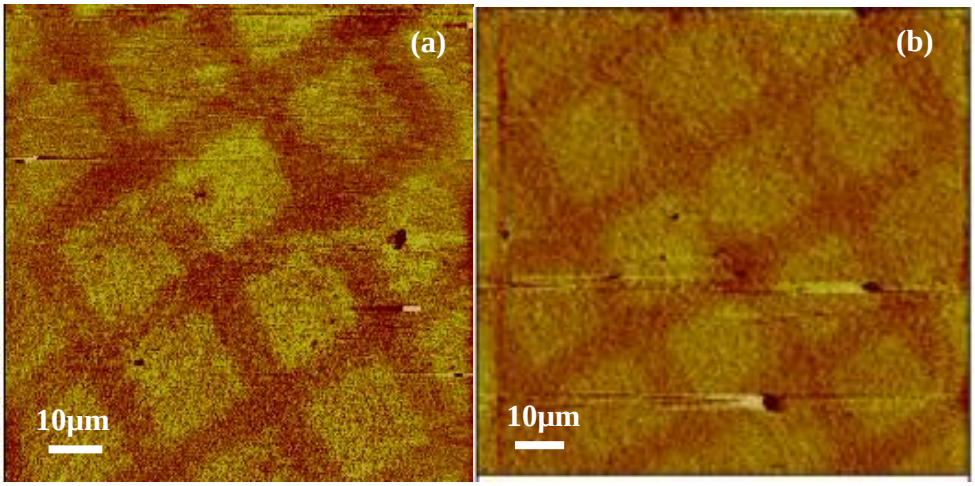

Fig. 3.5. FFM images of photopatterned NPPOC monolayers showing clear contrast between exposed and unexposed areas

3.3.2 Maskless photolithography without a spatial light modulator and friction force microscopy

The diffraction limited spot was created by maskless setup without the spatial light modulator. Patterns were created on selective areas of NPPOC protected aminosiloxane monolayers by focused stationary spot and the speed of the piezo motor was controlled with LABVIEW software. The patterned surfaces were characterized by friction force microscopy (FFM) but no patterned structures were found. Different exposure doses were used at different speed but due to poor contrast between UV deprotected and NPPOC protected regions no successfully friction force data was acquired. However, the pattern structures were present on the surface as was confirmed by polymer brush growth data on UV deprotected regions. This is further discussed in section 3.3.3.

3.3.3 Maskless photolithography without a spatial light modulator and PMPC brushes

Maskless photopatterns were created with the diffraction limited focused spot on selective areas of the sample which was mounted on the piezo motor and the speed of the piezo motor was controlled with the LABVIEW software.

In this study, we first look at the width of structures created through maskless setup without the spatial light modulator at a fixed polymerization time, and then discuss how speed and laser power can be used to increase the polymer brush thickness on the underlying patterned surface. Thereafter we investigate how the polymerization time controls the brush thickness on the surface patterned at multiple speed.

3.3.3.1 Line structures variation with a speed and exposure power

Line structures were written on selective areas of SAM by a stationary focused laser spot with a Gaussian energy distribution. Polymer brushes were grown on NPPOC deprotected patterned surfaces and the width and height of the resultant PMPC brush structure was characterized with AFM. A series of patterned structures acquired through far-field pattering show line width variation at different writing speed. Fig. 3.6 (a-c) show the full width half maximum (FWHM) of the line written at a speed of 25 μms^{-1}, 30 μms^{-1} and 32 μms^{-1} and an exposure power of 140 µW. The line width is that of the polymer brushes on the underlying patterned surface, which is significantly larger than the UV defined pattern [184]. It is seen

that the polymer brush height and line width of the patterned structures vary significantly with speed.

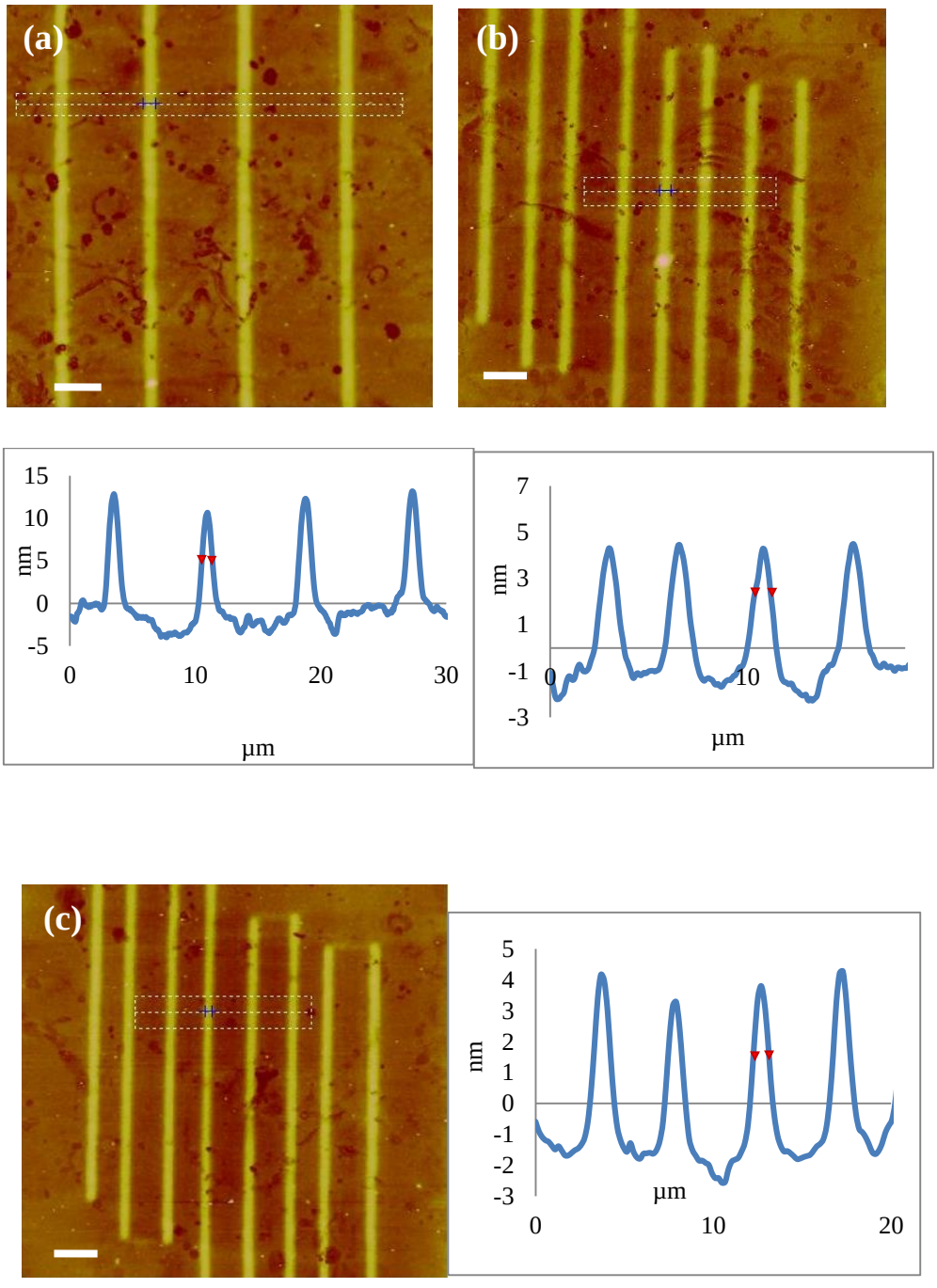

Fig. 3.6. (a-c) Tapping mode height images of the patterned structures with PMPC brushes at speed of 25 µms^{-1}, 30 µms^{-1} and 32 µms^{-1} having a line width of 925 ± 4 nm, 832 ± 6 nm and 732 ± 5 nm, respectively. Scale bar for all image size (a-c) is 4 µm.

The smaller line width was obtained by adjusting the spot size with a neutral density filter which was used to remove the excessive scattered light in the surrounding area of the diffraction limited spot. A line patterned was obtained at speed of 5μms^{-1} and 9 μms^{-1}, the height of which is 4 and 5 nm and FWHM is 530 ± 5 and 420 ± 10 nm.

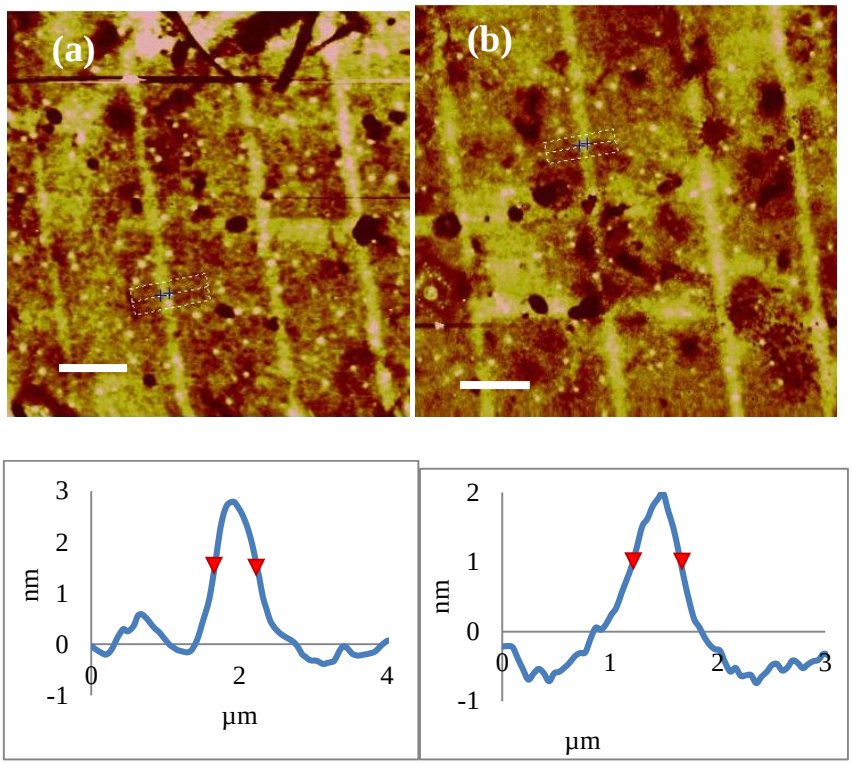

Fig. 3.7. (a-b) Tapping mode height images of the patterned structures obtained at the speed of 5 μms $^{-1}$ and 9 μms $^{-1}$ with the line width of 530 ± 5 nm and 420 ± 10 nm. Scale bar for all image size (d-e) is 4 μm.

Fig. 3.8 (a-h) also presents a series of the pattern structures clearly showing the significant decreased of polymer brushes height with speed. Polymer height variation provides the information about PMPC morphology at different speed (1 μms^{-1}, 6 μms^{-1}, 13 μms^{-1}, 20μms^{-1}, 28 μms^{-1}, 32 μms^{-1}, 36 μms^{-1}, 40 μms^{-1}). Fig. 3.8 (a) shows a height image of the pattern structure obtained at a laser power of 140 μW with a speed of 1 μms^{-1}. The line cross-sections show the maximum polymer brush height acquired in a dry state in this study. The brush thickness reduces with higher speed and minimum thickness was found at 40 μms^{-1}.

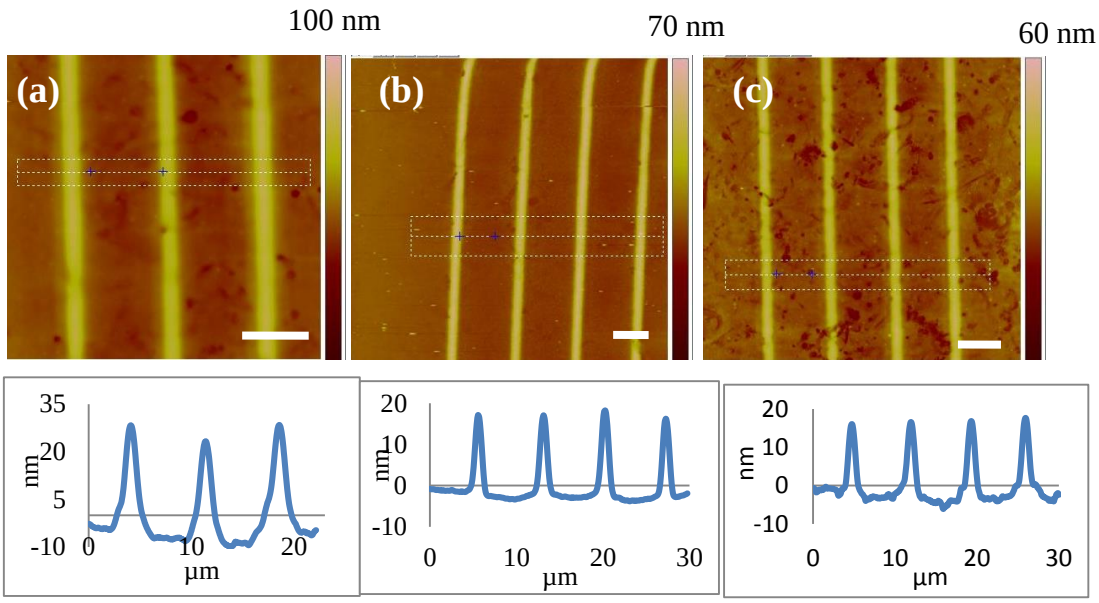
100 nm
70 nm
60 nm
(a)
(b)
(c)
35
20
5
-10
nm
0
10
20
µm
20
10
0
-10
nm
0
10
20
30
µm
20
10
0
-10
nm
0
10
20
30
µm

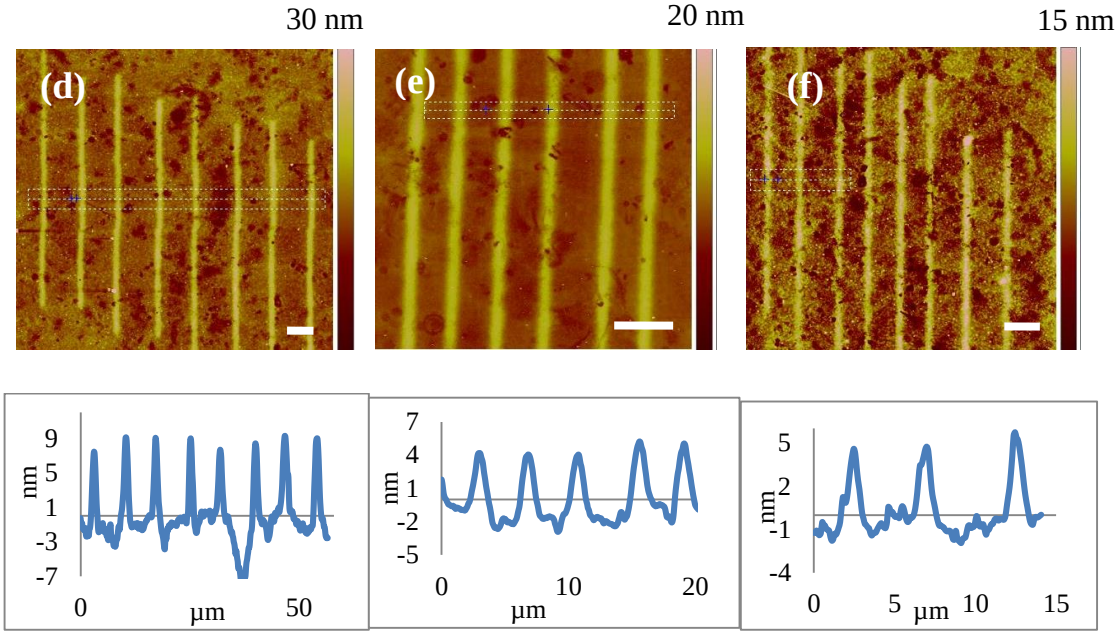
30 nm
20 nm
15 nm
(d)
(e)
(f)
9
5
1
-3
-7
nm
0
µm
50
7
4
1
-2
-5
nm
0
10
µm
20
5
2
-1
-4
nm
0
5
µm
10
15

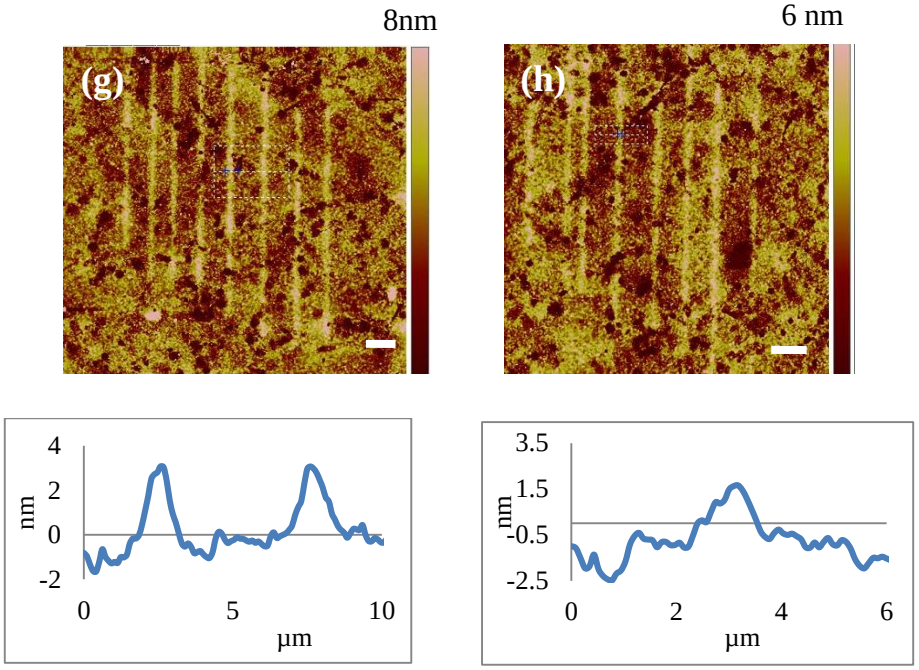

Fig. 3.8. (a-f (previous page) and g-h) Tapping mode images of patterned PMPC brush structures obtained at speed of 1 μms^{-1}, 6 μms^{-1}, 13 μms^{-1}, 20μms^{-1}, 28 μms^{-1}, 32 μms^{-1},36 μms^{-1}, 40 μms^{-1} and cross sections of their height profiles, showing how the polymer brush thickness decreased with increased speed. Scale bar for all images is 5 µm. The colour bar represents the height variation of polymer brush.

Fig. 3.9 shows the structure width variation of NPPOC protected aminosiloxane monolayers as a function of speed obtained at different exposure doses. An exposure power of 140 µW fabricated the broadest lines at low speed of the piezo motor. A decrease in width was observed with a linear increase of speed until it almost reached the diffraction limit of the numerical aperture used. Similar behaviour was observed at different laser power.

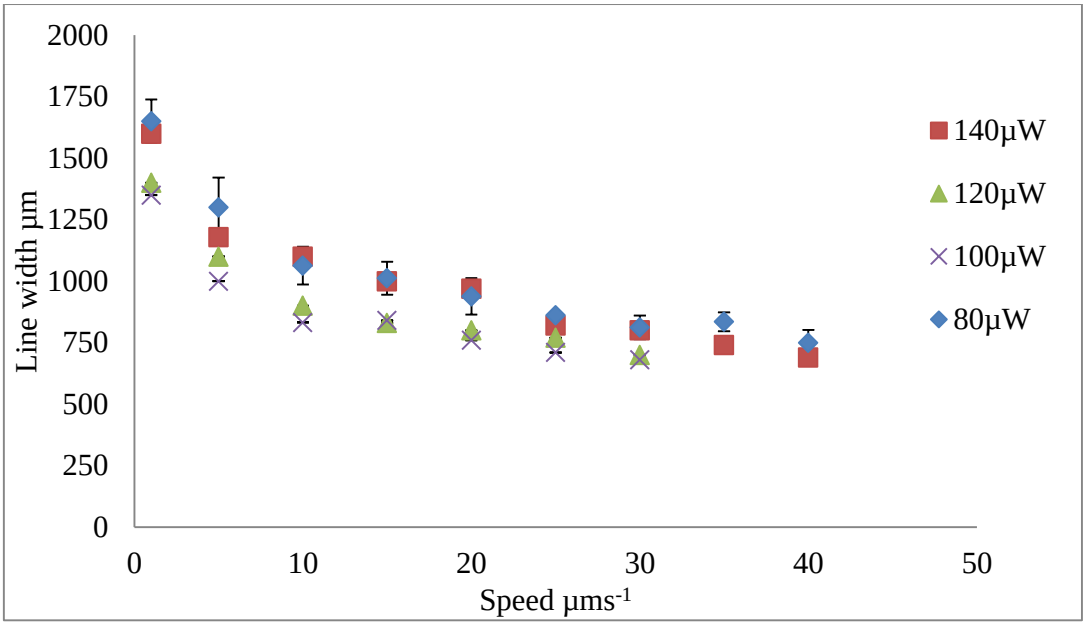

Fig. 3.9. Graph showing pattern width variation as a function of speed of the piezo motor at the same laser power for different laser powers, in all cases showing a reduction in line width towards higher speed.

Fig. 3.10 shows how the pattern width varies with exposure power at constant speed of the piezo motor. The graph shows a roughly linear increase in line width as a function of the laser power at each speed.

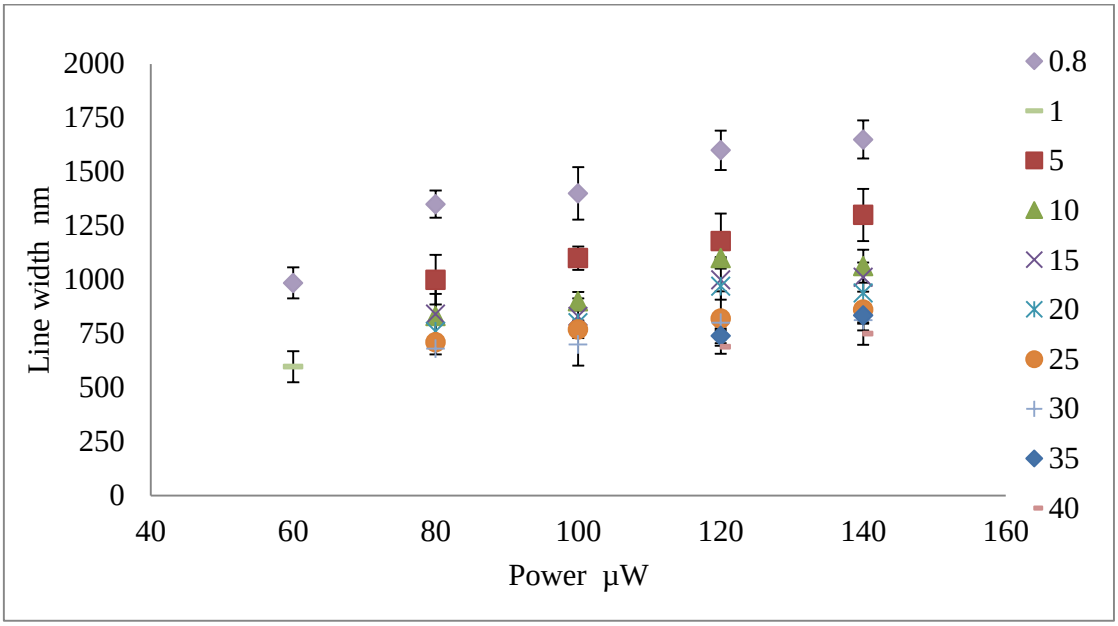

Fig. 3.10. Graph showing pattern width variations as a function of exposure dose at different speed.

As can be seen in Fig. 3.11, intensity is inversely proportional to speed of the piezo motor. As has been shown in Fig. 3.9, the line width was reduced at higher speed, corresponding to a decrease in intensity. At smaller speed, a large portion of the Gaussian profile of the laser spot was use to fabricate a wide line width in contrast to high speed that used only the central area of the profile. It is clear that line width increases both at greater intensity and slower writing speeds. From this we suggest that the using SAMs as resist material shows a linear decrease of line width as a function of speed.

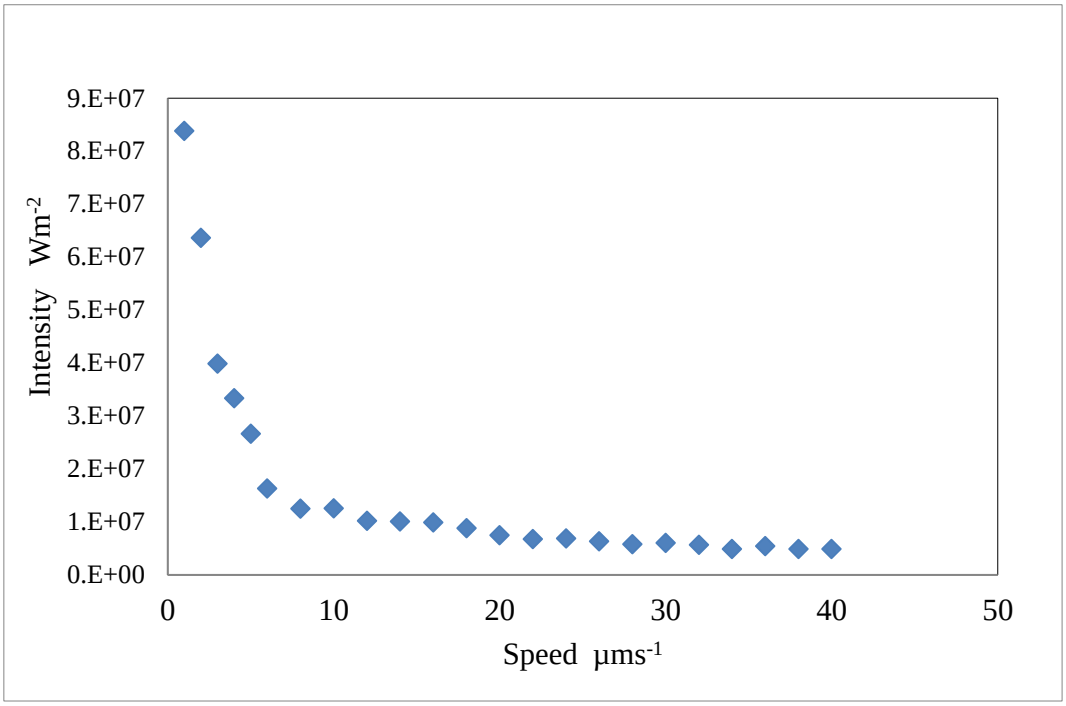

Fig. 3.11. Laser intensity as a function of speed of the piezo motor.

The height of the polymer brushes was measured with AFM on the patterned surfaces and plotted as a function of the line width as shown in Fig. 3.12. These results were obtained at a laser power of 140 µW with continuous decrease of speed from 40 to 1 μms^{-1}. The maximum brush thickness of 32.7 ± 1.3 nm was found at 1μms^{-1} speed and 60 min polymerization time. Increasing speed reduced the light energy per unit area incident on the sample surface. Increasing speed causes a reduction in photo deprotection and hence a reduction in the grafting density in the subsequently grown brush. This reduction in grafting density causes a reduction in brush thickness. The line width and brush thickness reduces with higher speed of the piezo motor and minimum line width and brush thickness was found 0.45 ± 12 nm and 1.6 nm, at speed of 45 μms^{-1}, respectively.

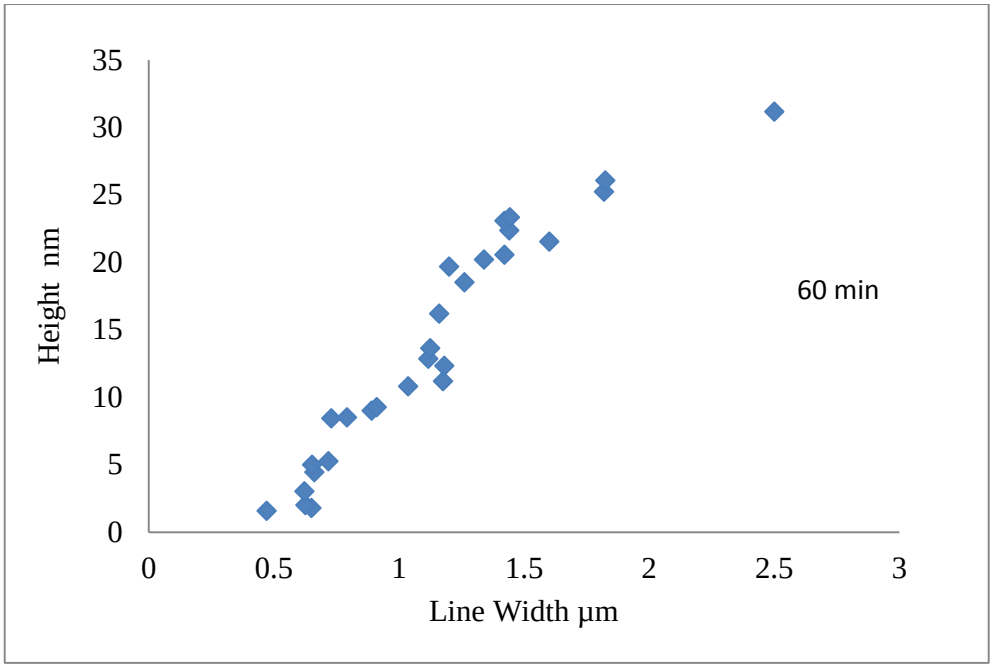

Fig. 3.12. Graph showing the maximum thickness of polymer brushes as a function of the line width. The line width with minimum thickness was obtained until the diffraction limit of the numerical aperture used was reached. All of the plotted data were acquired at 60 min polymerization time in the dry state.

Arbitrary pattern were fabricated after controlling the piezo motor x and y axis speed with LABVIEW software. All patterns were acquired at exposure power of 140 µW at polymerization time of 60 min.

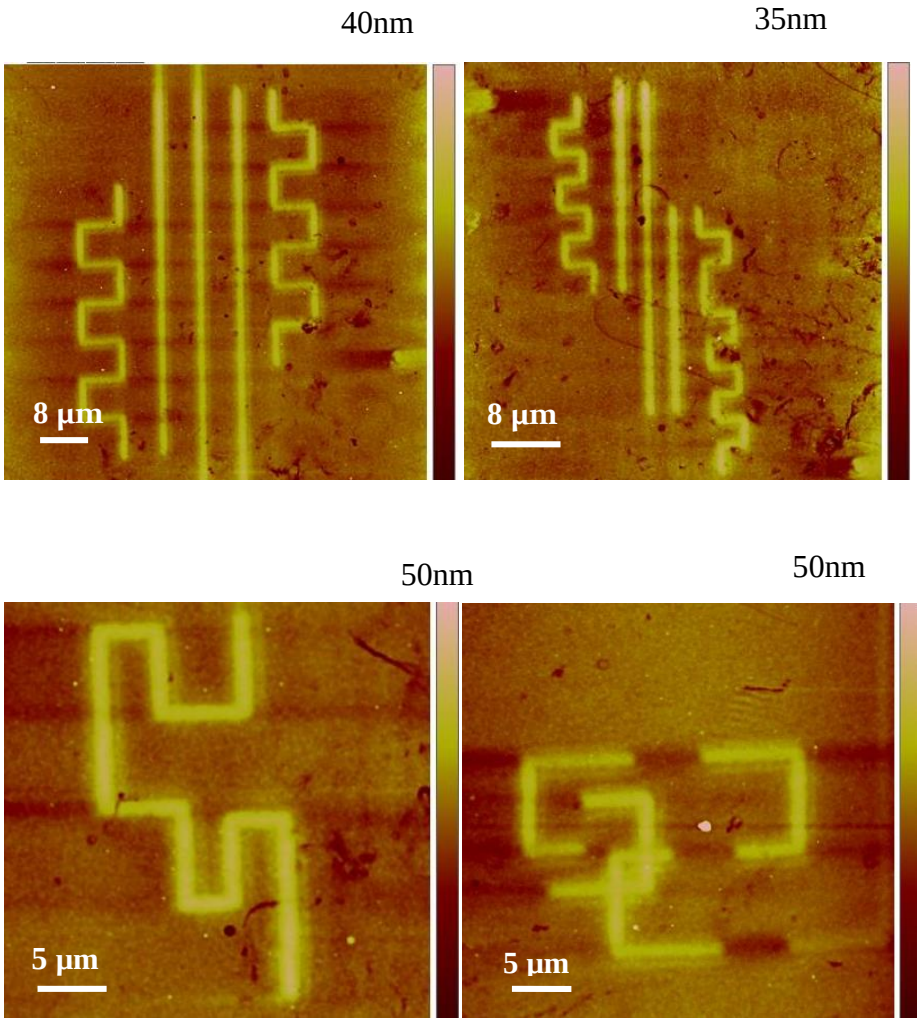

Fig. 3.13. Tapping mode images of arbitrary patterns obtained with the direct writing lithography setup.

3.3.3.2 Polymer bush thickness variation with speed in a dry state and good solvent

A diffraction limited spot was created with the maskless setup without the SLM and a Stationary spot was focused on selective areas of the sample to fabricate the line width. Multiple line widths were created on the same patterned area by controlling the piezo motor speed with LABVIEW software for each line. In this study, we investigated the PMPC bush thickness variation and grafting density at different speed, in a dry state and in a solvent, and at different polymerization times.

Polymer brush height on the underlying patterned structure depends upon the polymerization time. All patterned structures were obtained under the same experimental condition but with different polymerization time. Individual patterned structures were acquired at speed of (5, 25, 50, 71, 100, 125, 167, 250, and 500) μms^{-1} at laser power of 160 µW. Polymer brush height was characterized in the dry state by AFM as shown in Fig. 3.14 (a-d). To calculate the swollen grafted polymer brush thickness, polymer brushes were immersed in water for 24 hours. AFM height images were acquired under water and a series of topographic images at different polymerization time are shown in Fig 3.14 (e-h).

All tapping modes images show the polymer brush thickness at different polymerization time and thickness varies with the increase of speed (5, 25, 50, 71, 100, 125, 167, 250, and 500) μms^{-1} in each patterned structure. Fig. 3.14 (a-h) shows the decrease in polymer brush height with increase of speed in any individual pattern as well as patterns acquired at different polymerization times. This result clearly shows that height of the polymer brush can directly be controlled with exposure power. Height profiles shows that polymer brush conformation was strongly influenced by water solvent, approximately doubling its thickness compared to the dry condition. Similarly, a significant difference in the polymer brush thickness in the dry state as well as under a good solvent was obtained at polymerization times of 60 min at a speed of 1 μms^{-1} i.e., 32 and 73 nm in contrast to 15 min polymerization time with brush thickness of 8 nm and 16 nm, respectively.

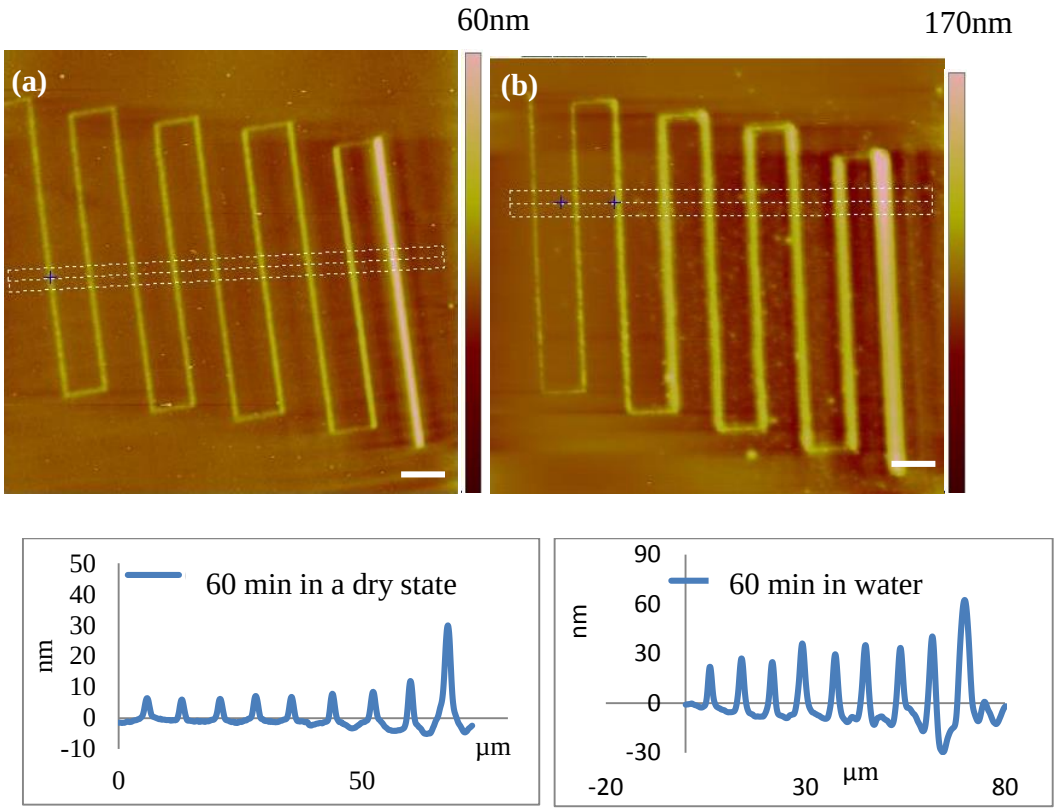
60nm
170nm
(a)
(b)
60 min in a dry state
nm
50
40
30
20
10
0
-10
0
50
µm
60 min in water
nm
90
60
30
0
-30
-20
30
80
µm

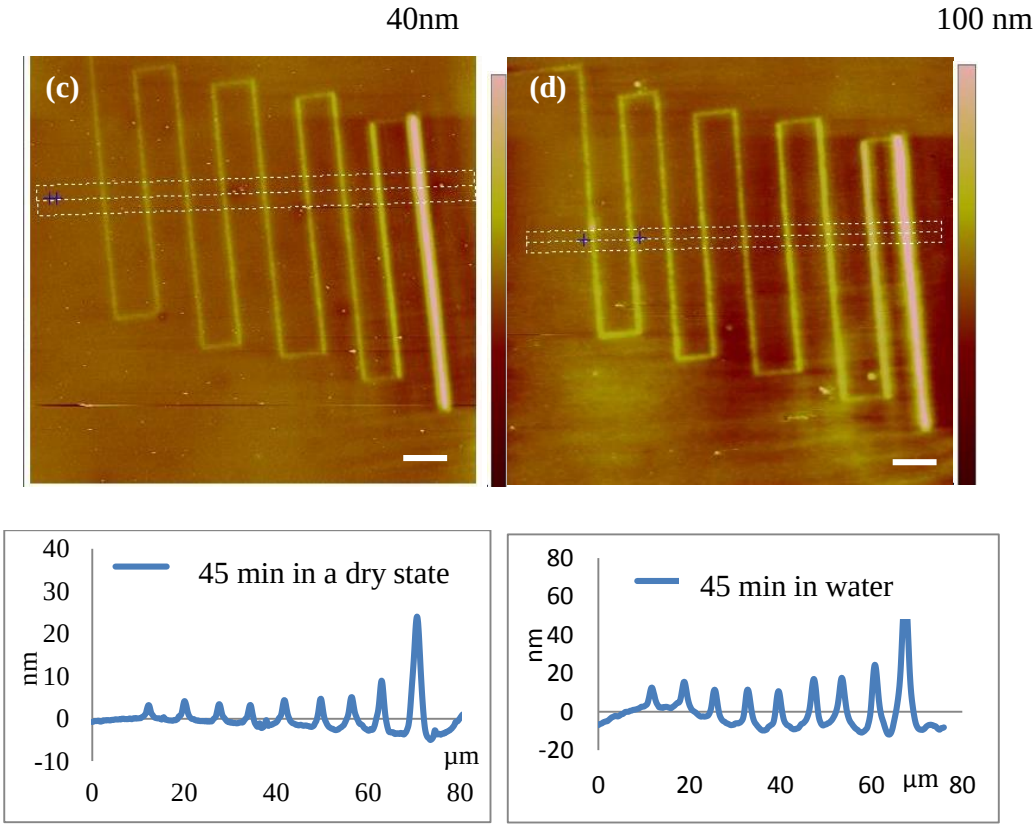
40nm
100 nm
(c)
(d)
45 min in a dry state
nm
40
30
20
10
0
-10
0
20
40
60
80
µm
45 min in water
nm
80
60
40
20
0
-20
0
20
40
60
µm
80

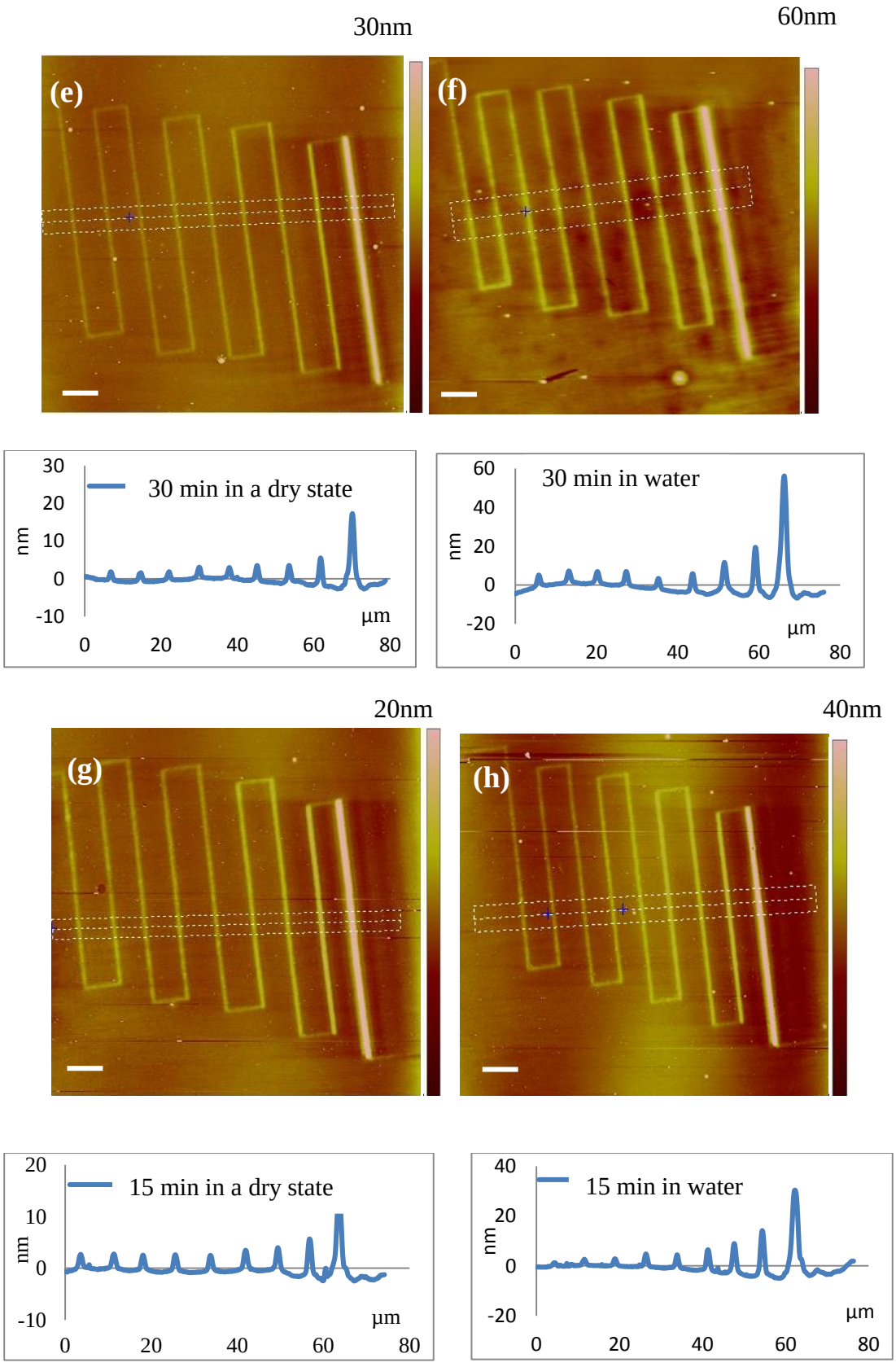

Fig. 3.14. (a-f (previous page), g-h) A series of AFM height images acquired in a dry state a1d under water and corresponding cross-section profiles showing the decrease of polymer thickness with polymerization time. Scale bar for all images are 5 µm. The colour bar represents the height variation.

Topography images show that polymer brush thickness varies with speed of the piezo motor in the dry state as well as in water. Reduction in thickness as a function of speed of the piezo motor indicates that grafting density directly depends upon the degree of amine reactive group after deprotection. These images (Fig. 3.14) show that as brush thickness decreases, polymer chains stand slightly farther apart from each other, thus getting more free volume per molecule which can then collapse the brush and fall laterally over the pattern surface [192].

Fig. 3.15 (a) shows a schematic representation of a polymer brush in the dry state, showing the decrease in brush height with decreasing density and further form a mushroom conformation [192,193]. The corresponding images of PMPC brushes under water are shown in Fig 3.15 (b). Water molecules solvate the brush, inducing a local solvent structure in which water molecules interact with individual MPC monomers and create a hydration sheet around the polymer chain that leads to a more extended polymer which is consistent with already reported studies [64].

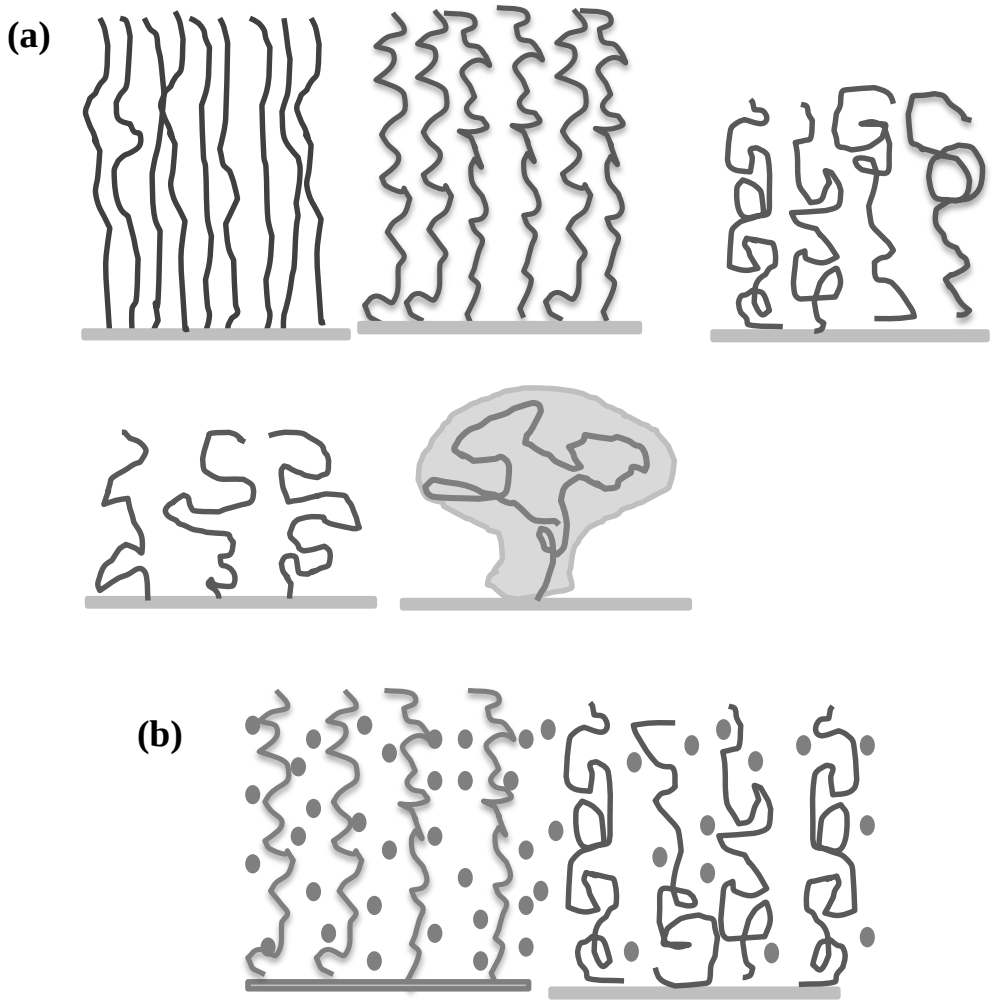

Fig. 3.15. Schematic representation of conformational changes of Poly MPC chains in dry state (a) and under water (b).

Fig. 3.16 graph data shows polymer brush thickness in the dry state and water at different polymerization time. These graphs describe the polymer thickness variation as a function of speed; thicker polymer brushes were observed at small speed and became thinner with an increase of speed. The almost double thickness was found at each speed under water in contrast to the dry state on the same pattern at one polymerization time. This behaviour was observed at all polymerization times.

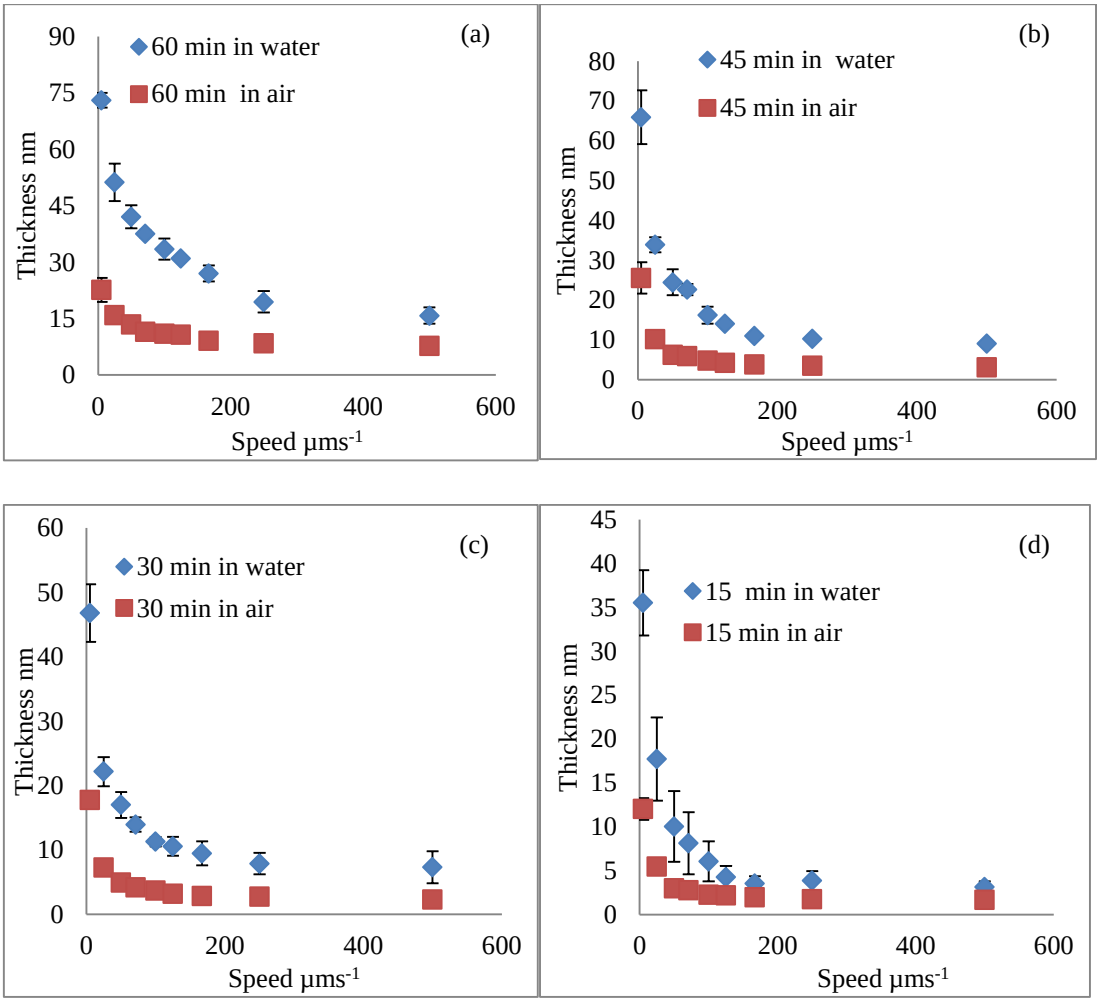

Fig. 3.16. Graphs showing brushes thickness as measured by AFM as a function of speed in the dry state and under water at polymerization times of (a) 60 min, (b) 45min, (c) 30 min, (d) 15 min.

The grafting density σ can be obtained from the following equation [64]

$$\sigma = (h_{dry}\, N_A \rho)/M_n \qquad (3.1)$$

where h_{dry} is the dry polymer brush thickness, ρ is the bulk density of the brush, M_n is the number average molecular weight which is equal to ($N.M_o$), N is the degree of polymerization

and M_o is the molecular weight of the polymer unit. N_A is Avogadro's number. The product ($N_A.\rho$) was kept constant in this experiment which makes the grafting density a function of h_{dry} /M_n [64].

The thickness of polymer brushes in good solvent can be described as

$$h_{(good)} = k\, N\, a^{2/5}\, \sigma^{1/3} \qquad (3.2)$$

where, $h_{(good)}$ is height of the polymer brush in solvent, N is the degree of polymerization, k is constant of proportionality and 'a' is the size of the monomer. The grafting density along with constant (σ/k) can be calculated by combining equation 3.1 and 3.2.

$$\frac{\sigma}{k} = \left(\frac{a^{2/5}\, N_A\, \rho}{M_o h_{(good)}/h_{dry}} \right)^{3/2} \qquad (3.3)$$

σ/k was calculated by plotting the $h_{(good)}$ as a function of h_{dry} at different polymerization time at constant speed (Fig. 3.17). Brush thickness increased almost linearly from 15 min to 45 min for all speed but then increased less rapidly from 45 to 60 min polymerization times. This change was greatest at higher speed.

Data acquired at the largest polymerization time on the sample area that had been exposed it at highest speed deviated from the trend shown by the rest of the data (Fig. 3.17). Specifically, linearity in the plots of h_{good} Vs h_{dry} was lost, we tentatively put this down to a change in 'brush' morphology possibly a transition from brushes to mushroom resulting in an increased probability in the more diffuse thickness or slow growth as the growing chain end is able to become entangled in the brush below. σ/k was acquired at polymerization times between 15 and 45 min by measuring the gradient of $h_{(good)}$ as a function of h_{dry} for nine different speed. σ/k of the PMPC polymer brushes could then be calculated by inserting the gradient ($h_{(good)}/h_{dry}$) into equation 3 and then normalized grafting density (σ/σ_{max}) was plotted as a function of the speed of the piezo motor as shown in Fig. 3.18. σ_{max} /k was acquired at maximum height of polymer brush.

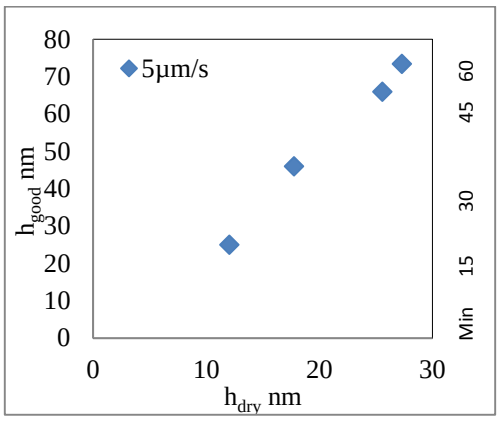
5µm/s
h good nm
h dry nm
Min

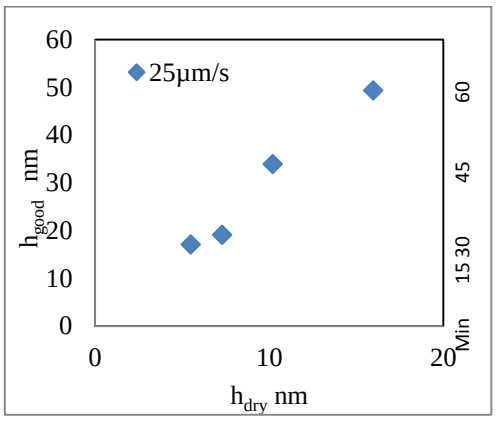
25µm/s
h good nm
h dry nm
Min

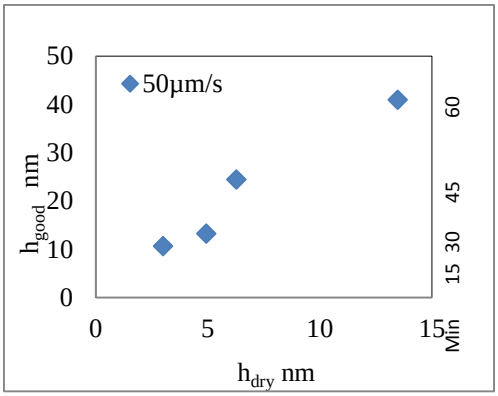
50µm/s
h good nm
h dry nm
Min

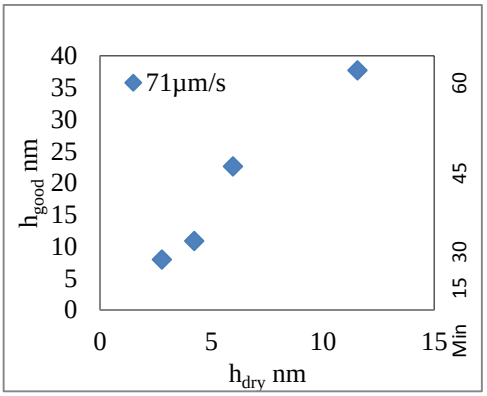
71µm/s
h good nm
h dry nm
Min

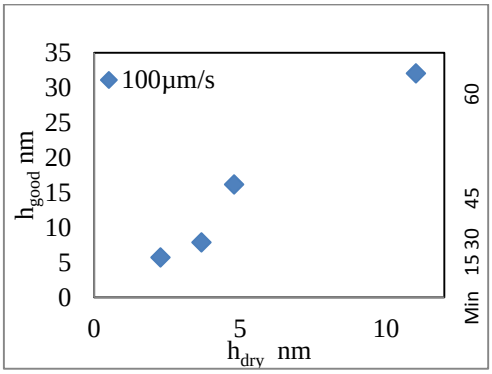
100µm/s
h good nm
h dry nm
Min

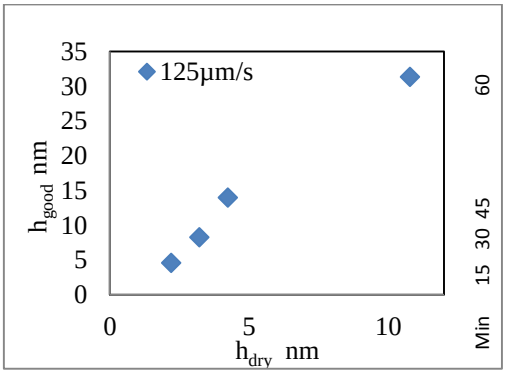
125µm/s
h good nm
h dry nm
Min

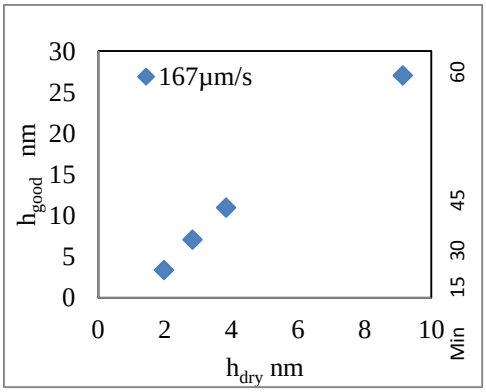
167µm/s
h good nm
h dry nm
Min

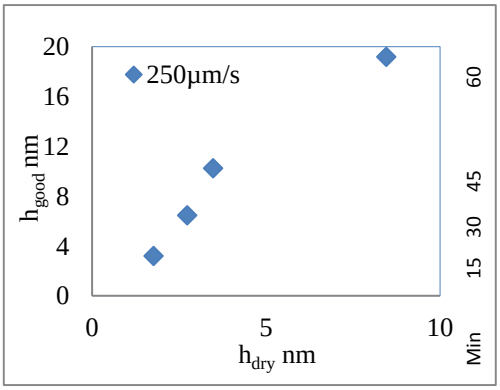
250µm/s
h good nm
h dry nm
Min

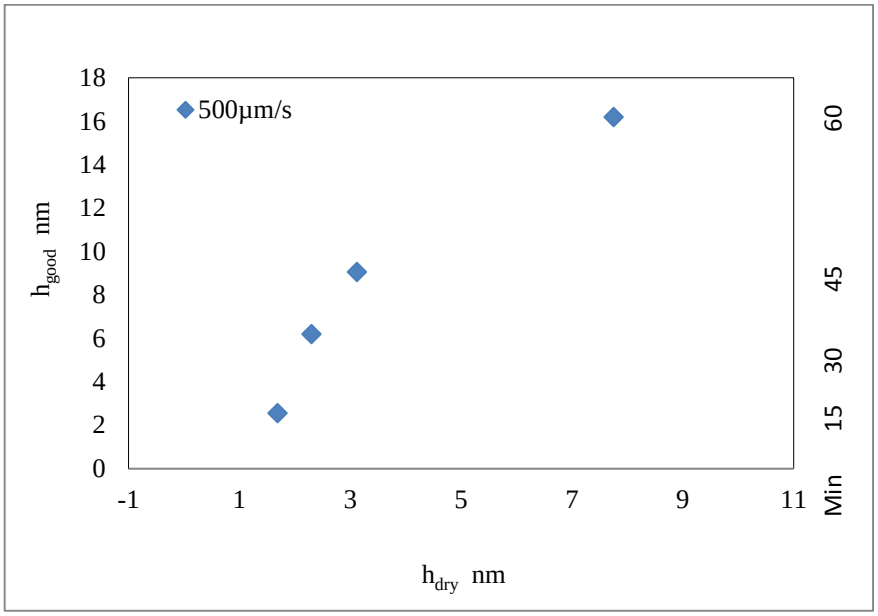

Fig. 3.17. (5-250 μms^{-1} (previous page) and 500 μms^{-1}) Polymer brush thickness in water plotted as a function of thickness in the dry state at different speed, different polymerization times are given on the right hand side.

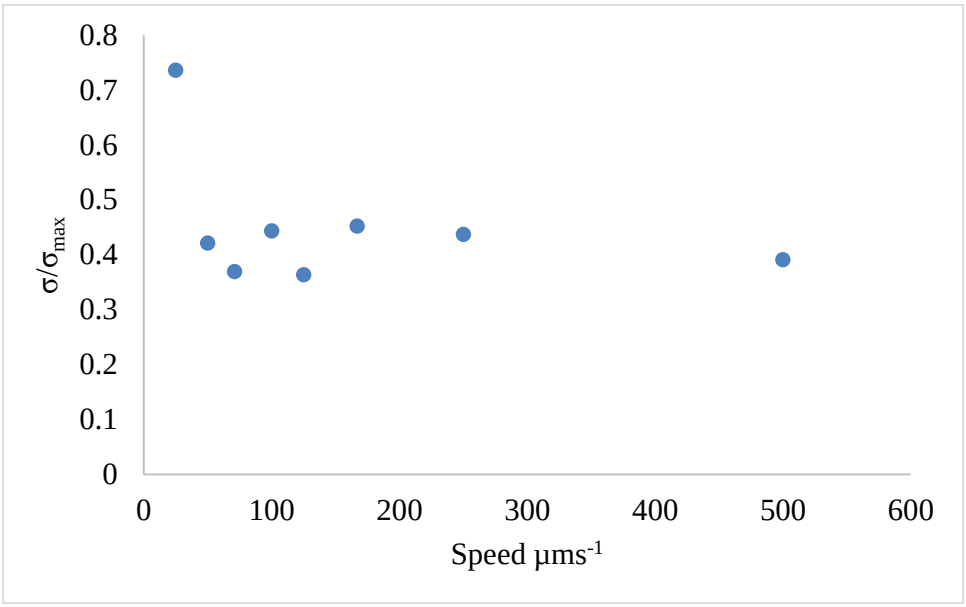

Fig. 3.18. Normalized grafting density (σ/σ_{max}) plotted as a function of speed of the piezo motor.

A continuous decrease in the normalized grafting density (σ/σmax) was observed below a speed of 71 μms^{-1} speed followed by a region of constant derived grafting density at higher speed. Experimental results suggested that polymer brushes are found in the higher grafting regime, found ($\sigma/k > 0.3\ nm^{-2}$) at 5 μms^{-1} and previous study also reported the dense brush with grafting density greater than 0.3 nm^{-2} [187,194]. However, normalized grafting density data at speed > 100 μms^{-1} does not show the consistent data. It is thought that at higher speed the polymer chains experience strong collapse and the collapse becomes less as the grafting density increase with lower speed of the piezo motor [194,195]. In this study, the mushroom plateau is not well understood due to inconsistent polymer thickness behaviour, we cannot draw exact conclusions about the brush-to-mushroom transition. However, the value obtained for grafting density (σ/k) at lower speed and the trend of decreasing density with increasing speed of the piezo motor and hence reduced exposure time are in good agreement with expectation. We suggest this process provides a simple approach for estimating relative grafting densities.

3.4 Maskless photolithography with a spatial light modulator and friction force microscopy

The diffraction limited spot was created by the spatial light modulator and focused stationary spot was used to fabricate the patterns on selective areas of NPPOC protected aminosiloxane monolayers by controlling the piezo motor speed with LABVIEW software. The patterned surfaces were characterized by friction force microscopy (FFM) but no patterned structures were found. Different exposure doses were used to acquire friction force data but due to poor contrast between UV deprotected and NPPOC protected regions, no successfully friction force data was acquired. However, the patterns were present on the surface as was confirmed by polymer brush growth data on UV deprotected regions. This is further discussed in next section.

3.4.1 Maskless photolithography with a spatial light modulator and polymer brush

Maskless photopatterns were fabricated with the stationary focused spot created by spatial light modulator on the selective areas of sample which was mounted on the piezo motor and the speed of the piezo motor was controlled with the LABVIEW software. Friction force microscopy (FFM) did not reveal any contrast between deprotected and NPPOC protected areas. In order to visualize the quality of the pattern, polymer brushes were grown on the deprotected areas and characterized by AFM in tapping mode in the dry state.

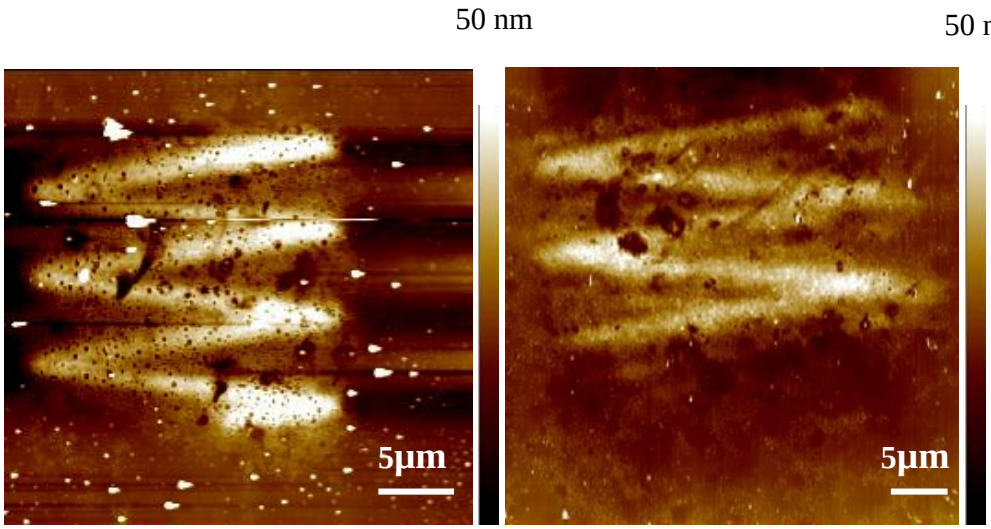

Fig. 3.19. AFM topography image of polymer brush.

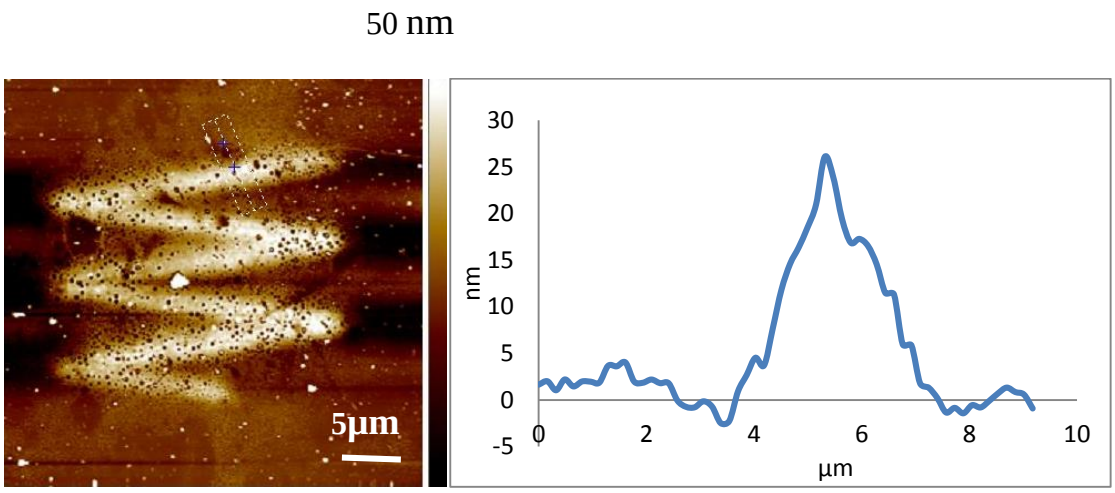

Fig. 3.20. Tapping mode height image and cross section profile of polymer brush on patterned deprotected areas.

It was found that patterns obtained with maskless far field photopatterning with the SLM had a broader structure at smaller speed, as shown in Fig 3.19 and 3.20. The line profile in Fig. 3.20 shows the non-uniform thickness of the polymer brush.

These micro structures were obtained successfully on different resist thicknesses but no clear and well defined patterned structures were obtained on the NPPOC protected siloxane monolayers. Laser power of 120 mW was used to create the diffraction limited spot by the

SLM and then used to create patterned structures on SAMS at a speed of 1 μms^{-1}. Moreover, it was not possible to obtain patterns at high speed due to less exposure energy per unit area because the SLM has a limitation of incident laser power, higher power may damage the SLM. The optical setup with the spatial light modulator requires further improvements, such as lower light wastage in the optical path after the SLM, or greater resistance to damage at high light intensities, if it is to be used in many applications.

3.5 Conclusion

In this study, two maskless photolithography experimental setups were characterized on NPPOC protected siloxane monolayers. Due to poor friction contrast it was not possible to acquire friction force microscopy data from samples prepared with maskless photolithography setups. However, we were able to fabricate patterned structures using a focused spot created with the maskless photo lithography setup without the SLM, and data obtained at different speed and different laser powers has been presented. A variation in line width was observed at different speed and exposure at polymerization time of 60 min in the dry state. The brush thickness was also vary with speed of the piezo motor and polymerization time. A significant difference was also observed in polymer brush thickness in the dry state compared to brushes that were measured in water. The case of patterning features with different exposure time using this methods allowed for the development of a simple approach for estimating grafting density and hence degree of polymerization. Maskless photolithography with SLM was also used to fabricate patterns on SAMs but it was found that the line width obtained was much broader compared to that achieved by maskless photolithography setup without the SLM. Using this simple optical setups, a robust methods for arbitrary chemically patterning a surface has been developed. Proof of principal has also been obtained for extending this to parallel writing though the use of a spatial light modulator. Further work to improve the optical setup with the spatial light modulator is required, however if it is to be used in many applications.

Chapter 4 - Atomic Force Microscope and the Peripheral Nervous System

4.1 Introduction

This chapter describes the topography and growth processing of two cell lines NG-108-15 neuronal cells and RN-22 Schwann cells as well as primary Schwann cells with AFM under live and fixed conditions.

The functioning of the peripheral nervous system requires connection between the neurons and the primary Schwann cells. The neurons extend into neurites (axon and dendrites) that contains sensory motile structures at their tips called growth cones which explore extracellular guidance cues through surface receptors for further development [196,197]. To study the topography and mechanical properties of neuronal cells and neurite outgrowth is important for understanding but also important for nerve re-generation after injury because nerve re-generation and controlling neurite outgrowth is one of greatest challenges in nerve engineering. Schwann cells are important players after nerve injury and they promote axonal regeneration and provide a favorable condition for neurite outgrowth towards a target location, moreover, much remains unclear about the interaction between the primary Schwann cells and neurites during growth.

The AFM has been used on many types of cells to determine the cell morphology precisely under fixed and physiological conditions, showing intracellular structure such as the cytoskeleton [198–201]. In the field of neuroscience, researchers have used AFM to study the peripheral nervous system which includes the neuron cell body, myelinated and demyelinated nerve fibres and synaptic vesicle [199,202–205]. But less consideration has been made to the Schwann cell and neurites (axons and dendrites) and the growth cone. Limited attempts have been made to explore them.

In this study, we have employed AFM imaging in tapping mode of three different types of cells, live primary Schwann cells, live and fixed RN-22 Schwann cells and fixed NG-108-15 neuronal cells to determine the topography of the cells and its growth pathways. We provide the first comprehensive topography of primary Schwann cells with AFM under physiological conditions. In addition, AFM images also provide the detailed filamentous structural organization of live RN-22 Schwann cell. We compare the topography of primary Schwann cells and RN-22 Schwann cells. We find that it is not possible to image live NG-108-15 neuronal cells due to poor substrate adhesion. AFM provides images of the fixed neuronal cells. The topography of small live neurites is also difficult to obtain as they are constantly

extending and retracting when probing or moving across a surface. AFM also provides the topography of the growth cone. The detailed study of all these cells may lead to a better understanding of peripheral nerve regeneration.

4.2 Material and Methods

4.2.1 Cell culture

Three different types of cells were cultivated. A mouse neuroblastoma and rat glioma hybrid NG-108-15 cell line was chosen because it has been well characterized previously [206]. RN-22 Schwann cells were purchased from the European Collection of the cell cultures. Primary Schwann cell harvest and culture was performed as elsewhere [207].

4.2.1.1 NG-108-15 and RN-22

Neuronal cells (NG-108-15) and RN-22 cells were cultivated in a T75 flask containing Dulbecco's 'modified Eagle's medium (DMEM, Biosera)) with 10% fetal calf serum (FCS), 100 μg ml^{-1} penicillin, 100 μg ml^{-1} streptomycin and 2 mM glutamine (Sigma) in a humidified incubator at 37° C. After 3-4 days incubation, cells were grown to approximately 70-80 % confluence. Then cells were centrifuged at 10000 rpm for 5 min and sub cultured in a T75 flask.

4.2.1.2 Substrate and sample preparation

The preparation of the substrate was important for supporting the function and survival of cells in vitro. The cover glass was sterilized with industrial methylated spirits (IMS) and phosphate-buffered saline (PBS). The NG-108-15 cells and RN-22 suspension was plated on 35 mm petri dish in serum free medium. Plated cells were placed in an incubator at 37° C in 5% CO_2 for 24 hours so that cells can attach and begin to process.

4.2.2 Cell fixation

NG-108-15 cells were fixed before imaging with atomic force microscopy (AFM). Cells were fixed by adding 4% para-formaldehyde (PFA) with PBS for 20 min. After fixation, plated cells were washed 3 x with PBS then imaged with AFM.

4.2.2.1 Primary Schwann cell

Primary Schwann cells were cultured on poly(l-lysine) coated T75 flasks containing growth medium of Dulbecco's modified Eagle's medium DMEM (PAA, UK), with 10% fetal calf

serum (FCS), 2 mM glutamine, 1% N_2 supplement (Gibco BRL, UK), 5 µM forskolin (Sigma, UK), 20 µg/mL bovine pituitary extract, penicillin/100µg/mL streptomycin at 37^0 C in a 5 % CO_2 humidified atmosphere.

4.2.2.2 Substrate and Sample preparation

The preparation of the substrate was important to facilitate cell attachment, growth, cell spreading and cell motility in vitro. 0.5 µg/ml poly(l-lysine) (PLL; Sigma-Aldrich) was coated on 35 mm petri dish to enhance the electrostatic interaction between the positively charged surface ions and the plasma membrane's negatively charged ions. The primary Schwann cells suspension was seeded on the poly(l-lysine) coated petri dish in culture medium. Plated primary Schwann cells were placed in the incubator at 37^0 C in 5% CO_2 for 24 hours prior to AFM imaging.

4.3 Atomic force microscopy

Cell imaging was carried out with an MFP-3D (Asylum Research), integrated with an inverted optical microscope. Tapping mode AFM in a culture medium was performed with commercial silicon nitride probes. The cantilever was V-shaped, 0.8 µm thick, 200 µm long and had a spring constant 0.06-0.32 Nm^{-1}. The tip was triangular in shape with nominal radius of curvature of 20-60 nm. For AFM imaging, fixed NG-108-15 neuronal cells and fixed Rn-22 Schwann cells on the cover glass slip were mounted on a 10 cm plastic cover slip with super glue. The small glass cover slip was filled with PBS and the cantilever tip was lowered manually until the tip approaches the cell surface in liquid. Similarly petri dishes with live primary Schwann cells or live RN-22 Schwann cells were directly placed under the AFM head and the cells were directly seen with an inverted optical microscope with 40x or 10x objectives. Laser alignment was again adjusted and the cantilever resonance frequency was determined from the thermal power spectral density. The drive voltage was adjusted to attain free amplitude of 0.5-0.65 V_{rms}. The scan rate was adjusted between 0.1-0.5 Hz to obtain good quality images. The set-point was also adjusted to maintain the minimum force on the sample surface. Images were captured at speed of 7-12 μms^{-1} at 256 x 256 pixels. Control parameters were further optimized to image live nerve cells and Schwann cells.

4.4 Results

Primary Schwann cells were imaged in tapping mode after 24 hours of culture on a poly(l-lysine) coated polystyrene petri dish. Fig. 4.1 shows the spindle shape morphology of a primary Schwann cell. The spindle shape cell body has 2.5-12 micron height with a long

thread like extension on the order of several hundred micrometres in length. Optical images of a primary Schwann cell (Fig. 4.1 (c-d)) shows the same morphology as acquired by AFM.

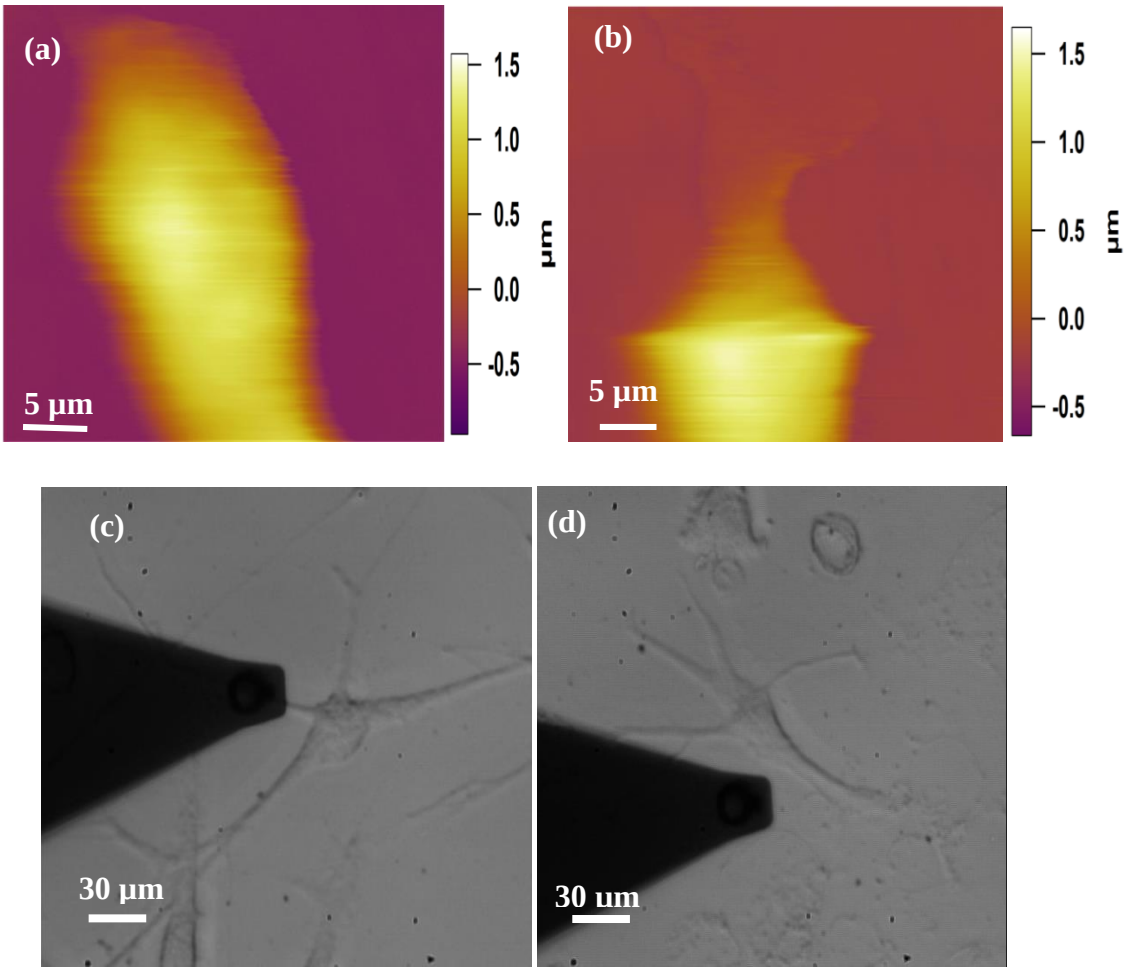

Fig. 4.1. (a & b) AFM tapping mode images of live primary Schwann cells obtained in culture medium at room temperature. (c-d) Optical images of primary Schwann cells.

Fig. 4.2 (a) shows a rod-like structure extending from the cell body with diameter of ~ 10 µm and height of ~ 350 nm. This thin rod like structure further spreads as a thin sheet. The length of the thin sheet is around 10 µm in the lateral direction. Later on, the thin, uniform flat membrane moves towards the leading edge of the cell. The black square region also shows non-uniform thickness that becomes thinner towards the cell leading edge. The line profile (4.2 (a)) shows the height of the rod like structure.

Fig. 4.2 (b) shows the thin membrane protrusion at one end and thick structure at the other end and also shows two threadlike filaments running parallel to each other providing information about the cell extension. The cross-section along the scan line in Fig. 4.2 (b) shows a height difference of 30-100 nm between the thin membrane protrusion and thick

edge. Fig. 4.2 (b) also shows two threads like filaments about 100 nm wide and 2-5 µm long. Both the thin filaments run parallel to each other and provide the pathway for further membrane protrusion. Fig. 4.2 (e & f) shows rod like structures extending from the cell body up to 10s of microns.

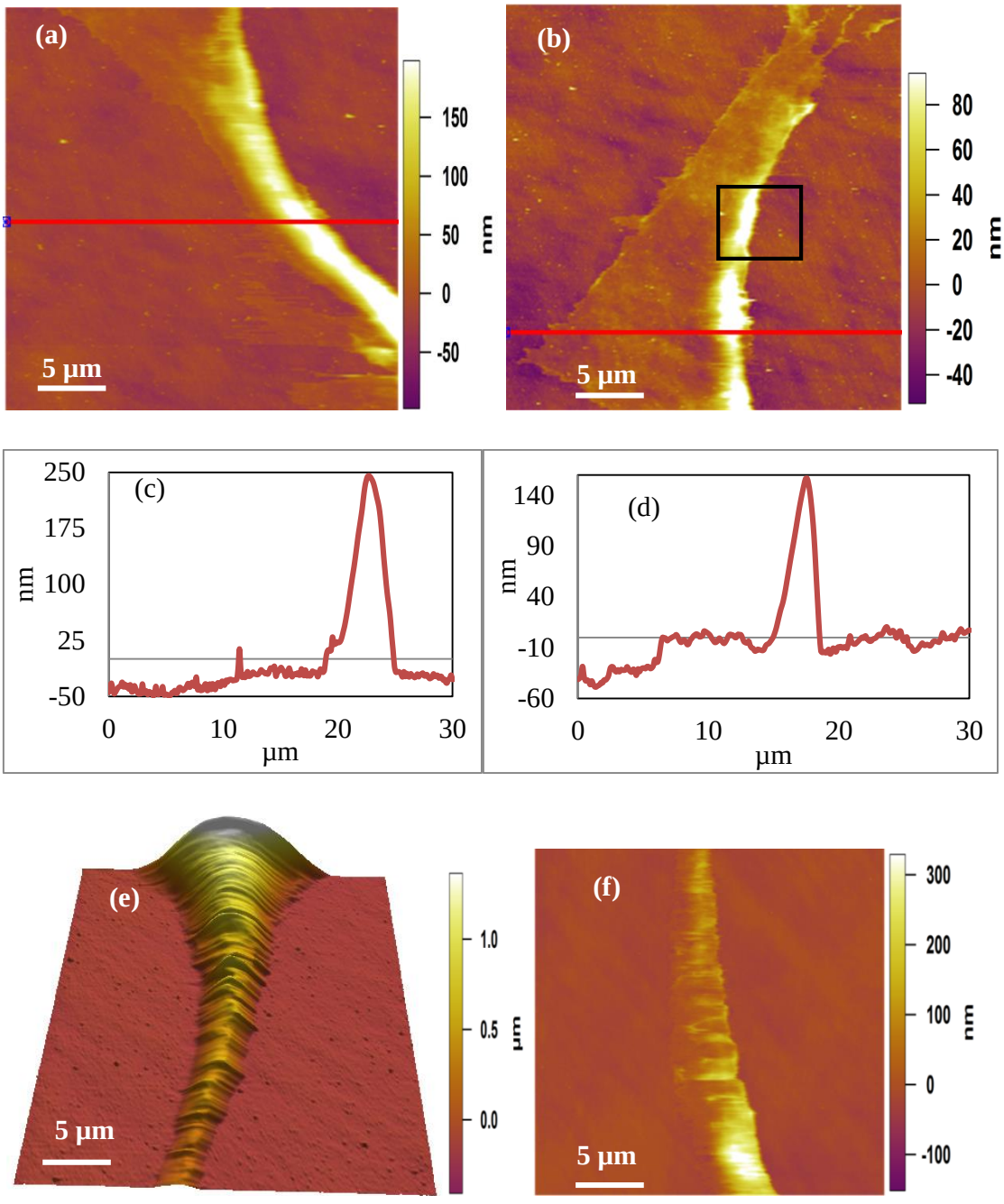

Fig. 4.2. (a-b) Tapping mode images of a live primary Schwann cell, (c-d) the cross section along the scan line shows a rod like structure and the height difference between the thick and thin membrane protrusion, respectively. (e & f) Show the 3D and 2D topography of a thin rod like structure extending from a primary Schwann cell body.

Fig. 4.3 (a) is an example of a primary Schwann cell extension from the cell body showing the filamentous structures with a big bump at one side and thin membrane at the other edge. This thin membrane protrusion growth appears in an arc shaped path with the same thickness as a leading edge. The cross section along the scan line shows a height difference between the thick and thin arc structure (Fig. 4.3 (b)) which is pointed by black arrowhead. Fig. 4.3 (c) is a software zoom of the area marked by a white square showing the membrane protrusion as a thin thread like structure with diameter 100-200 nm.

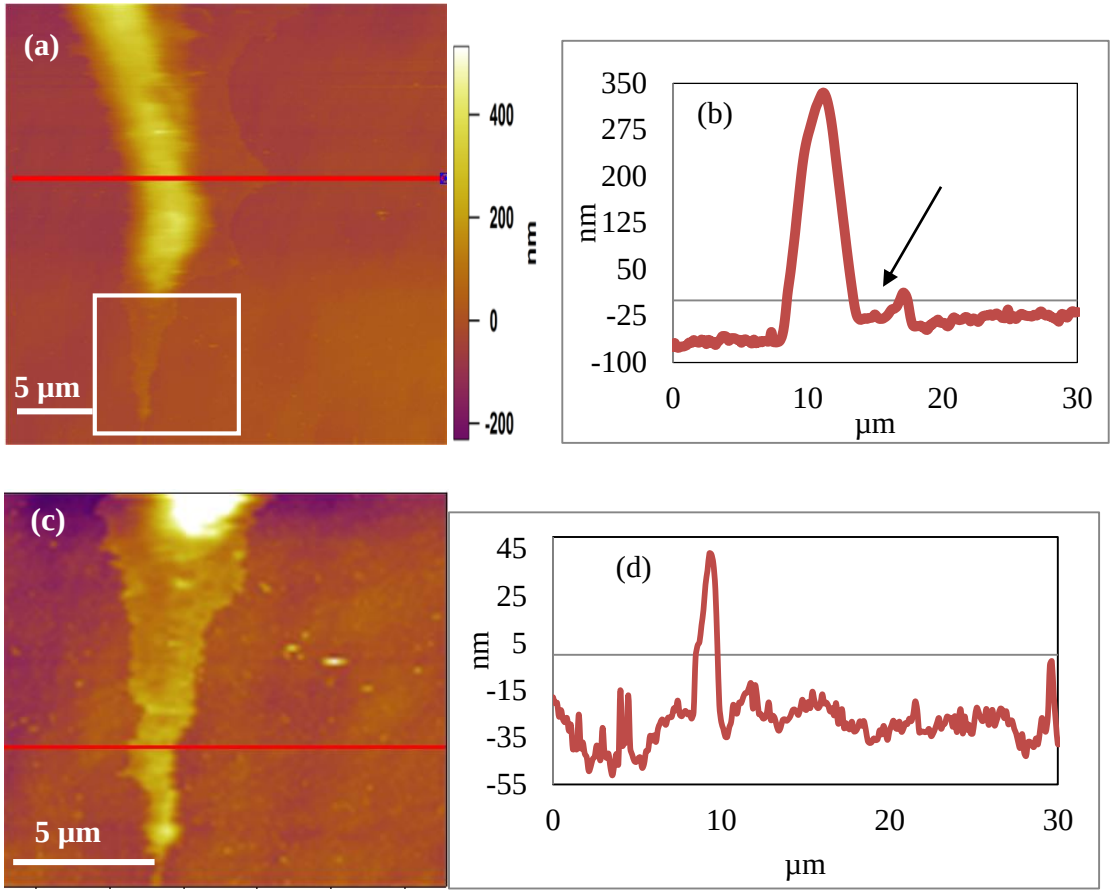

Fig. 4.3. (a) Tapping mode images of a live primary Schwann cell, (b) the cross section along the scan line shows a height difference between the big bump and thin structure. Arrowhead indicates the thin membrane protrusion. (c) A zoomed area of (a) indicated by the white square, and the height profile (d) of leading edge is consistent with the profile (b) at the point indicated by the arrowhead.

To make a comparison with primary Schwann cells topography, RN-22 Schwann cells were also imaged with AFM under fixed and live conditions. Fig. 4.4 (a) shows the live RN-22 Schwann cell body with extended thin filamentous structure up to 30-40 µm wide and 15-35 µm long. Numerous thin filaments of approximately the same length scale are also visible

along with thick filaments in Fig. 4.4 (b). The height and diameter of the thin filaments are on the order of hundreds of nm. Fig. 4.4 (c and d) show a cell extension path way that is somewhat different form Fig. 4.4 (a and b). The cell spreads like a single thick filamentous structure rather than thin parallel and randomly oriented filaments. Optical images of RN-22 Schwann cells are shown in Fig. 4.4 (e-f). AFM images provide the detailed filaments structures in contrast to optical images.

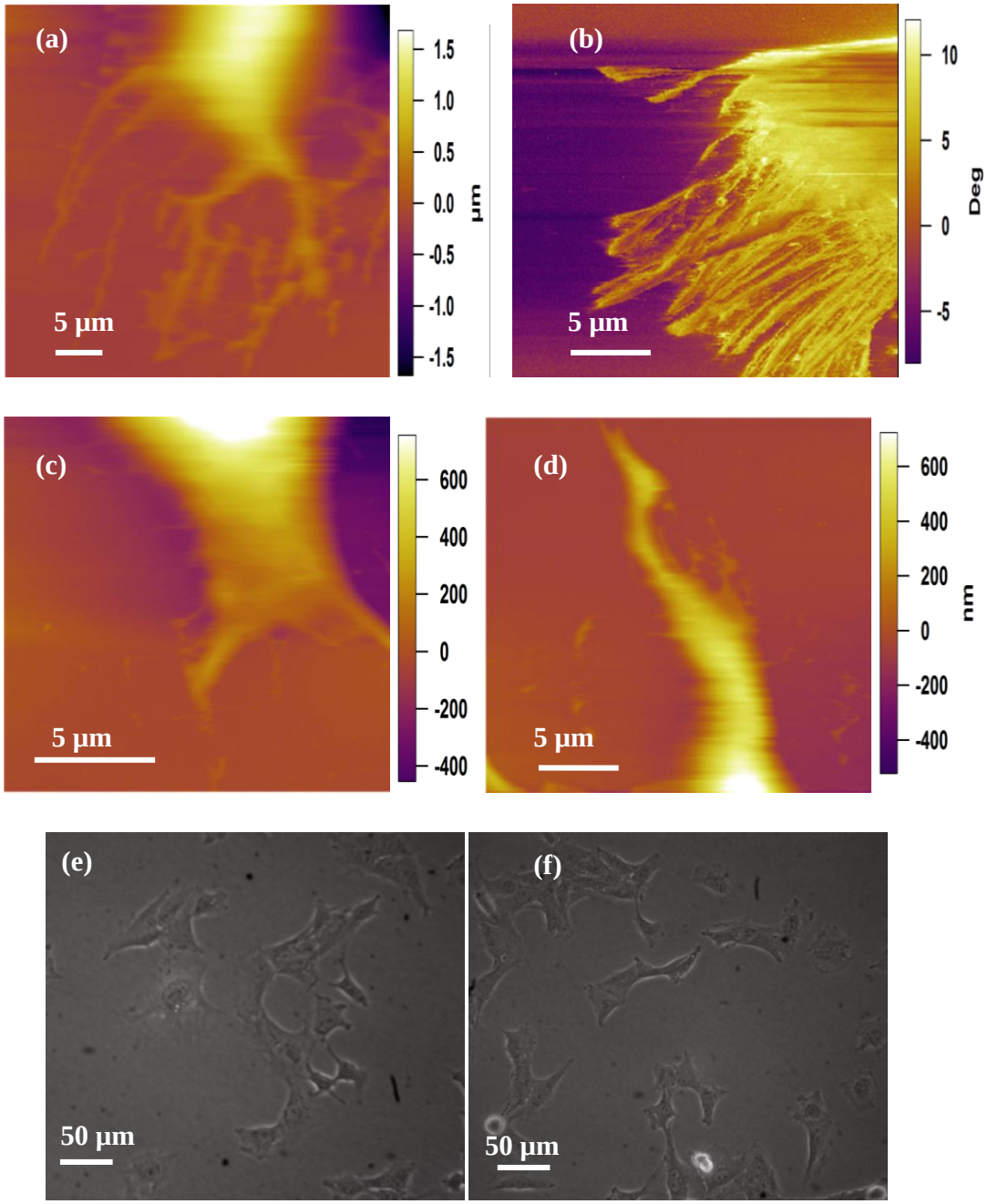

Fig. 4.4. (a, c-d) Tapping mode height images of live RN-22 Schwann cells, (b) shows a phase image of a live RN-22 Schwann cell. (e-f) Optical images of RN-22 Schwann cells.

Tapping mode height images of fixed RN-22 Schwann cells were recorded under phosphate-buffered saline (PBS). Fig. 4.5 (a) shows a tapping mode height image of a fixed RN-22 Schwann cell. The area marked by an arrowhead is further zoomed by hardware to resolve the cytoskeletal structures enclosed in the plasma membrane (Fig. 4.5 (b)). The cell edges have a diameter of 1.3 µm and height of 160 nm. The thickness and spacing between first the two filaments are 1 µm and 1.5 µm respectively. Fig. 4.5 (c) show a phase images of a fixed Rn-22 Schwann cell clearly resolving the nucleus and cytoskeletal structures and Fig. 4.5 (d) shows the cell body and some hint of the cytoskeletal structure.

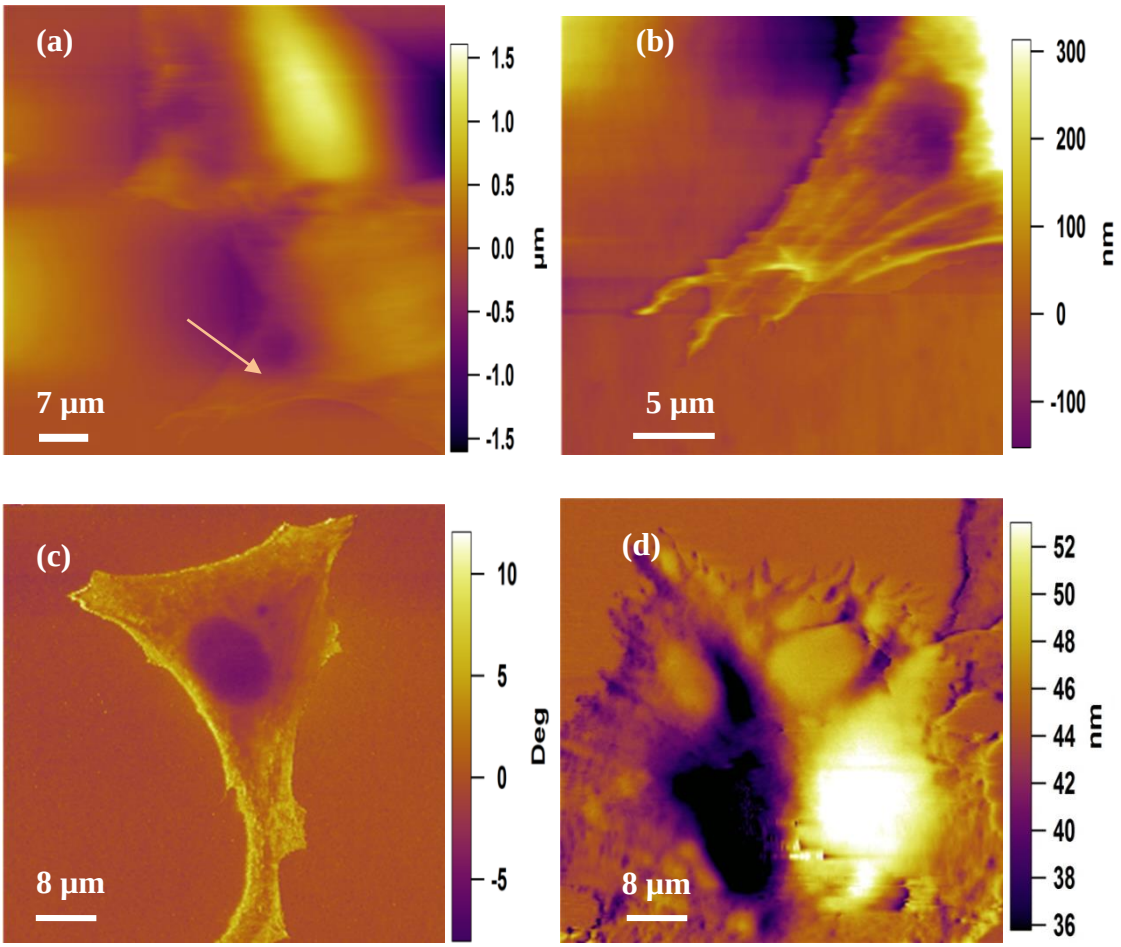

Fig. 4.5. (a & b) illustrates fixed RN-22 Schwann cell topographic images,(b) is a zoom area of (a) in the cell indicated by the arrowhead, (c) phase image of a fixed RN-22 Schwann cell and (d) an amplitude image of a fixed RN-22 Schwann cell.

It was not possible to image live NG-108-15 neuronal cells due to poor substrate adhesion. The tip drags the cells and the cells lose their contact-point during each scan and finally the tip pulls it from the substrate. Fig. 4.6 (a) shows the live neuronal cell tapping mode height image. No stable image is visible. Fig. 4.6 (b) is the AFM amplitude image of a fixed NG-

108-15 neuronal cell revealing the dome shape of the cell body with a height range of 8-15 µm. In addition, the neuronal cells display a highly complex organized filamentous neurite structure at the edges [124,203,208,209]. A software zoom of Fig 4.6 (b) provides the topography information of cell spreading in Fig. 4.6 (c & d) showing the bump and brush like structures at its edges. In Fig. 4.6 (c), the bumpy structure is 6 µm wide with a height of 800 nm and the height of the brush like filamentous structure (Fig 4.6 (d)) is 400 nm with a width of 4 µm at edges.

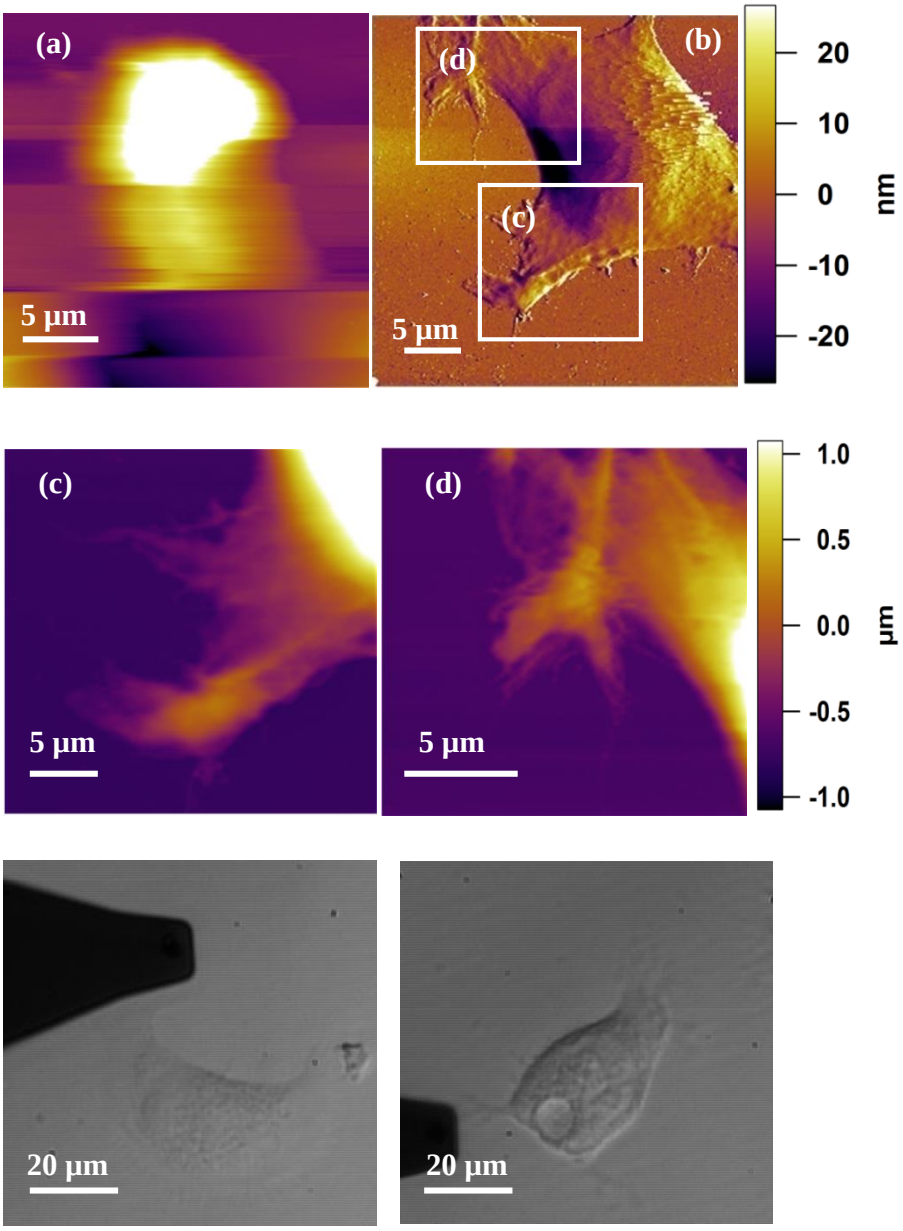

Fig. 4.6. (a) Tapping mode height image of a live NG-108-15 neuronal cell, (b) an amplitude image of fixed neuronal cell shows the membrane protrusion at the cell edges, (c & d) height images (zoomed area of white squares in (b) reveal the brush like branched filaments and bumpy structures of the cell membrane protrusion.

An example of the NG-108-15 neuronal cells (Fig. 4.7 (a)) that shows cell extension in the form of a thin sheet at its edges which is 13 µm wide and 325 nm high. A software zoomed area of Fig 4.7 (a) pointed out by the arrowhead provides the cell spreading information in Fig. 4.7 (b). Fig. 4.7 (c) presents an AFM image of the neuronal cell along with detailed structural organization of the neurites and the growth cone. At one end of the cell (marked with a white square), a single neurite splits into two branches. At the other end of the cell edge, thick neurites further extend on a small neurite at one side and form a growth cone (marked with a red square). At its leading edge the growth cone is composed of the filamentous structures, with a thick central region. Three filaments have different length, one on the order of 3 µm, the other on the order of 1 µm and the third one a few hundred nanometres. The central region of the growth cone is of non-uniform in appearance and has a maximum height of 360 nm.

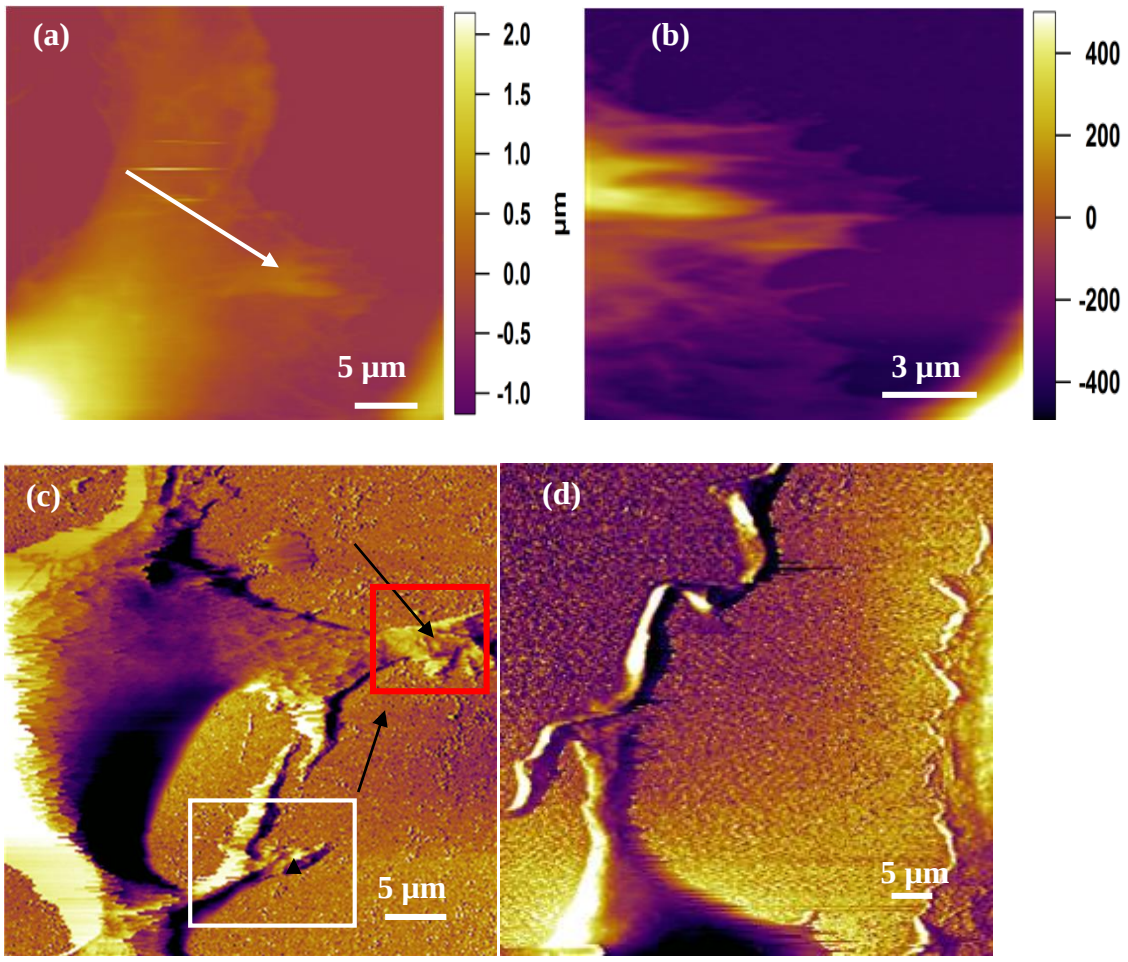

Fig. 4.7. (a) Tapping mode height image of the NG-108-15 neuronal cells edges. (b) Zoom region marked by white arrowhead shows the cell spreading. (c) Illustrates the formation of

multiple neurites at the cell edges and the growth cone at one end of the neurite that leads to the cell spreading and (d) shows the branch structure of wiggly neurite

4.5 Discussion

In this study, topography and the growth pathway of three different cells were imaged with AFM. This AFM study provides the first detailed topography and cell membrane protrusion pathway for primary Schwann cells. Tapping mode images show live primary Schwann cell growth development at the nanometre-scale. These data provide additional detail beyond confocal and optical microscopy [119,210]. Tapping mode images indicate that the AFM tip does not affect the cell and its growth as shown in Fig. 2 (b) and 4.3 (c). Knowing the time frame of the cell viability at room temperature, the experiment is performed within 5-6 hours before the cell loses its contact with the poly(l-lysine) substrate. AFM images of live RN-22 Schwann cells reveal the variation in the cell morphology. Some of them were round shape with thin and long filaments, a few having a thick filaments structure. AFM images reveal the cytoskeletal internal structure enclosed in the plasma membrane as shown in Fig. 4.4 (a-b). Significant difference was observed in morphology and cell extension between live primary Schwann cells and RN-22 Schwann cell. All the primary Schwann cell images show a spindle shaped cell body but RN-22 Schwann cells show variation in cell body topography. The primary Schwann cell usually spread like a spindle shape cell body with bipolar or tri-polar neurite in contrast to RN-22 Schwann cells. Thin membrane protrusion at leading edges of the primary Schwann cell suggested lamellipodia formation which is actin rich filaments are in a good agreement with fish keratocyte lamellipodium [211]. Similarly, comparison was also made between live and fixed RN-22 Schwann cells; chemically fixed Rn-22 Schwann cells have clear analogy with the live cells except for the cell membrane. In live cells, the membrane is very thin and tip can interact with the structure below the membrane and reveals the filament structure underneath the membrane but in chemically fixed cells the membrane became stiff and it was difficult to resolve detailed information of the cytoskeleton except at the edges of cells.

AFM images of NG-108-15 neuronal cells comprised of two main regions, the cell body and neurites (dendrites and axon) that is consistent with that seen with optical microscopy and previously existing AFM data [127,203,205,212]. Tapping mode images were acquired from fixed NG-108-15 neuronal cells because live images of NG-108-15 neuronal cells were not possible to obtain due to poor cell substrate attachment. Fixed NG-108-15 neuronal cells provide information about the cells topography along with neurites (axons and dendrites).

Fig. 4.6 (d)) show the cell extension in the form of a ‘brush’ in contrast to neurite extension (Fig. 4.7 (c)) where the growth cone of extending the neurite explorer the local environment [127].

4.6 Conclusion

In this chapter, AFM tapping mode images revealed the topography of live primary Schwann cells and RN-22 Schwann cells and its cell path ways. To our knowledge, these were first AFM images of primary Schwann cells and RN-22 Schwann cells, both had different morphology. Comparison was made between of live primary Schwann cells and live RN-22 cells as well as live and fixed RN-22 cells. Similarly, NG-108-15 neuronal cells were also imaged with AFM. It was not possible to image the live NG-108-15 neuronal cells with AFM due to poor substrate adhesion and fixed neuronal cells provided the information about topography, neurites and the growth cone. The topography of NG-108-15 neuronal cell is the same as described earlier [213] but the cell extension, neurite and growth cones path ways was imaged for the first time with AFM showing the different morphological changes in the cell topography during different stages. The neuronal cells change morphology in different stages as described in chapter 1 (section 1.9.2) which are consistent with experimental data obtained with AFM and already existing findings observed with optical and confocal microscopy [208,214].

Chapter 5 – Nano- and Micromechanical Properties of primary Schwann cells and Neuronal Cells with Atomic Force Microscopy

5.1 Introduction

This chapter describes the investigation of the mechanical properties of the peripheral nervous system with AFM. In this study, two different probes, colloidal and sharp probes, were used to measure the mechanical properties of primary Schwann cells, neuronal cells and growth cones, and sharp probes were used to describe the properties of neurites.

Neuronal cells are the most complex and intricate cells in the body. This cell complexity makes it difficult to obtain a detailed structural understanding, either in terms of the growth cone or neurite outgrowth. Neurite outgrowth is a complex process because it involves interaction through surface receptors with the extracellular inhomogeneous environment for the detection of guidance cues towards the appropriate location [196,197]. Chemical and mechanical interaction plays a potential role for neurite outgrowth. Researchers have also made extensive efforts to design various micro patterns for nerve guidance cues. They have investigated the chemically modified patterned surface and how that influences neuronal adhesion in vitro. Various micro-patterning techniques have been employed to study the growth cone extension along with neurite (axon and dendrite) extension in vitro [124].

When nerve injury has occurred, the distal end of the injured axon sprouts into regenerating units. The distal end of the axon sprout unit has a growth cone that consists of actin rich filopodia. The tip of these filopodia explores the environment and retracts back into the growth cone body if they make no contact with primary Schwann cells. By contrast, if the filopodia tip makes contact with primary Schwann cells then the entire growth cone advances into a column pathway provided by Schwann cell organization. The number of Schwann cells and their state is strictly controlled by the axon both during development and following repair [210].

The AFM is a potential tool for nano- and micro-mechanical measurement. AFM has been applied to different cells to determine the elastic modulus of fixed and live cells under different conditions. In the area of the nervous system, the majority of AFM researchers have focused on the topography of the cell body of dorsal root ganglion (DRG) neurons,chicken embryo spinal cord neurons and hippocampal neurons under fixed and live condition [199,203,205,208]. Moreover, some researchers have paid attention to the topography of sub cellular features of the growth cone and have described the detailed topography of fixed

growth cones at various stage during axon extension [215]. AFM studies have also revealed the mechanical properties of growth cones [108,204,216,217] and myelinated and de-myelinated axons [218]. Recently, the elasticity of NG-108-15 neuronal cell growth cones have been investigated with a modified the Hertz model [219]. But limited attention has been focused on the mechanical properties of the peripheral nervous system such as primary Schwann cells, neuronal cells and its corresponding growth cones and neurites.

In this chapter, we describe details of the experimental method and the Hertz model that is used to analyze the force curve data acquired through two different probes i.e., sharp and colloidal probes over neuronal cells, neurites and growth cones to investigate the local and average elasticity, respectively.

5. 2 Method and Material

5.2.1 AFM indentation measurements

AFM experiments were performed with an MFP-3D (Asylum Research), integrated with an inverted optical microscope that was used to visually position the AFM cantilever with respect to the cell. Two different type of force measurement were made: micrometre-scale and nanometre-scale measurement were employed on live primary Schwann cells, live NG-108-15 neuronal cells and growth cones and nanometre-scale measurements were carried out on neurites. For nanometre-scale measurements, triangular tips with a nominal tip radius of 20-60 nm on a V shape 200 µm long silicon nitride cantilever with a nominal spring constant of 0.02 Nm^{-1} was used. For micrometre-scale measurement, colloidal probes were made by gluing polystyrene beads onto the back of triangular tips on V shaped silicon nitride cantilevers. Bead fixation was carried out with the help of an inverted optical microscope. The cantilever was mounted into the cantilever holder of the MFP-3D. A small amount of glue (UV curable Norland optical adhesive) was placed on a glass slide and placed under the microscope stage. The cantilever was carefully lowered onto the UV curable glue until a slight cantilever deflection was observed in the S & D meter. Next, the glue slide was replaced with a slide onto which spheres had been deposited. Using the bottom view optic (40x objective) the cantilever was positioned carefully on top of a single bead and the head lowered to make contact. Once the cantilever made contact with the bead, the cantilever was withdrawn. Following this, the cantilever was exposed to UV light (λ = 365 nm) for 5 min to cure the glue and secure the bead.

AFM measurements were based on recording the elastic response of the cell by using AFM tips as either a colloidal or nano probes. Force-displacement curves were recorded on the cell body of live primary Schwann cells and live NG-108-15 cells, the growth cone and at different regions of the neurites. To obtain a constant and precise maximum applied force, a maximum tip deflection value (trigger value) was set. The detectors provided deflection values in volts. However, to obtain the cantilever tip deflection in the length unit, i.e., nanometre, the optical lever system had to be calibrated for a given cantilever tip. For such calibration, force-displacement curves were acquired with the same cantilever on hard poly(l-ysine) coated petri dish surfaces, which are considered as an infinitely stiff sample surface. The resulting contact region slope provides the inverse optical lever sensitivity of the cantilever (InVOLS). The InVOLS converts the cantilever deflection from the photodiode voltage to nanometres of displacement. The InVOLS value was further used to correct the force curve experimental data to acquire the force-indentation data. The force-displacement curves were recorded at the same the trigger deflection (20 nm) which corresponds to approximately 220-290 pN force for the nanometre indentation and micrometre indentation experiments. The cells topography and the elastic modulus were determined from force-volume maps acquired by collecting force-indentation curves in a grid pattern over the sample surface.

5.2.2 Data acquisition and analysis

To determine the cell elasticity, the AFM was operated in force-volume mode allowing force-distance curves to be collected on a grid pattern. All force curve data was recorded at the same force curve frequency of 1 Hz.

Force displacement curves were changed into force indentation curves by subtracting the cantilever deflection from the piezo displacement. All force-indentation curves were analyzed using the ARgyle™ software [220]. The force-versus-indentation curves describe the cell mechanical response to the applied load, Fig. 5.1 shows a schematic representation of indentation experiments for sharp and colloidal probes.

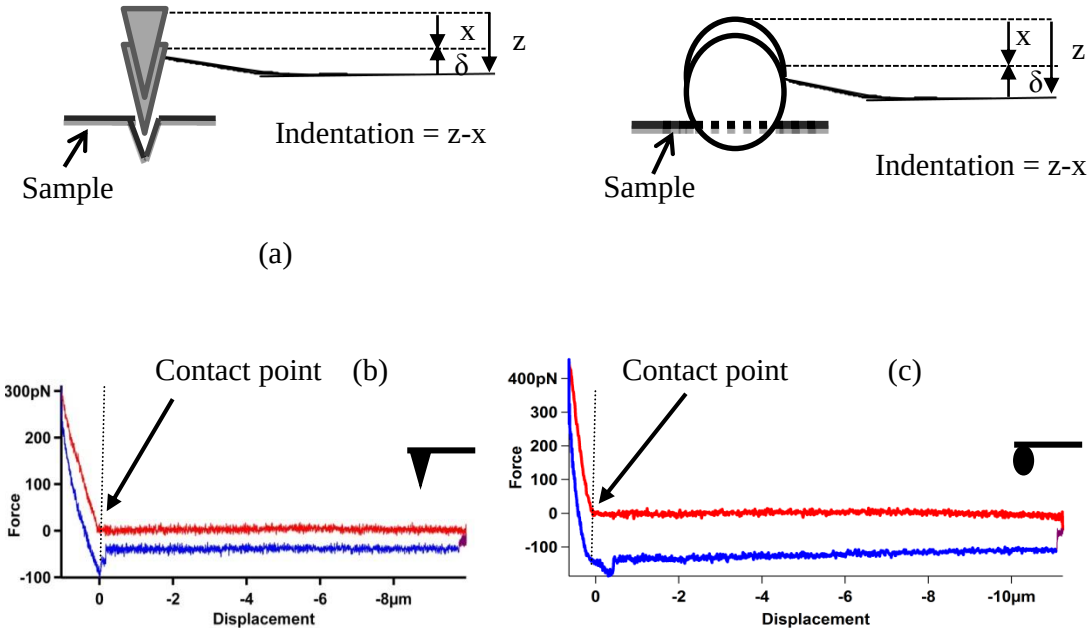

Fig. 5.1. (a) Schematic representation of indentation experiments for sharp and colloidal probes. (b-c) Cantilevers start moving towards the sample surface by a distance z until it touches the surface. The sample indented and cantilever tip bends and its deflection reaches the trigger value (20 nm deflections equal to 220-290 pN). After that the cantilever reverses back and covers the ramp size distance.

All the force curves were taken at room temperature; primary Schwann cells have good substrate adhesion and remain alive for 7-8 hours but NG-108-15 cells started showing negative effects on growth after 4 hours of force curve data. The cells began to retract and acquired a round shape and lost their adhesion point with the poly(l-lysine) coated substrate. Therefore, force curve data was recorded within three hours.

5.2.3 Elastic modulus measurement

The Hertz model has been used in the majority of articles on cell mechanics for the evaluation of elastic modulus. The Hertz model and Sneddon's modification to the Hertz model was used to describe the behaviour of an elastic half space under indentation force by an infinitely stiff indenter. The model assumes that the sample is homogenous, isotropic, incompressible and frictionless at small deformation, which is not completely true for biological cells [221]. Most of the biological samples are neither homogeneous nor completely elastic, however, elastic modulus measurement on biological samples using the Hertz model have been used by many researchers for cell stiffness characterization [108,222–227]. AFM indentation depth for elastic modulus calculation is limited. In general, it is assumed that the Hertz model is valid for 10% of the cell thickness and other studies also reported that the Hertz model was also

reasonably valid for all indentation range from 4 % to 30% [228–232]. The indentation depth range in the Hertz model has been widely discussed among researchers in this field. In this study, two different probes were used to investigate the cell mechanics at relatively large indentation depth. The measured modulus is denoted by E_H as it is not strictly the Young's modulus considering the viscoelastic and heterogeneous nature of the cells.

Force as a function of indentation for AFM sphere probes can be described by [93].

$$F = \frac{4\,E}{3\,(1-\nu^2)}\,R\,\delta^{2/3} \qquad (5.1)$$

Here, R is radius of the spherical probe, E is the elastic modulus and ν is the Poisson ratio. Poisson ratio is generally assumed to be the 0.5 for biological samples [233] i.e., compressible.

For a conical tip, we employed the Sneddon's modification of the Hertz model to measure the elastic modulus from force indentation data [234]. The force on a conical indenter is given by this relation

$$F = \frac{2\,E}{\pi\,(1-\nu^2)}\,\delta^2 \tan\alpha \qquad (5.2)$$

Where α is the half angle of the AFM conical indenter.

Force-volume maps of primary Schwann and NG-108-15 neuronal cells and growth cones were recorded with sharp probes and colloidal probes and sharp probes were also used to acquire force-volume maps on thin neurites around the cell and single long neuritis. Colloidal probes could not be used on the thin neuritis due to poor lateral resolution and larger contact area. Force-indentation data were analyzed to measure the elasticity of the cell membrane and internal cytoskeletal structure. Contact-point height maps were reconstructed from the raw force curve data after detecting the initial contact-point which is based upon a local gradient-based algorithm. The ARgyle™ software can easily compute the algorithm and detect the initial contact-point of approach force curves at the pixels that constitutes the topography image. Therefore topography obtained from the contact points force-volume maps further

compare with the set-points maps. The stiffness maps were reconstructed from the set-point force curve data using the InVOLS measurements. InVOLS was measured from the slope of contact region of each force curve and InVOLS measurements directly correspond to the stiffness variation over the sample surface. Fig. 5.2 shows the Hertz fit at large indentation range on force-indentation curves acquired with sharp and colloidal probes.

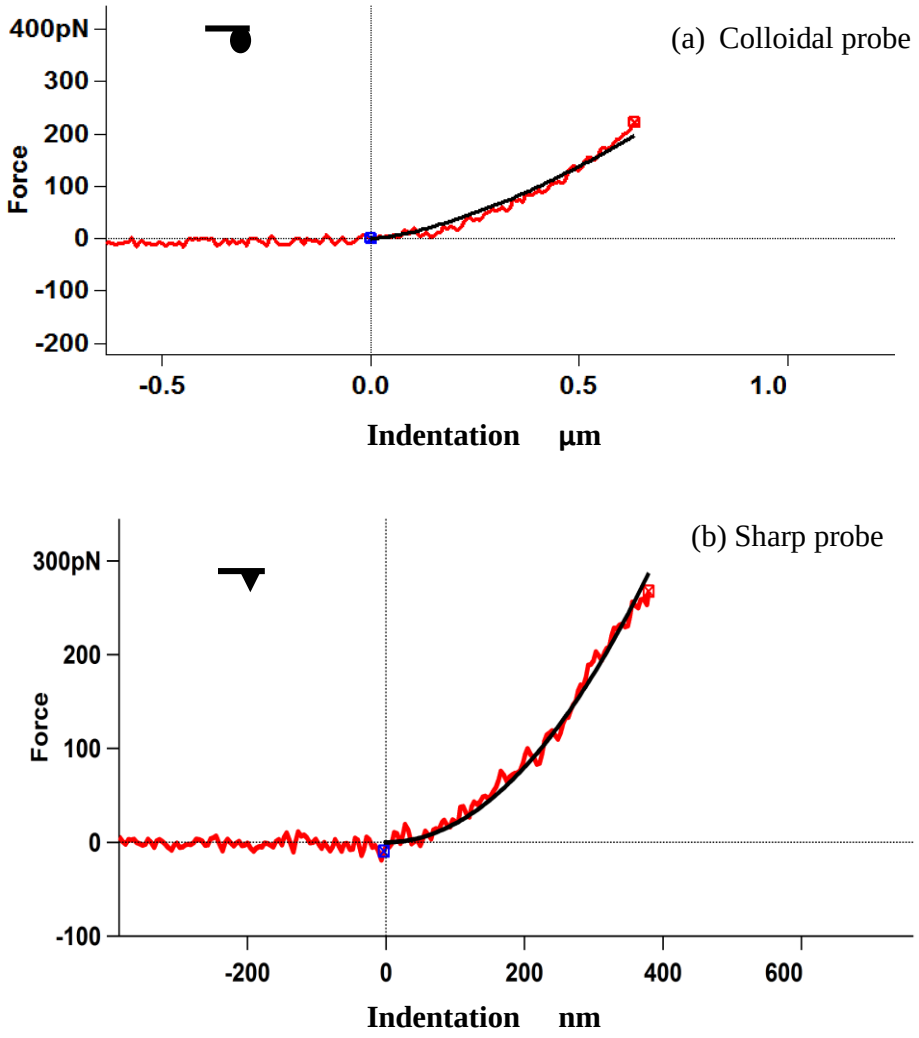

Fig. 5.2. Force curves recorded with the colloidal probe on the primary Schwann cell and with the sharp tip on the neurite showing the Hertz fit at large indentation range in (a and b).

5.3 Results

5.3.1 Nano- and micromechanical properties of primary Schwann cells

Figs. 5.3-5.5 (a-c) present force-volume maps of primary Schwann cells acquired on arrays of 50 x 50 curves with the sharp tips nominal (radius 20 nm) showing the set-point height and

contact-point height maps. Contact-point height maps display the real cell topography derived by estimating the contact-point in force curves automatically using the ARgyle™ software. Stiffness maps of each individual cell are reconstructed from the automated force curve analysis of the set-point force curve data which displays stiffness by colour at each of the force curve points collected on the cell and substrate. Each of Figs.5 3-5.5 shows different examples of primary Schwann cells.

Force-volume maps also acquired on arrays of 50 x 50 points with colloidal probes (radius 10 µm) on primary Schwann cells are shown in Figs. (5.6-5.8). Figs. 5.6-5.8 (b-c) shows contact-point maps and stiffness maps reveal cells stiffness variability across its surface.

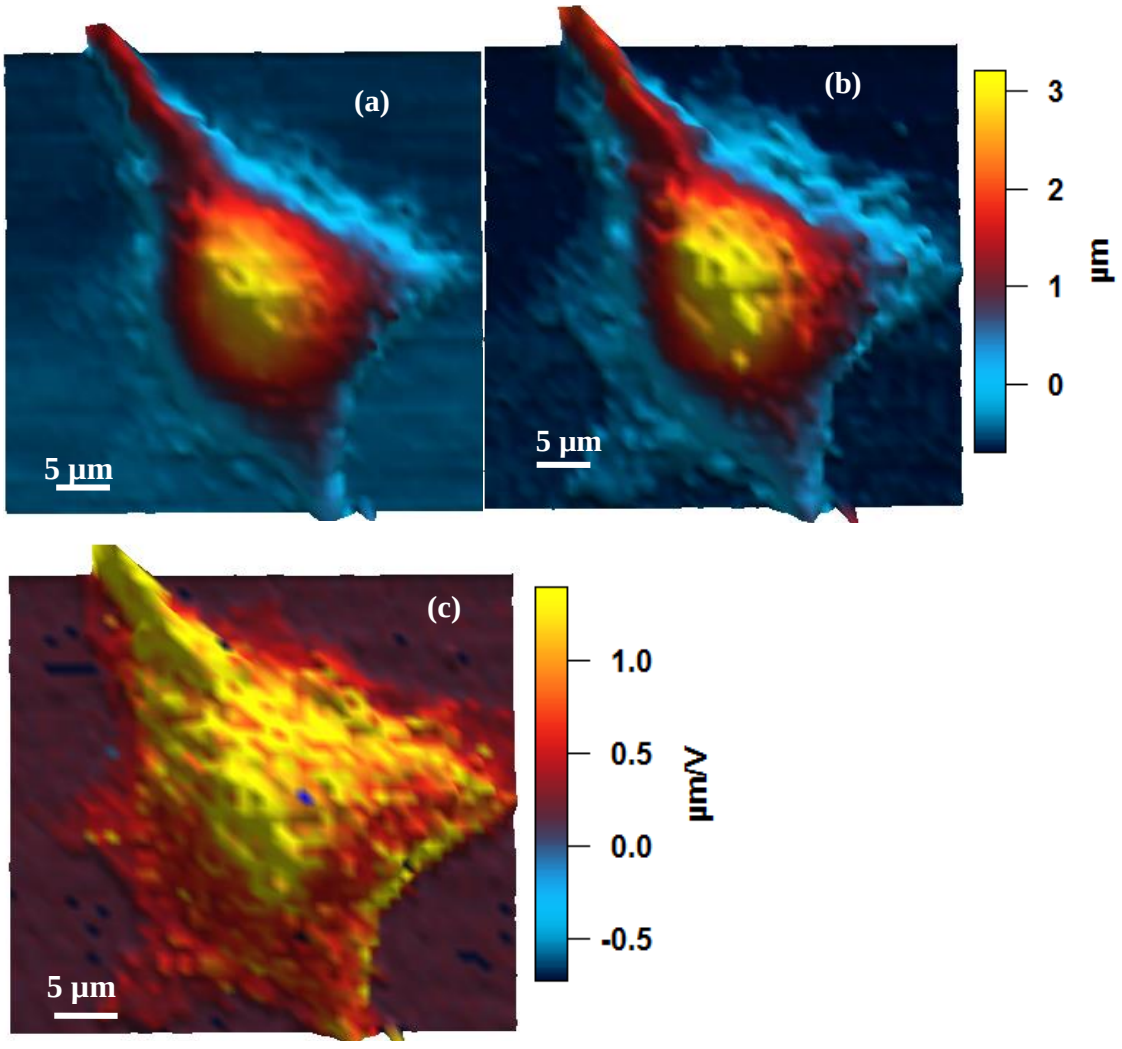

Fig. 5.3. AFM force-volume maps of a primary Schwann cell. (a) Set-point topography map (i.e., height plotted is height at the trigger point), (b) contact-point topography map (i.e., height at the point of initial contact), (c) stiffness map, the colour bar represents the height and the stiffness variation of the cell and in the stiffness map the top of the colour bar corresponds to a softer area of the cell.

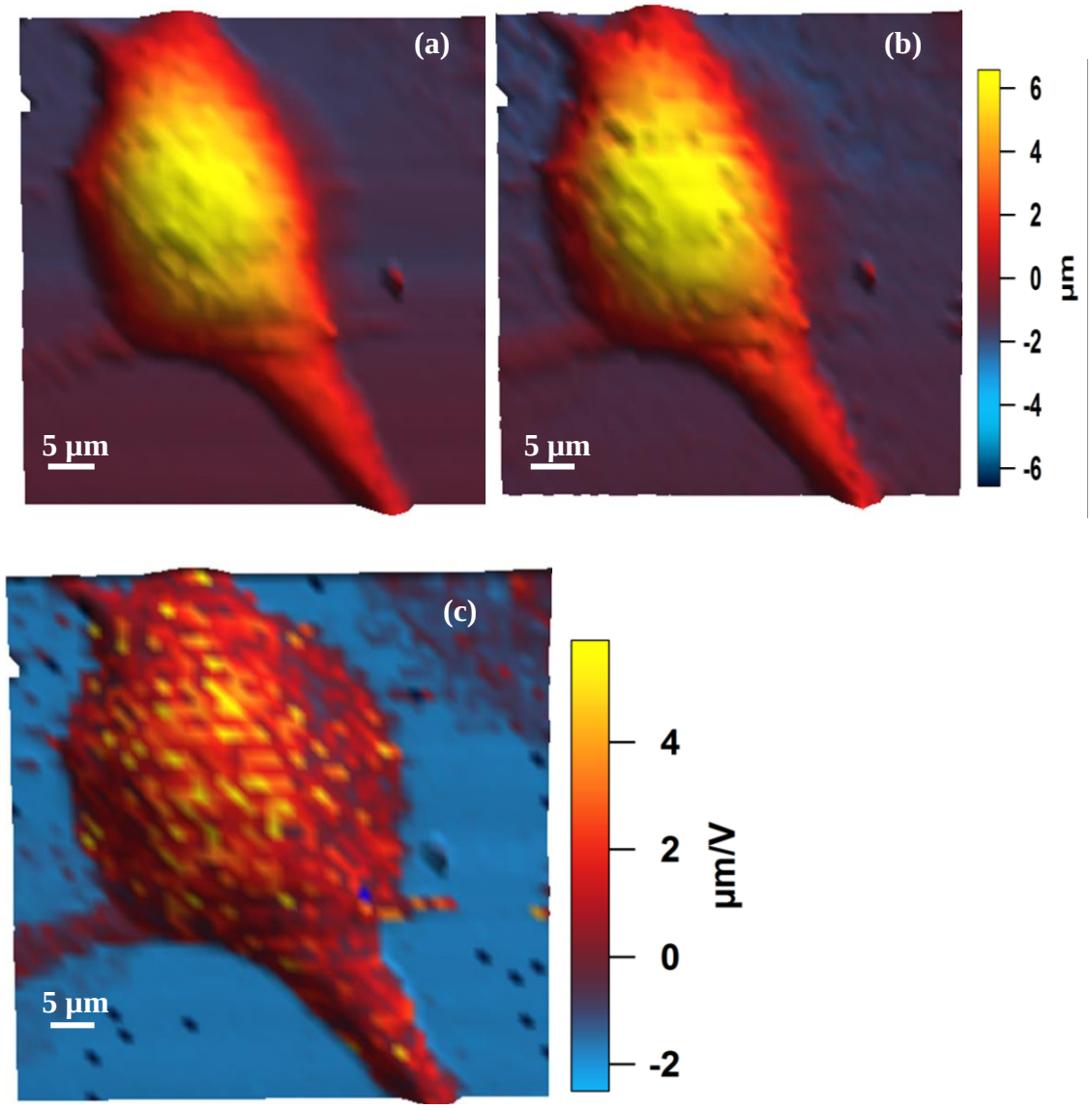

Fig. 5.4. AFM force-volume maps of a primary Schwann cell. (a) Set-point topography map, (b) contact-point topography map, (c) stiffness map, the colour bar represents the height and the stiffness variation of the cell and the top of the colour bar in the stiffness map corresponds to a softer area of the cell.

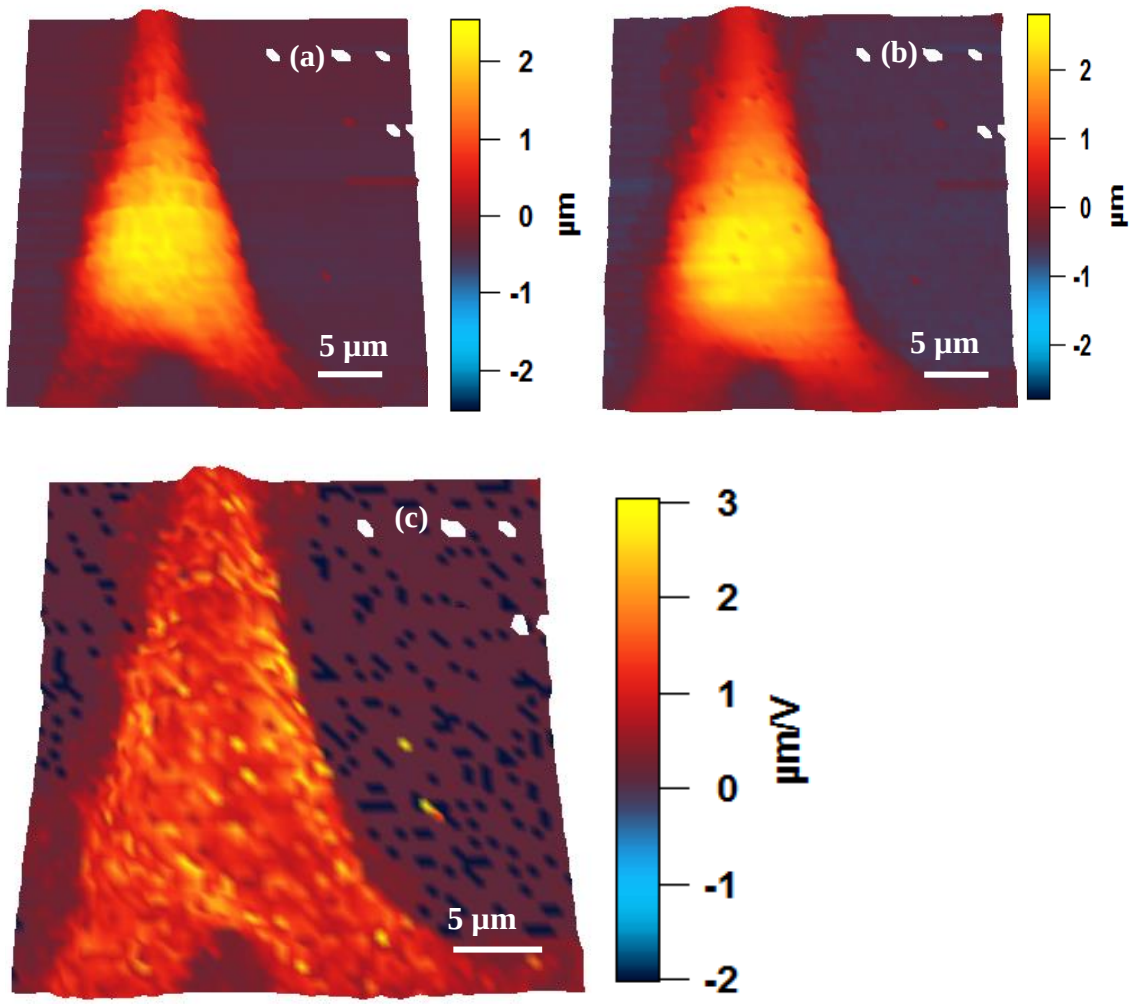

Fig. 5.5. AFM force-volume maps of a primary Schwann cell. (a) Set-point map, (b) contact-point map, (c) stiffness map, the colour bar represents the height and the stiffness variation of the cell. In the stiffness map, the top of the colour bar corresponds to a softer area of the cell.

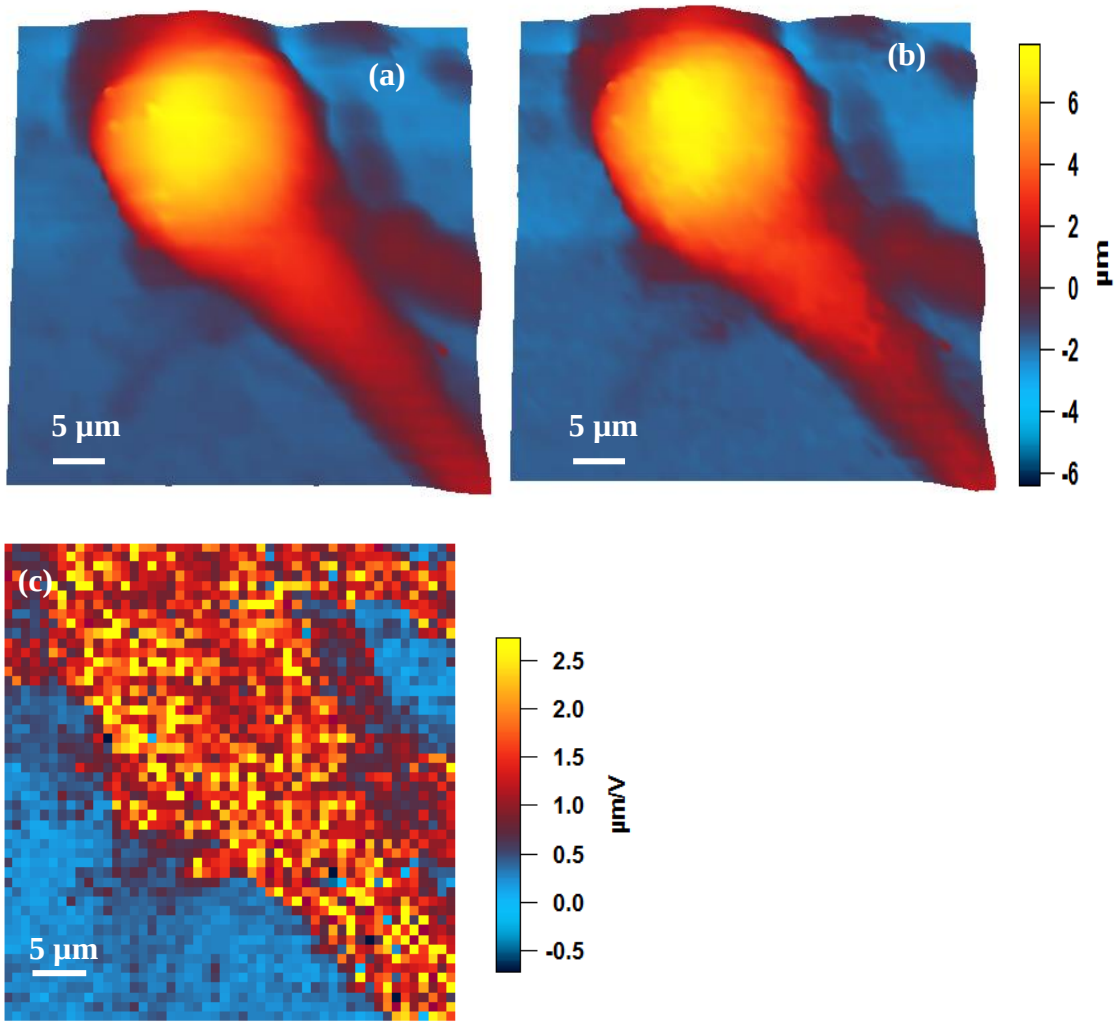

Fig. 5.6. AFM force-volume maps of a primary Schwann cell with a colloidal probe. (a) Set-point topography map, (b) contact-point topography map, (c) stiffness map, the colour bar represents the height and stiffness variation and the top of the colour bar in the stiffness map corresponds to a softer area of the cell.

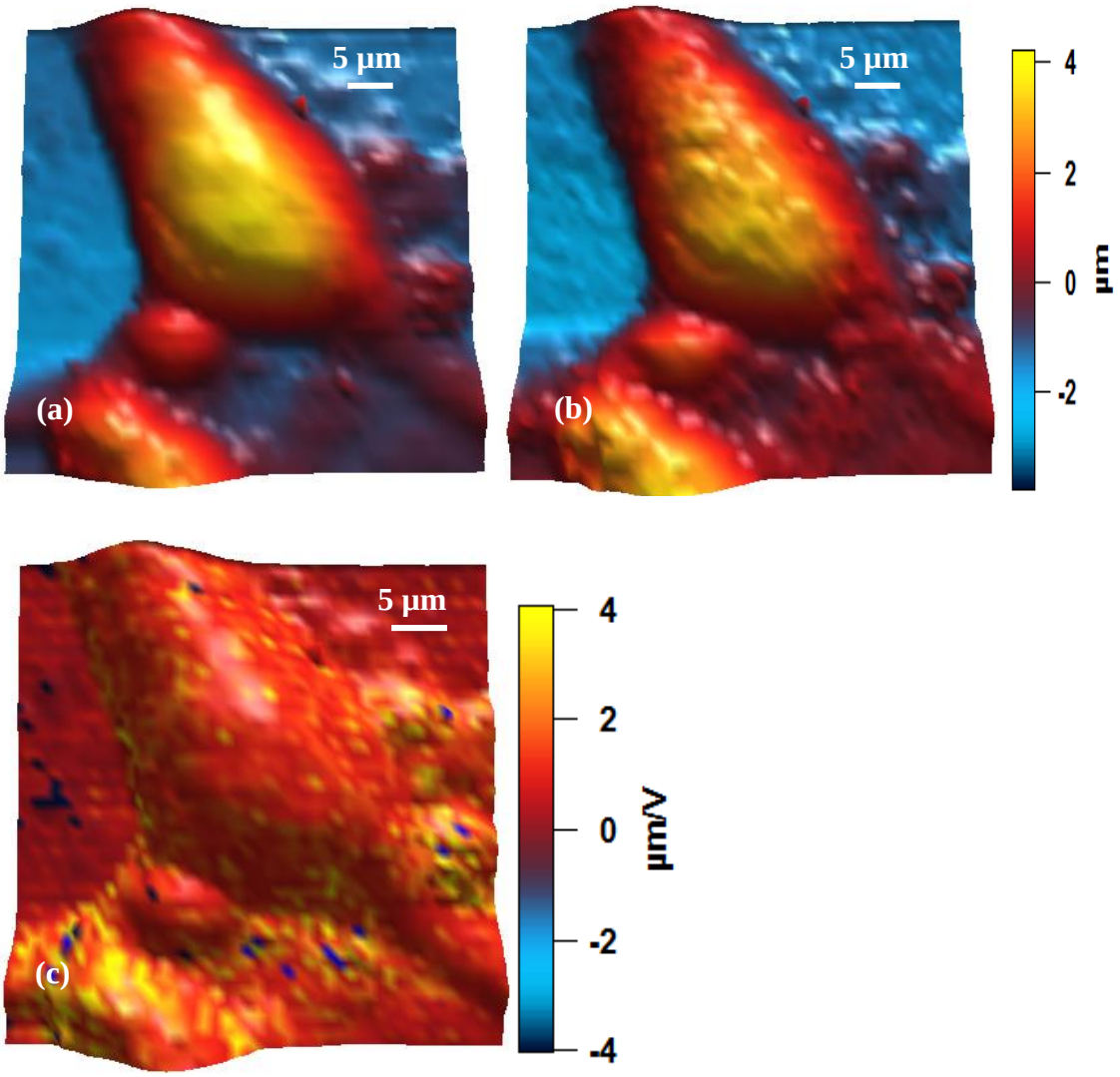

Fig. 5.7. AFM force-volume maps of primary Schwann cell. (a) Set-point topography map, (b) contact-point topography map, (c) stiffness map, the colour bar represents the height and the stiffness variation of the cell and in the stiffness map the top of the colour bar corresponds to a softer area of the cell.

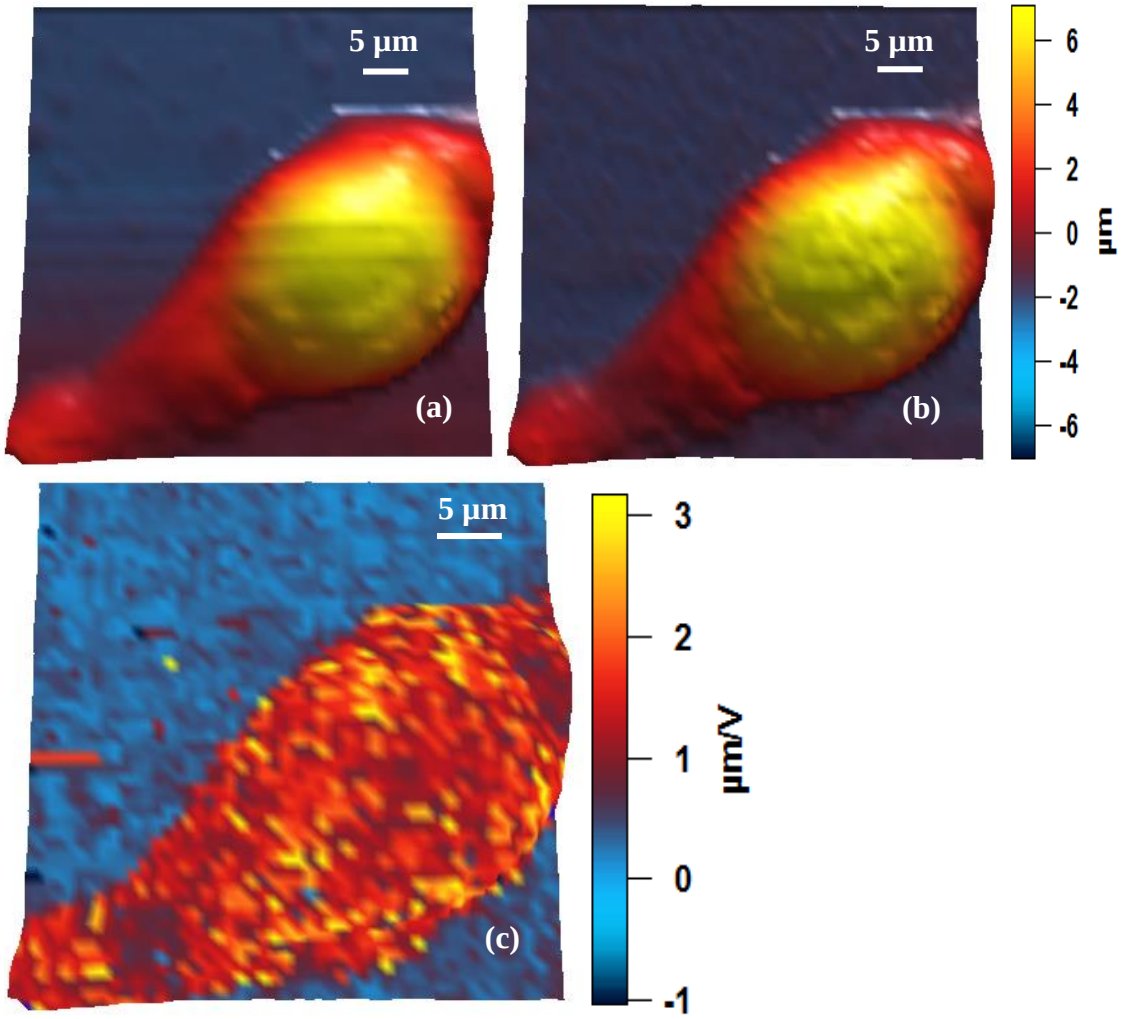

Fig. 5.8. AFM force-volume maps of a primary Schwann cell. (a) Set-point map (b) contact-point map (c) stiffness map and the colour bar represent the height and the stiffness variation of the cell. In the stiffness map, the top of the colour bar corresponds to a softer area of the cell.

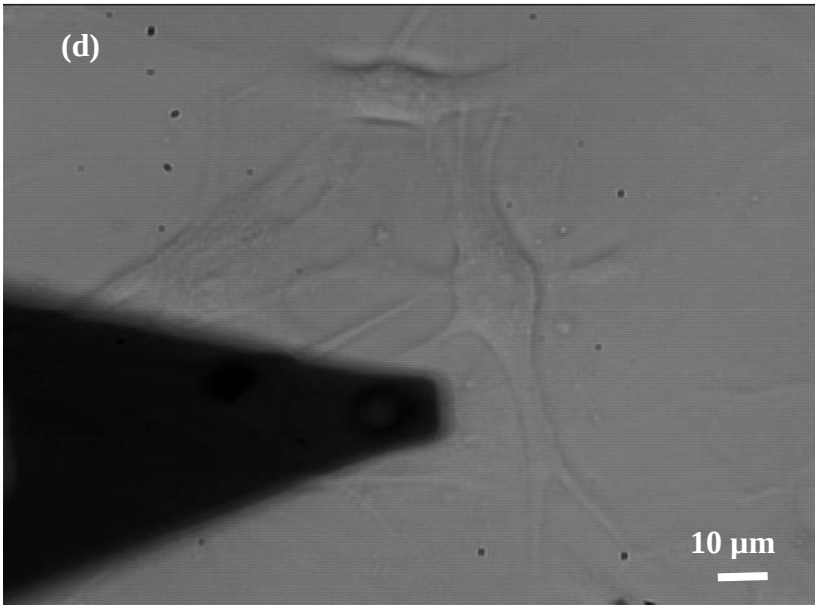

Fig. 5.9. An optical image of a primary Schwann cell.

Contact-point images were reconstructed through with the sharp tip and colloidal probe force curve data. The cells in contact-point images with sharp tips appear relatively broad with clearly resolved cell edge protrusions. Presentation of the 50 x 50 array of force curve data as a contact-point image is a meaningful way to represent the true topography of the cell. Set-point height maps do not resolve the cell edges with as much detail as the contact-point images. It is apparent that set-point 'images' lose significant information in the periphery of the cell, presumably as the tip has pushed through to the level of the substrate. Contact-point images also appear to show the cell surfaces as being rougher and more 'knobbly' than the set-point images, probably a better reflection of the complex and structural membrane surface. Contact-point images were also reconstructed from the colloidal probes force curve data which does not clearly determine the cell edge features in all the contact maps in contrast to the set-point force-volume maps. It is suggested that contact-point maps reconstructed through the sharp tip data clearly resolves the cell edge protrusions in contrast to data obtained with colloidal probes. Moreover, the set-point force curve data was used to reconstruct the stiffness maps that show the inherent stiffness of the cells as shown in Figs. 5.3-5.5 (c) and Figs. 5.6-5.8 (c). Fig. 5.3 (c) shows the stiffness variation within the cell, where the central region was found to be softer than the cell edges. With sharp tips, both contact-point and stiffness maps reveal the cell morphology right up to the edges. We suggest that 'contact point' force-volume maps is an effective method for obtaining images of soft cells that are hard to image conventionally with AFM.

An elastic modulus was determined after analyzing the force displacement curves from individual cells with the Hertz model at indention greater than 500 nm with sharp triangular tips (nominal radius 20 nm). The sets of data are given as histograms along with the log normal distribution curves in Fig. 5.10 (a-d). The histograms in Fig. 5.10 (a-c) correspond to the analyzed force curve data from the displayed force-volume maps in Figs. 5.3-5.5 (a). Fig. 5.10 (d) is a histogram overlaid with a Log normal distribution curve showing the E_H variation of primary Schwann cells for five cells. The average elastic modulus, E_H, (median values ± median absolute deviation) was found to be 3.1 ± 1.9 kPa for five cells. For the sake of completeness, Fig 5.10 (e) shows the raw stiffness histograms of two of the primary Schwann cells. Fig. 5.10 (g) shows some examples force-indentation curves which clearly show the wide variation across the cells in agreement with the histograms.

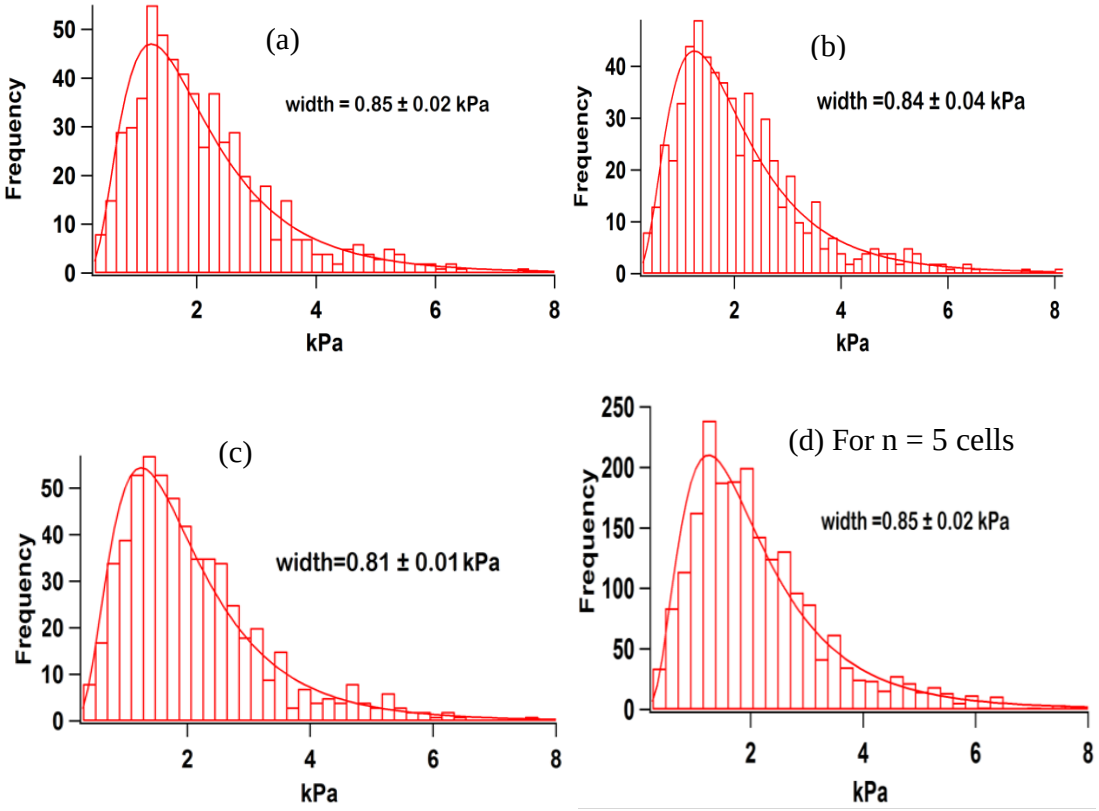

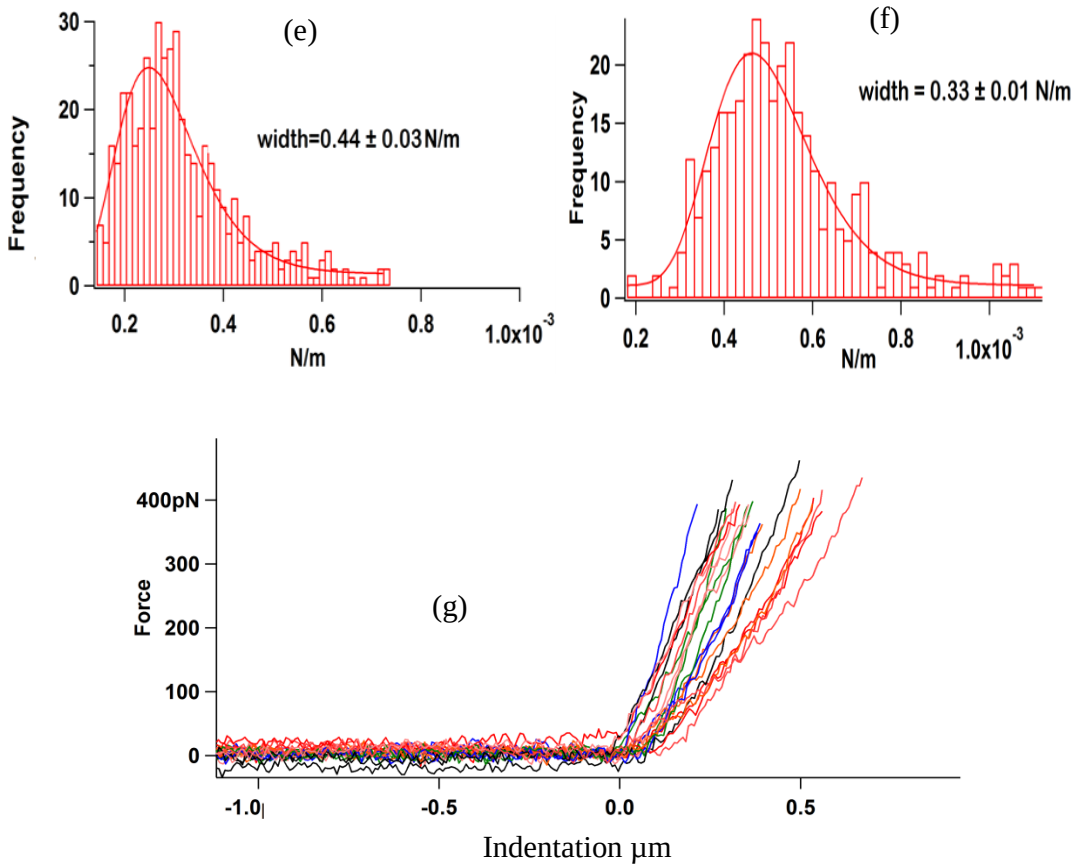

Fig. 5.10. Histograms of analyzed force curve data with sharp probes, E_H for the individual cells and multiple cells in (a-d (previous page)). (e-f) Stiffness histograms of two cells acquired from the slope of the approach force curve data. (g) Examples of force curves recorded with a sharp tip at different locations correspond to different indentation at the same force.

Next, colloidal probe force curves of each individual cell were analyzed and histograms with log normal distribution curve for individual cells and multiple cells are shown in Fig 5.11 (a-d). The average measured elastic modulus (median values ± median absolute deviation) value was found to be 93 ± 49 Pa for cells (n = 5). Fig. 5.11(e-f) shows the stiffness histograms of the primary Schwann cell acquired from the slope of the approach force curve data and the cell stiffness of both the cells was found to be in the range of 0.1-0.8 Nm^{-1}. Fig. 5.12 shows force-indentation curves acquired from the different cell regions.

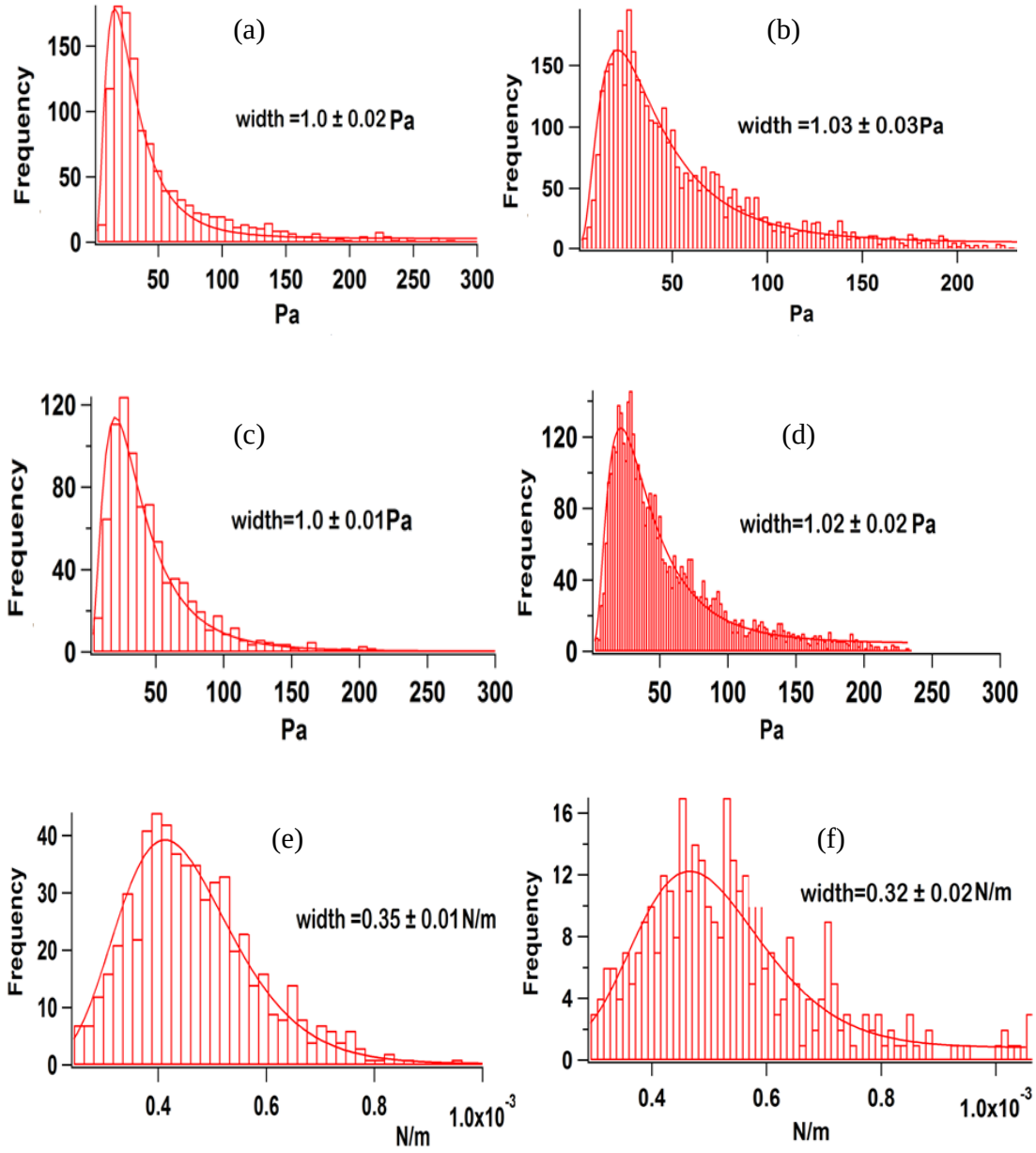

Fig. 5.11. (a-d) Histograms of analyzed force curve data with colloidal E_H for the individual and multiple primary Schwann cells. (e-f) Stiffness histograms acquired from the slope of the approach force curve data.

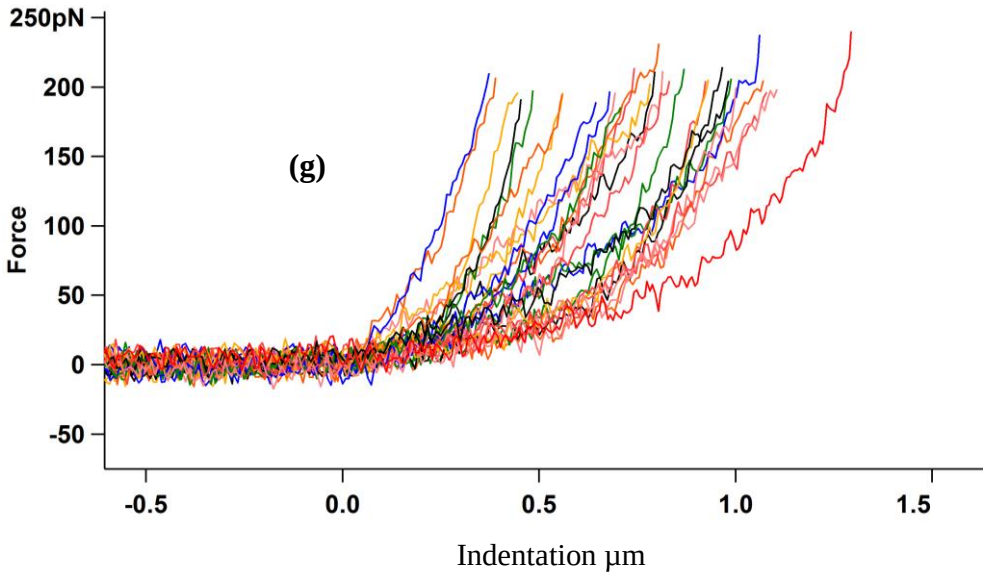

Fig. 5.12. Set of force-indentation curves at different regions of the primary Schwann cell showing different indentation at the same force.

The topography of primary Schwann cells acquired through the force-volume maps and contact maps show the same spindle shape morphology as shown in optical images (Fig.5.9 (d) and previously obtained AFM tapping mode images (chapter 4) [236]. Primary Schwann cells are 3-14 µm high and the mechanical properties of the primary Schwann cells were measured with two types of the probes, the sharp probes and the colloidal probes. We believe this AFM study is the first detailed topographic and mechanical analysis of live primary Schwann cells. The elastic modulus, E_H after computing the nano-mechanical measurement at large indentation depth on primary Schwann cells was found to be in the range of 3.1 ± 1.9 kPa (n = 5 cells) [203,236,237] and the elastic modulus E_H was found to be 93 ± 50 from micro-mechanical measurements [222,238]. Therefore, significantly larger elastic modulus was found using the sharp probe force-indentation data in contrast to that obtained with a colloidal probe [160,221,239]. The width of the log normal distribution curve is wider for colloidal probes in comparison to the sharp tip data. The cell stiffness histograms obtained from the slope of full force displacement curve data gave a stiffness value in the range of 0.1-0.6 mNm^{-1} for the sharp tip and 0.1-0.8 mNm^{-1} for colloidal probes and the width of the distribution is slightly wider for sharp tips in contrast to colloidal probes [240].

5.3.2 Nano- and micromechanical properties of neuronal cells

The set-point force-volume maps and the contact maps of NG-108-15 neuronal cells provide the topography information and the stiffness maps provide the stiffness variation of the cells. Force-volume maps were derived from 60 x 60 (i.e., 3600), 34 x 34 and 40 X 40 force curves respectively. Figs. 5.13-14 (a-b) displayed as the set-point and contact-point force-volume map and 5.15 (a) presents the set-point topographic map of NG-108-15 neuronal cell. Figs. 5.13-5.14 (c) and 5.15 (b) shows the corresponding stiffness maps. The colour of the bars represents the stiffness variation of the cell and the stiffness decreases from the bottom to the top of the colour bar. Fig.5.15 (c-d) show optical images of the neuronal cells.

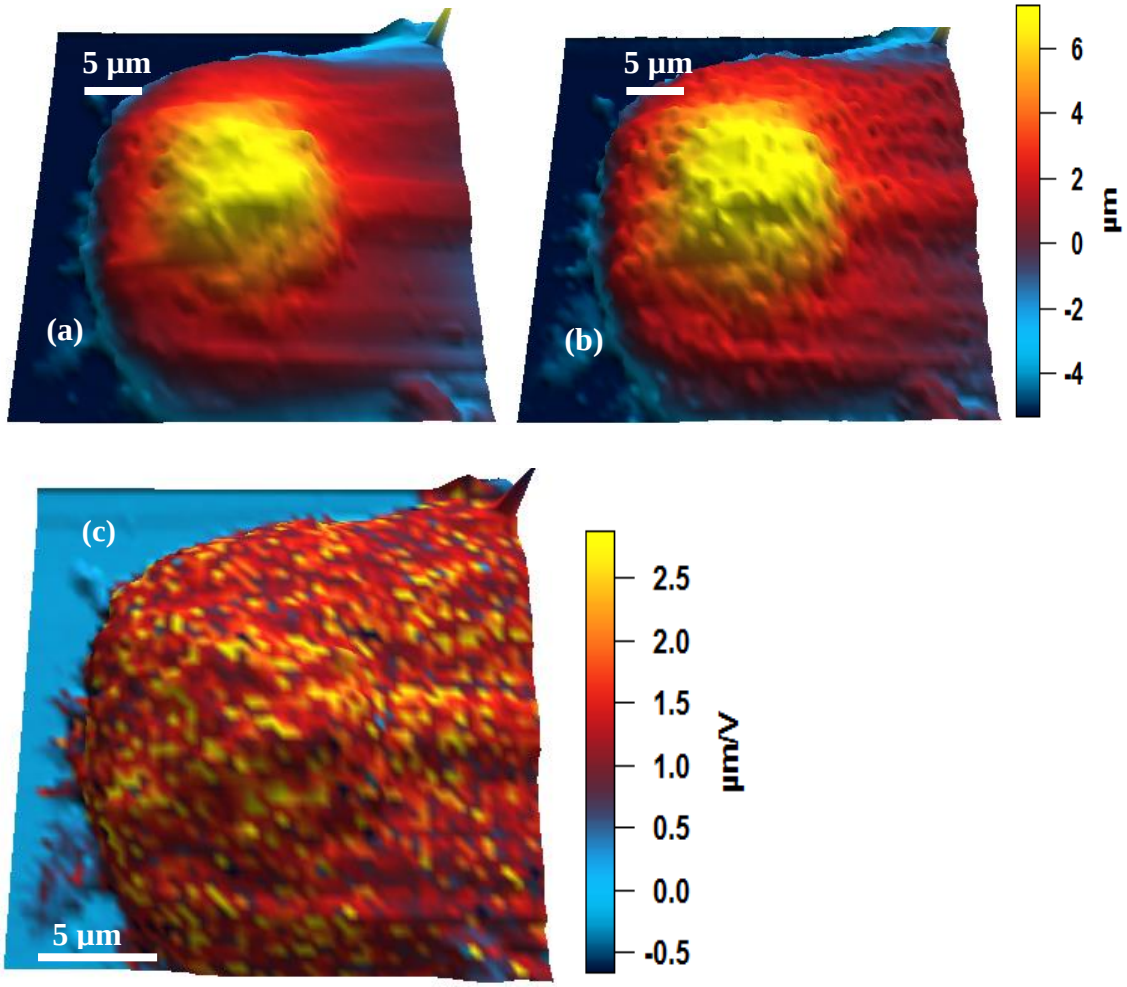

Fig. 5.13. AFM force-volume maps of the NG-108-15 neuronal cell (a) Set-point map, (b) contact-point map, (c) stiffness map, the colour bar represents height and the stiffness variation of the cell. In the stiffness map, the top of the colour bar corresponds to a softer area of the cell.

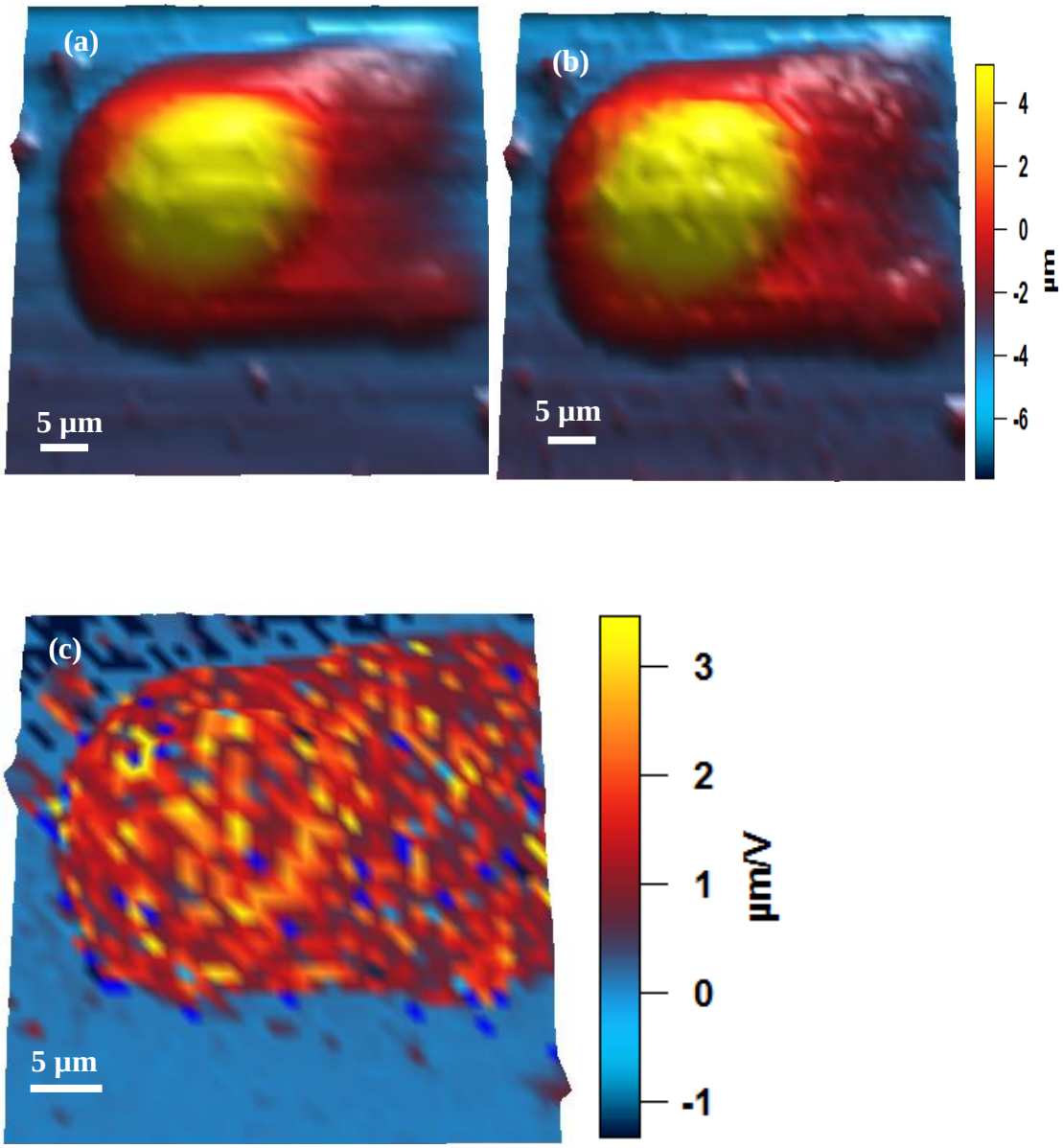

Fig. 5.14. 3D AFM force-volume maps of the NG-108-15 neuronal cell. (a) Set-point map, (b) contact-point map, (c) stiffness map, the colour bar represents height and the stiffness variation of the cell. In the stiffness colour bar, the stiffness decreases from the bottom to the top which corresponds to a softer area of the cell.

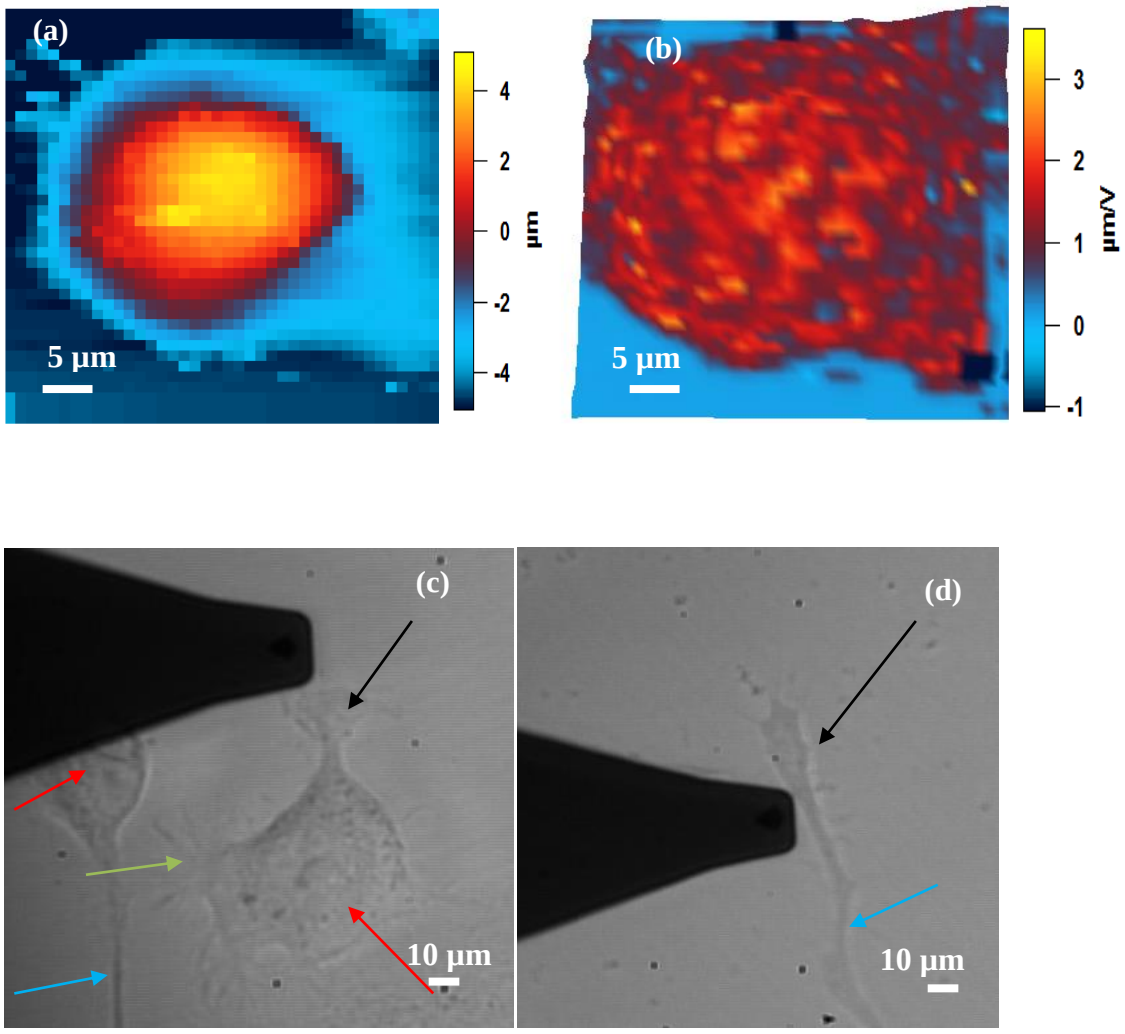

Fig. 5.15. AFM force-volume maps of the NG-108-15 neuronal cell. (a) Set-point map, (b) stiffness map, the colour bar represents height and the stiffness variation of the cell. In the stiffness colour bar, the stiffness decrease from the bottom to the top which corresponds to a softer area of the cell. (c-d) Optical images of NG-108-15 cells with the cell body (red arrowhead), the growth cone (black arrowhead) and the small neurite (green arrow head) and the long neurite (blue arrowhead).

Micrometre-indentations were performed with a colloidal probe (radius 10 µm) on Ng-108-15 neuronal cells. Set-point maps, contact-point maps and stiffness maps showing the cell topography and the cell stiffness are given in Figs. 5.16-5.18 (a-c).

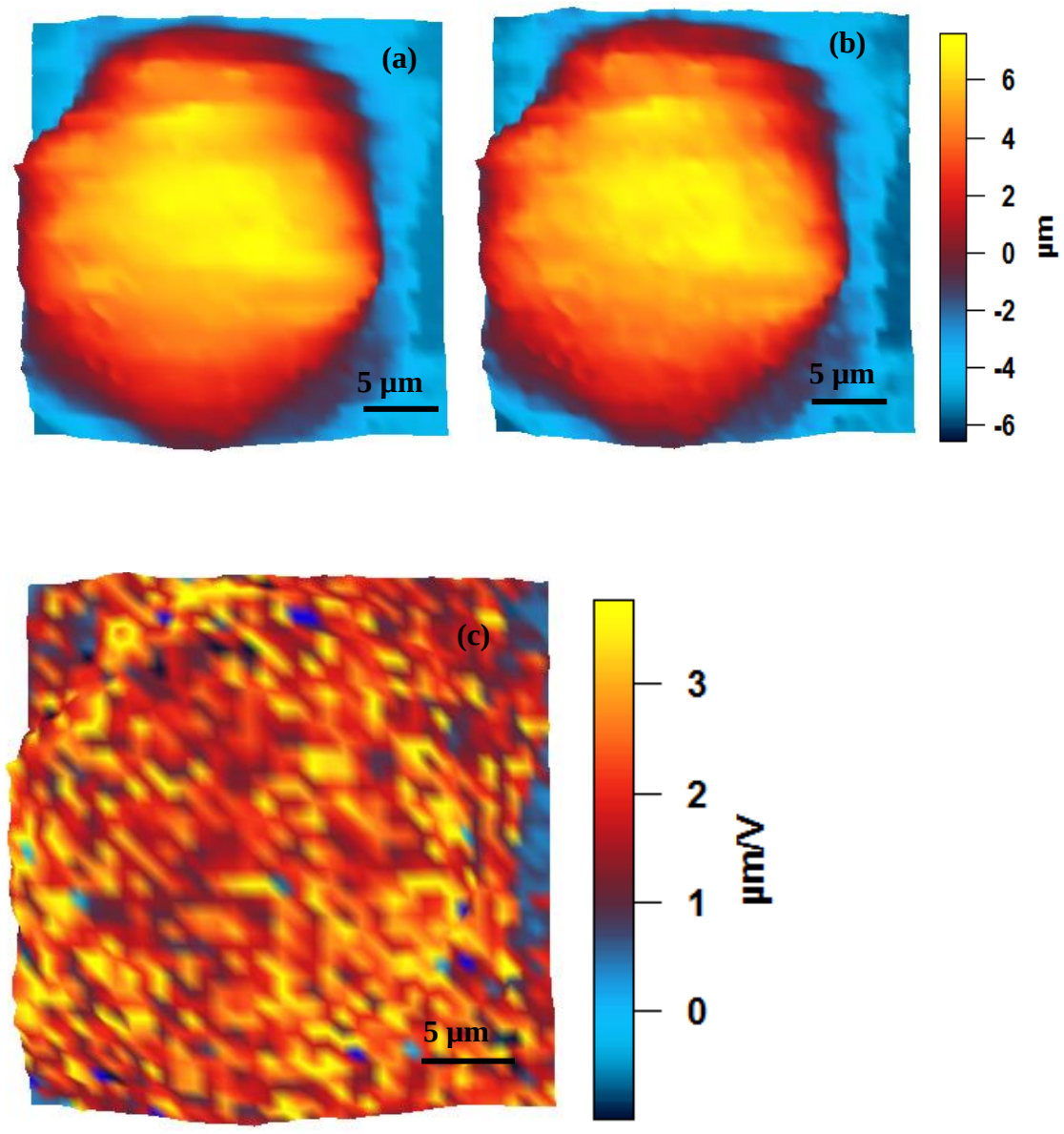

Fig. 5.16. AFM force-volume maps of the neuronal cell. (a) Set-point topography, (b) contact-point map, (c) stiffness map, the colour bar represents the height and the stiffness variation of the cell where the top of the colour bar corresponds to a softer cell area.

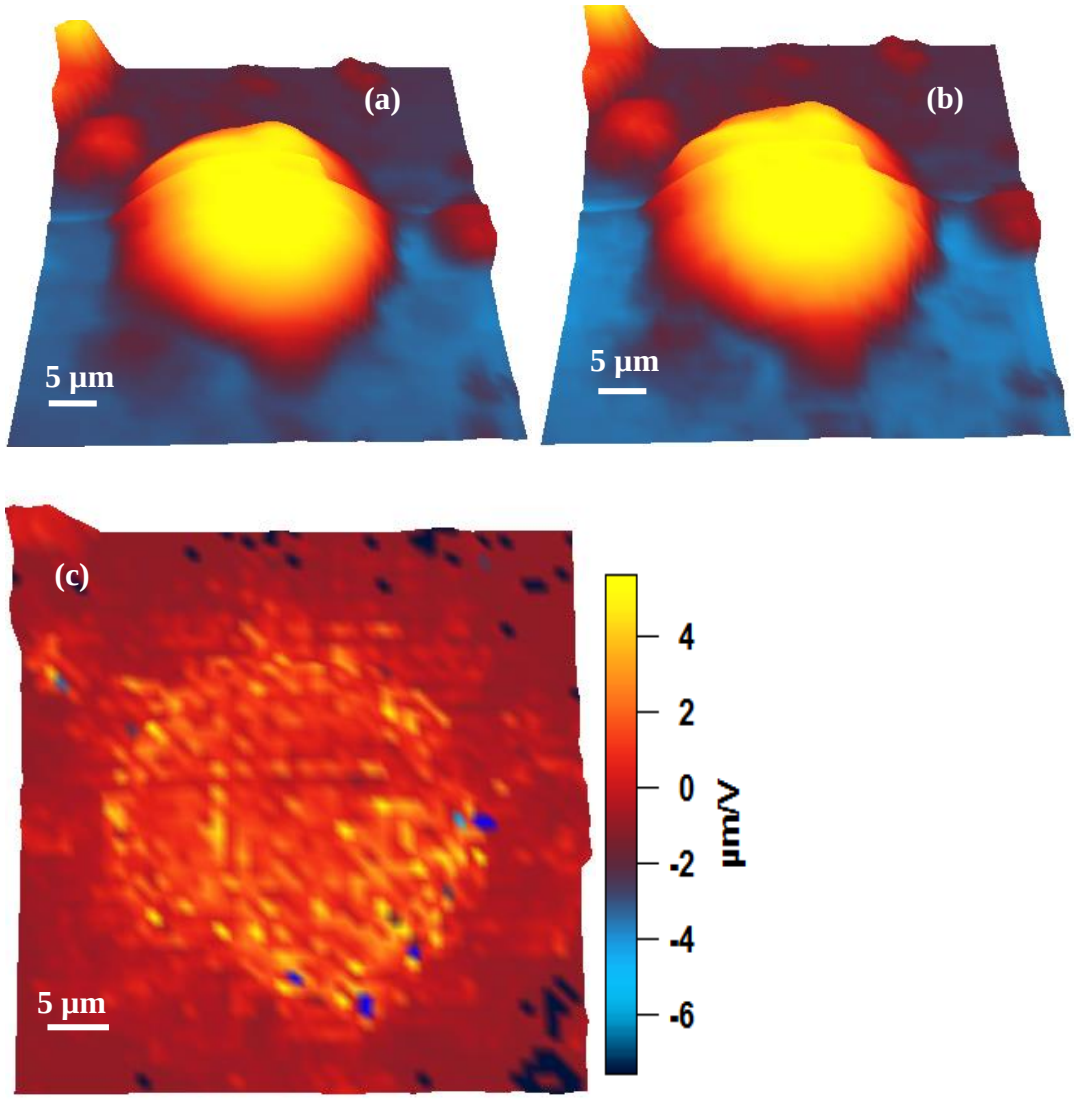

Fig. 5.17. AFM force-volume maps of the neuronal cell. (a) Set-point topography map, (b) contact-point topography map, (c) stiffness map, the colour bar represents the height and the stiffness variation of the cell and the top of the colour bar in the stiffness map corresponds to a softer area of the cell.

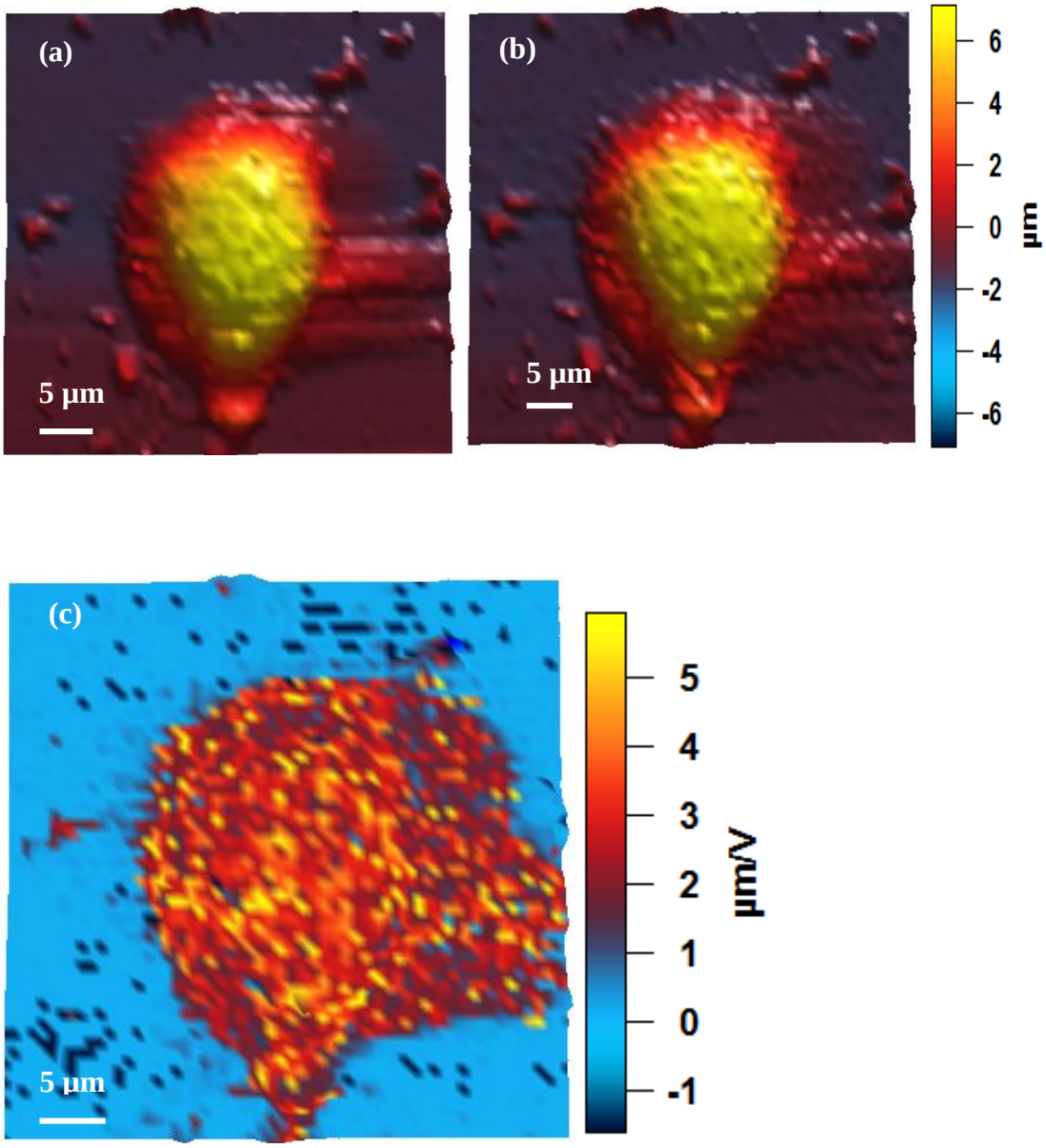

Fig. 5.18. AFM force-volume maps of the neuronal cell. (a) Set-point map, (b) contact-point map (c) stiffness map, the colour bar represents the height and the stiffness variation of the cell and the top of the colour bar in the stiffness map corresponds to a softer area of the cell.

Contact-point maps reconstructed through sharp and colloidal probes force curve data show the same cell edge morphology as obtained in the set-point maps. Little difference was observed even in contact-point maps acquired by sharp tips and colloidal probes. It is

suggested that it was not possible to resolve the cell edges features due to 11-14 µm due to height of the neuronal cells. The stiffness maps show the inherent stiffness of the cells as shown in Figs. 5.13-5.14 (c), 5 15 (b) and Figs. 5.16-5.18 (c). Fig. 5.17 (c) shows the stiffness variation obtained with colloidal probes where the cell edge was found to be stiffer than the cell body. In Fig. 5.17 (c) the stiffness map resolves the cell edge filamentous structures in much detail in contrast to contact-point force-volume maps. It is apparent that the cell edge filamentous structures are present in contact-point images but cannot be clearly resolved due to the 13-15 µm neuronal cell height.

An elastic modulus was determined from the nano-mechanical measurements on NG-108-15 neuronal cells, growth cones, and neurites with sharp triangular tips (nominal radius 20 nm). Forces curves for all of the cells were analyzed and the resultant histograms are shown in Fig. 5.19 (a-c). The average elastic modulus (median values ± median absolute deviation) was found to be in the range of 0.97 ± 0.4 kPa for the cells (n = 5) and the histogram by fitting the log normal distribution curve for the cells (n = 5) is shown in Fig. 5.19 (d). Each cell stiffness histogram was also obtained from the gradient of the full force curve data (Fig. 5.19 (e-g)). Force-indentation curves acquired from the different cell regions corresponding different indentation at the same force (Fig. 5.19 (h)).

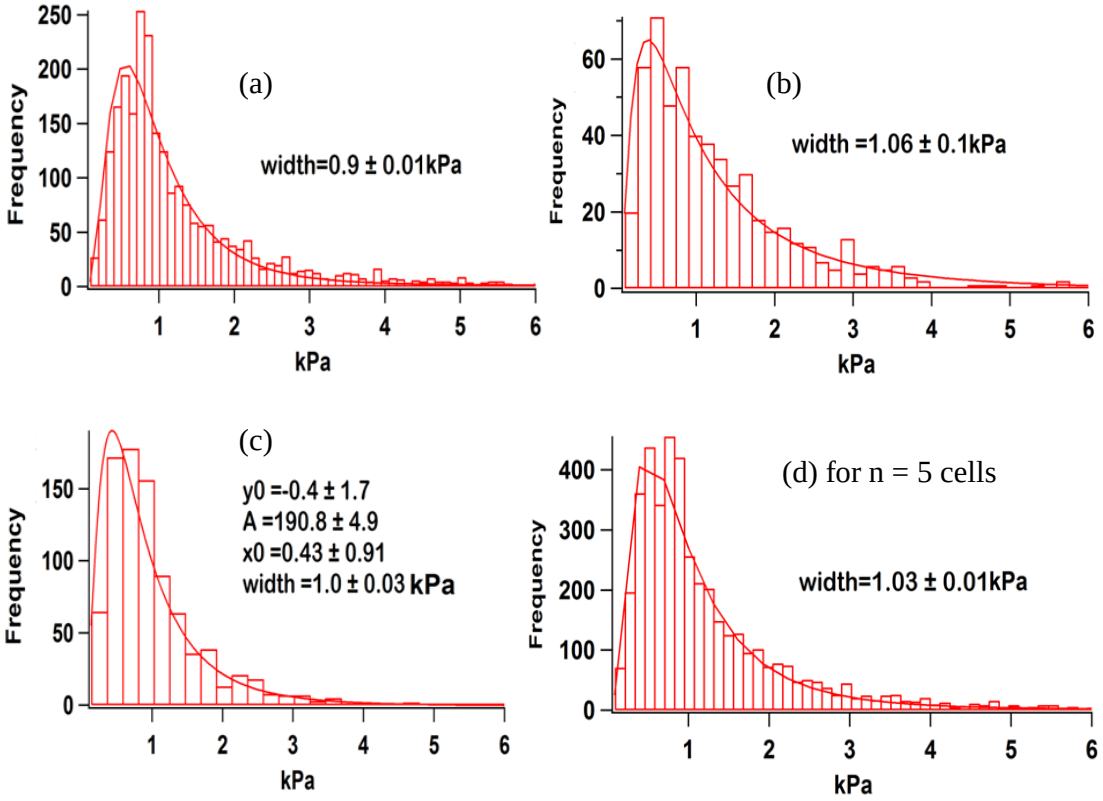

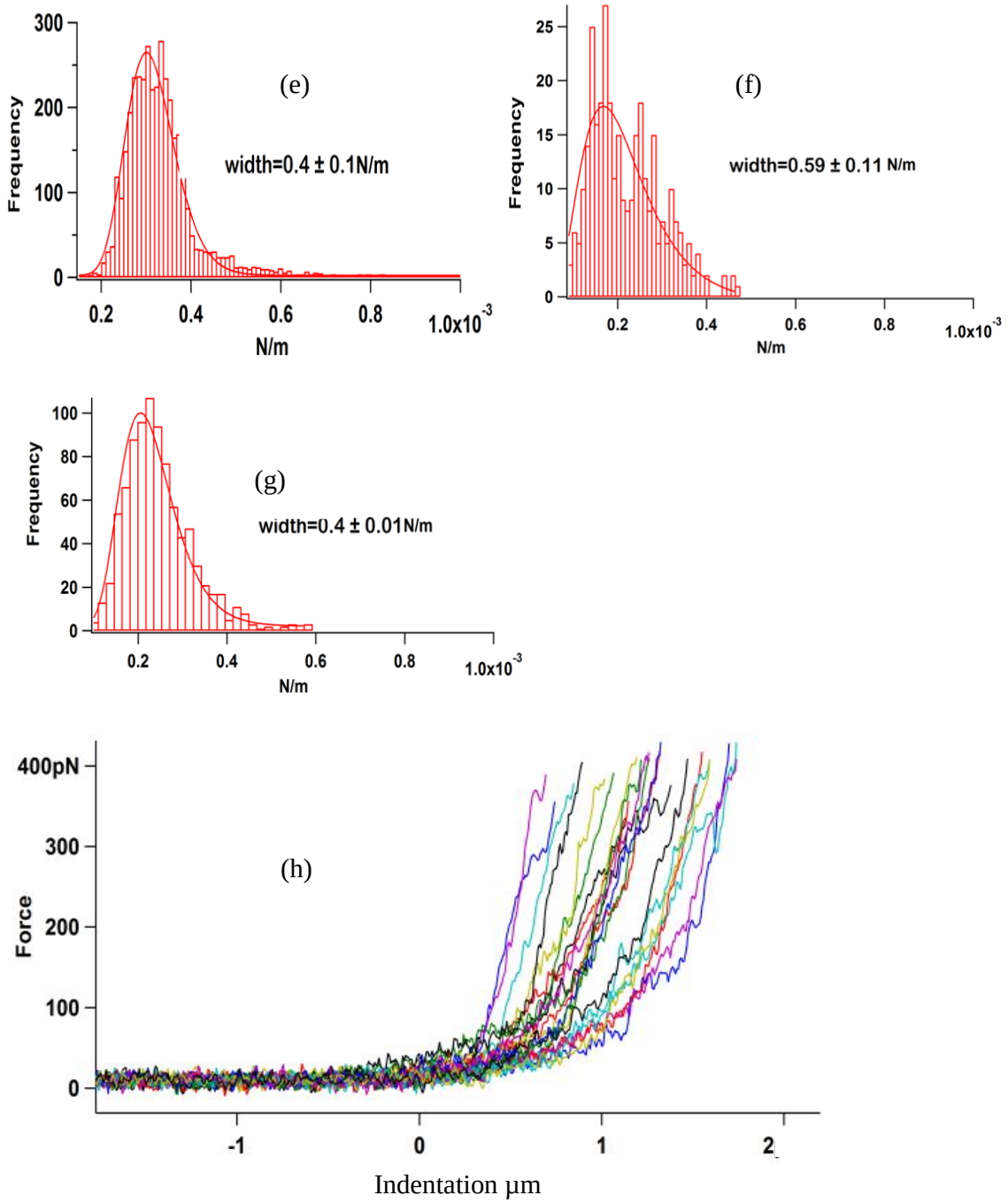

Fig. 5.19. (a-d (previous page) and e-h) Histograms of analyzed force indentation measurements with sharp tips, E_H for individual neuronal cells and multiple cells (a-d (previous page)). (e-g) Three cells stiffness histograms acquired from the slope of the approach force curve data. (h) Some examples of force curves recorded at different regions of the cell correspond to different indentation at the same force.

An elastic modulus was also determined from the micro-mechanical measurements on NG-108-15 neuronal cells and growth cones with colloidal probes. Individual cells and multiple cells elastic modulus E_H data was plotted as histograms with log normal distribution curve is

shown in Fig. 5.20 (a-d). The elastic modulus E_H value (median values ± median absolute deviation),was found to be 86.2 ± 41.8 Pa for neuronal cells (n = 5) [222,238]. Fig. 5.20 (e-g) shows the stiffness histograms of the NG-108-15 neuronal cells acquired from the slope of the approach force curve data and the cell stiffness of the three cells was found to be in the range of 0.1-0.8 mNm^{-1}. Fig. 20 (h) shows force-indentation curves acquired from the different cell regions correspond different indentation at the same force.

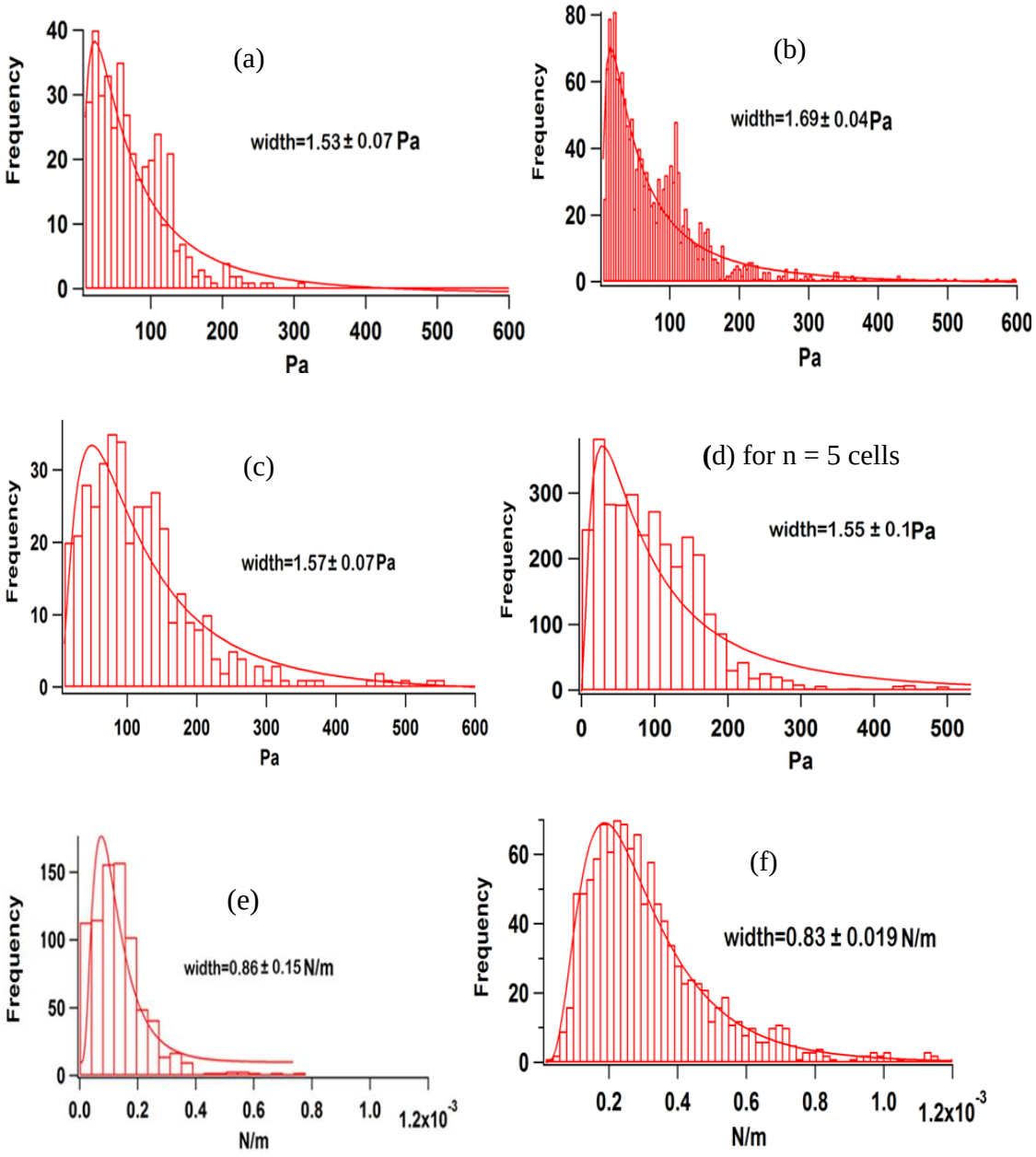

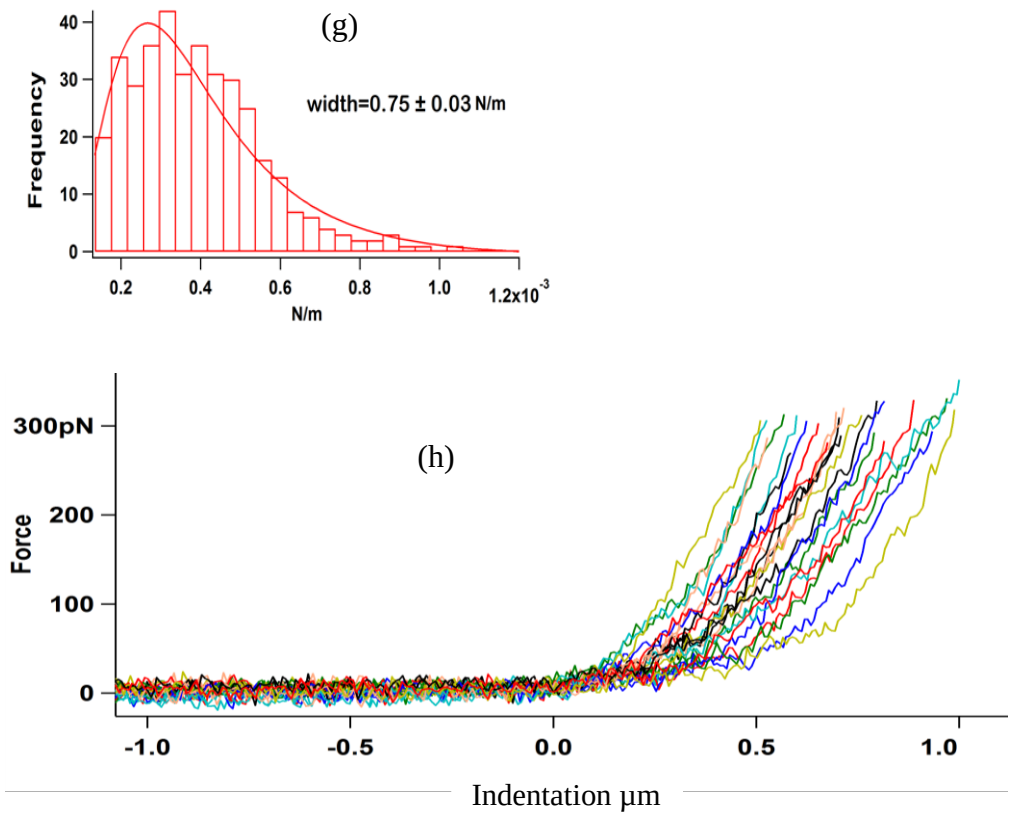

Fig. 5.20. (a-f (previous page) and g-h) Histogram showing the elasticity variation (E_H) of the individual and multiple NG-108-15 neuronal cells in (a-d). (e-g) Stiffness histograms of three cells acquired from the slope of the approach force curve data. (h) Example force curves recorded with sharps tip at different locations which correspond to different indentation at the same force.

This is the first AFM study to investigate the mechanical properties of NG-108-15 neuronal cells with sharp and colloidal probes. The average modulus of the neuronal cells (n = 5) was found to be 86.2 ± 42 Pa and 0.97 ± 0.4 kPa which are in agreements with the previous studies made by various researchers by colloidal probes [222,238] and the sharp tips [217,228,231] on various cells. The width of the log normal distribution histograms is wider for sharp probes as compared to colloidal probes and the stiffness histograms with the sharp tips also show more stiffness the variation in contrast to colloidal probes. The stiffness was found in the range of 0.1-0.4 mNm^{-1} for the sharp tips cells data which is slightly lower than the stiffness measured with colloidal probes measured cells stiffness (0.1-0.8 mNm^{-1}) [135,241].

5.3.3 Nanomechanical mechanical properties of neurites

An attempt was made to measure the elastic properties of neurites and to compare this with the elasticity of the cells and growth cones. We believe this is the first detailed mechanical analysis of the NG-108-15 neuronal cell neurites. Sharp tips were used to explore the stiffness variation between nerurites. Force-volume maps were recorded at different regions of long neurites as well as from thin neurites.

Fig. 5.21 (a and b) shows the set-point force-volume maps of long neurites and arrowhead regions were further zoomed to acquire the force-volume maps. Set-point maps, contact-point maps, stiffness maps and elastic modulus maps are shown in Figs. 5.22-24 (a-d). Set-point maps are derived from 40 x 40 (i.e., 1600) force curves with the sharp tip. Contact-point maps (Figs. 5.22-5.24 (b)) reveal the true neurite topography. The colour bar represents the height variation of the neurite. Stiffness maps (Figs. 5.22-5.24 (c)) show the stiffness variation within each neurite region and the top of the colour bar corresponds to a softer area of the neurite. The central region of Fig. 5.24 (c) in the stiffness map shows different stiffness with respect to the edges and the stiffness map in Fig. 5.23 (c) shows the left side of the thin neurite edge is significantly stiffer than the right side.

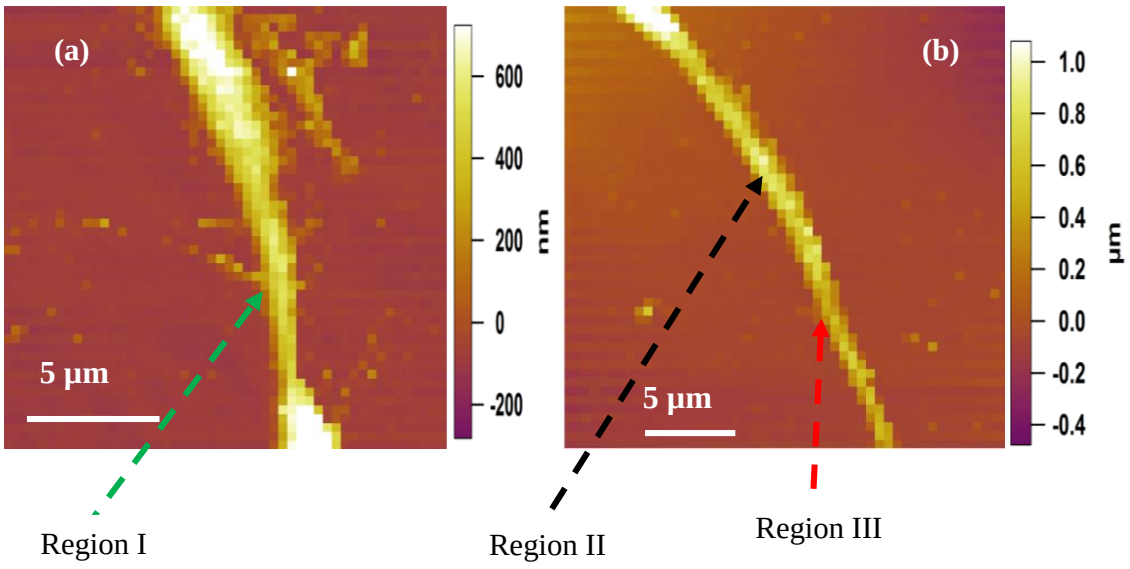

Fig. 5.21 (a-b). AFM force-volume maps of the long neurites. The region indicated by arrowhead was further zoomed and a force map of the smaller region was recorded with a sharp tip and the colour bar represents the height variation.

Figs. 5.23-5.24 (d)) show the elastic modulus (E_H) variation within the neurite, in region II and III, significantly different modulus was observed within every single scan line that presumably corresponds to microtubule structure running parallel between actin and other cytoskeleton filaments. A cross section of the line (red arrowhead) shows different modulus value in Fig. 5.24 (e).

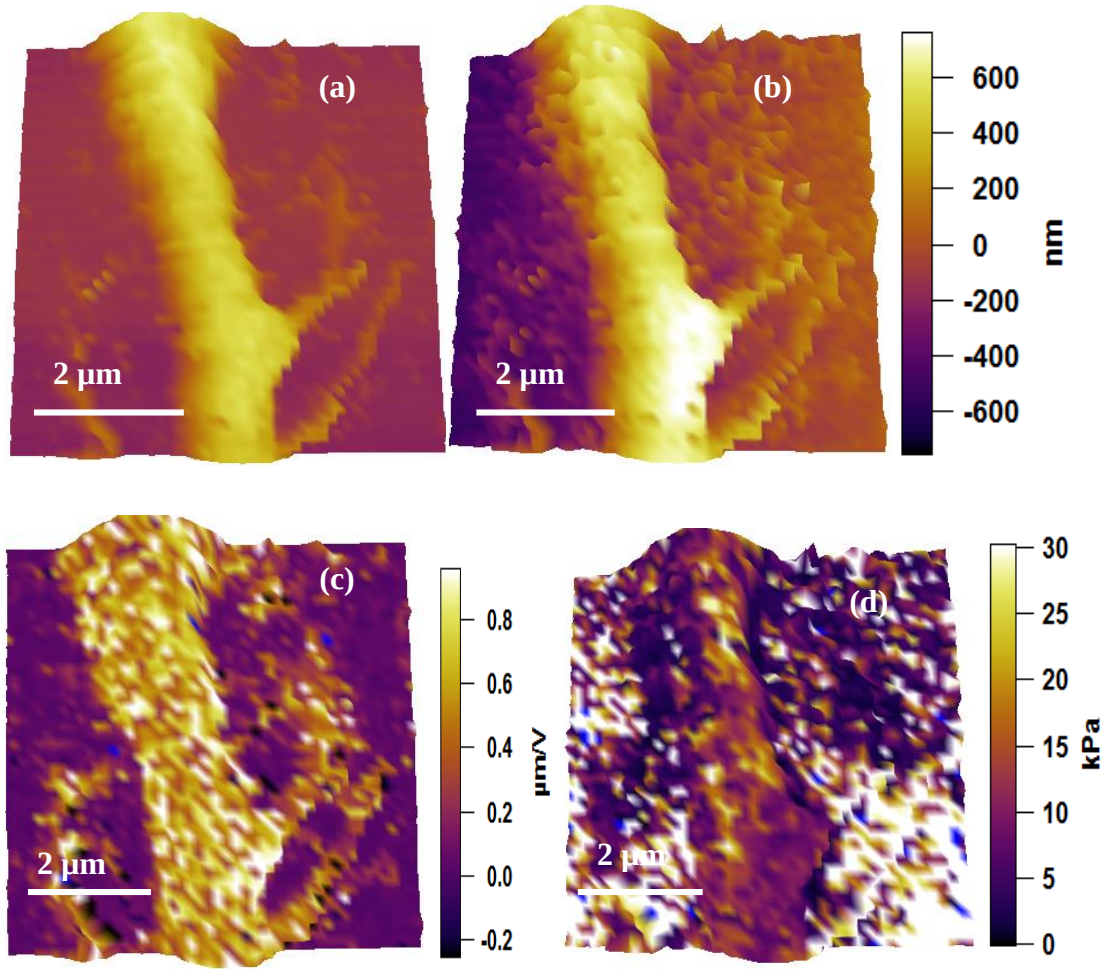

Fig. 5.22. AFM force-volume maps of the region I (a) Set-point force map, (b) contact-point map, (c) stiffness map, (d) elastic modulus map, the colour bar represents the height, the stiffness and the elastic modulus variation. In the stiffness map, the top of the colour bar corresponds to a softer areas of the neurite. In the elastic modulus, the top of the colour bar corresponds to a stiffer region of the neurite.

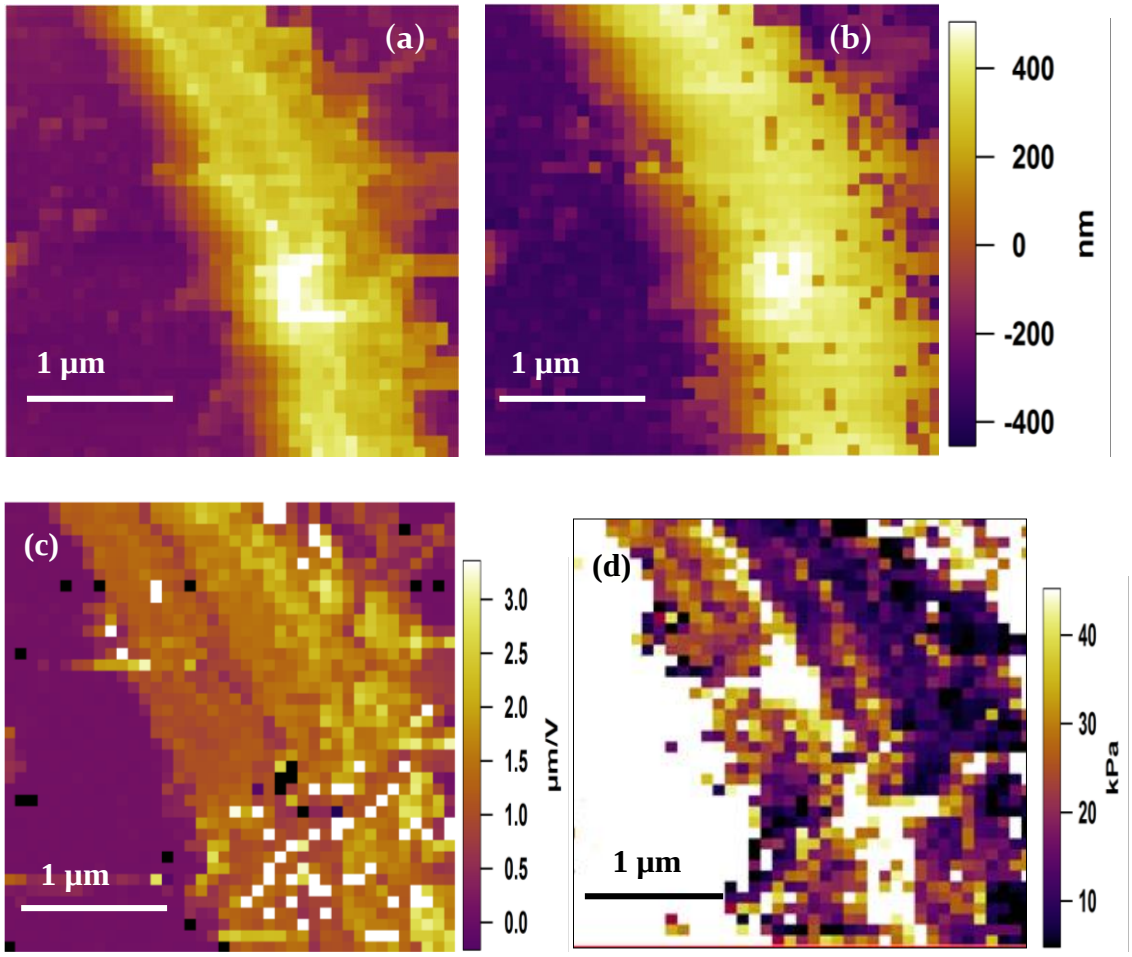

Fig. 5.23. AFM force-volume maps of the region II. (a) Set-point map, (b) contact-point map, (c) stiffness map, (d) elastic modulus map, the colours bars represents the height variation in set-point and contact-point maps. The top of the colour bar in the stiffness map corresponds to a softer area of the neurite and in the elastic modulus the top of the colour bar corresponds to a stiffer region of the neurite.

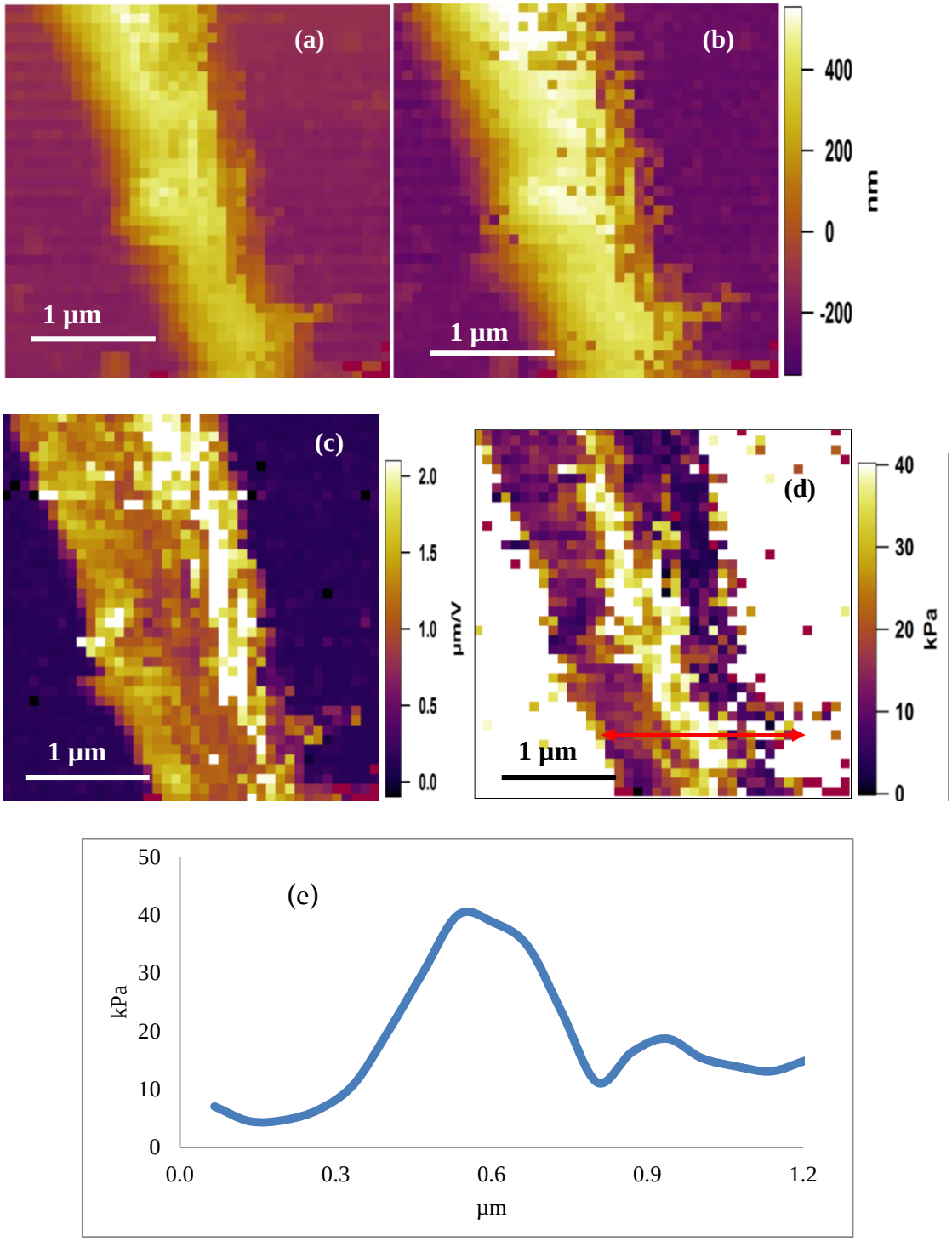

Fig. 5.24. AFM force-volume maps of the region III. (a) Set-point map, (b) contact-point map, (c) stiffness map, (d) elastic modulus map, (e) shows the elastic modulus variation across the line cross-section pointed out by red line in Fig. 5.24 (d).The colour bars represent the height, the stiffness and the elasticity variation. In stiffness map the top of the colour bar corresponds to a softer area of the neurite and the top of the colour bar in the elastic modulus map corresponds to a stifferer region of the neurite.

In Fig. 5.25 (a) an optical image shows the NG-108-15 neuronal cell with multiple immature neurites around the cell as well as a long neurite. Force-volume maps also acquired on arrays of 40 x 40 force curves on small neurites. The contact-point maps and the stiffness maps that were reconstructed from force curve raw data are shown in Figs. 5.25 to 5.26 (b-d). The contact-point map in Fig. 5.25 (c) shows the smaller neurite edge protrusions in detail that is not possible to see in the set-point map. The stiffness map in Fig. 5.26 (c) shows the stiffness variation from the distal end to the leading edges of the small neurite and the leading edges apparently seem softer.

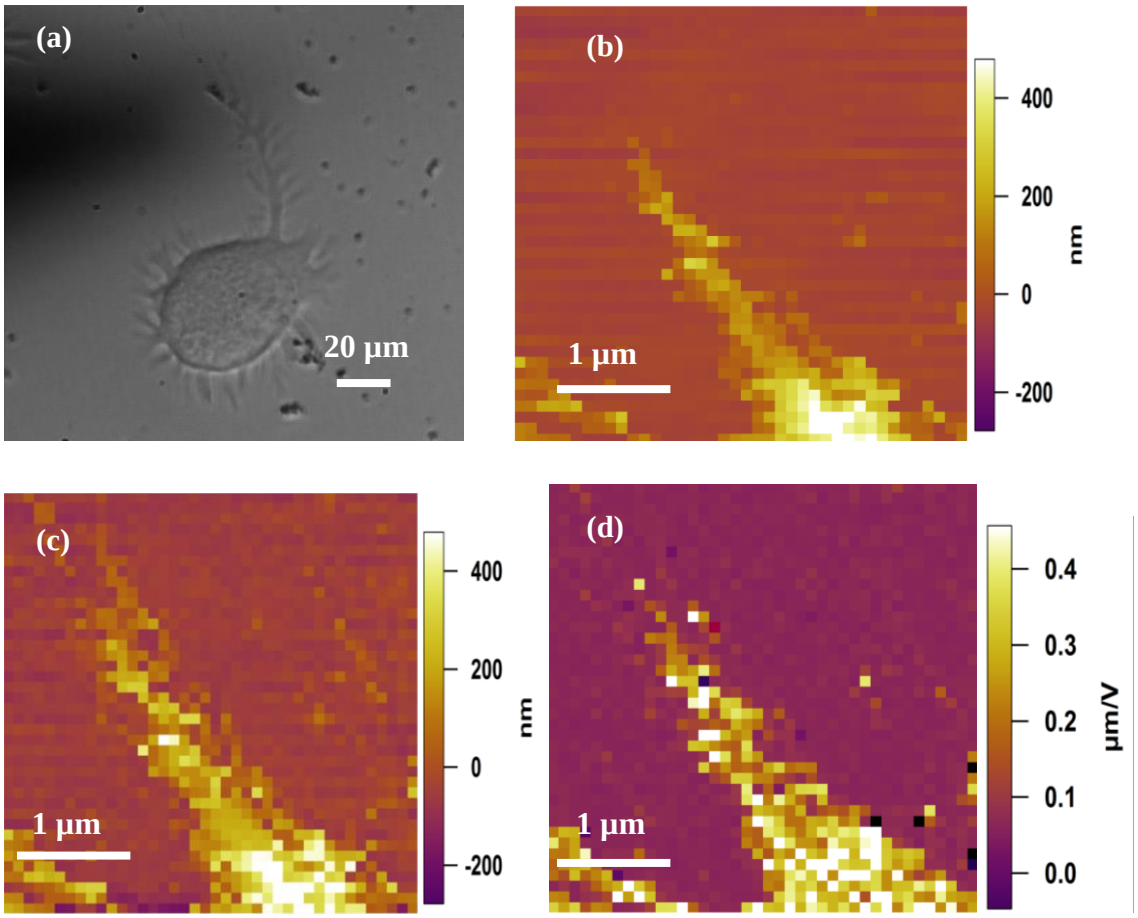

Fig. 5.25. (a) An optical image of NG-108-15 neuronal cell. AFM force-volume maps of the smaller neurite around the cell. (b) Set-point topographic map, (c) contact-point maps, (d) stiffness map and the colour bar represents the height and the stiffness variation. In stiffness map, the top of the colour bar corresponds to a softer area of the neurite.

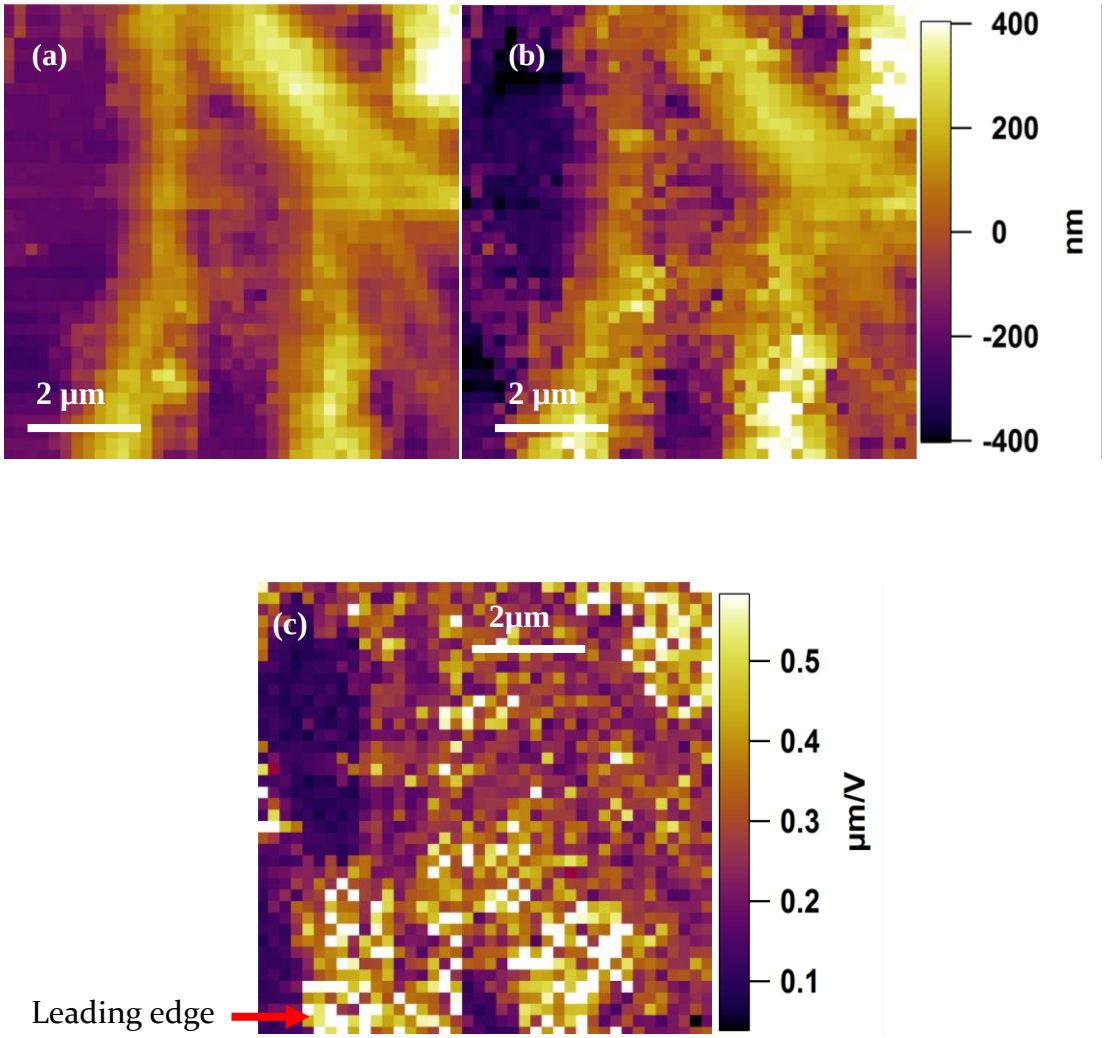

Fig. 5.26. Force-volume maps of the smaller neurite around the cell. (a) Set-point map, (b) contact-point map, (c) stiffness map and the colour bar represents the height and the stiffness variation and the top of the colour bar in the stiffness map corresponds to a softer area of the neurite.

The contact-point maps also show the broad and clearly resolved neurite edges in contrast to set-point force-volume maps. The contact-point map representation is an effective way to get the true topography of the neurite with clearly resolved neurite edge protrusions. As it is not possible to image the delicate live neurites, set-point and contact-point maps provide a meaningful way to compare neurite topography while the stiffness maps provide significant information about the stiffness of the different regions of the neurites.

An elastic modulus E_H was measured and is shown in Fig. 5.27 (a-d)) for individual neurites and as well as multiple neurites. The width of the log normal distribution curve from the

histograms was different for the three regions of the neurite. An increase in the elastic modulus was observed from region II to region III that shows an increase in the stiffness toward the leading edge [217,242]. The average elastic modulus of seven regions of long neurites was found to be 14.9 ± 8.8 kPa i.e., median values ± median absolute deviation and the average elastic modulus found to be 55.4 ± 30.8 kPa for smaller neurite around the cell. Fig. 5.27 (e-h) shows the stiffness histograms of different regions of the long neurites. The variation in the stiffness was found between different regions of the neurite and the stiffness was found to be in the range of 0.1-0.3 mNm^{-1} for all neurites. Fig. 5.27 (i) shows force-indentation curves acquired from the different cell regions correspond in different indentation at the same force

(a) Region I

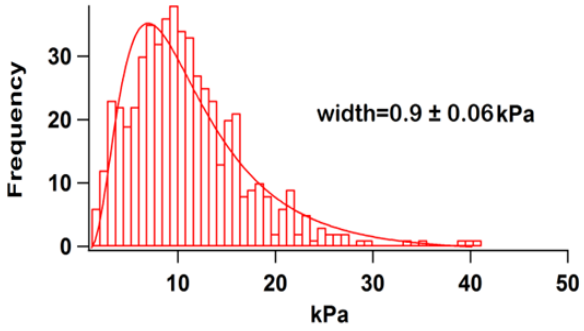

(b) Region II

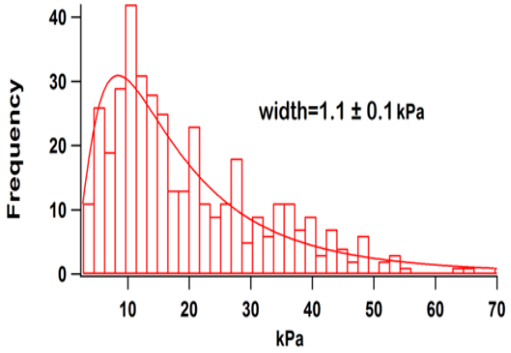

(c) Region III

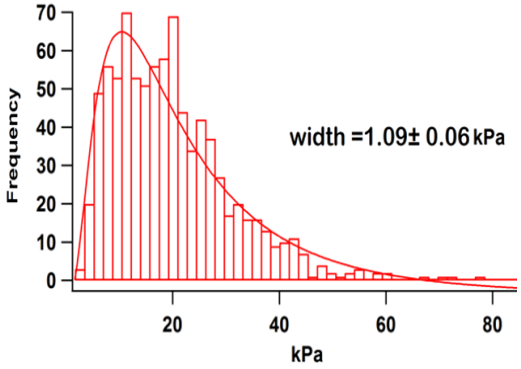

(d) for n = 7 neurite regions

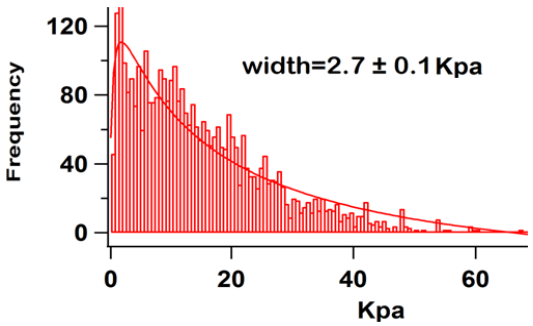

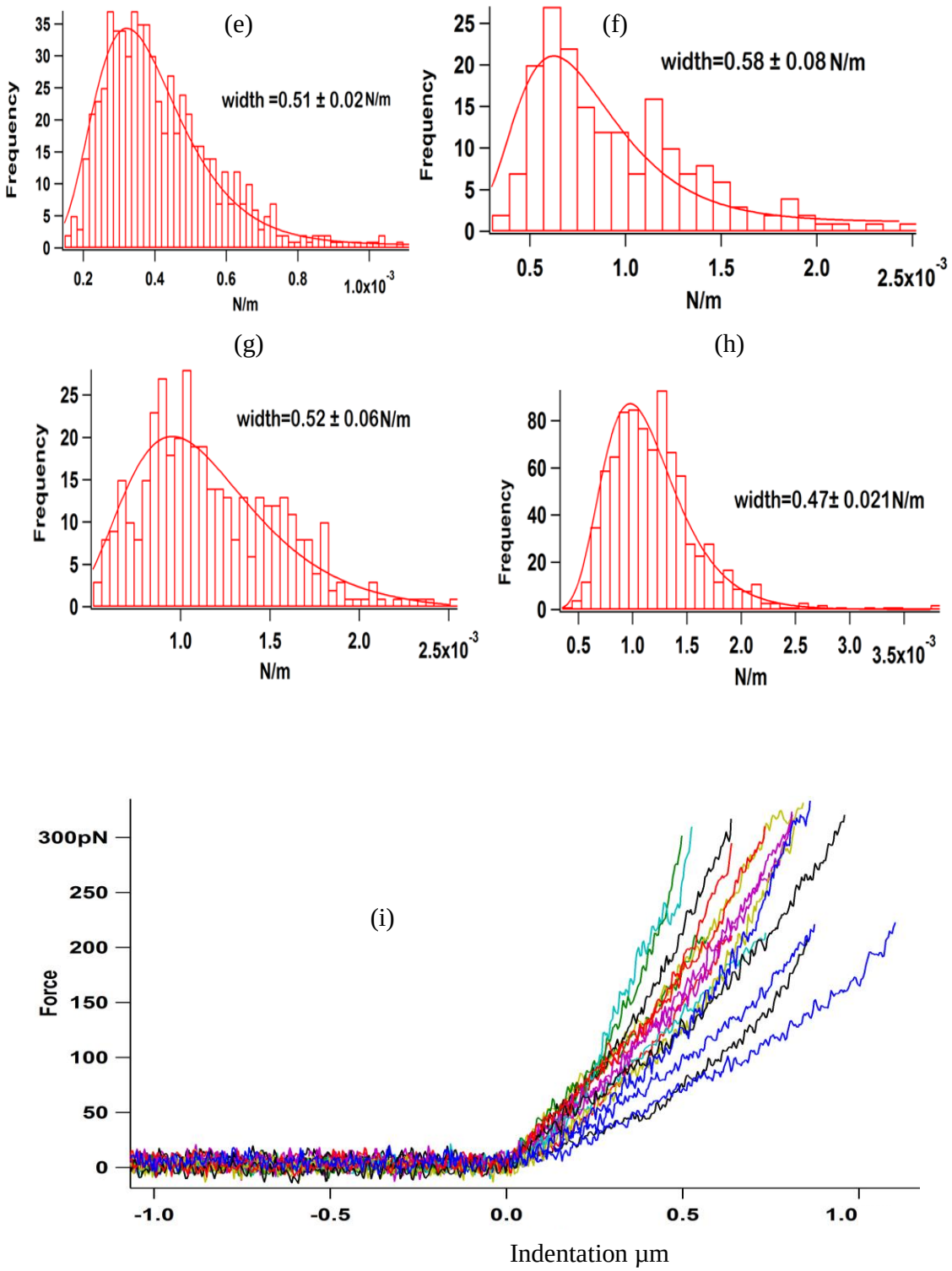

Fig. 5.27. (a-d (previous page) and e-i). Histograms of analyzed force curve data with sharp tips, E_H for different regions of the long neurite in (a-c). (d) Histogram of multiple neurites (n = 7). (e-h) Stiffness histograms of different neurites. (i) Some example of force curves acquired from different locations of the neurite correspond to different indentation at the same force.

An elastic modulus E_H was measured and is shown in Figs. 5.28 (a-b)) for individual neurites. The width of the log normal distribution curve from the histograms was different for the two regions of the neurite.

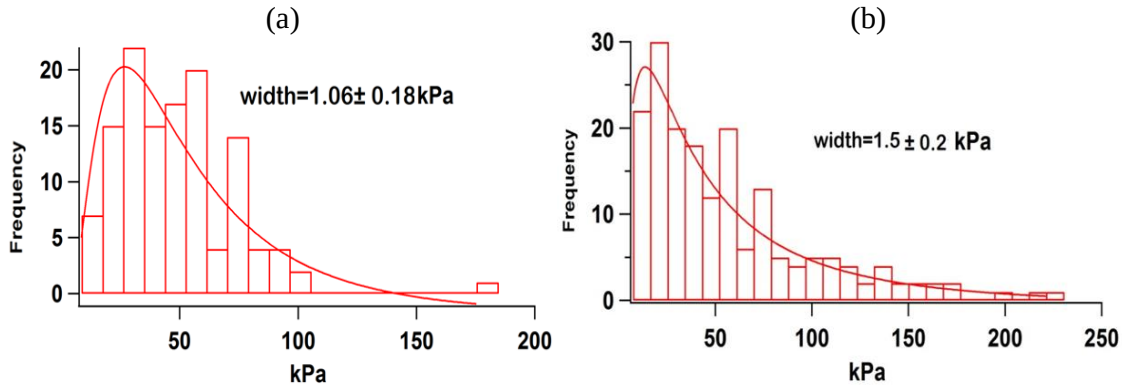

Fig. 5.28. Histograms of analyzed force curve data, E_H for individual neurites around the cell in (a-b).

This is the first detailed AFM topography and mechanical information of NG-108-15 neuronal cell neurites. Set-point and contact-point maps provide detailed topographic information and stiffness and modulus maps provide the point to point stiffness variation between different regions of the smaller neurites. The long neurites were found to be stiffer than the neuronal cell and the smaller neurite was even stiffer than the long neurite. In the long neurite, the stiffness increased from the distal to the leading edge. A previous study reported the stable and steady motion of fish epidermal cells where the highest rigidity was found at the leading protruding edge of vertical lamellipodia and the stiffness decreased with the distance from the edge [242]. The leading edge of lamellipodium exhibited highest modulus that reduced towards the distal end [242]. Elise Spedden also studied the effect of neurite extension on the neuronal cell body (cortical neuron) and measured the cell body elasticity during active neurite extension under controlled environment [217] but neurite topography and mechanical properties has not been studied yet. We find that the long neurite becomes stiffer towards the leading end and variation in the stiffness was found at the distal and leading edge for small neurites, some small neurite becomes stiffer towards the leading edge and a few of neurites growing tip is less stiff than the distal end.

5.3.4 Nano- and micromechanical properties of growth cones

To obtain the complete characterization of the mechanical properties of growth cones sharp and colloidal probes were used to acquire force-volume maps. 40 x 40 (i.e., 1600) force curves were recorded with sharp tips and displayed as set-point maps, contact-point maps and

stiffness maps were also reconstructed from the force curve data as shown in Figs. 5.29-5.31 (a-c). Contact-point maps (Figs. 5.29-5.31 (b)) reveal the detailed topographic information in contrast to set-point maps (Figs. 5.29-5.31 (a)). Stiffness maps (Figs. 5.29-5.31 (c)) show the growth cone stiffness variation where the thin filamentous structure was found to be stiffer than the central region. These finding are consistent with previous growth cone studies [108,109], we can assume that the long thin filaments comprise of actin bundles and the central region consisted of microtubules. The stiffness map of the growth cone in Figs. 5.29 - 5.31 (c) were reconstructed form the set-point force curve data.

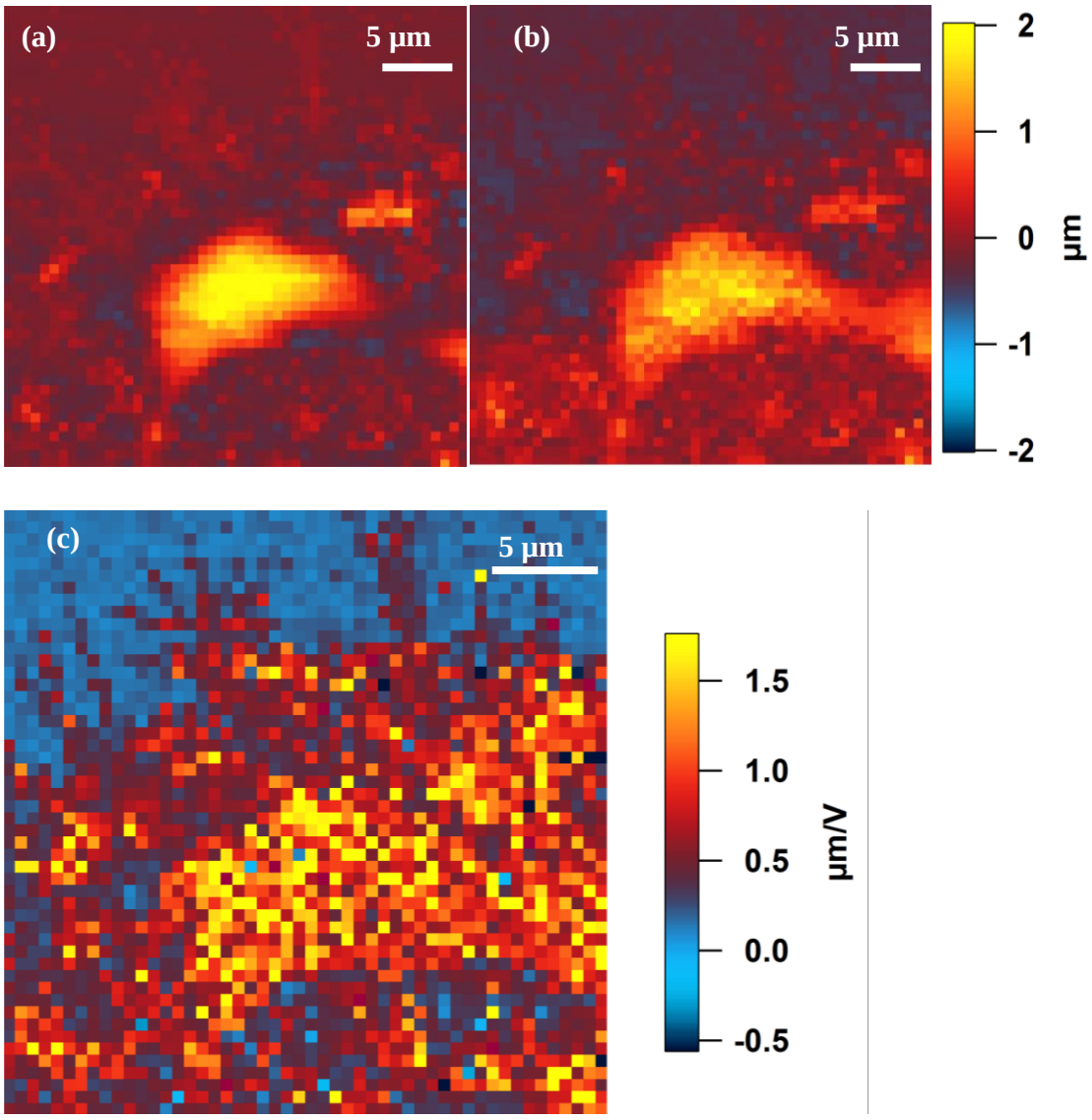

Fig. 5.29. AFM force-volume maps of the NG-108-15 growth cone acquired with a sharp tip. (a) Set-point map, (b) contact-point map, (c) stiffness map, the colour bar represents the height and the stiffness variation and the top of the colour bar in the stiffness map corresponds to a softer area of the growth cone.

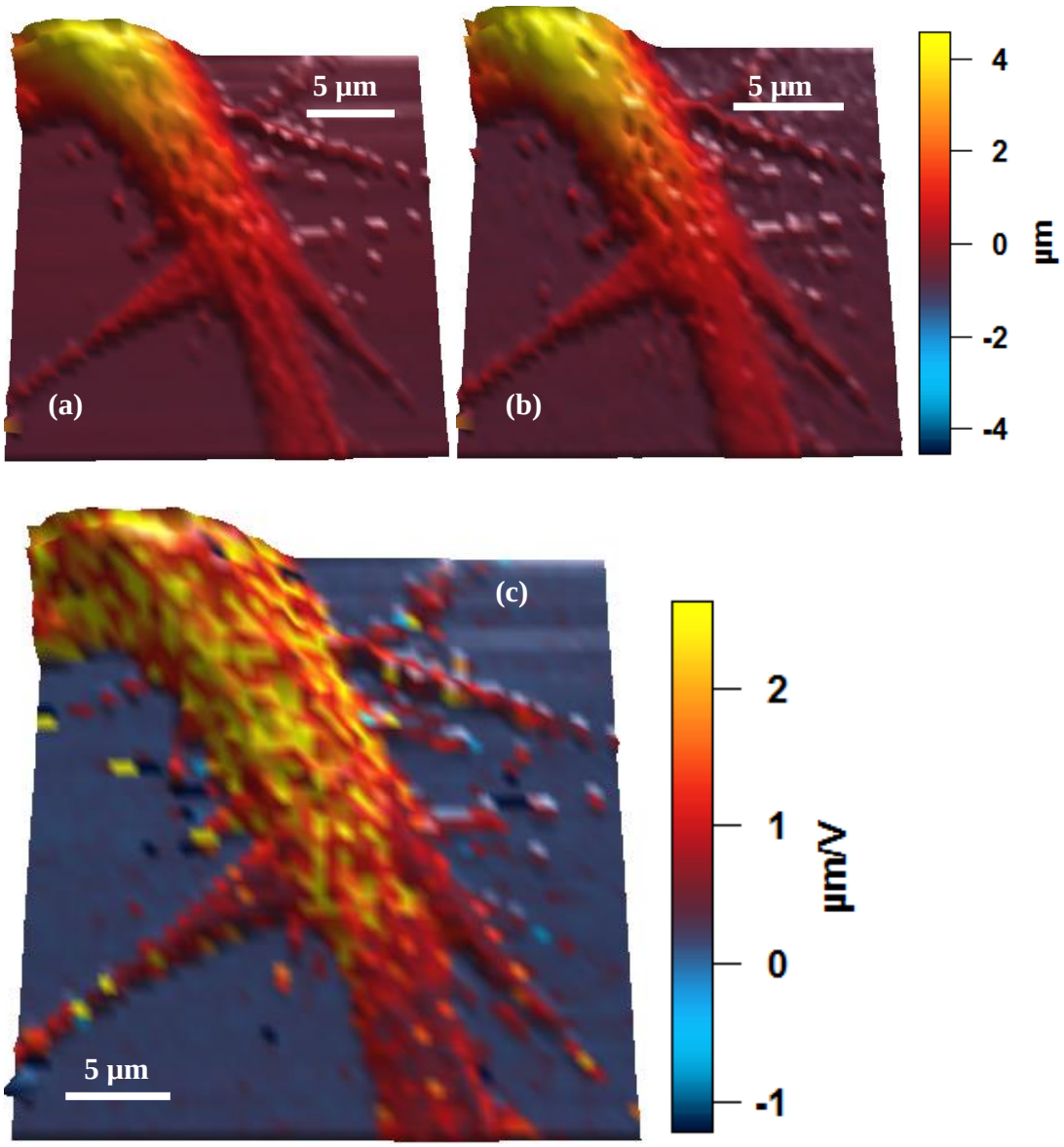

Fig. 5.30. AFM force-volume maps of the NG-108-15 growth cone obtained with sharp tip. (a) Set-point map, (b) contact-point map, (c) stiffness map, the colour bar represents the height and the stiffness variation and the top of the colour bar in the stiffness map corresponds to a softer area of the growth cone.

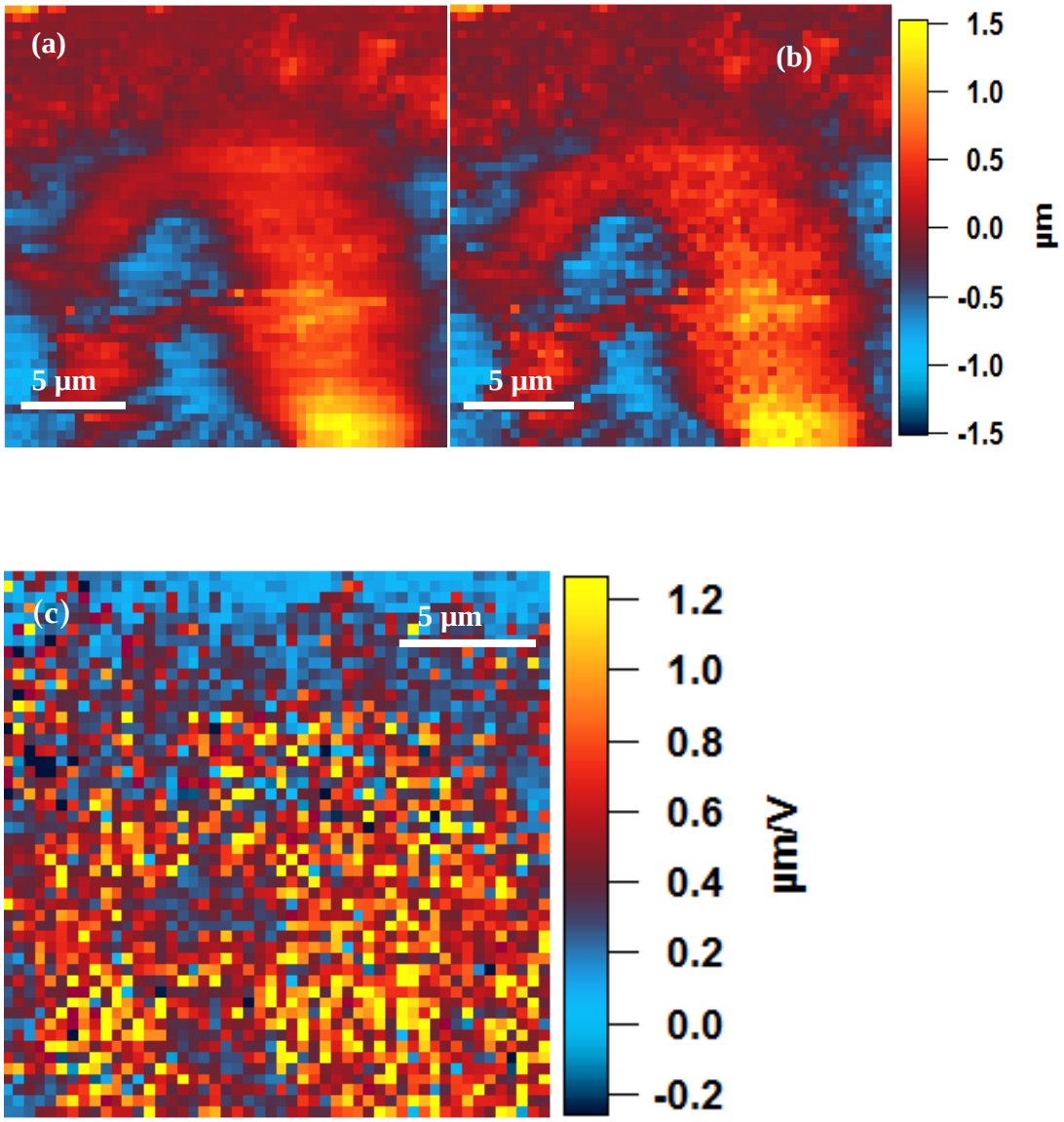

Fig. 5.31. AFM force-volume maps of the NG-108-15 growth cone acquired with sharp tip. (a) Set-point map, (b) contact-point map, (c) stiffness map, the colour bar represents the height and the stiffness variation and the top of the colour bar in the stiffness map corresponds to a softer area of the growth cone.

Next, force-volume maps were obtained from the growth cone with colloidal probes, 50 x 50 force-displacements were recorded and displayed as set-point maps, contact-point maps and stiffness maps as shown in Figs. 5.32-5.34 (a-c).

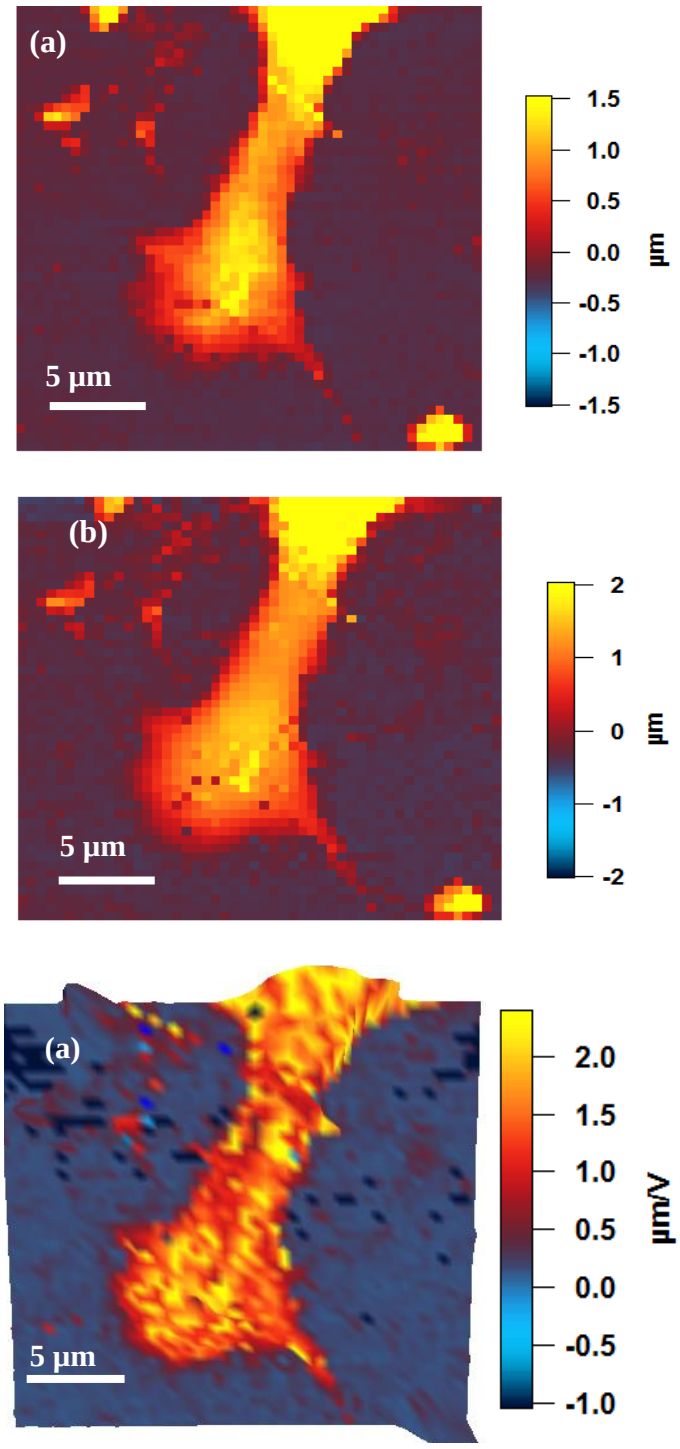

Fig. 5.32. AFM force map of growth cone acquired with a colloidal probe. (a) Set-point map, (b) contact-point map, (c) stiffness map, the colour bar represents the height and the stiffness variation and the top of the colour bar in the stiffness map corresponds to a softer area of the growth cone.

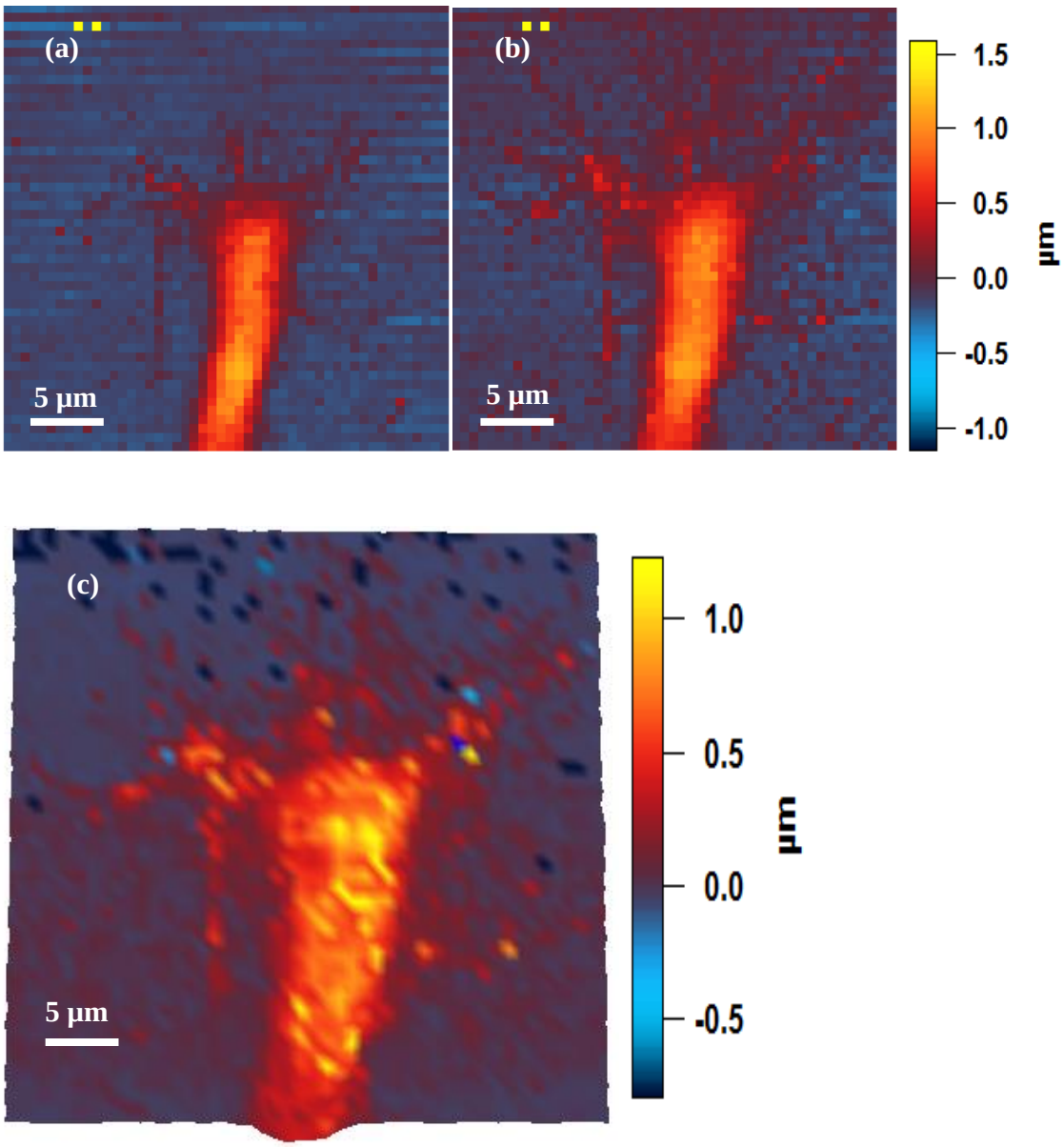

Fig. 5.33. AFM force-volume maps of the NG-108-15 growth cone acquired a colloidal probe. (a) Set-point map, (b) contact-point map, (c) stiffness map, the colour bar represents the height and the stiffness variation and the top of the colour bar in the stiffness map corresponds to a softer area of the growth cone.

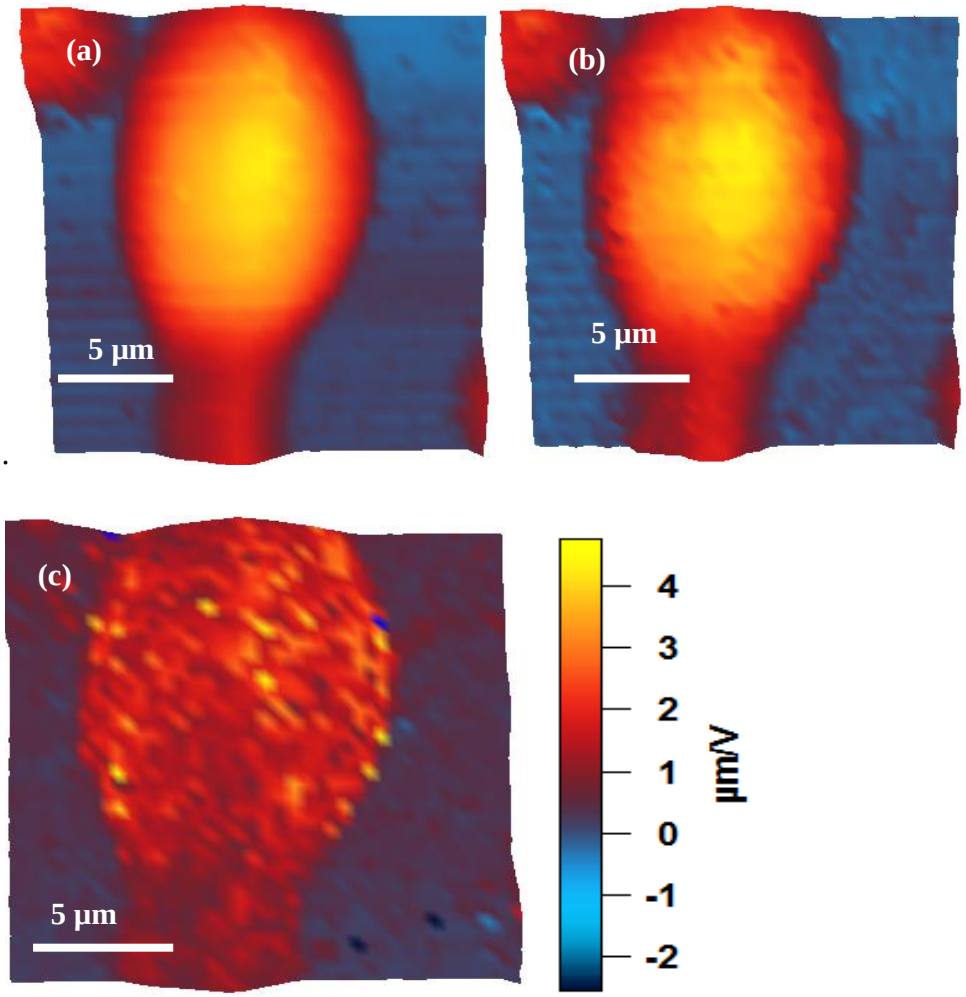

Fig. 5.34. AFM force-volume maps of the growth cone acquired with a colloidal probe. (a) Set-point map, (b) contact-point map, (c) stiffness map, the colour bar represents the height and the stiffness variation and the top of the colour bar in the stiffness map corresponds to a softer area of the growth cone.

Contact-point maps acquired with the colloidal probes do not provide accurate information about the thin filaments and growth cone edges. The use of colloidal probes (R =10 µm) is not a good approach to acquire the detailed topography of small filaments on account of the large contact area. These images failed to provide the important filaments growth information. Moreover, the sharp tips provide significant information about the growth cone filaments in contrast to colloidal probes and clearly resolve the edge protrusion and filaments. Using the sharp tip, 50 x 50 arrays of recorded force curves on the growth cone were computed and the data plotted in a histogram. Individual cells and multiple cells elastic modulus E_H data was plotted as histograms with log normal distribution curve is shown in Fig. 5.35 (a-d). The

average modulus (median values ± median absolute deviation) was found to be 4.1 ± 2.4 kPa for n = 5 growth cones [108,223]. Each growth cone stiffness histograms was also acquired from the gradient of the approach force curve data.as shown in Fig. 5.35 (e-g). Fig.5.35 (h) shows some examples of force curves recorded at different regions of the growth cone at the same force corresponds different indentation.

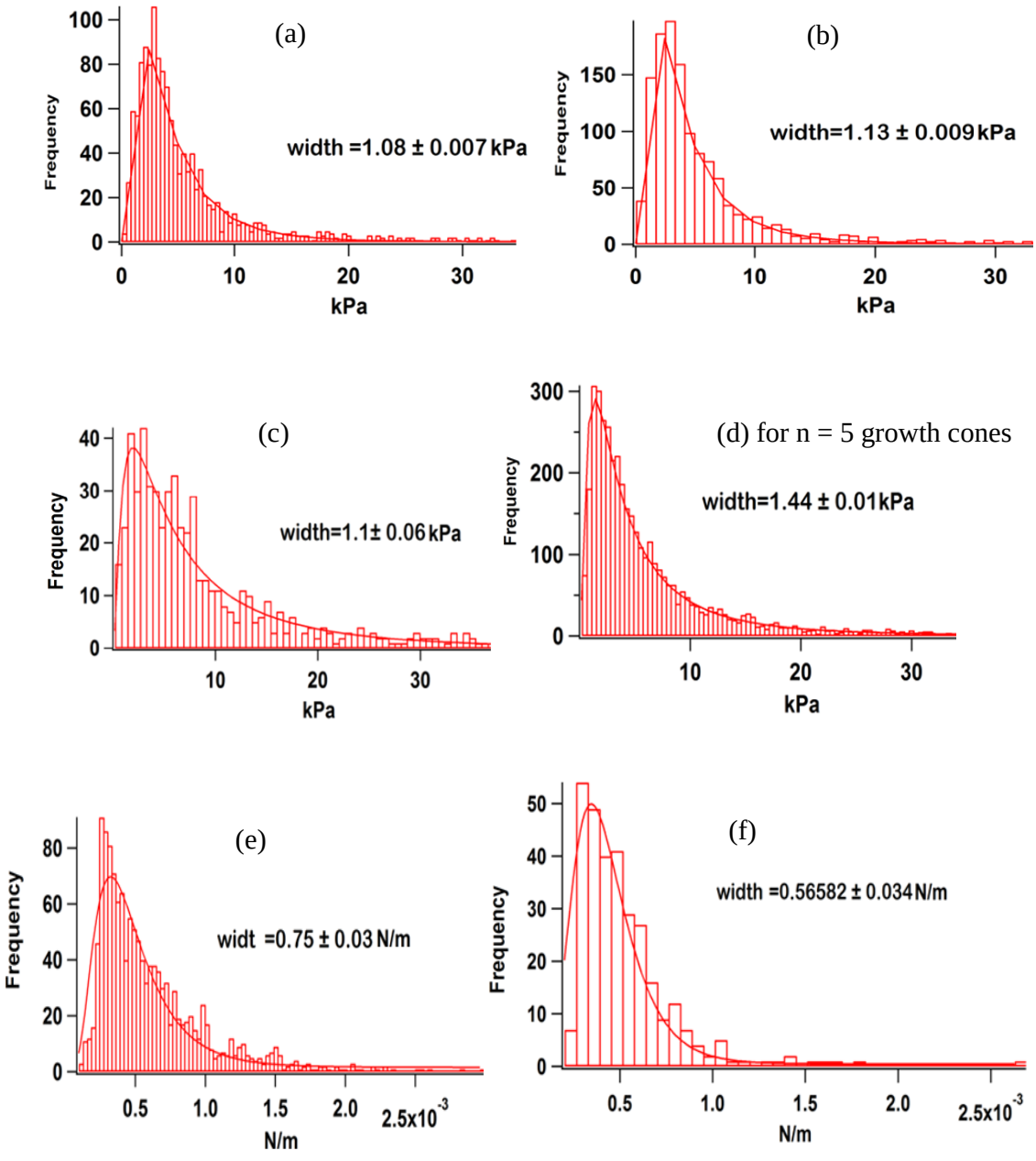

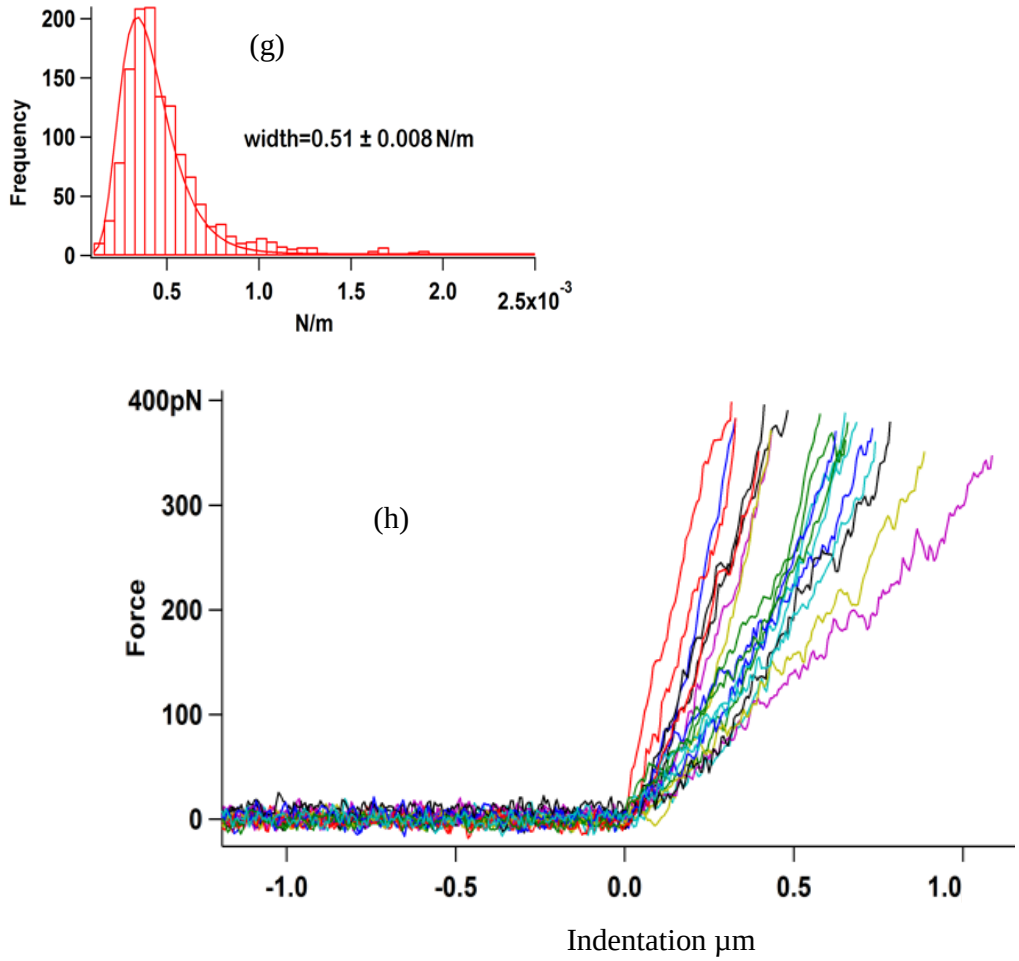

Fig. 5.35. (a-f (previous page) and g-h) Histograms of analyzed force curve data with sharp tips, E_H for individual and multiple growth cones as shown in (a-d). (e-f) Stiffness histograms acquired from the slope of the approach force curve data. (h) Set of force-indentation curves at different regions of the growth cone correspond to different indentation at the same force.

Force curve data obtained using colloidal probes is plotted as histograms with the corresponding distribution profile for the individual growth cone and multiple growth cones as shown in (Fig. 5.36 (a-d)). The average modulus value was found to be in the range of 99 ± 60 Pa (median values ± median absolute deviation) for growth cones (n = 5) [219]. Each growth cone stiffness histogram was also acquired from the slope of the full force curve data and these histograms fitted with the log normal distribution curves are shown in Fig. 5.36 (e-g). Some of example force curves acquired from different locations of the growth cone are shown in Fig. 5.36 (h).

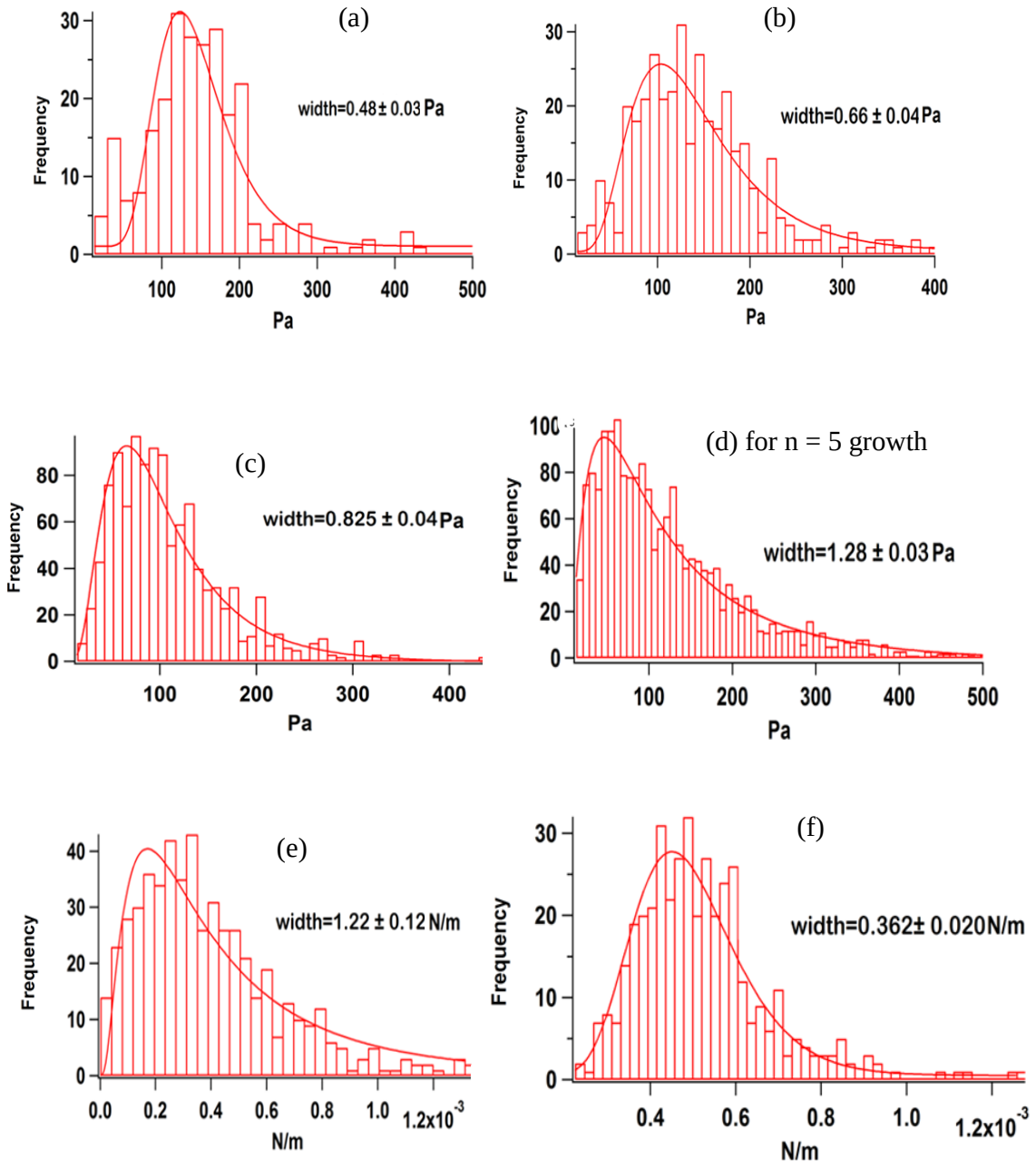
(a)
width=0.48± 0.03 Pa
Frequency
Pa
(b)
width=0.66 ± 0.04 Pa
Frequency
Pa
(c)
width=0.825 ± 0.04 Pa
Frequency
Pa
(d) for n = 5 growth
width=1.28 ± 0.03 Pa
Frequency
Pa
(e)
width=1.22 ± 0.12 N/m
Frequency
N/m
1.2x10-3
(f)
width=0.362± 0.020N/m
Frequency
N/m
1.2x10-3

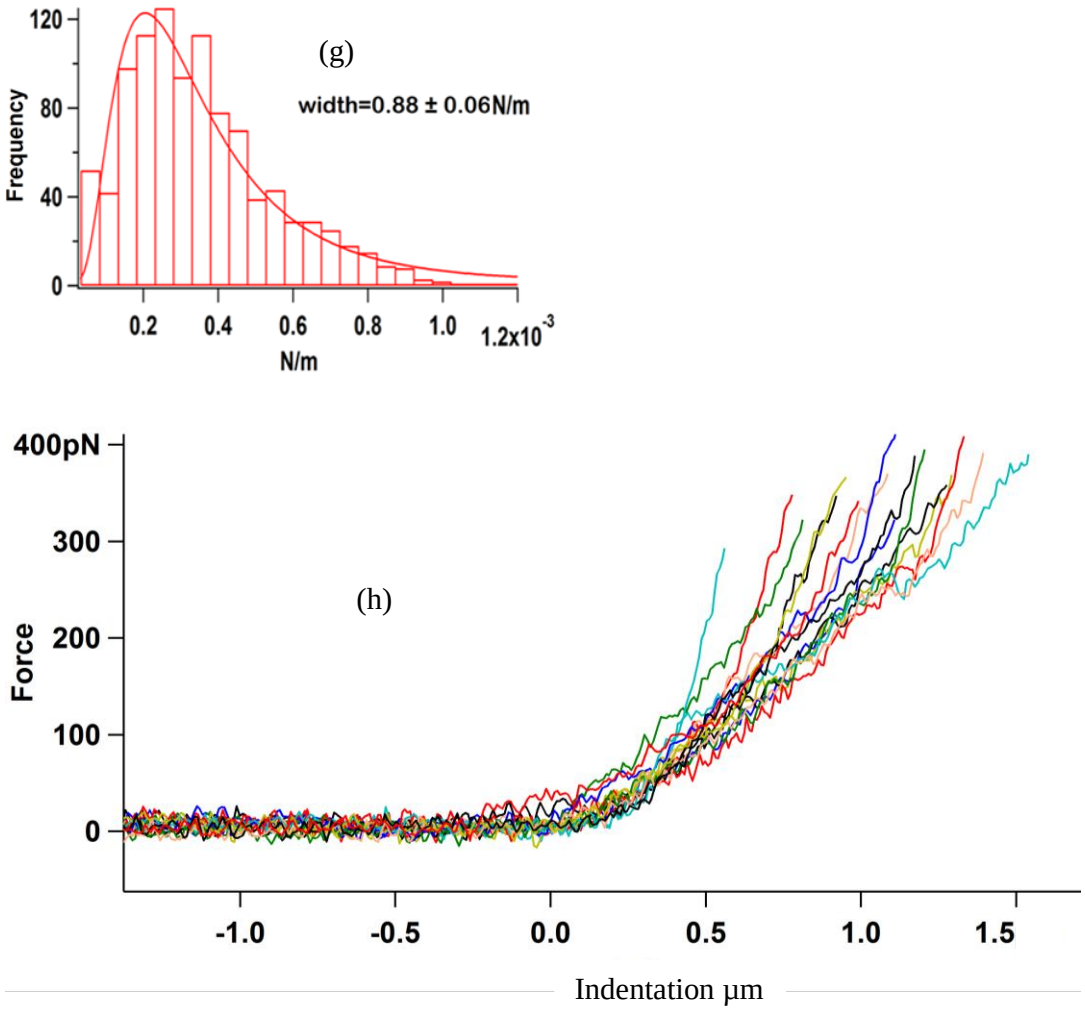

Fig. 5.33. (a-f (previous page) and g-h) Histogram of analyzed force curve data with colloidal probes, E_H for the individual (a-c) multiple growth cones (d). (e-h) growth cones stiffness histograms acquired from the slope of the approach curve data. (h) A number of forces curves acquired at different regions of a growth cone correspond different indentation at the same force.

5.4 Discussion

In this study, sharp tips and colloidal probes provide the elastic properties of the cells (primary Schwann cell and NG-108-15 neuronal cells), neurites and growth cones. Primary Schwann cells were found to be significantly stiffer than NG-108-15 neuronal cells with sharp tips (3.1 ± 1.9 kPa for primary Schwann cell and 0.97 ± 0.4 kPa for NG-108-15 cells) but almost same modulus was found in colloidal probes measurements for both the cell types (92.8 ± 49.6 Pa) for primary Schwann cells (86.2 ± 41.8 Pa) for NG-108-15 neuronal cells. Growth cones were found to be stiffer than the neuronal cells for the mechanical measurements made with both the probe types and the neurites were found to be much stiffer than neuronal cells and growth

cones. Therefore their modulus values were found to be 0.97 ± 0.4 kPa (NG-108-15 neuronal cells), 4.1 ± 2.4 kPa (growth cones), 14.9 ± 8.8 kPa (long neurite), and 55.4 ± 30.8 kPa (small neurite). Higher elastic modulus have been reported previously in various AFM sharp tips studies in contrast to spherical probes [160,221,239] and similar results were also reported in this study. Previously, two times higher elastic modulus E_H was reported with a sharp tip for the alveolar epithet cell and the living Chinese hamster cell and four times higher elastic modulus was found for macrophages as compare to colloidal probes [221,243]. The sharp tip with smaller contact area provides the local elastic information in the vicinity of probe and the colloidal probe is used to measure the average elastic properties of the cells. The significant difference in the stiffness was found in the sharp probe analyzed force curve data of primary Schwann cells and NG-108-15 neuronal cells. Primary Schwann cell cells were found to be stiffer than neuronal cells but the stiffness was found to be almost similar in the colloidal probe data of primary Schwann cell and NG-108-15 neuronal cells. Growth cones were observed to be stiffer than primary Schwann cells and NG-108-15 neuronal cells but in neuritis the stiffness was found twice higher than the cells and growth cones. The neurites stiffness increased towards the leading direction.

At the same lever stiffness and approximately the same force, colloidal probes apply a lower stress as its contact area is larger while it makes contact with the surface. As a result the peak stress reached with colloidal probes is lower than the minimum detectable stress with the sharp tips. The sharp tip with the small area indented further and measured mechanical properties of probably different regions of the cytoskeleton in contrast to colloidal probes and hence a yields higher modulus value. Force-indentation curves acquired on the cell surface with the sharp tip are rather linear and the Hertz model analysis may not be robust or ideal model for cell mechanics but currently there is no good alternative available in the literature.

Mechanical properties of different cells have been determined not only with nano and micro indentation experiments but the elastic modulus has also been measured with magnetic and optical tweezers [221]. These technique experiences less force in contrast to AFM cantilevers due to lower spring constant and higher sensitivity. In magnetic and optical tweezers experiments, the elastic modulus of 350 Pa and 450 Pa was reported for macrophages, respectively [221,244,245]. Colloidal probes data can be compared with already existing AFM data as well as optical and magnetic tweezers data. Therefore, the elastic modulus obtained from colloidal probe cells data produced the same order of magnitude as reported by optical and magnetic tweezers. Results obtained from nano-indentation cannot be over- or under-estimated because no parallel technique was available to compare nano-mechanical

properties except from already published AFM data. The nano-indenter provides the local elastic variation information in the vicinity of the probe but the colloidal probe provides the average dynamic change of the whole cell elasticity. For the sharp probe data the elastic information was obtained using the conventional Sneddon equation. In a recent study, the finite tip radius effect was quantified in the conventional Sneddon equation and the associated error was calculated for the deformation of a solid [246]. The elastic properties of the skeletal muscle and cardiac muscle was calculated by assuming the blunt cone geometry with the spherical cap and slightly lower elastic modulus was obtained as compared to the sharp tips [228]. Next, the tip deformation was characterized by the tip radius fluctuation under indentation and found that the tip deformation depends upon the material property [247]. All of these results put light on many concepts related to nano-indentation experiments but many open questions still remain. Therefore, considering the finite radius effect and the blunt cone geometry with a spherical cap may be a good approach for the elastic modulus measurement in nano-indentation experiments but the radius of the indenter is not provided by the manufacture with great accuracy which can be an issue for the actual elastic modulus determination.

The growth cone analysis with the sharp and colloidal probes provides the local and average elastic properties, respectively. In this study, all micro and nano-indentation experimental measurement were performed in serum free medium. Significant difference in the measured elastic modulus was found between those measurements made with the sharp tips and colloidal probes. The sharp tip resulted the modulus of 4.1 ± 2.4 kPa for n = 5 growth cones and colloidal probes gave the modulus of 99 ± 60 Pa for n= 5 growth cones. The Log normal distribution width is wider for the sharp tip compared to the colloidal probes. Mechanical properties of the NG-108-15 growth cone were previously reported by using the modified Hertz model with frequency-dependent viscoelastic behaviour and the elastic modulus was found to be different compared to that we measured in our study with sharp tips. The central region was found much stiffer than edges in the reported study this higher stiffness might be due to the presence of 2.5% of serum medium and the viscous effect [219].

Previous studies reported the elastic modulus of different regions of the Aplysia and dorsal root ganglion (DRG) growth cones with sharp probe, in this study sharp probes recorded force map of the full growth cones and the elastic modulus of different regions of the growth cone are in consistent with the Aplysia and DRG growth cones [108,204].

In this study, we measured the elastic modulus of three different regions of the NG-108-15 neuronal cell; the cell body, neurites and the growth cone. The elastic modulus for the cells,

growth cones and neurites are 0.97 ± 0.4 kPa, 4.1 ± 2.4 kPa, 14.9 ± 8.8 kPa and 55.4 ± 31 kPa respectively as measured with the sharp tips and moduli of 86.2 ± 42 Pa and 99 ± 60 Pa were measured with the colloidal probes for neuronal cells and growth cones. These results are consistent with the previous chicken dorsal root ganglion (DRG) neurons study, where the largest increase in stiffness was found in neurite outgrowth extensions due to microtubule disruption of the cell [217]. Another recent AFM study suggested an increase in the elasticity of the DRG neuronal growth cone due to modification in the inner framework of structural protein [204].

Previous neuronal cells, growth cones and the nervous tissue supporting cells (glial cells including primary Schwann cells) studies reported that one should take into account the viscoelastic material and heterogeneity of these cells because their mechanical response directly depends on the loading rate, control environment and applied force. Elise Spedden et al. reported three different neuronal cells including DRG, cortical and PC-19 with elastic moduli in the range of 0.1-2 kPa, 0.4 kPa and 0.2 kPa respectively [203,217]. McNally et al. reported the chicken DRG elastic modulus of 60 kPa at 35^{o} C and a reduction in the elasticity was observed with time [216].

The Mann-Whitney test is a non-parametric test that is used to compare the difference between two independent groups [248]. The Mann-Whitney test is used to test the null hypothesis (i.e., generally describe, there is no relationship exist between two measured group observations) and used when data is not normally distributed. One cannot interpret the probability value (p value) unless the null hypothesis is being tested. If the probability value is less than a significant level ($p < 0.05$) then the null hypothesis is rejected and outcome is said to be statistically significant (i.e., groups observations are distant). If the probability value is greater than significant level ($p > 0.05$) then the null hypothesis is approved and outcome is said to be not statistically significant (i.e., groups observations are similar). IBM SPSS Statistics software was used to perform the Mann-Whitney test on primary Schwann cells and the Ng-108-15 neuronal cells.

A Mann-Whitney test was applied to two different cells as well as similar cells data acquired with two different probes. The entire conclusion was drawn on the basis of $P < 0.05$ or $P > 0.05$ after applying the Mann-Whitney test. Significant level ($P < 0.05$) was found between all the sharp tip data of individual and multiple cells of primary Schwann cells, neuronal cells, growth cone and neurite which correspond to cells are statistically significant. Similarly Mann-Whitney test was also applied to the colloidal probe data and a significant level was found between the individual primary Schwann cells, neuronal cells and growth cone data

with $P < 0.05$ value that conclude cells are statistically significant. On the other hand significance level as determined for multiple primary Schwann cells and multiple neuronal cells as well as multiple primary Schwann cells and multiple growth cone data was found greater than 0.05 ($P > 0.05$) that conclude cells are not statistically different.

5.5 Conclusion

In this study, the AFM revealed the difference in the elastic properties of primary Schwann cells, neuronal cells, growth cones and neurites. We analyzed the mechanical properties of neuronal cells, and growth cones with sharp and colloidal probes and neurites were analyzed with sharp probes only. The average elastic modulus was obtained in the range of 3± 1.9 kPa and 0.97 ± 0.4 kPa [217,249–251] with the sharp tips and93 ± 50Pa and 86 ± 42 Pa [219,233] with colloidal probes for the primary Schwann cells and the NG-108-15 neuronal cells, respectively.

Nano mechanical measurement was also performed on neurites of NG-108-15 neuronal cells. We believe this is the first detailed mechanical study of the small and long neurites which provides new insight into cytoskeleton variation in a very small region that was not possible to study with other conventional means. Nano-mechanical properties were analyzed at different regions of the long neurites and the average elastic modulus of the long neurites (15 ± 9 kPa) was found to be higher than for growth cones (4 ± 2.4 kPa) and the cells (0.97 ± 0.4 kPa) and in long neurite, elastic modulus and stiffness increased towards the neurite leading edge [252]. Similarly the average elastic modulus of smaller neurites with multiple branches ending around the cell was also measured at smaller indentation and the average elastic modulus of 55.4 ± 31 kPa was found, higher than the cell body, long neurite, and growth cones. All of these observations about higher stiffness were supported by previous AFM study of Aplysia and DRG growth cones where the leading edge of the growth come was found stiffer than central region [108,204].

The average elastic modulus acquired on the growth cone with both probes provides a larger elastic modulus in contrast to the neuronal cells. Sharp tips resolved the complete filamentous structure that was not possible with colloidal probes. The average elastic modulus was found in the range of 15 ± 9 kPa and 99 ± 60 Pa for nano and micro mechanical measurements, respectively. These results are consistent with previous studies of different neuronal cells and growth cones (chicken, DRG, Aplysia) [108,204,215,216,219]. The stiffness maps show the stiffness variation between different regions of growth cones indicating the different cytoskeleton structure at the edges and centre as reported earlier [214].

The contact-point force-volume maps are an effective and meaningful way to present force curve data to acquire the true topography of the cells edges especially the small neurites. The contact-point images clearly resolve the cell edge protrusions and provide significant information that is probably lost in the set-point force-volume maps. Detailed mechanical study of the primary Schwann cells, the neuronal cells, the neurites and growth cones provide information to certain limits because the formation and guidance of actin filaments and microtubules are still unclear.

In conclusion, the AFM study provides detailed mechanical properties of live primary Schwann cells, live NG-108-15 neuronal cells, growth cones and neurites with two different probes. In primary Schwann cells, variation in stiffness was found between different regions of the cell. The cell periphery was found stiffer than the cell central region. Similarly significant variation in the stiffness was observed between NG-108-15 neuronal cells, growth cones and neurites. The neuronal cells stiffness was found smaller than growth cones and neurites. The growth cone stiffness was found higher than neuronal cells and the primary Schwann cells. Moreover, variation in the stiffness between different regions of the neurites as well as within the small region of the neurite was found. Cell mechanical properties provide information in two forms in regards to nerve regeneration. First, to produce a nerve guide with similar mechanical properties as that of the nerve tissue (i.e., made up of different neuronal cells) itself. Second, to provide the suitable patterned substrate that is optimal for the neuronal and Schwann cell growth [253]. Finally, it gives new information about the mechanics of the cell structure and how this varies within the particularly complex structures of nerve cells, providing improved understanding of cell biophysics.

Chapter 6 - Conclusion

6.1 Maskless photolithography on BPRS-100 resist and on NPPOC protected aminosiloxane monolayers

Maskless far-field photolithography is an attractive, low cost, simple method offering a high degree of flexibility in contrast to mask based photolithography setups where photo-mask design is getting more complex and costly. Maskless photolithography is a potential alternative route for micron to sub-micron fabrication on different substrate.

The present study has shown the ability of maskless far-field photolithography setups to fabricate patterned structures on two different substrates. Maskless photolithography with spatial light modulator and without spatial light modulator was used to fabricate the patterns on BPRS-100 resist by UV light. Next, maskless setups without SLM was used for the fabrication of patterned structures on NPPOC protected aminosiloxane monolayers on selective areas by UV exposure. The reactive patterned SAM surface was further chemically functionalized with poly(2-(methacryloyloxy)ethyl phosphoryl choline) (PMPC) brush. The patterned line width was obtained as a function of speed of piezo motor at different exposure doses and the minimum line width was acquired close to be diffraction limit of the objective (NA = 0.60) used. The polymer brush thickness on patterned structures at different polymerization times was obtained at different patterning speed in the dry state and under water a good solvent. The grafting density of PMPC brushes were measured by analysis of the brush thickness data in water and in the dry state. Finally, maskless photolithography with a spatial light modulator fabricated patterned structures on NPPOC protected SAM by UV light. The use of high resolution maskless patterning of SAMs has not been carried out with this approach before. It provides a good alternative to near field patterning and offer more flexibility and higher speeds for certain approach.

6.2 Live and fixed cells imaging and mechanical properties of the neuronal and primary Schwann cells using atomic force microscopy

Over the past three decade the AFM has been considered as a potential tool from the life science. In the cell biology field, AFM has been extensively used to study live cells under physiological conditions. However, unlike conventional optical microscopy imaging techniques, AFM live cell imaging is very challenging. A number of factors are involved in successful AFM imaging including sample preparation, the right choice of cantilever, a stable physiological conditions, imaging parameters and stable measurement system. In this work it was found live primary Schwann cells and RN-22 Schwann cells tapping mode imaging

requires different parameter settings to acquire good quality images. Generally a small set-point amplitude was required for live cell imaging. Tapping mode revealed live primary Schwann cell and RN-22 Schwann cell topography and the cells pathway. Live and fixed RN-22 Schwann cell image comparison showed that the cell membrane of fixed cells is visible and clearly resolved the cytoskeleton structures but live cells only show the cytoskeleton structure. Different scan parameter were used for fixed RN-22 Schwann cells and fixed NG-108-15 neuronal cells because fixed cells are stiffer then live cells. The live NG-108-15 neuronal cells were not possible to image due to poor substrate attachments and unable to provide the topography information of the cell body, neuritis and the growth cone.

The AFM has been used for mechanical measurements of various biological cells under physiology condition. In cell mechanics pico-Newton forces were applied and the cell response measured at relatively large indention depths. The Hertz model was used to analyze the force indentation data to derive an elastic modulus. In this study, the Hertz model was used independently on each force curves at the entire force indentation curve length. A linear fit was observed in the whole range of force curves and found that measured elastic modulus was decreasing as a function of indentation. The Hertz model may not be a robust or reliable model for determining quantitative cell mechanical properties but there is no other well established method for measuring cell mechanics with AFM. Force-volume maps in contact mode were recorded on primary Schwann cell and neuronal cells with two different probes sizes namely the colloidal probes and sharp tips. The colloidal probes were prepared by attaching 10 μm polystyrene beads at the back end of the cantilever tip. Primary Schwann cells contact-point maps clearly resolve the cell morphology up to the edges in contrast to set-point force-volume maps. The average elastic modulus was found to be in the range of 3.1 ± 1.9 kPa with the sharp probe. Similarly the elastic modulus of the neuronal cells was measured to be in the range of 0.97 ± 0.4 kPa. Primary Schwann cells were found stiffer than the neuronal cells. Colloidal probes were used to acquire the force curves on primary Schwann cell and neuronal cells and the elastic modulus was found to be in the range of 93 ± 50 Pa and 86.2 ± 42 Pa, respectively. The colloidal probe measures the small modulus value due to large contact area and provides the average elastic properties of the cells. The sharp tip with the small contact area provides the local elastic information in the vicinity of probe and measured higher modulus value.

Similarly the elastic modulus was obtained from force curve data acquired with colloidal and sharp probes over the neuronal cell growth cones. The average elastic modulus was found to be in the range of 4.1 ± 2.4 kPa and 99 ± 60 Pa for nano and micro mechanical measurements,

respectively. Growth cones were found to be stiffer than the cells with both probes. The growth cone filamentous structures were found to be stiffer than the central region. Sharp tip force-volume maps and contact-point maps reveal more detail of the growth cone filaments.

In this study, NG-108-15 neurite mechanics was also investigated. We believe this is the first detailed mechanical study of smaller and long neurite which provide information about cytoskeleton variation in a very small region that was not possible to study with other conventional means, such as optical microscope and confocal microscope The elastic modulus was measured at different regions of long neurite and a high elastic modulus was found towards its leading edge. The average elastic modulus of long neurites was found to be higher than growth cones and cells. The stiffness maps show the stiffness variation within small neurites as well as different regions of the long neurite.

In conclusion, this thesis provides the successfully developed maskless photolithography setups and its characterization on two different substrates for the fabrication of micron to sub-micron structures. Second this thesis describes interesting results about cell mechanics of primary Schwann cells, neuronal cells and growth cones with two different probes and neurite mechanics with sharp tips. Significant variation in the stiffness was observed between primary Schwann cells and neuronal cells as well as within cells. Similarly, stiffness variation was also observed between neuronal cell body, growth cone and neurite. The stiffness of the growth cone was found higher than the neuronal cell and the primary Schwann cell. Furthermore, the stiffness variation was found between different regions of neurite as well as within the small neurite region. AFM study provides new information about the cell structure mechanics and how it varies within the complex structure of the peripheral nervous system. Cell mechanical properties also give information to observe the nerve regeneration in two ways. First, to make a nerve guide with similar mechanical properties as that of the neuronal cell itself. Second, to provide the appropriate patterned substrate that is optimal for the neuronal and Schwann cell growth.

The long term project into which this thesis will contribute is to use the maskless patterning technology developed to pattern topographic surfaces that can then be used to guide the growth and hence regeneration of nerve cells.

Neuronal cell are known to responds to mechanical and chemical cues and different synthetic material has been used to provide the guidance cues. But the use of synthetic material for peripheral nerve regeneration is usually confined to a few biodegradable material including polylactic acid (PLA), polyglycolic acid (PGA), polycaprolactone (PCL). The mechanical

properties of these materials, when used as nerve guides, have a Young's modulus of approximately 1000 MPa which is remarkably high in contrast to neuronal and Schwann cells measured in this study. Peptide and alkine amine substrates can be potentially used as cell adhesion promotion for the neuronal and Schwann cells growth. In this study, NPPOC protected aminosiloxane monolayers were exposed to UV light to create patterned amine reactive surface which was further functionalized with PMPC brush.

Future work

6.3 Investigation the mechanical properties of the neuronal cell and primary Schwann cells under different condition

Here a few suggestions are made for possible future work on the NG-108-15 neuronal cell mechanics that are being proposed on the basis of data acquired by the author in this study which may lead to a better understanding in the field of the peripheral nervous system. In AFM studies of NG-108-15 neuronal cells, growth cones and neurites, maintenance of temperature is really important for acquiring data, different conflicting results were obtained with no temperature control. Physiological conditions directly affect the mechanical properties resulting variation in elastic modulus. Here are a few suggestions for the investigation of mechanical properties of the neuronal cells, growth cones and neurites and primary Schwann cells.

- Study how the temperature affects the mechanical properties of growth cones and neurites. Acquire data at different temperature in serum free medium.
- Investigate mechanical properties of growth cones under different concentration of FCS and also investigate the effect of neurotrophins on neuritie mechanics.
- Investigate how the different substrates e.g., laminin and poly(l-lysine) affect the mechanical properties of the growth cone and neuritis.
- Investigate the mechanical properties of primary Schwann cells on laminin and compare it with the author is acquired mechanical properties on poly(l-lysine).
- Develop better method for the sharp tip indentation for cell mechanics study.

6.4 Maskless photolithography and primary Schwann cells

Micro pattern can be created on NPEOC by UV light 351 nm or 225 nm. A deprotected surface can be further functionalized with laminin and then primary Schwann cells may seeded on the patterned surface and can observed the Schwann cell cytoplasm out growth due

to available chemical cues. We can also observe the role of functionalized surface for cell-surface adhesion promotion and migration.

Maskless far-field photopatterning technique can be used to fabricate 3D objects as SAMs are surface specific resist and maskless patterning does not require a flat surface. The 3D patterned surfaces would be plated with neural cells in culture medium, allowed to process and the capacity of the 3D patterned surface for controlled neurite out growth will be characterized. All the investigations made by the author in this study that provide information about the cell height, size, volume and length will help to fabricate the 3D pattern surface to control the neurite outgrowth. This information would provide an opportunity to define the length scale of 3D pattering toward the control of neurite outgrowth.

6.5 Maskless photolithography and polymer brushes under different solvent

Maskless far-field photolithography direct write setup can be used to create the micro patterned on NPPOC protected SAMs by UV (λ = 351 nm) light and deprotected reactive surface would be further functionalized with PMPC or Poly (OEGMA) brushes. Here a few suggestions are made for the investigation of polymer brush thickness for the calculation of grafting density and degree of polymerization on patterned surfaces obtained at different speed.

Investigate the polymer brush thickness on patterned surface in the dry state and under different solvent e.g., alcohol, acetone and water and compare their grafting density. Investigate the variation in brush thickness with temperature under different solvent and compare their grafting densities.

This work was to develop a method for chemically patterning 3D structures with guidance cues for neurites growth and then to follow the growth process in situ with AFM, determining how cell mechanical properties were affected by guided growth. A maskless chemical patterning system has been developed and characterized. The cell mechanics of stationary neurites and primary Schwann cells have been characterized. In the future, it is hoped that these methods can be combined to make progress towards nerve regeneration.

References

[1] Pease R F and Chou S Y 2008 Lithography and other patterning techniques for future electronics *Proc. IEEE* **96** 248–70

[2] Gates B D, Xu Q, Stewart M, Ryan D, Willson C G and Whitesides G M 2005 New approaches to nanofabrication : molding , printing , and other techniques *Chem. Rev.* **105** 1171–96

[3] Menon R, Patel A, Gil1 D and Smith H I 2005 Maskless lithography *Mater Today* **8** 26–33

[4] Chiu G L and Shaw J M 1997 Optical lithography: introduction *IBM. J. Res. Dev.* **41** 3 – 6

[5] Sanders D P 2010 Advances in patterning materials for 193 nm immersion lithography *Chem. Rev.* **110** 321–60

[6] Wagner C and Harned N 2010 EUV lithography: lithography gets extreme *Nat. Photonics* **4** 24–6

[7] Pimpin A and Srituravanich W 2012 Review on micro- and nanolithography techniques and their applications *Eng. J.* **16** 37–56

[8] Hecht E 2001 *Optics 4th edition* (Addison-Wesley)

[9] https://www.src.org/newsroom/press-release/2014/564/

[10] Rothschild M, Horn M W, Keast C L, Kunz R R, Palmateer S C, Doran S P, Forte A R, Goodman R B, Sedlacek J H C, Uttaro R S, Corliss D and Grenville A 2009 Photolithography at 193 nm *J. Vac. Sci. Technol. B: Microelectron Nanom. Struct.* **10** 2989-96

[11] Rothschild M 1996 How practical is 193 nm lithography? *J. Vac. Sci. Technol .B: Microelectron Nanom. Struct.* **14** 4157–61

[12] Rothschild M, Bloomstein T M, Fedynyshyn T H, Kunz R R, Liberman V, Switkes M, Efremow N N, Palmacci S T and Sedlacek 2003 Optical Lithography *Lincoln lab. J.* **14** 221–36

[13] M. Hibbs, R. Kunz and M R 1997 193-nm Lithography at MIT Lincoln Lab *Solid State Technol.* **38** 69–78

[14] Mrksich M, Sigal G B and Whitesides G M 1995 Surface plasmon resonance permits *Langmuir* **11** 4383–5

[15] Hines M A and Todd J A 1996 Conformation of alkanethiols on Au, Ag (111), and Pt (111) electrodes: a vibrational spectroscopy study *Langmuir* **11** 493–7

[16] Saito N, Hayashi K, Sugimura H and Takai O 2002 The decomposition mechanism of p-chloromethylphenyltrimethoxysiloxane self-assembled monolayers on vacuum ultraviolet irradiation *J. Mater Chem.* **12** 2684–7

[17] Sun S, Leggett G J, Uni V, Hill B and Sheffield S 2007 Micrometer and nanometer scale photopatterning of self-assembled monolayers of phosphonic acids on aluminum oxide *Nano Lett.* **7** 3753–8

[18] Huang J, Dahlgren D A and Hemminger J C 1994 Photopatterning of self-assembled alkanethiolate monolayers on gold: a simple monolayer photoresist utilizing aqueous chemistry *Langmuir* **10** 626–8

[19] Lewis M, Tarlov M and Carron K 1995 Study of the Photooxidation process of self-assembled alkanethiol monolayers *J. Am. Chem. Soc.* **117** 9574–5

[20] Greg G, Joe B, Michael J T and Donald R 1994 Molecular imaging secondary ion mass spectrometry for the characterization *Anal. Chem*. **66** 2170–4

[21] Ahmad S A A, Wong L S, Hobbs J K, Leggett G J, Micklefield J, Uni V, Hill B and Sheffield S 2009 Micrometer and nanometer-scale photopatterning using 2-nitrophenylpropyloxycarbonyl-protected aminosiloxane monolayers *J. Am. Chem. Soc.* **131** 1513–22

[22] http://www.zyvex.com/nanotech/nano4/whitesidesAbstract.html

[23] Boeckl B M, Graham D and Matters M 2006 Self-assembled monolayers : advantages of pure alkanethiols *Mater Matters* **12** 3–7

[24] Arshak K, Mihov M, Arshak A, Mcdonagh D and Sutton D 2004 Focused ion beam lithography-overview and new amroaches *24th International conference on Microelectonics* **2** 16–9

[25] McCord M 1997 Electron beam lithography for 0.13 μm manufacturing *J. Vac. Sci. Technol.* **15** 2125-29

[26] Watson G P, Aksyuk V, Simon M E, Tennant D M, Cirelli R A, Mansfield W M, Pardo F, Lopez D O, Bolle C A, Papazian A R, Basavanhally N, Lee J, Fullowan R, Klemens F, Miner J, Kornblit A, Sorsch T, Fetter L, Peabody M, Bower J E, Weiner J S and Low Y L 2006 Spatial light modulator for maskless optical projection lithography *J. Vac. Sci. Technol. B: microelectron Nanom. Struct.* **24** 2852-56

[27] Smith H I, Menon R, Patel A, Chao D, Walsh M and Barbastathis G 2006 Zone-plate-array lithography: A low-cost complement or competitor to scanning-electron-beam lithography *Microelectron Eng.* **83** 956–61

[28] Memon R 2000 *P.hD thesis zone plate array lithography* (Massachusetts Institute of Technology)

[29] Spangenberg A, Hobeika N, Stehlin F, Malval J, Wieder F, Prabhakaran P, Baldeck P and Soppera 2013 Recent updates in advanced lithography *InTech* 35-5

[30] Lee K, Prabhakaran P, Park J, Kim R H, Cho N, Yang D, Park S H, Lim T W and Yong S 2008 Recent advances in two-photon lithography *CIF'8 Proceedings*

[31] Xia Y, Rogers J A, Paul K E and Whitesides G M 1999 Unconventional methods for fabricating and patterning nanostructures *Chem. Rev.* **99** 1823–48

[32] Tseng A A, Chen K and Chen C D 2003 Electron beam lithography in nanoscale fabrication : recent development *IEEE Transction Electron Packag Manfactureing* **26** 141–9

[33] Pallandre A, Glinel K, Jonas A M and Nysten B 2004 Binary nanopatterned surfaces prepared from silane monolayers *Nano Lett.* **4** 365–71

[34] Leggett G J 2006 Scanning near-field photolithography-surface photochemistry with nanoscale spatial resolution *Chem. Soc. Rev.* **35** 1150–61

[35] http://www.azonano.com/article.aspx?ArticleID=2389 2–4

[36] E.H. Synge 1928 A suggested method for extending the microscopic resolution into the ultramicroscopic region *Phil. Mag.* **6** 356-62

[37] Novotny L 2007 The history of near-field optics *Prog. Opt.* **50** 137–84

[38] Bashevoy M 2008 *P.hD Thesis Plasmon excitations in metallic nanostructures* (University of Southampton)

[39] Betzig E, Trautman J K, Wolfe R, Gyorgy E M and Finn P L 1992 Near-field and high density data storage *App. Phys. Lett.* **61** 142–4

[40] Krausch G, Wegscheider S, Kirsch A, Bielefeldt H, Meiners J C and Mlynek J 1995 Near field microscopy and lithography with uncoated fiber tips : a comparison *Opt. Commun.* **119** 283–8

[41] Madsen S, Bozhevolnyi S I, Birkelund K, Müllenborn M, Hvam J M and Grey F 1997 Oxidation of hydrogen-passivated silicon surfaces by scanning near-field optical lithography using uncoated and aluminum-coated fiber probes *J. Appl. Phys.* **82** 49-53

[42] Demers L M, Ginger D S, Park S-J, Li Z, Chung S-W and Mirkin C a 2002 Direct patterning of modified oligonucleotides on metals and insulators by dip-pen nanolithography *Science* **296** 1836–8

[43] Ginger D S, Zhang H and Mirkin C A 2004 The evolution of dip-pen nanolithography *Angew. Chem. Int.* **43** 30–45

[44] Cajal S R y, Kulkarni R and Collier C P 2003 Texture of the nervous system of man and the vertebrates *J. Neurol. Neurosur. Psyc.***70** 12096–7

[45] Piner R D 1999 Dip-pen nanolithography *Science* **283** 661–3

[46] Xia Y and Whitesides G M 1998 Soft Lithography *Angew. Chemie. Int. Ed*. **37** 550–75

[47] Leggett G J 2011 Micro and nanometer scale photopatterning of self- assembled monolayers *Mater Matters* **6** 1–6

[48] Nuzzo R G and Allara D L 1983 Adsorption of bifunctional organic disulfides on gold surfaces *J. Am. Chem. Soc.* 105 4481–3

[49] Lucy Netzer J S 1983 A New Approach to construction of artificial monolayer assemblies *J. Am. Chem. Soc.* **105** 674–6

[50] Love J C, Estroff L A, Kriebel J K, Nuzzo R G and Whitesides G M 2005 Self-assembled monolayers of thiolates on metals as a form of nanotechnology *Chem. Rev.* **105** 1103–69

[51] Chem T J 2008 Microcontact printing of an alkylsilane monolayer on the surface of glass *Turk. J. Chem.* **32** 313–21

[52] Jeon N L, Finnie K, Branshaw K and Nuzzo R G 1997 Structure and stability of patterned self-assembled films of octadecyltrichlorosilane formed by contact printing *Langmuir* **7463** 3382–91

[53] httpwww.uni-leipzig.de~pwmwebsection=introduction&page=neurons

[54] Graham D J, Price D D and Ratner B D 2002 Solution assembled and microcontact printed monolayers of dodecanethiol on gold : a multivariate exploration of chemistry and contamination *Langmuir* **18** 1518–27

[55] Chou S Y, Krauss P R and Renstrom P J 1996 Nanoimprint lithography *Americian Vac. Soc.* **14** 4129–33

[56] Guo L J 2007 Nanoimprint lithography: methods and material requirements *Adv. Mater* **19** 495–513

[57] Laibinis P E and Whitesides G M 1992 of copper slow the onto the surfaces (SAMs) derived from adsorption of n-alkanethiols monolayers *J. Am. Chem. Soc.* **114** 9022–8

[58] Ihs A and Liedberg B 1999 Infrared study of ethyl and octyl xanthate ions adsorbed on metallic and sulfidized copper and silver surfaces *Langmuir* **10** 734–40

[59] Ulman A and Tillman N 1989 Self-assembling double layers on gold surfaces: the merging of two chemistries *Langmuir* **5** 1418–20

[60] http://efutures.group.shef.ac.uk/publictions/pdf/127_12.%20James%20Craven%20

[61].Garipcan B, Winters J, Atchison J S, Cathell M D, Schiffman J D, Leaffer O D, Nonnenmann S S, Schauer C L, Pişkin E, Nabet B and Spanier J E 2008 Controllable formation of nanoscale patterns on TiO2 by conductive-AFM nanolithography *Langmuir* **24** 8944–9

[62] Sugimura H 2002 Organosilane self-assembled monolayers formed at the vapour/solid interface *Surf. Interface Analy.* 34 550–554

[63] Schreiber F 2000 Structure and growth of self-assembling monolayers *Prog. Surf. Sci.* **65** 151–257

[64] Brittain W J and Minko S 2007 A structural definition of polymer brushes *J. Polym. Sci. Part A Polym. Chem.* **45** 3505–12

[65] Azzaroni O 2012 Polymer brushes here, there, and everywhere: Recent advances in their practical applications and emerging opportunities in multiple research fields *J. Polym. Sci. Part A Polym. Chem.* **50** 3225–58

[66] Liu X, Guo S and Mirkin C A. 2003 Surface and site-specific ring-opening metathesis polymerization initiated by dip-pen nanolithography *Angew. Chemie.* **115** 4933–7

[67] Voccia S, Bech L, Gilbert B, Jérôme R and Jérôme C 2004 Preparation of poly(epsilon-caprolactone) brushes at the surface of conducting substrates *Langmuir* **20** 10670–8

[68] Brinks M K and Studer A 2009 Polymer brushes by nitroxide-mediated polymerization *Macromol Rapid Commun.* **30** 1043–57

[69] Sokolov I Y and Henderson G S 2002 Simulation of the observability of atomic defects by atomic force microscopy in contact and non-contact modes *Surf. Sci.* **499** 135–40

[70] Stefanis, A D Tomlinson 1997 *Surface analysis - The principal techniques* (John Wiley & Sons)

[71] Monolayers S, Colburn T J and Leggett G J 2007 Influence of solvent environment and tip chemistry on the contact mechanics of tip-sample interactions in friction force microscopy *Langmuir* **23** 4959–64

[72] Hurley C R and Leggett G J 2009 2/3 *ACS Appl. Mater Inter.* **1** 4179–83

[73] Zhong Q, Inniss D, Kjoller K and Elings V B 1993 Fractured polymer/silica fiber surface studied by tapping mode atomic force microscopy *Surf. Sci.* **290** L688–L692

[74] Manhee L and Wonho J 2006 General Theory of Amplitude-Modulation Atomic Force Microscopy *Phys. Rev. Lett.* 97, 036104 -4

[75] Pe Â and Garcõ R 2002 Dynamic atomic force microscopy methods *Surf. Sci. Rep.* **47** 197–301

[76] Ebeling D and Solares S D 2013 Amplitude modulation dynamic force microscopy imaging in liquids with atomic resolution: comparison of phase contrasts in single and dual mode operation. *Nanotechnology* **24** 135702

[77] Aranta Vilalta-Clemente K G 1996 Principles of atomic force microscopy 1-10

[78] Hansma P K, Cleveland J P, Radmacher M, Walters D A, Hillner P E, Bezanilla M, Fritz M, Vie D, Hansma H G, Prater C B, Massie J, Fukunaga L, Gurley J and Elings V 1994 Tapping mode atomic force microscopy in liquids *Appl. Phys. Lett.* **64** 1738-40

[79] Putman C A J, Wetf K Van Der, Grooth B G De, Hulst N F Van and Greve J 1994 Tapping mode atomic force microscopy in liquid *Appl. Phys. Lett.* **64** 2454-56

[80] Stefanis A D and Tomlinson A A G 2001 *Scanning Probe Microscopies: from Surface Structure to Nano-scale Engineering* (Trans Tech Publication)

[81] Martin Y, Williams C C and Wickramasinghe H K 1987 Atomic force microscope–force mapping and profiling on a sub 100-Å scale *J. Appl. Phys.* **61** 4723

[82] Albrecht T R, Grütter P, Horne D and Rugar D 1991 Frequency modulation detection using high-Q cantilevers for enhanced force microscope sensitivity *J. Appl. Phys.* **69** 668

[83] Higgins M J, Riener C K, Uchihashi T, Sader J E, McKendry R and Jarvis S P 2005 Frequency modulation atomic force microscopy: a dynamic measurement technique for biological systems *Nanotechnology* **16** S85–S89

[84] Wang D, Tsau L and Wang K L 1994 Nanometer-structure writing on Si(100) surfaces using a non-contact-mode atomic force microscope *Appl. Phys. Lett.* **65** 1415

[85] Leggett G J 2003 Friction force microscopy of self-assembled monolayers: probing molecular organisation at the nanometre scale *Anal. Chim. Acta.* **479** 17–38

[86] Frisbie C D, Rozsnyai L F, Noy A, Wrighton M S and Lieber C M 1994 Functional group imaging by chemical force microscopy *Science* **265** 2071-4

[87] Ogletree D F, Carpick R W and Salmeron M 2007 Calibration of frictional forces in atomic force microscopy *Rev. Sci. Instruments* **67** 3298–306

[88] Meyer G and Amer N M 1990 Optical-beam-deflection atomic force microscopy: The NaCl (001) surface *Appl. Phys. Lett.* **56** 2100

[89] Brewer N J, Beake B D and Leggett G J 2001 Friction force microscopy of self-assembled monolayers : influence of adsorbate alkyl chain length , terminal group chemistry , and scan speed *Langmuir* **17** 1970–4

[90] Song Q and Grainger D W 1996 Structure and frictional properties of self-assembled surfactant monolayers *Langmuir* **69** 1235–44

[91] Beake B D, Leggett G J and Shipway P H 1999 Frictional, adhesive and mechanical properties of polyester films probed by scanning force microscopy *Surf. Interface Anal.* **1091** 1084–91

[92] Deng Z, Smolyanitsky A, Li Q, Feng X-Q and Cannara R J 2012 Adhesion-dependent negative friction coefficient on chemically modified graphite at the nanoscale *Nat. Mater* **11** 1032–7

[93] Hertz H 1881 *Über die Berührung fester elastischer Körper, Journal für die reine und angewandte J. Mathematic* **92** 156-71

[94] Heinz W F and Hoh J H 1999 Spatially resolved force spectroscopy of biological surfaces using the atomic force microscope *Nanotechnology* **17** 143–50

[95] Butt H-J, Cappella B and Kappl M 2005 Force measurements with the atomic force microscope: Technique, interpretation and applications *Surf. Sci. Rep.* **59** 1–152

[96] Sarah E Cross, Yu-Sheng Jin, Julianne Tondre, Roger Wong, JianYu Rao and James K Gimzewski 2008 AFM-based analysis of human metastatic cancer cells *Nanotechnology* **19** 384003-11

[97] Guck J, chinkinger S, Lincoln B, Wottawah F, Ebert S, Romeyke M, Lenz D, Erickson H M, Ananthakrishnan R, Mitchell D, Käs J, Ulvick S and Bilby C 2005 Optical deformability as an inherent cell marker for testing malignant transformation and metastatic competence *Biophys. J.* **88** 3689–98

[98] Sokolov I 2007 Atomic force microscopy in cancer cell research *In Nalwa HN, Webster T editors Cancer Nanotechnology Amercian Scientific Publishers* 1–17

[99] Feng S and Huang G 2001 Effects of emulsifiers on the controlled release of paclitaxel (Taxol) from nanospheres of biodegradable polymers. *J. Control Release* **71** 53–69

[100] Alberts B, Bray D Lewis J and Raff M 2008 *Molecular biology of the cell* (Garland Science)

[101] Eric Kandel, James Schwartz and Thomas J 2000 *Principles of Neural Science* (McGraw-Hill Professional)

[102] Williams R W and Herrup K 1988 The control of neuron number *Annu. Rev. Neurosci.* **11** 423–53

[103] Chen T, Jordan R and Zauscher S 2011 Extending micro-contact printing for patterning complex polymer brush microstructures *Polymer* **52** 2461–7

[104] Mueller B K 1999 Growth cone guidance: first steps towards a deeper understanding *Annu. Rev. Neurosci.* **22** 351–88

[105] Sotelo C 2004 The neurotropic theory of Santiago Ramón y Cajal *IBRO Hist. Neurosci.* 1–6

[106] Keshishian H 2004 Ross Harrison's the outgrowth of the nerve fiber as a mode of protoplasmic movement *J. Exp. Zool. A Comp. Exp. Biol.* **301** 201–3

[107] Gordon-Weeks P R 2004 Microtubules and growth cone function *J. Neurobiol.* **58** 70–8

[108] Xiong Y, Lee A C, Suter D M and Lee G U 2009 Topography and nanomechanics of live neuronal growth cones analyzed by atomic force microscopy *Biophys. J.* **96** 5060–72

[109] http://www.uni-leipzig.de/~pwm/web/?section=introduction&page=neurons

[110] Tojima T and Ito E 2004 Signal transduction cascades underlying de novo protein synthesis required for neuronal morphogenesis in differentiating neurons *Prog. Neurobiol.* **72** 183–93

[111] Pawlizak S 2009 *Diploma Thesis Mechanosensitive Behavior of Neuronal Growth Cones* (University of Leipzig)

[112] Koch D 2007 *Diploma Thesis Stochastic Lamellipodium Dynamics and Forces in Cell Motility* (University of Leipzig)

[113] Wissner-Gross Z D, Scott M a, Ku D, Ramaswamy P and Fatih Yanik M 2011 Large-scale analysis of neurite growth dynamics on micropatterned substrates *Integr. Biol.* **3** 65–74

[114] Arimura N and Kaibuchi K 2007 Neuronal polarity : from extracellular signals to intracellular mechanisms *Nat. Rev. Neurosci.* **8** 194–205

[115] Barnes A P and Polleux F 2009 Establishment of axon-dendrite polarity in developing neurons *Annu. Rev. Neurosci.* **32** 347–81

[116] Susan E. Mackinnon A L 1988 *Surgery of the Peripheral Nerve* (Thieme Medical Publishers)

[117] http://nervestudy.com/wallerian-degeneration/

[118] Gaudet A D, Popovich P G and Ramer M S 2011 Wallerian degeneration: gaining perspective on inflammatory events after peripheral nerve injury *J. Neuro inflammation* **8** 110

[119] Thompson D M and Buettner H M 2006 Neurite outgrowth is directed by schwann cell alignment in the absence of other guidance cues *Ann. Biomed. Eng.* **34** 669–76

[120] Bunge R P 1994 The role of the Schwann cell in trophic support and regeneration. *J. Neurol.* **242** S19–21

[121] Bunge B Y R P 1987 Tissue culture observations relevant to the study of axon-schwann cell interactions during peripheral nerve development *J. exp. Biol.* **132** 21–34

[122] Dubey N, Letourneau P C and Tranquillo R T 1999 Guided neurite elongation and schwann cell invasion into magnetically aligned collagen in simulated peripheral nerve regeneration *Exp. Neurol.* **158** 338–50

[123] Hospital Q V, Grinstead E, Hospital N P and Volume E 1995 Orientated mats of fibronectin material for use in peripheral as a conduit *J. Hand. Surg. Br.* **20** 429–36

[124] Clark P, Britland S and Connolly P 1993 Growth cone guidance and neuron morphology on micropatterned laminin surfaces *J. Cell Sci.* **105** 203–12

[125] Sorribas H, Padeste C and Tiefenauer L 2002 Photolithographic generation of protein micropatterns for neuron culture applications *Biomaterials* **23** 893–900

[126] Chang W C and Sretavan D W 2008 Novel high-resolution micropatterning for neuron culture using polylysine adsorption on a cell repellant, plasma-polymerized background *Langmuir* **82** 13048–57

[127] Clark P, Britland S and Connolly P 1993 Growth cone guidance and neuron morphology on micropatterned laminin surfaces *J. Cell Sci.* **105** 203–12

[128] Tai H C and Buettner H M 1998 Neurite outgrowth and growth cone morphology on micropatterned surfaces *Biotechno. Prog.* **14** 364–70

[129] Kofron C M, Fong V J and Hoffman-Kim D 2009 Neurite outgrowth at the interface of 2D and 3D growth environments *J. Neural. Eng.* **6** 160

[130] Wang S and Cai L 2010 Polymers for fabricating nerve conduits *Int. J. Polym. Sci.* **2010** 1–20

[131] Daud M F 2013 *P.hD Thesis An organized 3D in vitro model for peripheral nerve studies* (University of Sheffield)

[132] Curley J L, Jennings S R and Moore M J 2011 Fabrication of micropatterned hydrogels for neural culture systems using dynamic mask projection photolithography *J. Vis. Exp.* **48** 1–6

[133] Gonzalez-Cruz R D, Fonseca V C and Darling E M 2012 Cellular mechanical properties reflect the differentiation potential of adipose-derived mesenchymal stem cells *Proc. Natl. Acad. Sci.* **109** 1523–9

[134] Chan E and Ulfendahl M 1999 Mechanically evoked shortening of outer hair cells isolated from the guinea pig organ of Corti *Hear Res.* **128** 166–74

[135] Chan E and Ulfendahl M 1997 Relationship between stiffness, internal cell pressure and shape of outer hair cells isolated from the guinea-pig hearing organ *Acta. Physiol. Scand.* **161** 533–9

[136] Wang N and Stamenović D 2000 Contribution of intermediate filaments to cell stiffness, stiffening, and growth *Am. J. Physiol. Cell Physi.* **279** 188–94

[137] Bertaud J, Qin Z and Buehler M J 2010 Intermediate filament-deficient cells are mechanically softer at large deformation: a multi-scale simulation study *Acta. Biomater* **6** 2457–66

[138] Haga H, Sasaki S, Kawabata K, Ito E, Ushiki T and Sambongi T 2000 Elasticity mapping of living broblasts by AFM and immuno uorescence observation of the cytoskeleton *Ultramicroscopy* **82** 253–8

[139] Wagh A A, Roan E, Chapman K E, Desai L P, Rendon D A, Eckstein E C and Waters C M 2008 Localized elasticity measured in epithelial cells migrating at a wound edge using atomic force microscopy *Am. J. Physiol. Lung Cell Mol. Physiol.* **1** 54–60

[140] Faria E C, Ma N, Gazi E, Gardner P, Brown M, Clarke N W and Snook R D 2008 Measurement of elastic properties of prostate cancer cells using AFM *Analyst.* **133** 1498–500

[141] Lieber S C, Aubry N, Pain J, Diaz G, Kim S-J and Vatner S F 2004 Aging increases stiffness of cardiac myocytes measured by atomic force microscopy nanoindentation *Am. J. Physiol. Heart Circ Physiol.* **287** H645–51

[142] Mitchison B Y J M and Swann M M 1954 The mechanical properties of the cell surface *J. Exp. Biol.* **32** 734–750.

[143] Rand R 1964 Mechanical properties of the red cell membrane *Biophys. J.* **4** 303–16

[144] Derganc J, Bozic B, Svetina S and Zeks B 2000 Stability analysis of micropipette aspiration of neutrophils *Biophys. J.* **79** 153–62

[145] Artmann G, Sung K and Horn T 1997 Micropipette aspiration of human erythrocytes induces echinocytes via membrane phospholipid translocation *Biophys. J.* **72** 1434–41

[146] Hochmuth R M 2000 Micropipette aspiration of living cells *J. Biomech.* **33** 15–22

[147] McPhee G M 2012 *P.hD elasticity as an indicator of cell responses to topography and chemically modified surfaces : an atomic force microscopy approach* (University of Glagow)

[148] Ashkin A 1970 Acceleration and trapping of particles by radiation pressure *Phys. Rev. Lett.* **24** 24–7

[149] Ashkin A and Dziedzic J M 1987 Optical trapping and manipulation of viruses and bacteria. *Science* **235** 1517–20

[150] Koss B A and Grier D G 2003 Optical peristalsis *Appl. Phys. Lett.* **82** 3985

[151] M P MacDonald, G C Spalding and K Dholakia 2003 Microfluidic sorting in an optical lattice *Nature* **426** 421–4

[152] Moffitt J R, Chemla Y R, Smith S B and Bustamante C 2008 Recent advances in optical tweezers *Annu. Rev. Biochem.* **77** 205–28

[153] Williams M C 2002 Optical tweezers : measuring piconewton forces *Mol Tech Biophys. Soc.* 1–14

[154] Bockelmann U, Thomen P, Essevaz-Roulet B, Viasnoff V and Heslot F 2002 Unzipping DNA with optical tweezers: high sequence sensitivity and force flips. *Biophys. J.* **82** 1537–53

[155] Wang M D, Yin H, Landick R, Gelles J and Block S M 1997 Stretching DNA with Optical Tweezers *Biophys. J.* **72** 1335–46

[156] Neuman K C and Block S M 2004 Optical trapping. *Rev. Sci. Instrum.* **75** 2787–809

[157] Kollmannsberger P, Mierke C T and Fabry B 2011 Nonlinear viscoelasticity of adherent cells is controlled by cytoskeletal tension *Soft Matter* **7** 3127

[158] Feneberg W, Aepfelbacher M and Sackmann E 2004 Microviscoelasticity of the apical cell surface of human umbilical vein endothelial cells (HUVEC) within confluent monolayers *Biophys. J.* **87** 1338–50

[159] Lunov O, Bespalova S and Zablotskii V 2007 A model for magnetic bead microrheometry *journel Magn. Magn. Mater* **311** 162–5

[160] Radmacher M, Fritz M, Kacher C M, Cleveland J P and Hansma P K 1996 Measuring the viscoelastic properties of human platelets with the atomic force microscope *Biophys. J.* **70** 556–67

[161] Rotsch C, Braet F, Wisse E and Radmacher M 1997 AFM imaging and elasticity measurements on living rat liver macrophages *Cell Biol. Int.* **21** 685–96

[162] Dvorak J A and Nagao E 1998 Kinetic analysis of the mitotic cycle of living vertebrate cells by atomic force microscopy *Exp. Cell Res.* **242** 69–74

[163] Karl I and Bereiter-Hahn J 1998 Cell contraction caused by microtubule disruption is accompanied by shape changes and an increased elasticity measured by scanning acoustic microscopy *Cell Biochem. Biophys.* **29** 225–41

[164] Wu H W, Kuhn T and Moy V T 1998 Mechanical properties of L929 cells measured by atomic force microscopy: effects of anticytoskeletal drugs and membrane crosslinking *Scanning* **20** 389–97

[165] Rotsch C and Radmacher M 2000 Drug-induced changes of cytoskeletal structure and mechanics in fibroblasts : An atomic force microscopy study *Biophys. J.* **78** 520–35

[166] Han D, Ma W, Liao F and Chen D 2004 Intracellular structural changes under the stress of applied force at a nanometre range investigated by atomic force microscopy *Nanotechnology* **15** 120–6

[167] Han D, Ma W, Liao F and Chen D Intracellular structural changes under the stress of applied force at a nanometre range investigated by atomic force *Nanotechnology* **15** 120-126

[168] Goldmann W H, Galneder R, Ludwig M, Kromm A and Ezzell R M 1998 Differences in F9 and 5.51 cell elasticity determined by cell poking and atomic force microscopy *FEBS Lett.* **424** 139–42

[169] Lekka M, Laidler P, Gil D, Lekki J, Stachura Z and Hrynkiewicz a Z 1999 Elasticity of normal and cancerous human bladder cells studied by scanning force microscopy *Eur. Biophys. J.* **28** 312–6

[170] Berdyyeva T K, Woodworth C D and Sokolov I 2005 Human epithelial cells increase their rigidity with ageing in vitro : direct measurements *Phys. Med. Biol.* **50** 81–92

[171] Strasser S, Zink A, Kada G, Hinterdorfer P, Peschel O, Heckl W M, Nerlich A G and Thalhammer S 2007 Age determination of blood spots in forensic medicine by force spectroscopy *Forensic Sci. Int.* **170** 8–14

[172] Kiani A, Venkatakrishnan K, Tan B and Venkataramanan V 2011 Maskless lithography using silicon oxide etch-stop layer induced by megahertz repetition femtosecond laser pulses *Opt. Express* **19** 10834–42

[173] www.bouldernonlinearsystems.com

[174] Leach J, Wulff K, Sinclair G, Jordan P, Courtial J, Thomson L, Gibson G, Karunwi K, Cooper J, Laczik Z J and Padgett M 2006 Interactive approach to optical tweezers control *Appl. Opt.* **45** 897–903

[175] Wilkinson T D, Henderson C D, Leyva D G and Crossland W A. 2006 Phase modulation with the next generation of liquid crystal over silicon technology *J. Mater Chem.* **16** 3359-65

[176] Lee D H 2010 Optical System with 4 ㎛ resolution for maskless lithography using digital micromirror device *J. Opt. Soc. Korea* **14** 266–76

[177] Rosa L G and Liang J 2009 Atomic force microscope nanolithography: dip-pen, nanoshaving, nanografting, tapping mode, electrochemical and thermal nanolithography *J. Phys. Condens. Matter* **21** 483001

[178] Piner R D 1999 dip-Pen nanolithography *Science* **283** 661–3

[179] Stephen Y. Chou P R K P J R 1996 mprint Lithography with 25-nanometer Resolution *Science* **272** 85–6

[180] Garcia R, Martinez R V and Martinez J 2006 Nano-chemistry and scanning probe nanolithographies *Chem. Soc. Rev.* **35** 29–38

[181] Slot E, Wieland M J, De Boer G, Kruit P, Ten B G F, Houkes A M C, Jager R, van D P T, Peijster J J M, Steenbrink S W H K, Teepen T F, Veen V A H V and Kampherbeek B J Mapper: high throughput maskless lithography *Proc. of SPIE* **6921** 69211P-1

[182] Pease R F 2005 Maskless lithography *Microelectron Eng.* **78-79** 381–92

[183] Parviz B A, Ryan D and Whitesides G M 2003 Using self-assembly for the fabrication of nano-scale electronic and photonic devices *IEEE Trans. Adv. Packag* **26** 233–41

[184] Mathieu M, Friebe A, Franzka S, Ulbricht M and Hartmann N 2009 Surface-initiated polymerization on laser-patterned templates: morphological scaling of nanoconfined polymer brushes *Langmuir* **25** 12393–8

[185] Ionov L, Sapra S, Synytska A, Rogach A. L, Stamm M and Diez S 2006 Fast and spatially resolved environmental probing using stimuli-responsive polymer layers and fluorescent nanocrystals *Adv. Mater* **18** 1453–7

[186] Ulbricht M 2006 Advanced functional polymer membranes *Polymer* **47** 2217–62

[187] Wu T, Efimenko K, Vlc P and Genzer J 2003 Formation and Properties of Anchored Polymers with a Gradual Variation of Grafting Densities on Flat Substrates *Macromolecules* **7** 2448–53

[188] Edmondson S, Nguyen N T, Lewis A L and Armes S P 2010 Co-nonsolvency effects for surface-initiated poly(2-(methacryloyloxy)ethyl phosphorylcholine) brushes in alcohol/water mixtures *Langmuir* **26** 7216–26

[189] K Nagarajan and K Levon A M 2000 Nucleating agents in polypropylene *J. Therm. Anal. Calorim*. **59** 497-508

[190] Ahmad S A A, Wong L S, Hobbs J K, Leggett G J and Micklefield J 2009 Micrometer and nanometer-scale photopatterning using 2-nitrophenylpropyloxycarbonyl-protected aminosiloxane monolayers *J. Am. Chem. Soc*. **13** 1513–22

[191] Beier M and Hoheisel J D 2000 Production by quantitative photolithographic synthesis of individually quality checked DNA microarrays *Nucleic Acids Res.* **28** E11

[192] Edmondson S, Nguyen N T, Lewis A L and Armes S P 2010 Co-nonsolvency effects for surface-initiated poly(2-(methacryloyloxy)ethyl phosphorylcholine) brushes in alcohol/water mixtures *Langmuir* **26** 7216–26

[193] ul Haq E, Liu Z, Zhang Y, Ahmad S A A, Wong L-S, Armes S P, Hobbs J K, Leggett G J, Micklefield J, Roberts C J and Weaver J M R 2010 Parallel scanning near-field photolithography: the snomipede *Nano Lett.* **10** 4375–80

[194] Moh L C H, Losego M D and Braun P V 2011 Solvent quality effects on scaling behavior of poly(methyl methacrylate) brushes in the moderate- and high-density regimes. *Langmuir* **27** 3698–702

[195] Mathieu M, Friebe A, Franzka S, Ulbricht M and Hartmann N 2009 Surface-initiated polymerization on laser-patterned templates: morphological scaling of nanoconfined polymer brushes *Langmuir* **25** 12393–8

[196] Dickson B J 2002 Molecular mechanisms of axon guidance *Science* **298** 1959–64

[197] Charron F and Tessier-Lavigne M 2005 Novel brain wiring functions for classical morphogens: a role as graded positional cues in axon guidance *Development* **132** 2251–62

[198] Liu F, Burgess J, Mizukami H and Ostafin A 2003 Sample preparation and imaging of erythrocyte cytoskeleton with the atomic force microscopy *Cell Biochem. Biophys.* **38** 14–6

[199] Mcnally H A, Rajwa B, Sturgis J and Robinson J P 2005 Comparative three-dimensional imaging of living neurons with confocal and atomic force microscopy *Nanotechnology* **142** 177–84

[200] Johnson W T 2008 *Live Cell Imaging with the AFM* pp1-7

[201] Takeuchi M, Miyamoto H, Sako Y, Komizu H and Kusumi A 1998 Structure of the erythrocyte membrane skeleton as observed by atomic force microscopy *Biophys. J.* **74** 2171–83

[202] Ponce L, Berquand A, Petersen M and Hafner M 2010 Combining atomic force microscopy and live cell imaging to study calcium responses in dorsal root ganglion neurons to a locally applied mechanical stimulus *Microscopy* **1** 530–6

[203] Spedden E and Staii C 2013 Neuron biomechanics probed by atomic force microscopy *Int. J. Mol. Sci.* **14** 16124–40

[204] Martin M, Benzina O, Szabo V, Végh A-G, Lucas O, Cloitre T, Scamps F and Gergely C 2013 Morphology and nanomechanics of sensory neurons growth cones following peripheral nerve injury *PLoS One* **8** e56286

[205] Yunxu S, Danying L, Yanfang R, Dong H and Wanyun M 2006 Three-dimensional structural changes in living hippocampal neurons imaged using magnetic AC mode atomic force microscopy *J. Electron Microsc.* **55** 165–72

[206] Tojima T, Yamane Y, Takahashi M and Ito E 2000 Acquisition of neuronal proteins during differentiation of NG108-15 cells *Neurosci. Res.* **37** 153–61

[207] Kaewkhaw R, Scutt A M and Haycock J W 2011 Anatomical site influences the differentiation of adipose-derived stem cells for schwann-cell phenotype and function *Glia* **749** 734–49

[208] Laishram J, Kondra S, Avossa D, Migliorini E, Lazzarino M and Torre V 2009 A morphological analysis of growth cones of DRG neurons combining atomic force and confocal microscopy *J. Struct. Biol.* **168** 366–77

[209] Markham J and Fifková E 1986 Actin filament organization within dendrites and dendritic spines during development *Brain Res.* **392** 263–9

[210] Salzer J L and Bunge R P 1980 Studies of Schwann cell proliferation. I. An analysis in tissue culture of proliferation during development, Wallerian degeneration, and direct injury *J. Cell Biol.* **84** 739–52

[211] Small J V, Herzog M and Anderson K 1995 Actin filament organization in the fish keratocyte lamellipodium *J. Cell Biol.* **129** 1275–86

[212] Ponce L, Berquand A, Petersen M and Hafner M 2010 Combining atomic force microscopy and live cell imaging to study calcium responses in dorsal root ganglion neurons to a locally applied mechanical stimulus *Microsc. Sci. Technol. Appl. Educ.* **1** 530–6

[213] Kawabata K, Ishizuka H, Nitta T, Haga H, Ito E, Abe K, Ushiki T and Sambongi T 1999 Time dependent viscoelastic image of living nerve cells using AFM *AIP Conf. Proc.* **235** 235–9

[214] Rauch P, Heine P, Goettgens B and Käs J a 2013 Different modes of growth cone collapse in NG 108-15 cells *Eur. Biophys. J.* **42** 591–605

[215] Grzywa E L, Lee A C, Lee G U and Suter D M 2006 High-resolution analysis of neuronal growth cone morphology by comparative atomic force and optical microscopy *J. Neurobiol.* **66** 1529–43

[216] Mustata M, Ritchie K and McNally H A 2010 Neuronal elasticity as measured by atomic force microscopy *J. Neurosci. Methods* **186** 35–41

[217] Spedden E, White J D, Naumova E N, Kaplan D L and Staii C 2012 Elasticity maps of living neurons measured by combined fluorescence and atomic force microscopy *Biophys. J.* **103** 868–77

[218] Heredia A, Bui C C, Suter U, Young P and Schäffer T E 2007 AFM combines functional and morphological analysis of peripheral myelinated and demyelinated nerve fibers *Neuroimage* **37** 1218–26

[219] Fuhs T, Reuter L, Vonderhaid I, Claudepierre T and Käs J A 2013 Inherently slow and weak forward forces of neuronal growth cones measured by a drift-stabilized atomic force microscope *Cytoskeleton* **70** 44–53

[220] https://support.asylumresearch.com/forum/content.php?4-Software

[221] Carl P and Schillers H 2008 Elasticity measurement of living cells with an atomic force microscope: data acquisition and processing *Eur. J. of physic.* **457** 551–9

[222] Mahaffy R E, Park S, Gerde E, Käs J and Shih C K 2004 Quantitative analysis of the viscoelastic properties of thin regions of fibroblasts using atomic force microscopy *Biophys. J.* **86** 1777–93

[223] Sirghi L, Ponti J, Broggi F and Rossi F 2008 Probing elasticity and adhesion of live cells by atomic force microscopy indentation *Eur. Biophys. J.* **37** 935–45

[224] Maciaszek J L, Andemariam B and lykotrafitis G 2011 microelasticity of red blood cells in sickle cell disease *J. Strain Anal*. **46** 368–79

[225] Smith B A 2004 *P.hD Thesis Cellular Biomechanics Investigated by Atomic Force Microscopy* (McGill University, Montréal)

[226] Ketene A N and Schmelz E M 2011 *The AFM study of ovarian cell structural mechanics in the progression of cancer* (Virginia Polytechnic and State University)

[227] Kuznetsova T G, Starodubtseva M N, Yegorenkov N I, Chizhik S A and Zhdanov R I 2007 Atomic force microscopy probing of cell elasticity *Micron.* **38** 824–33

[228] Mathur A B, Collinsworth A M, Reichert W M, Kraus W E and Truskey G a 2001 Endothelial, cardiac muscle and skeletal muscle exhibit different viscous and elastic properties as determined by atomic force microscopy *J. Biomech.* **34** 1545–53

[229] Sen S, Subramanian S and Discher D E 2005 Indentation and adhesive probing of a cell membrane with AFM: theoretical model and experiments *Biophys. J.* **89** 3203–13

[230] Domke J and Radmacher M 1998 Measuring the Elastic Properties of Thin Polymer Films with the Atomic Force Microscope *Langmuir* **7463** 3320–5

[231] Pogoda K and Jaczewska J 2012 Depth-sensing analysis of cytoskeleton organization based on AFM data *Eur. Biophys. J.* **42** 79–87

[232] Ketene A N, Schmelz E M, Roberts P C and Agah M 2012 The effects of cancer progression on the viscoelasticity of ovarian cell cytoskeleton structures *Nanomedicine* **8** 93–102

[233] Fung Y 2012 *Blood cell - an overview of studies in hematology* (In Tech)

[234] Sneddon I A N N 1965 the total depth of penetration of the tip of the punch, and for *Int. J. Eng. Sci.* **3** 47–57

[235] Nawaz S, Sánchez P, Bodensiek K, Li S, Simons M and Schaap I A T 2012 Cell visco-elasticity measured with AFM and optical trapping at sub-micrometer deformations *PLoS One* **7** 45297

[236] Shen Y, Sun J L, Zhang A, Hu J and Xu L X 2007 A new image correction method for live cell atomic force microscopy *Phys. Med. Biol.* **52** 2185–96

[237] Rotsch C, Jacobson K and Radmacher M 1999 Dimensional and mechanical dynamics of active and stable edges in motile fibroblasts investigated by using atomic force microscopy *Proc. Natl. Acad. Sci.* **96** 921–6

[238] Spedden E, White J D, Naumova E N, Kaplan D L and Staii C 2012 Elasticity maps of living neurons measured by combined fluorescence and atomic force microscopy *Biophys. J.* **103** 868–77

[239] Kendall M a F, Chong Y F and Cock A 2007 The mechanical properties of the skin epidermis in relation to targeted gene and drug delivery *Biomaterials* **28** 4968–77

[240] Chan E and Ulfendahl M 1997 Relationship between stiffness, internal cell pressure and shape of outer hair cells isolated from the guinea-pig hearing organ *Acta. Physiol. Scand.* **161** 533–9

[241] Fearn L a, Bartoo M L, Myers J A and Pollack G H 1993 An optical fiber transducer for single myofibril force measurement *IEEE Trans. Biomed. Eng.* **40** 1127–32

[242] Laurent V M, Kasas S, Yersin A, Schäffer T E, Catsicas S, Dietler G, Verkhovsky A B and Meister J-J 2005 Gradient of rigidity in the lamellipodia of migrating cells revealed by atomic force microscopy *Biophys. J.* **89** 667–75

[243] Leporatti S, Gerth A, Köhler G, Kohlstrunk B, Hauschildt S and Donath E 2006 Elasticity and adhesion of resting and lipopolysaccharide-stimulated macrophages *FEBS Lett.* **580** 450–4

[244] Rocha M S and Mesquita O N 2007 New tools to study biophysical properties of single molecules and single cells *An Acad. Bras Ciênc.* **79** 17–28

[245] Bausch a R, Möller W and Sackmann E 1999 Measurement of local viscoelasticity and forces in living cells by magnetic tweezers *Biophys. J.* **76** 573–9

[246] Poon B, Rittel D and Ravichandran G 2008 An analysis of nanoindentation in linearly elastic solids *Int. J. Solids Struct.* **45** 6018–33

[247] Jeong S M and Lee H L 2005 Finite element analysis of the tip deformation effect on nanoindentation hardness *Thin Solid Films* **492** 173–9

[248] Whitney H B M and D R 1947 On a test of whether one of two random variables is stochastically larger than the other *Ann. Math. Stat.* **18** 50–60

[249] Ng L, Hung H H, Sprunt A, Chubinskaya S, Ortiz C and Grodzinsky A 2007 Nanomechanical properties of individual chondrocytes and their developing growth factor-stimulated pericellular matrix *J. Biomech.* **40** 1011–23

[250] Magdesian M H, Sanchez F S, Lopez M, Thostrup P, Durisic N, Belkaid W, Liazoghli D, Grütter P and Colman D R 2012 Atomic force microscopy reveals important differences in axonal resistance to injury *Biophys. J.* **103** 405–14

[251] Guilak F, Tedrow J R and Burgkart R 2000 Viscoelastic properties of the cell nucleus. *Biochem. Biophys. Res. Commun.* **269** 781–6

[252] Spedden E, White J D, Naumova E N, Kaplan D L and Staii C 2012 Elasticity maps of living neurons measured by combined fluorescence and atomic force microscopy *Biophys. J.* **103** 868–77

[253] Rimmer S and Haycock J 2011 Scaffolds with controlled mechanical properties for nerve regeneration